

Redox-active Modification of Silica Surfaces via Silicon-Carbon Bond Formation

Redox-aktive Modifizierung von Kieselgeloberflächen durch Bildung von Silizium-Kohlenstoff-Bindungen

DISSERTATION

der Fakultät für Chemie und Pharmazie
der Eberhard-Karls-Universität Tübingen

zur Erlangung des Grades eines Doktors
der Naturwissenschaften

2009

vorgelegt von
NICOLAS PLUMERE

Tag der mündlichen Prüfung:

30. Januar 2009

Dekan:

Prof. Dr. L. Wesemann

1. Berichterstatter:

Prof. Dr. B. Speiser

2. Berichterstatter:

Prof. Dr. L. Wesemann

3. Berichterstatter:

Prof. Dr. J. Pesek

This doctoral thesis was carried at the Institut für Organische Chemie, Fakultät für Chemie und Pharmazie, Eberhard-Karls-Universität Tübingen, Germany, under the guidance of Prof. Dr. Bernd Speiser.

Foremost, I am indebted to Prof. Dr. Bernd Speiser, my supervisor, for his support and excellent guidance during this research work. I thank him not only for providing me with the lab facilities and a perfect working environment but also for his confidence and almost unlimited freedom he has given me. I could not have learnt more about chemistry, scientific research and communication during the course of this work.

I thank all my working group members for valuable discussions and their friendly nature. I would like to specially thank Dr. K. Ludwig, Dr. W. Märkle, C. Tittel, Dr. F. Novak, A. Ruff, B. Sandig, S. Benthin, J. Schaefer, T. Wener, C. Muñoz, T. Reissig and B. Rochier.

I would like to thank Prof. Dr. Hermann A. Mayer, for his comments and discussions which proved to be very valuable for several parts of this thesis.

I thank Prof. Dr. Joseph J. Pesek for welcoming me in his laboratory at the San Jose State University.

I thank the Deutsche Forschungsgemeinschaft (Graduiertenkolleg 441 “Chemie in Interphasen”) and the Max-Buchner-Forschungstiftung for generous support of my thesis.

I thank the members of the Graduiertenkolleg for the enriching cooperation and especially Pavel Levkin and Wolfgang Leis for the many useful and stimulating discussions as well as David Ruiz Abad, Dominik Joosten and Benjamin Dietrich for their assistance in several experiments. I thank Prof. Dr. Klaus Albert, Prof. Dr. Lars Wesemann, Prof. Dr. Hermann A. Mayer and Dr. Egelhaaf for making the successful cooperation with their working groups possible.

I personally thank Prof. Dr. Wilbur H. Campbell for introducing me into the fascinating world of scientific research and for stimulating my interests for chemistry.

Finally, I am thankful to my family and to Stephanie for their support and for the inspiration they gave me.

Parts of this thesis are already accepted for publication:

A. Budny, F. Novak, N. Plumeré, B. Schetter, B. Speiser, D. Straub, H. A. Mayer, M. Reginek, Redox-active silica nanoparticles. Part 1. Electrochemistry and catalytic activity of spherical, nonporous silica particles with nanometric diameters and covalently bound redox-active modifications, *Langmuir* **2006**, *22*, 10605 – 10611.

N. Plumeré, B. Speiser, Redox-active silica nanoparticles Part 2. Photochemical hydrosilylation on a hydride modified silica particle surface for the covalent immobilization of ferrocene *Electrochim. Acta.* **2007**, *53*, 1244 – 1251.

N. Plumeré, B. Speiser, H. A. Mayer, D. Joosten and L. Wesemann, Redox-active silica nanoparticles. Part 3. High-temperature chlorination-reduction sequence for the preparation of silicon hydride modified silica surfaces. *Chem. Eur. J.*, **2009**, *15*, 936 – 946.

Table of content

Abbreviations

| | |
|--|----------|
| Introduction | 1 |
| 1 Stöber particles | 9 |
| 1.1 Introduction | 9 |
| 1.1.1 The Stöber process and mechanism | 9 |
| 1.1.1.1 Hydrolysis | 11 |
| 1.1.1.2 Condensation | 12 |
| 1.1.1.3 Nucleation of primary particles | 12 |
| 1.1.1.4 Aggregation of primary particles | 13 |
| 1.1.1.5 Growth by monomer addition | 14 |
| 1.1.2 General properties | 14 |
| 1.1.2.1 Shape | 15 |
| 1.1.2.2 Porosity | 15 |
| 1.1.2.3 Size distribution | 15 |
| 1.1.2.4 Dimensions | 16 |
| 1.2 Synthesis of the Stöber particles | 18 |
| 1.3 Characterization of the Stöber particles | 20 |
| 1.3.1 Particle shape | 20 |
| 1.3.1.1 Optical microscopy | 20 |
| 1.3.1.2 Scanning electron microscopy | 21 |
| 1.3.2 Particle size and size distribution | 23 |
| 1.3.2.1 SEM measurements | 23 |
| 1.3.2.2 Dynamic light scattering | 25 |
| 1.3.3 specific surface area and pore size distribution | 27 |
| 1.3.3.1 Geometrical specific surface area from SEM | 27 |
| 1.3.3.2 Physisorption isotherms | 27 |
| 1.3.3.2.1 Surface area from the BET method | 29 |
| 1.3.3.2.2 Porosity | 33 |
| 1.3.3.2.2.1 Micropores from the t-method | 33 |
| 1.3.3.2.2.2 Mesopores from the BJH method | 34 |
| 1.4 The optimal particle size | 35 |

| | |
|--|-----------|
| 2 Silicon hydride modified silica surface | 36 |
| 2.1 Preparation of Si–H modified silica materials | 38 |
| 2.2 Physical properties of the Si–H modified silica materials | 40 |
| 2.2.1 Size determination by SEM and DLS | 41 |
| 2.2.2 Surface characterization by nitrogen adsorption-desorption isotherms | 42 |
| 2.3 Chemical properties of the Si–H modified silica materials..... | 43 |
| 2.3.1 The silicon hydride groups (Si–H) | 43 |
| 2.3.2 The silanol groups (Si–OH) | 47 |
| 2.3.3 The nature of the T _H groups | 48 |
| 2.3.4 Nature of the Q groups | 50 |
| 2.3.5 The importance of the chlorination step..... | 52 |
| 2.3.6 Optimal reduction temperature..... | 55 |
| 2.2 Conclusion..... | 55 |
| 3 Silicon-carbon bond formation | 56 |
| 3.1 Free radical initiated hydrosilylation..... | 56 |
| 3.1.1 Photochemical hydrosilylation | 57 |
| 3.1.1.1 Immobilization of 10-undecylenic acid via photochemical hydrosilylation on non-porous M_{SiH} materials..... | 58 |
| 3.1.1.2 Photochemical reaction of 10-undecylenic acid with the porous M_{2SiH} materials | 61 |
| 3.1.2 Thermal hydrosilylation | 61 |
| 3.1.2.1 Immobilization of 1-octadecene via thermal hydrosilylation..... | 62 |
| 3.1.2.2 Immobilization of 1,7-octadiene via thermal hydrosilylation..... | 65 |
| 3.2 Base catalyzed dehydrogenative coupling of Si-H with terminal alkyne | 68 |
| 3.2.1 Base catalyzed dehydrogenative coupling between triethylsilane and 1-hexyne | 70 |
| 3.2.1.1 Kinetics..... | 72 |
| 3.2.1.2 Mechanism | 74 |
| 3.2.2 Dehydrogenative coupling on the Si-H modified silica surface | 75 |

| | |
|--|------------|
| 4 The redox-active molecules | 77 |
| 4.1 Introduction | 77 |
| 4.2 Synthesis of ferrocene derivatives..... | 79 |
| 4.3 Synthesis of diamine(ether–phosphine)dichlororuthenium(II) complexes | 81 |
| 4.4 Synthesis of biphenylamine derivatives 3a-c | 85 |
| 4.4.1 1-bromo-4-(R)-benzenes (4a-c) | 86 |
| 4.4.2 3,5-di- <i>tert</i> -butyl-4-iminocyclohexa-2,5-dien-1-one (5) | 88 |
| 4.4.3 3,5-di- <i>tert</i> -butyl-4-imino-1-(4-R-phenyl)cyclohexa-2,5-dien-1-ol (6a-c) | 89 |
| 4.4.4 3,5-di- <i>tert</i> -butyl-4'-R-1,1'-biphenyl-4-amine (3a-c) | 89 |
| 4.5 Conclusion..... | 89 |
| | |
| 5 Covalent attachment of active molecules on the silica surface via the radical addition of Si-H to C=C bonds | 90 |
| 5.1 Covalent attachment of active molecules on the silica surface via route I | 90 |
| 5.1.1 Ferrocene attachment | 91 |
| 5.1.2 Ruthenium complex attachment..... | 92 |
| 5.1.3 Biphenylamine attachment..... | 92 |
| 5.2 Covalent attachment of active molecules on the silica surface via route II | 93 |
| 5.2.1 Immobilization of ferrocene by means of an activated carboxylic acid modified silica surface | 93 |
| 5.2.2 Free radical induced hydrobromination of carbon-carbon double bond modified silica surface | 97 |
| 5.3 Conclusion..... | 101 |
| | |
| 6 Applications | 102 |
| 6.1 HPLC separation with M2_{SiH} and M2_{C18} | 102 |
| 6.1.1 HPLC separation of SRM 870 with M2_{SiH} | 105 |
| 6.1.2 HPLC separation of SRM 870 with M2_{C18} | 107 |
| 6.1.3 Conclusion..... | 109 |
| 6.2 Electrochemical properties of material M1_{gFc} | 110 |
| 6.2.1 2D arrangement of silica particles on Pt surface..... | 111 |
| 6.2.2 Spontaneous adsorption of M1_{gFc} on platinum electrode surfaces..... | 114 |
| 6.2.3 Electrochemistry of M1_{gFc} | 116 |

| | |
|--|------------|
| 6.2.4 Conclusion..... | 120 |
| 7 Experimental part | 120 |
| 7.1 General procedures..... | 120 |
| 7.2 Materials..... | 121 |
| 7.3 Analytical techniques | 121 |
| 7.4 Synthetic procedures | 127 |
| 8 Appendix | 142 |
| 8.1 Polydispersity index | 142 |
| 8.2 Geometrical specific surface area | 143 |
| 8.3 Surface concentration of ferrocene on M1_{Fc} from cyclic voltammetry | 143 |
| 9 Conclusion..... | 144 |
| References | 149 |

Abbreviations

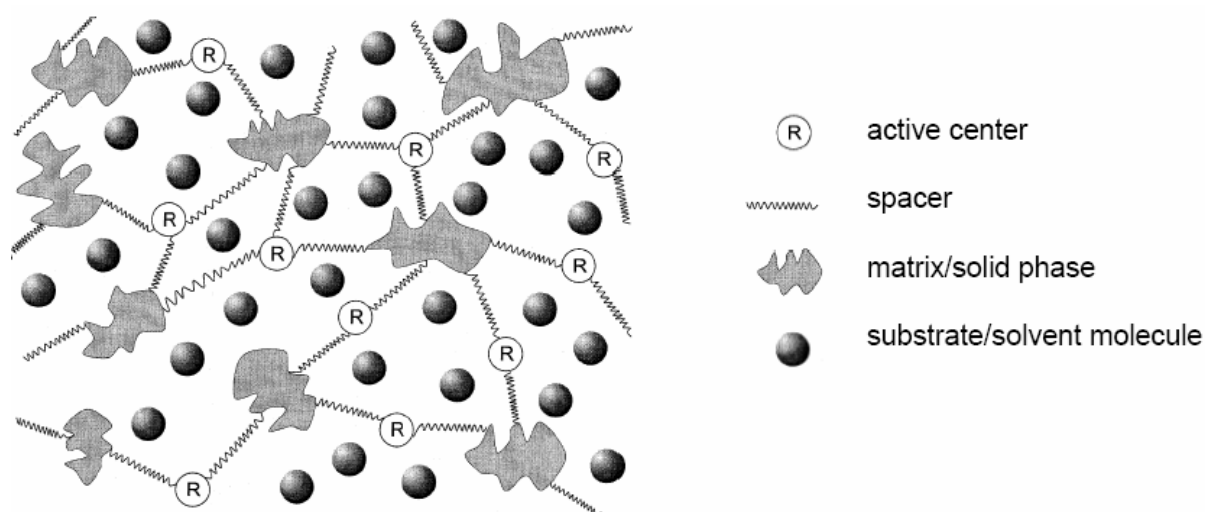
| | |
|--------------|--|
| 2D | Two dimensional |
| 3D | Three dimensional |
| A | Specific surface area |
| Å | Ångström |
| AAS | Atomic absorption spectroscopy |
| ACF | Autocorrelation function |
| aq. | Aqueous |
| arom. | Aromatic |
| A_s | Peak asymmetry |
| BET | Brunauer-Emmet-Teller |
| BJH | Barett-Joyner-Halenda |
| br | Broad (NMR) |
| bp | Boiling point |
| Bu | Butyl |
| C18 | Alkyl chain with 18 carbon atoms |
| CP | Cross-polarization |
| cv | Coefficient of variation |
| CV | Cyclic voltammogram |
| γ | Surface tension |
| Γ | Surface concentration |
| δ | Chemical shift in ppm (NMR) |
| δ | Bending vibration (IR) |
| δ | Diffusion layer thickness (CV) |
| ΔE_p | Peak potential separation (CV) |
| d | Doublet (NMR) |
| d | Diameter |
| D | Diffusion coefficient |
| DLS | Dynamic light scattering |
| dppf | 1,1'-Bis(diphenylphosphino)ferrocene |
| DRIFT | Diffuse reflectance infrared Fourier transform |
| E^0 | Formal potential |
| E_p^{ox} | Oxidation peak potential |

| | |
|--------------------|---|
| E_p^{red} | Reduction peak potential |
| EI | Electron impact |
| ESI | Electrospray ionization |
| Et | Ethyl |
| Et ₂ O | Diethyl ether |
| F | Faraday constant |
| FAB | Fast-atom bombardment |
| Fc | Ferrocene |
| GC | Gas chromatography |
| h | Planck constant |
| IUPAC | International Union of Pure and Applied Chemistry |
| η | Viscosity |
| HPLC | High performance liquid chromatography |
| HR-MS | High resolution mass spectrometry |
| i_p | Peak current |
| IR | Infrared |
| J | Coupling constant |
| k' | Retention factor |
| k_B | Boltzmann constant |
| m | Multiplet (NMR) |
| m | Medium (IR) |
| MAS | Magic angle spinning |
| Me | Methyl |
| MeOH | Methanol |
| M_N | Number average molecular weight |
| mp | Melting point |
| MS | Mass spectroscopy |
| M_W | Weight average molecular weight |
| m/z | Mass to charge ratio (MS) |
| n | Specific amount |
| N | Efficiency |
| N_A | Avogadro constant |
| n_m | Monolayer capacity |
| NMR | Nuclear magnetic resonance |

| | |
|---------------|-------------------------------------|
| v | Scan rate (CV) |
| ν | Stretching vibration (IR) |
| $\tilde{\nu}$ | Wavenumber in cm^{-1} (IR) |
| P° | Saturation pressure |
| P/P° | Relative pressure |
| PDI | Polydispersity index |
| Ph | Phenyl |
| ppm | Parts per millions |
| q | Quartet (NMR) |
| Q | Charge |
| ρ | Density |
| R | Ideal gas constant |
| RT | Room temperature |
| s | Singlet (NMR) |
| s | strong (IR) |
| sat. | Saturated |
| SDP | Size distribution processor |
| SEM | Scanning electron microscopy |
| SRM | Standard reference material |
| STP | Standard temperature and pressure |
| σ | Standard deviation |
| T | Temperature |
| t | Triplet (NMR) |
| t | Time |
| t_0 | Void time |
| TCD | Thermal conductivity detector |
| TEOS | Tetraethoxysilane |
| TES | Triethoxysilane |
| THF | Tetrahydrofuran |
| TMS | Tetramethylsilane |
| UV | Ultraviolet |
| v/v | Volume to volume |
| w | Weak (IR) |
| w/w | Weight to weight |

Introduction

“Interphase” systems [1], in which active molecules are immobilized on a high surface-area matrix with access to a mobile liquid phase, have triggered advances in several fields of chemistry. This concept is based on the covalent attachment of active centers on an inert matrix via a flexible spacer (Scheme 1). The interphase is the region where the stationary phase and a mobile phase interpenetrate.

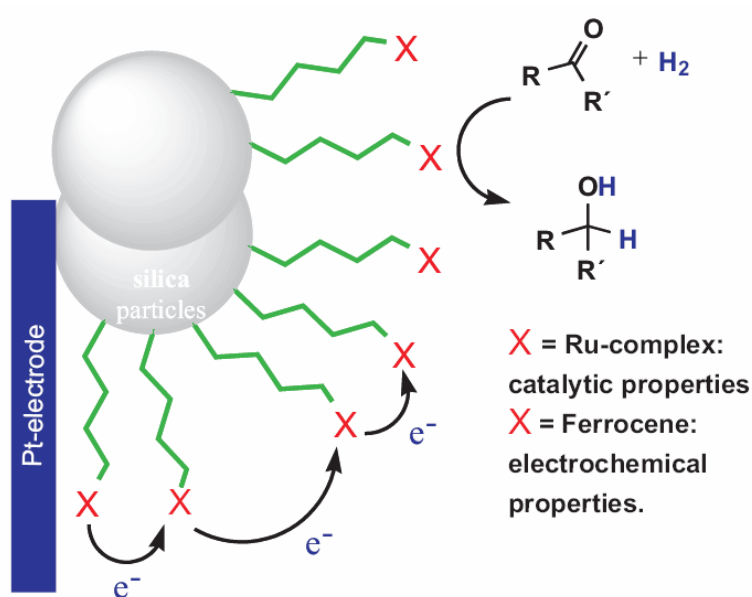


Scheme 1: Schematic representation of an interphase [1].

In the field of catalysis, transition metal complexes are immobilized in such interphase systems in order to combine the advantages of homogeneous (high selectivity) [2] and heterogeneous (simple separation) catalysis [1]. For example, Noyori's hydrogenation catalysts were successfully bound to a polysiloxane matrix with retention of its activity and the ability to be recycled [3].

Interphase systems are also encountered in separation science. For example, in reverse phase HPLC, the organic modification on the solid matrix (e.g. C18 on silica [4]) interpenetrates with the mobile phase and interacts with the selectands in homogeneous conditions. Similarly, in gas chromatography, chiral selectors are covalently attached to polysiloxane supports and interact with the analytes in the gaseous mobile phase [5, 6]. The realization of interphase systems has greatly enhanced the separation power in both HPLC and GC.

Within this context, our particular interest lies in redox-active modifications of interphase systems. The use of redox probes as models for active centers makes it possible to apply electrochemical tools to the interphase systems. In particular, the mobility, the accessibility and the interactions of the active centers, which are essential in both catalysis and separation science, may be investigated with electrochemical methods. For example, the kinetics of a charge transfer between redox centers [7] within an interphase system and the proportion of active molecules that are accessible to the redox reaction may be determined. Electrochemical redox processes may also switch catalytic activity through changes in the oxidation state of the catalyst's central metal atom or the ligand [8, 9].



Scheme 2: Non-porous spherical particles for electrochemical and catalytic applications of interphase systems.

Electrochemical methods are easily applied to the investigation of homogeneous redox-active molecules which can diffuse to the electrode surface where the redox reaction takes place. In the case of an interphase system where porous matrices are used, a direct contact between the electrode surface and the immobilized catalysts is not straightforward. Therefore, as a simplified matrix for the interphase system, we will choose to use spherical non-porous particles of sub-micrometer diameters instead of porous or swellable materials. The presence of all redox centers on the outer surface of the particles provides a unique environment for the modifying molecules (Scheme 2). We regard nonporosity to be an important feature for our

current purpose: Although the possible loading with redox-active materials is inferior to that of highly porous materials, the binding sites are expected to be much more homogeneous, holding all redox-active molecules in a similar environment. Furthermore, electron transfer to the bound molecules should be easier as compared to the corresponding reaction of redox-active centers embedded in bulk systems. Indeed, a direct contact between the immobilized redox-active centers and an electrode surface becomes possible. Finally, a controlled geometry (narrow polydispersity, well defined shape and dimension of particles) may allow to study the intermolecular charge transfer between the redox-active molecules on the particle surface (Scheme 2).

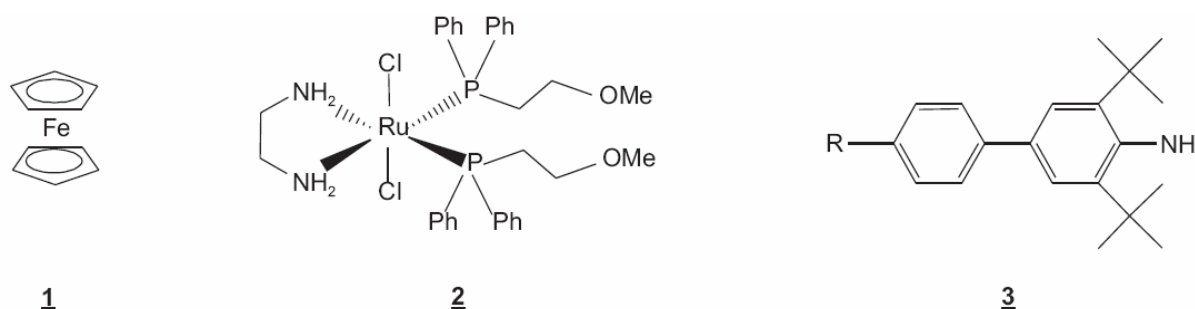
Moreover, non-porous particles have additional advantages for the catalysis itself: The absence of pores facilitates the diffusion of the substrate to the catalytic centers, which is often the rate determining step for reactions in porous systems [10]. Improved accessibility of active centers is expected, especially for large molecules. Also, the homogeneous surface environment of the molecules bound by linkers to the non-porous particles may limit the decrease of catalytic selectivity, which is often observed when immobilizing a catalyst.

Silica particles obtained from the Stöber process [11] are good candidates to fulfill the monodispersity, porosity, size and shape requirements for both catalytic and electrochemical applications. The first objective of this thesis is to synthesize particles with the optimal characteristics with respect to the requirements presented above.

Three different types of redox-active probes were chosen for the modification of the silica particles:

1. Ferrocene (**1**) is a simple one-electron redox system regarded as a standard for various properties, e.g. redox potential [12]. It is a convenient model for the study of redox interactions in an interphase.
2. Ruthenium complexes with a diamine/diphosphine ligand set (Noyori type catalysts) (**2**) exhibit catalytic activity for the hydrogenation of unsaturated ketones and reversible redox properties [13].
3. Sterically hindered biphenyl amines (**3**) are an example of redox-active organic molecules showing stable radical cation states and may be used as electron mediators in redox reactions.

The functionalization of these redox-active molecules to make a covalent attachment with a silica surface possible is one of the objectives of the thesis.

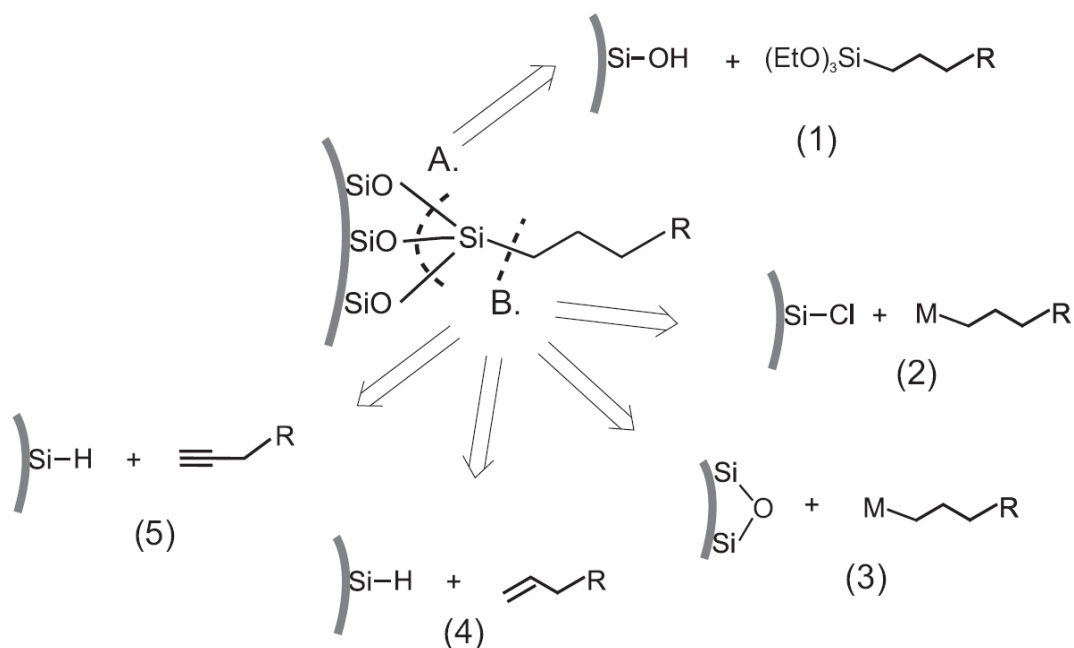


The design of a general method for the covalent attachment of redox-active molecules (or, in general, active centers) on the silica surface is another goal of this work. The basic requirements are as follows:

1. All the synthetic steps on the silica surface are solid phase reactions. Unreacted educts as well as side-products bound to the silica surface can not be separated from the product. Therefore, high yield and selectivity for the desired product are necessary.
2. Sources of impurities should be avoided as much as possible. In particular, the use of transition metals catalyst for the surface reactions is not appropriate since the metal may remain on the silica surface. Transition metal impurities may interfere with both catalytic and electrochemical experiments.
3. The silica surface after modification should not interact with the active molecules. In particular, in the case of catalysis in an interphase, the catalyst is ideally expected to be in homogeneous conditions. Any interactions with the support would induce heterogeneity at the active centers.
4. The stability of the bond must be sufficient to withstand the conditions of both the subsequent modification steps as well as the application of the interphase systems.
5. The binding between the silica surface and the molecular modifiers must be well defined and homogeneous. Indeed, the spacer length and flexibility influences the mobility of the active molecules and therefore, its interactions in the interphase [1].

For the modification of the silica surface with organic modifiers, the hydrolytically stable silicon-carbon bond [14, 15] between the matrix and the spacer could be ideal: The low polarity and high strength of the Si-C bond result in good stability in a wide range of

conditions [16]. Five rather different approaches may be taken toward the preparation of organosilica derivatives via Si-C bonds (Scheme 3).



Scheme 3: Retrosynthetic pathways to modified silica surfaces via Si-C links.

The standard method for silica surface modification involves condensation of the surface silanol groups with functionalized silanes, forming siloxane bonds (silylation, Scheme 3, method A, reaction 1) [1, 17, 20 - 23]. This method is the most straightforward to carry out, and by far the most popular approach for silica modification with chromatographic selectors [21, 22] as well as transition metal catalysts [24, 25]. However, this approach presents several limitations:

1. Because of the use of a trifunctional silane moiety [26], one to three siloxane bonds between the modifier molecules and the silica surface may be formed. The siloxane bonds resulting from silylation are prone to hydrolysis in an aqueous environment [16, 30, 31], in particular at extreme pH values [15, 18, 32 - 35]. The loss of active centers from the solid support occurs primarily by the cleavage of T¹ and T² groups (Figure 1) while the more stable T³ groups [36], are less sensitive due to the higher extent of cross-linking. If only one or two siloxane links are present, the hydrolytic stability of the molecular modification is not sufficient for the conditions of interphase applications. In particular, the leaching of catalysts [37] and HPLC selectors [33, 34] under harsh catalytic and separation conditions are drawbacks directly linked to the silylation method of modification.

2. The formation of T^1 and T^2 , besides T^3 groups from the use of trifunctional silanes also introduces inhomogeneities in the surface attachment. Moreover, the polymerization of the silane group, a second source of inhomogeneities, can not be excluded if trace amounts of water are present. The use of a monofunctional silane [38] yields a homogeneous binding as polymerization is prevented and only one siloxane link can be obtained between the silica surface and the attached molecules. However, the resulting formation of M groups (Figure 1) even worsens the problem of hydrolytic stability.

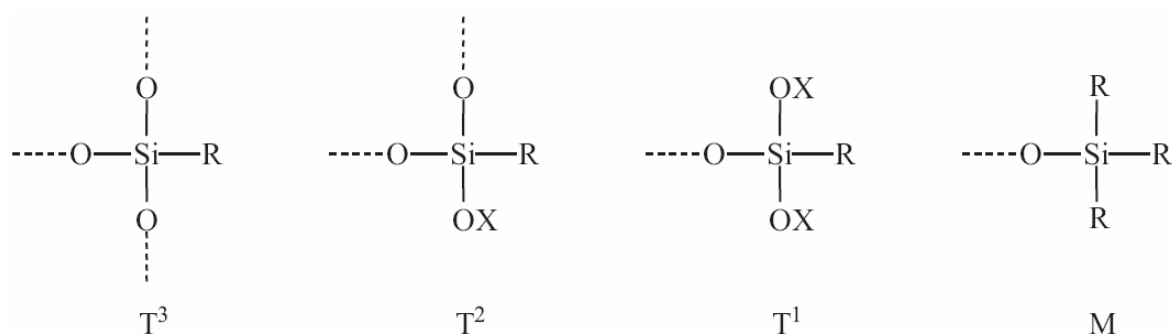


Figure 1: Nomenclature of siloxane species [1]. The dashed lines represent Si-O bonds to the silica bulk.

3. The silylation is not quantitative, and unreacted acidic surface silanol groups remain on the silica surface [39]. These acidic groups may undergo undesired interactions with the active centers or with molecules from the homogeneous phase. In reverse phase HPLC, for example, the presence of silanol groups results in poor separation (tailing) of organic bases [32, 40, 41]. In catalysis, the Si-OH groups can interact with the supported catalyst [42, 43] lowering its specific activity and selectivity [2, 44]. In particular, enantioselectivity of the catalytic reaction may be lost [45, 46]. Moreover, the Si-OH groups may coordinate to transition metal centers, especially to oxophilic early transition metals. For example, organometallic Zr or Ti complexes react with the silica surface [47]. Late transition metals (Rh for example) may bind to the silica surface as well [47]. As defined in the interphase concept, the active centers must be in (pseudo-)homogeneous conditions, and therefore no direct interaction with the matrix is allowed. A possible remedy, capping of the silanol groups [48], is not generally applicable owing to potential reactions of the active centers or ligands with the capping agent [49].

In summary, the silylation method is not optimal for interphase applications due to the poor binding stability and heterogeneity as well as the presence of remaining Si-OH groups.

In order to obtain a homogeneous and stable linkage via T³ groups only, it is desirable to produce a direct Si-C bond [14, 15, 30] between the silica matrix and the spacer (Scheme 3, method B).

The reaction of Si-Cl [50] (Scheme 3, reaction 2) or strained Si-O-Si bonds [30] (Scheme 3, reaction 3) with organometallic reagents produces a Si-C bond. This type of bonding is also obtained from the addition of Si-H groups to terminal C=C bonds (hydrosilylation reaction, Scheme 3, reaction 4) [15, 39] as well as from the coupling of terminal C≡C bond with Si-H groups (dehydrogenative coupling or dehydro-condensation, Scheme 3, reaction 5) [51]. Reactions 2 to 4 were previously performed on silica surfaces [15, 30, 50]. On the other hand, reaction 5 was only described on monomeric silane species [51] so far.

When reactions 2 and 3 are performed on modified silica surfaces (Scheme 3), the organometallic reagents do not yield the monoalkylated silane only. Indeed, Si-O-Si links may be cleaved and more than one Si-C bond per silicon atom is obtained [50]. Therefore, the resulting modified surface shows a poor hydrolytic stability as well as inhomogeneity.

In the case of reaction 4, however, the hydrosilylation reaction yields a modified silica surface with enhanced hydrolytic stability [14]. The absence of a strong base in this reaction prevents the undesired cleavage of the siloxane bonds and a more homogeneous surface modification is expected.

In the choice of the modification method, the presence of the remaining Si-OH must also be considered. These groups are produced by the cleavage of the siloxane bonds in reaction 3 or are produced after hydrolysis of unreacted silicon chloride groups in reaction 2. On the other hand, reaction 4, which consists in the addition of a silicon hydride bond to a carbon-carbon double bond [52] does not involve nor produce any Si-OH group. Moreover, the Si-H groups that might remain after the hydrosilylation reaction, are not expected to undergo interactions in the interphase to the same extent as the silanol groups. Because of their relative inertness, the Si-H groups are potentially optimal starting materials for further surface modification, provided that homogeneous and silanol free silica surfaces with Si-H groups linked via 3 Si-O-Si bonds may be prepared.

In summary, the hydrosilylation reaction, if we consider both the homogenous formation of T³ groups and the resulting inert matrix lacking the Si-OH group, is potentially well suited for the immobilization of active molecules in such interphases. A variety of methods [53], involving catalytic [4, 15, 55] or radical [56] mechanisms have been described to produce Si-

C bonds from Si–H groups on silica surfaces. Considering our interest in electrochemical and catalytic applications, a non-catalytic hydrosilylation is desired in order to avoid metal impurities on the silica surface.

Both the preparation of the desired Si-H starting material and the adequate hydrosilylation reaction need to be adapted to our purposes.

The preparation of the silica particles, their Si-H surface modification, the functionalization of the redox-active molecules with C=C bonds, and the development of an adequate hydrosilylation reaction are the main synthetic challenges of this thesis. In parallel to this new modification pathway, the standard silylation route will be used for the immobilization of the redox-active molecules, mostly for comparison purposes. The possibility to apply a dehydrogenative coupling pathway starting from an alkyne for the silica surface modification will also be explored.

As a last objective, potential applications of the synthesized materials will be studied. In particular, the Stöber particles redox-actively modified via the Si-C bond will be investigated with electrochemical tools in order to determine the redox-active molecule's interactions in this model interphase system. The advantage of the Si-C modification route from a Si-H surface will also be evaluated for general interphase applications. In particular, the HPLC performance of materials resulting from these synthetic strategies will be assessed.

In summary, as the basis for the application of electrochemical tools to interphase systems (investigation of the active centers behavior, control of redox catalysis within the interphases), the aim of this thesis is to synthesize and characterize the solid matrix and the model redox-active molecules as well as to design a surface modification method via the Si-H and Si-C bond formation. The achievement of this goals will be verified by testing the resulting materials in concrete interphase applications.

1 Stöber particles

1.1 Introduction

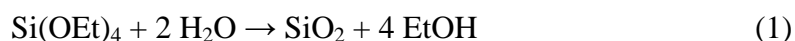
The catalytic and electrochemical applications to be addressed in this work require spherical, non-porous and monodisperse particles. Particles that fulfill these geometrical requirements can be produced from a wide range of organic [57] and inorganic [58 - 61] materials. As a support for the redox-active molecules, inorganic materials are preferred for their mechanical and chemical stability. Within the variety of inorganic materials, silica is the support of choice [32]: Silica particles can be produced in the complete colloidal range and a variety of chemical routes are available for the silica surface functionalization, especially based on derivatization of the surface silanol groups [20 – 23].

Silica particles obtained from the Stöber sol/gel-process [11] are chosen as a support for the immobilization of redox-active molecules in the present work. The rigorous characterization of the particles' physical properties is a key step. Indeed, the matrix physical properties will have to be well-defined for the theoretical interpretation of their electrochemical investigation.

1.1.1 The Stöber process and mechanism

In 1968, Stöber and coworkers reported that, under basic conditions, the hydrolysis of tetraethoxysilane in alcoholic solutions can be controlled to produce monodisperse, non-porous, spherical particles of amorphous silica [11]. The main advantages of the process are that the size of the particles can be tuned by changing the reaction conditions and the reaction proceeds at high concentrations, yielding large amounts of product.

The reaction consists of the hydrolysis of tetraethoxysilane (TEOS) in a water, ethanol and ammonia mixture, where the overall reaction is



The mechanism can be summarized as the hydrolysis of the alkoxysilane followed by the condensation of the resulting silicic acid. The base, ammonia, acts as the catalyst in both hydrolysis and condensation reactions.

In Stöber's work, the control of the particle properties was achieved by empirical experiments. Since these early investigations, several growth and formation mechanisms have been proposed.

The first model describes the nucleation of nanometer sized primary particles which then grow by the addition of silicic acid monomer on their surface (the monomer addition growth model [62 - 63]), in analogy to the LaMer precipitation model [64] (Figure 2).

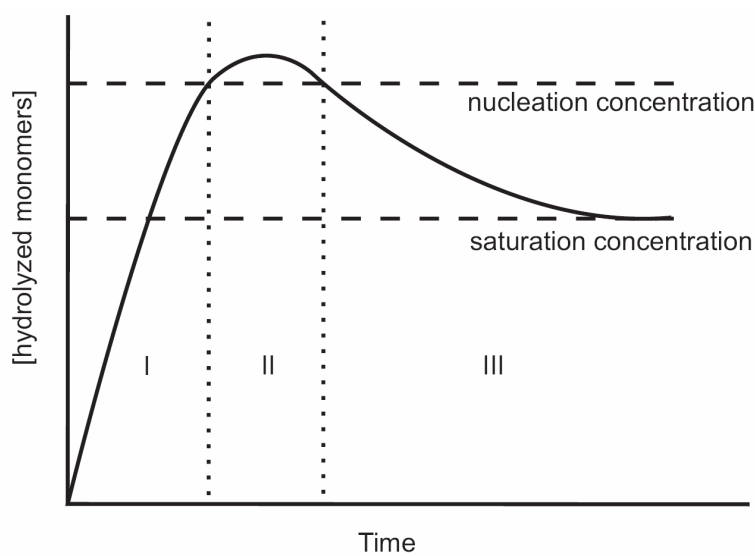


Figure 2: Schematic representation of the concentration of hydrolyzed monomers, before and after nucleation (LaMer diagram [64]): I. Monomer hydrolysis, II. Nucleation period, III. Particle growth by monomer diffusion.

It mainly focuses on the hydrolysis and condensation rates, which determine the final particle size. This model is in accordance with only some experimental observations and accounts for the properties of the resulting particles (monodispersity, smooth surface, spherical shape).

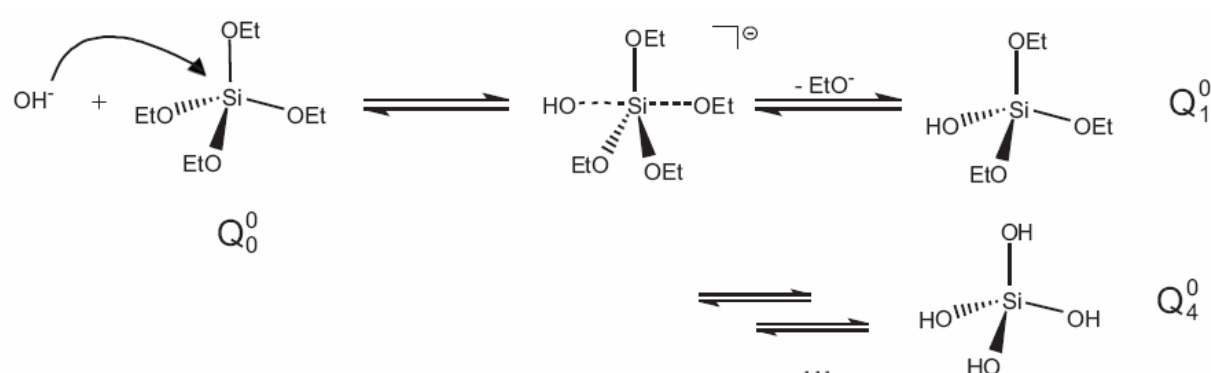
The second model, the aggregation growth model [65], states that particle growth occurs via the aggregation of primary particles. In this case, the final particle size is determined by the different parameters affecting the colloidal stability, like ionic strength, temperature, charges on the particle surface, pH and solvent properties. This model correlates better with experimental observations. However, the smoothness of the particle surface can only be explained by the monomer addition growth model.

The most recent model [66 - 68] assumes that Stöber particles are first formed by an aggregation mechanism of nanometer-sized particles and, when the colloidal stability is

reached, further growth of the particles occurs via the monomer addition mechanism. This model is backed by all experimental observations and is currently accepted as the most probable mechanism. The different steps of this mechanism are hydrolysis, condensation, nucleation, aggregation and monomer addition.

1.1.1.1 Hydrolysis

Ammonia catalyses the reaction by deprotonating the water molecules. The resulting hydroxide ions react with the tetraalkoxysilane in a nucleophilic reaction [67, 69].



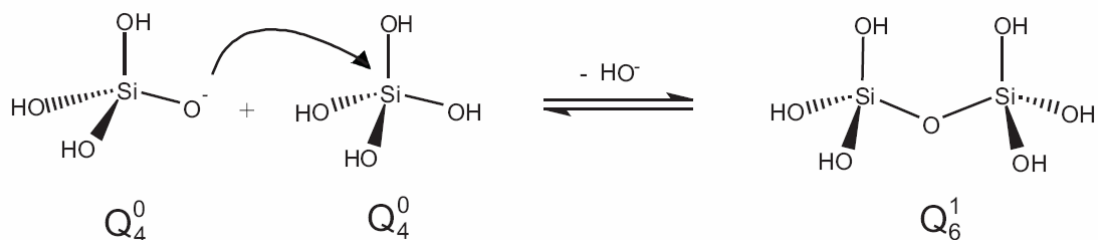
Scheme 4: Hydrolysis of TEOS. The Q_i^j notation denotes Q as a tetrafunctional silicon site, the subscript i is the number of silanol bonds, and the superscript j the number of siloxane bridges on the Si atom.

Subsequent hydrolysis steps yield the Q_2^0 , Q_3^0 and Q_4^0 monomers [70] (Scheme 4). Hydrolysis of Q_0^0 is typically the rate-limiting step to particle formation [63, 71]. The subsequent hydrolyses of the three remaining ethoxy groups from Q_1^0 proceed faster the more alkoxy groups are already removed. This increase in rate is caused by the increasing stabilizing effect of the hydroxy groups on the transition state and the decreasing steric hindrance of the ethoxy groups [69].

Under base-catalyzed conditions, the nucleophilic substitution in both the hydrolysis and the condensation (see below) reactions occurs via an associative pathway involving a penta-coordinate transition state [69].

1.1.1.2 Condensation

The condensation reaction is also base-catalyzed: Ammonia first deprotonates the silylic acid, which in turn reacts with another monomer in a nucleophilic substitution [67, 69]. As an example, the condensation between two Q_4^0 monomers resulting in Q_6^1 is displayed in Scheme 5.



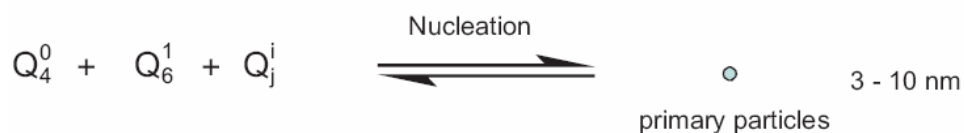
Scheme 5: Condensation of hydrolyzed monomers.

Under the Stöber process conditions, the monomers observed in solution during the whole reaction are typically TEOS and the first hydrolysis product, Q_1^0 [72, 73]. The fact that Q_4^0 species are not experimentally detected suggests that the condensation of the fully hydrolyzed monomer is faster than hydrolysis [71]. For the partially hydrolyzed monomers, hydrolysis is typically faster than condensation.

The degree of hydrolysis of the monomers before condensation is controlled by the relative hydrolysis and condensation rate of the individual steps [74]. Under most Stöber conditions, the fully hydrolyzed monomers, Q_4^0 , are obtained [71]. In experiments using low water and ammonia content, for the preparation of small particles in particular [75], however, the hydrolysis rates are lower and partially hydrolysed monomers, Q_2^0 and Q_3^0 , are detected [74].

1.1.1.3 Nucleation of primary particles

When a critical supersaturation concentration of hydrolyzed monomers is achieved, the nucleation of primary particles takes place [68, 73, 76] (Scheme 6).



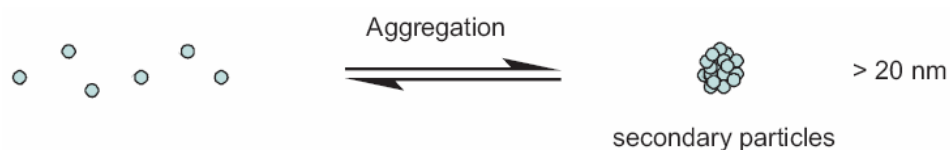
Scheme 6: Nucleation of primary particles.

The nucleation process is included in both the aggregation and the monomer addition growth models.

It is believed that the condensation of the hydrolyzed monomers and oligomers first yields low density expanded polymeric structures [73]. When the concentration of hydrolyzed monomers is above the critical supersaturation concentration [64] (Figure 2), the polymers reach a size and degree of cross-linking where they become insoluble. At this point, the intramolecular enthalpic attraction overcomes the entropic solvation forces, and the molecule collapses to form the primary particles [73]. The size of the primary particles depends on the interactions of the polymeric intermediates with the solvent [74] (thermodynamic control), whereas the amount that is produced depends on the concentration of hydrolyzed monomers and the relative rate of hydrolysis and condensation (kinetic control).

1.1.1.4 Aggregation of primary particles

According to the aggregation growth model, the primary particles are not stable under the reaction conditions and aggregate [67, 71] (Scheme 7). The aggregation yields the secondary particles (also called seed particles or agglomerates [77]).



Scheme 7: Aggregation of primary particles.

This aggregation takes place until the resulting secondary particles are large enough to achieve colloidal stability [67]. The size of the secondary particles is controlled by the parameters influencing the colloidal stability (thermodynamic control) and the size and amount of the primary particles (kinetic control).

1.1.1.5 Growth by monomer addition

When colloidal stability is achieved, an important part of the monomers has been consumed. According to LaMer [64] and the monomer addition growth model, the nucleation of primary particles occurs only in the early stage of the process when the concentration of monomers is maximal. In the later stage, when the monomer concentration is lower, the nucleation of primary particles can not take place anymore. Indeed, in the base catalyzed sol-gel process of alkoxy silanes [78], the attacking nucleophile for the condensation reaction is a deprotonated silanol group. The acidity of a silanol group strongly increases if the silicon atom which it is bonded to is linked with other silicon atoms through siloxane bonds. This ensures that the monomers react preferentially with higher polymerized species [79], which prevents the build-up of hydrolyzed monomers in the solution. Therefore, once nucleation has ended, further growth of the particles only occurs via monomer addition (Scheme 8).



Scheme 8: Growth by monomer addition.

In summary, the formation of the Stöber particle is a balance between aggregation of primary particles and monomer addition, with both processes depending on the relative condensation and hydrolysis rates. The experimental parameters define the extent of each step, and therefore, the final particle properties.

1.1.2 General properties

Understanding the details of the mechanisms of the Stöber particle formation is expected to lead to a better control of the relevant particle characteristics including the shape, size, size distribution, and porosity of the particles.

1.1.2.1 Shape

Amorphous colloid materials typically display spherical shapes due to the random addition of monomer on the primary particle surface [60], while crystalline colloid materials display crystal shapes [59]. The sol-gel process of TEOS under basic conditions yields amorphous materials [66]. Moreover, the strength of the base controls the relative hydrolysis and condensation rates, which will determine the subsequent nucleation. In order to ensure a spherical shape, a weak base like ammonia is required as the catalyst. Indeed, in the absence of ammonia, the silica precipitates in irregularly shaped particles [11], while the use of stronger bases yields a wide range of porous materials [79].

Moreover, a spherical shape is obtained provided that stirring of the reaction mixture is strong enough to avoid the sedimentation and agglomeration of large particles.

1.1.2.2 Porosity

The relative rate of the hydrolysis and the condensation reaction controls the degree of hydrolysis of the monomers, which determines the cross-linking of the silica structure. As shown above, the monomers are fully hydrolyzed under most conditions of the Stöber process. Consequently, a large proportion of Q^4 structures is obtained and mesopores (Table 1) are absent. However, the silica particles are not fully condensed and contain micropores (Table 1) [69]. In particular, at low water and low ammonia concentrations, due to the slower hydrolysis rates, particles of high microporosity are obtained [75].

Table 1: Types of pores in solid materials.

| description | ethymology (greek) | diameter |
|-------------|--------------------|-----------|
| micropores | micro = small | < 2 nm |
| mesopores | meso = middle | 2 - 50 nm |
| macropores | macro = large | > 50 nm |

1.1.2.3 Size distribution

The monodispersity obtained for many colloid systems [58 - 60] has been explained by a self sharpening effect [60, 64, 80], consistent with the monomer addition growth model [62 - 63].

A short burst of nucleation occurs when a critical supersaturation concentration of hydrolyzed monomers (or nucleation concentration) is reached [64]. The resulting particles then grow by addition of the remaining monomers. The consumption of monomers is sufficiently rapid so that their concentration remains below the nucleation concentration and therefore, further nucleation is avoided. The separation of the nucleation and growth steps is the key for the formation of monodisperse colloids.

However, this mechanism is only valid for dilute solutions. If the initial concentration of monomer is high, several bursts of nucleation may occur and the final size of any given particle will depend upon when it was formed [64]. A polydisperse sol is the result in this case. In the Stöber process, high monomer concentrations are used ([TEOS] up to 0.5 M). Consequently, the soluble silica concentration is above that required for nucleation until late in the precipitation reaction [68, 74]. Therefore, the self sharpening effect can not explain the monodispersity of the Stöber particles.

The mechanism responsible for the monodispersity of the Stöber particles is actually the aggregation of the primary particles into the secondary particles, which correlates with the aggregation growth model: The size and monodispersity of the secondary particles are precisely defined by the parameters controlling the colloidal stability (ionic strength, pH, charge on the particles, temperature, solvent viscosity and dielectric constant) [67, 81, 82]. Once the concentration of hydrolyzed monomers is too low for further nucleation to occur, the final particles are obtained by monomer addition to the secondary particles. Therefore, the final polydispersity is directly linked to that of the secondary particles.

In order to guarantee the monodispersity of the Stöber particles, the concentration of ammonia, water and TEOS must be kept in a narrow range [81] and the parameters controlling the colloidal stability must be kept uniform in the reaction mixture. In order to satisfy the latter condition, adequate stirring of the reaction mixture is needed and large upscaling of the process should be avoided [81]. Still, it has been observed that upscaling up to 5 L has no significant effect on polydispersity [83].

1.1.2.4 Dimensions

According to the Stöber process mechanism, the final particle size depends on the amount and size of secondary particles on which the remaining monomers will condense.

The amount of secondary particles partially depends on the mass of primary particles produced and therefore on the reaction kinetics (see above). Consequently, the temperature, the concentration of TEOS, H₂O and NH₃, will all contribute to determine the amount of secondary particles and the final particle size. Indeed, experimental observations show that the factors that accelerate the rates of condensation and hydrolysis reactions tend to produce smaller particles [82]. For example, an increase in temperature, typically between 20 and 60 °C, yields smaller Stöber particles [84, 85].

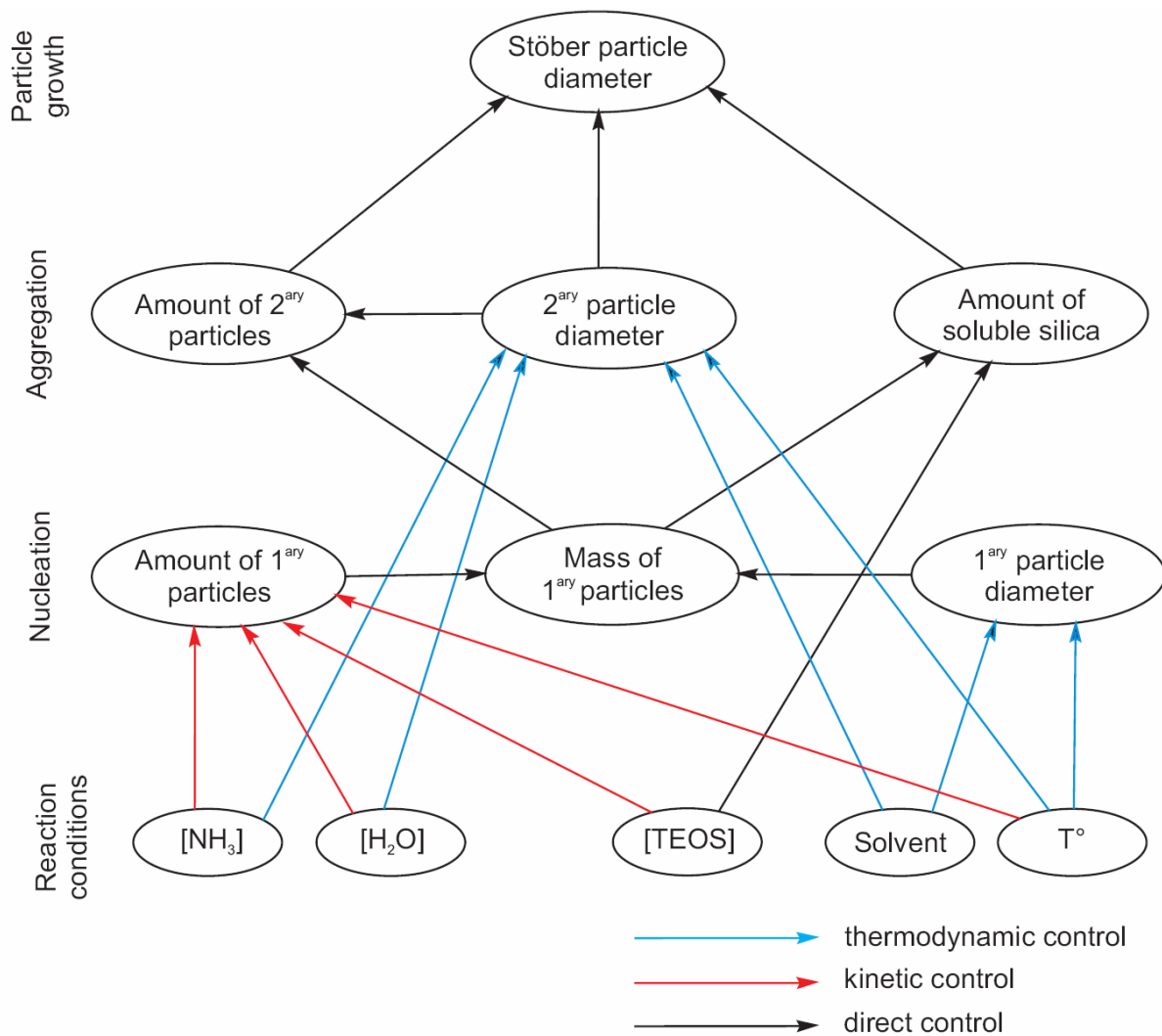


Figure 3: Conditions controlling the Stöber particle diameter; only the effects backed by experimental observations are displayed.

On the other hand, the size of the secondary particles is controlled by the factors determining the colloidal stability [65, 67, 71]. For example, the addition of salts to the reaction mixture

results in an increase in final particle size without significant impact on the hydrolysis and condensation rates [67, 71].

The effects of the reaction conditions on the final particle size are summarized in Figure 3. The fact that some parameters influence both the reaction kinetics and the colloidal stability, makes it difficult to predict which particle size will result from a given set of experimental conditions. It is even difficult to predict whether an increase or a decrease in particle diameter will result from a given modification in the experimental conditions. For example, changes in [H₂O] and [NH₃], which influence both the reaction kinetics and the colloidal stability, have a complex effect on the particle size: The increase in [H₂O] and [NH₃] first yields larger particle diameters until a maximum is reached. A further increase in [H₂O] and [NH₃] then results in smaller particle diameters [81].

In summary, the general mechanism of the Stöber particle formation and the influence of the experimental conditions on the particle diameter is mostly understood. However, in order to obtain a given particle size, empirical experiments remain necessary.

Moreover, it is not possible to obtain monodisperse particles with sizes covering the whole sub-micrometric domain (100 - 1000 nm) by varying only one single parameter. The variation in [NH₃] or the change of solvent alone, allows a maximum change in particle size of about 300 nm. By varying the temperature between -20 and 60 °C, the whole colloidal range can be produced but the polydispersity of the particles is high for the extreme temperature values [84, 85]. Typically, temperature, solvent and ammonia as well as water concentration are tuned simultaneously to obtain the desired particle size.

On the other hand, variations in [TEOS] are not employed to control the size, since the highest possible concentration is usually used for which the maximum yield is obtained and the spherical shape is retained.

1.2 Synthesis of the Stöber particles

Stöber particles of low porosity, low polydispersity, and with diameters between 100 and 800 nm are desired. The syntheses in this work were performed by adapting a known procedure [86]. In order to cover the desired diameter range, the water and ammonia concentrations were varied and various solvents were used (Table 2). We will designate the resulting silica materials as **M1** with a suffix letter to define the different preparations.

Table 2: Experimental conditions for the preparation of silica particles in this work.

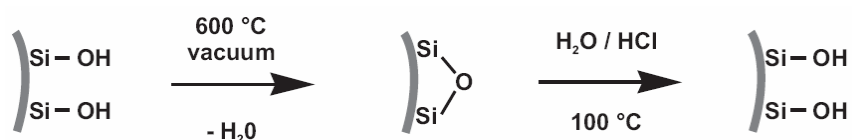
| material | concentration / M | | |
|-------------------------------|-------------------|--------------------|--------------------|
| | [TEOS] | [NH ₃] | [H ₂ O] |
| M1a ^[a] | 0.2 | 0.41 | 15.61 |
| M1b ^[a] | 0.25 | 0.47 | 9.30 |
| M1c ^[a] | 0.25 | 0.47 | 9.30 |
| M1d ^[b] | 0.3 | 0.58 | 8.00 |
| M1e ^{[b],[c]} | 0.53 | 0.59 | 4.70 |

[a] reaction in ethanol, [b] in isopropanol [c] prepared by D. Straub [83].

The materials **M1b** and **M1c** are two batches resulting from the same experimental conditions (Table 2) to test the reproducibility of the sol-gel process.

In order to obtain smaller particle diameters, a higher temperature was used compared to reference [86] and kept constant for all experiments (45 °C). Besides switching the solvent from isopropanol to ethanol, the water concentration is the main parameter used to control the particle size. Typically, low water concentrations are used for the production of small particles [81]. In our case, the opposite strategy will be used in order to lower the porosity of the Stöber particles: The large water concentration employed to obtain the smallest particles is expected to increase the cross-linking and decrease the amount of remaining ethoxy groups (see B.A.A). As mentioned before, the TEOS concentration was chosen as high as possible and increasing [NH₃] were used for increasing particle diameters.

Moreover, after the synthesis, the materials were tempered at 600 °C under vacuum [87] in order to further reduce the microporosity and eliminate any remaining solvent and ammonia molecules from the silica matrix. The thermal treatment also induces the condensation of surface silanol groups [88]. This has the advantage of condensing the internal silanol groups into siloxane bonds, yielding a more condensed matrix, but simultaneously, the surface silanol groups are also lost. The surface silanol groups are later needed as functional groups for the subsequent chemical modification of the silica surface. In order to rehydroxylate the silica surface, the materials were treated with diluted hydrochloric acid after tempering. The acid is used as a catalyst for the hydrolysis of the surface siloxane bonds. In this process, the internal siloxane bonds are not accessible and remain unchanged. Consequently, the thermal treatment yields a condensed matrix, while the rehydroxylation regenerates the surface silanol groups (Scheme 9).



Scheme 9: Thermal treatment and rehydroxylation of Stöber particles.

1.3 Characterization of the Stöber particles

A variety of methods is available for the investigation of the physical properties of the Stöber particles. The morphology of the particles may be studied with optical or scanning electron microscopy (SEM). The size and size distribution may also be obtained from SEM as well as from dynamic light scattering (DLS). Surface area and porosity information is obtained from gas adsorption/desorption isotherms.

1.3.1 Particle shape

1.3.1.1 Optical microscopy

Optical microscopy uses visible light and a series of lenses to magnify the image of a sample. This method enables a fast and straightforward investigation. However, the resolving power of an optical microscope is limited by the wavelength of visible light. In practice, objects down to 200 nm may be detected by this method.

Stöber particles in the submicrometric range can be detected by optical microscopy [89] (Figure 4). This method is not suited for the quantitative size determination of the particles because the absolute scale of the micrograph can not be precisely determined. However, it makes it possible to check the shape of the particles immediately after the synthesis and compare the relative size of the particles **M1a** to **M1e**.

For the larger particles (**M1d** and **M1e**), the optical micrographs clearly display monodisperse spherical particles. In the case of the smaller particles (**M1a** –**M1c**), the resolving power of the method is not sufficient to evaluate the polydispersity and the shape.

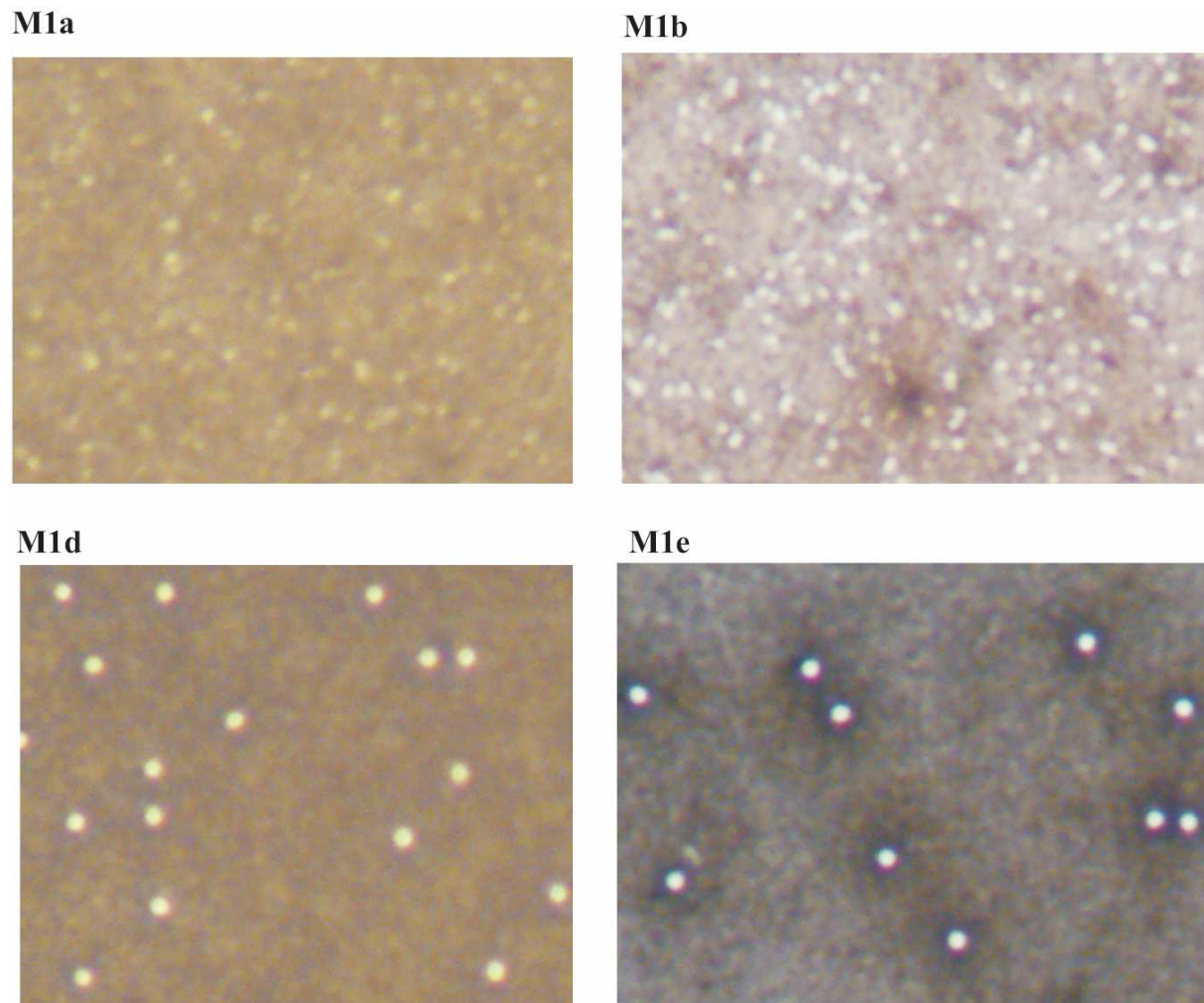


*Figure 4: Optical micrographs of particles **M1a** – **M1e** before thermal treatment.*

1.3.1.2 Scanning electron microscopy

In scanning electron microscopy, an electron beam is focused by lenses on a spot about 1 to 5 nm in diameter [90]. The beam is deflected by electrodes in order to scan the surface of the sample. When the electron beam interacts with the samples, the electrons lose energy by random scattering and absorption. The beam current absorbed by the sample is detected and used to create an image of the scanned area. For conventional imaging in SEM, samples must be electrically conductive, at least at the surface, and electrically grounded to prevent the accumulation of electrostatic charge on the surface.

SEM, due to its higher resolving power, is better suited than optical microscopy for investigations in the submicrometric range. Although our samples are not conducting, no sputtering with conducting materials (Au or Pt) was performed in order to leave the particle

diameter unchanged. The absence of sputtering has a drawback, i.e. a poorer definition of the resulting SEM images.

The SEM pictures of **M1a** to **M1e** (Figure 5), recorded after the thermal treatment and rehydroxylation of the silica surface, confirm the spherical shape of the Stöber particles, including the smaller particles. Also, the SEM investigations do not reveal the presence of damaged or irregular particles, demonstrating the high uniformity in shape obtained with the Stöber process.

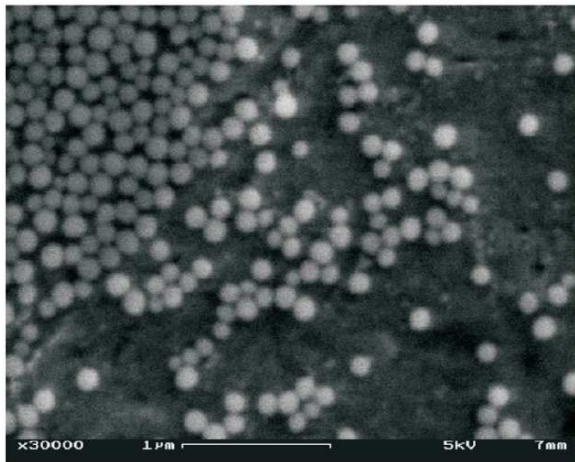
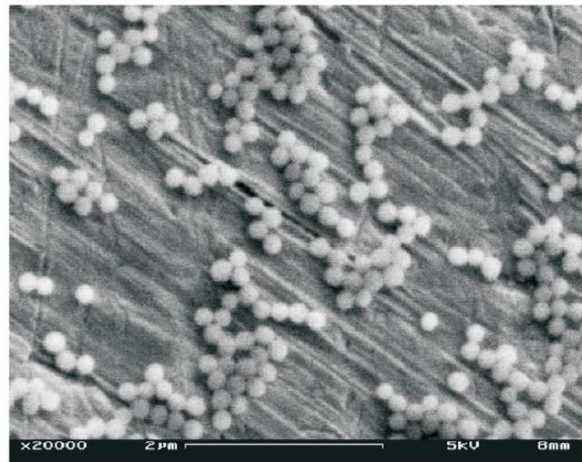
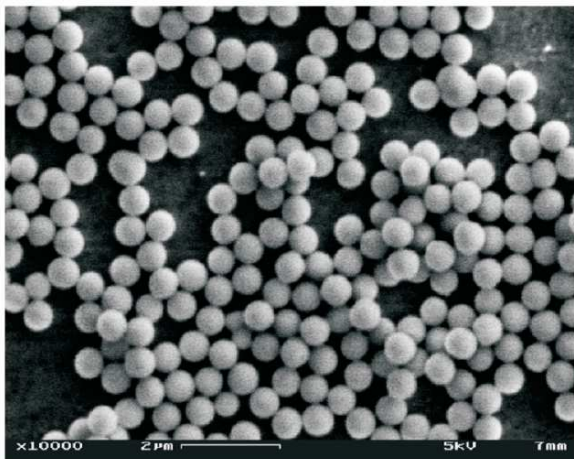
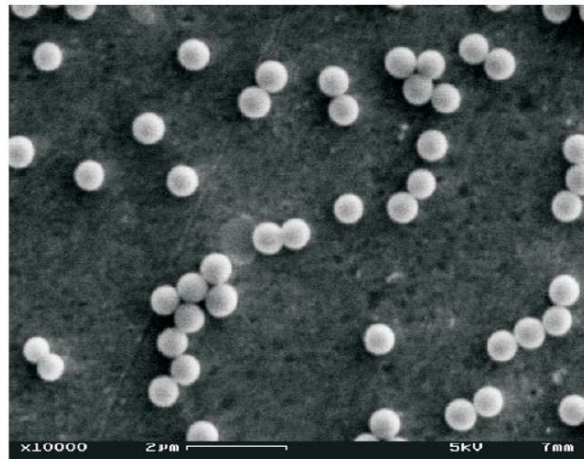
M1a**M1b****M1d****M1e**

Figure 5: SEM pictures of particles M1a – M1e after thermal treatment.

1.3.2 Particle size and size distribution

1.3.2.1 SEM measurements

The average particle diameters and their standard deviations are determined by measuring a large number of particles from the SEM pictures (Table 3).

Table 3: Diameters and statistical data from SEM measurements.

| material | number of SEM pictures | number of evaluated particles | d_{SEM} | σ | cv | PDI |
|--------------------------|------------------------|-------------------------------|-----------|----------|-------|---------|
| M1a | 6 | 205 | 140 | 18 | 0.129 | 1.0165 |
| M1b | 6 | 212 | 252 | 25 | 0.099 | 1.00984 |
| M1c | 5 | 250 | 262 | 19 | 0.073 | 1.00526 |
| M1d | 6 | 284 | 592 | 25 | 0.042 | 1.00178 |
| M1e^[a] | 6 | 210 | 769 | 27 | 0.035 | 1.00123 |

[a] prepared by D.Straub and sputtered with gold [83].

As an example, the particle size distribution for **M1b** obtained from the measurement of 212 particles is presented in Figure 6. The size distribution follows approximately a Gaussian distribution.

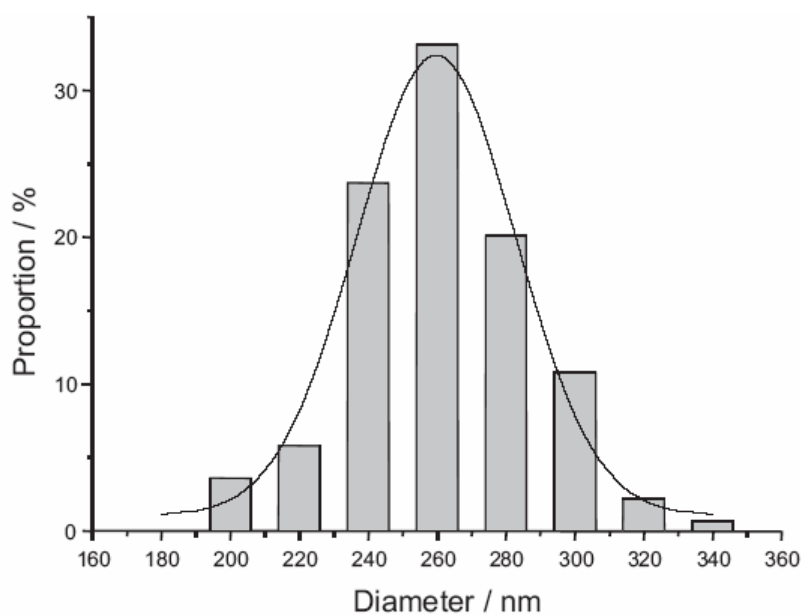


Figure 6: Particle size distribution for **M1b** obtained from SEM measurements fitted to a Gauss function.

According to the statistical analysis of the SEM measurements, Stöber particles with a diameter (d) between 140 and 769 nm have been produced under the given experimental conditions (Table 2). The standard deviation of the particle diameter (σ) is about 25 nm independently of the particle size. The diameter and standard deviation from the statistical analysis are close to the one obtained from the Gaussian distribution (for **M1b**: 252 ± 25 nm and 260 ± 23 nm, respectively).

The polydispersity of the particles is given by the relative standard deviation, also called coefficient of variation (cv) or g-index [91]:

$$cv = \sigma / d \quad (2)$$

If the particles are perfectly monodisperse, $cv = 0$ and an increase in polydispersity yields higher cv values. The cv values for the **M1** materials are between 0.035 and 0.129 (Table 3).

The polydispersity can also be characterized by the polydispersity index (PDI) [92], which is used in polymer chemistry. The polydispersity index is derived from the cv (see 8.1):

$$PDI = 1 + cv^2 \quad (3)$$

If $PDI = 1$, the particles are perfectly monodisperse, whereas for polydisperse systems, PDI becomes always greater than 1. Compared to samples in polymer chemistry, where PDI commonly equals 2, the Stöber particles have a very low PDI ($1 < PDI < 1.02$ for all **M1** materials, Table 3). Because of the low polydispersity of the Stöber particles, the cv is better suited to describe their polydispersity than the PDI (Table 3).

The general trend is that the smaller particles are more polydisperse than the larger ones: **M1e** has a cv value of only 0.035 while that of **M1a** is 0.129. As in our materials σ is approximately constant, the cv value is proportional to $1/d$ (Equation 2). Therefore, in our samples, the polydispersity increases in a hyperbolic manner with the decrease in particle diameter. This is one of the factors preventing the synthesis of very small (< 100 nm) monodisperse Stöber particles. This observation agrees with previous experiments [81, 85].

Materials **M1b** and **M1c** have been produced under the same conditions. Both syntheses were performed with exactly the same chemicals and the same equipment within a small time scale.

In this case, both materials display diameters of about 250 nm (Table 3). The difference in diameter ($\Delta d \approx 10$ nm) is lower than their standard deviation. This demonstrates that the Stöber process can yield reproducible results. It should be noted, however, that only small changes, including unintentional variations, in the experimental conditions can have dramatic effects on the particle diameter, with Δd up to 46 nm (Table 7, page 39, **M1f** and **M1g**). The two main parameters responsible for shifts in the particle diameter were identified as being the inaccurate control of the temperature and the concentration of the ammonia solution. A shift of only few degrees in the temperature directly induces a significant change in particle diameter [84]. Also, the concentration of the ammonia solution varies with time during storage due to the evaporation of NH_3 . A titration of the ammonia solution is necessary if a reproducible particle diameter is desired [85].

1.3.2.2 Dynamic light scattering

Dynamic light scattering enables the determination of the diameter of any particle that may be suspended in a solvent. The particle diameter is obtained by measuring the rate of diffusion of the particles in the solvent at a constant temperature [93]. Under these conditions, the particle diameter is directly related to the diffusion coefficient (D) according to the Stokes-Einstein equation (Equation 4).

$$D = \frac{k_B T}{3\pi\eta d} \quad (4)$$

where k_B = Boltzmann constant (1.38×10^{-23} J K⁻¹)

η = viscosity (1.2×10^{-3} Pa s at 293.1 K for ethanol)

In order to measure the diffusion coefficient, the particles are irradiated by a laser beam. The light scattered by the particles is measured by a detector placed at a particular angle with respect to the optical axis (typically 90°). The light intensity at the detector changes as the particles' position changes in the fluid due to Brownian motion. The light intensity fluctuations are recorded and mathematically transformed into an autocorrelation function (ACF) from which the diffusion coefficient and the diameter of the particles are obtained [93].

Table 4: Diffusion coefficient (D) and particle diameter (d_{DLS}) from DLS of the **M1** materials.

| material | $D / \text{m}^2 \text{s}^{-1}$ [a] | $d_{\text{DLS}} / \text{nm}$ |
|------------|------------------------------------|------------------------------|
| M1a | 2.38×10^{-12} | 150 |
| M1b | 1.47×10^{-12} | 244 |
| M1c | 1.23×10^{-12} | 290 |
| M1d | 5.60×10^{-13} | 639 |
| M1e | 4.74×10^{-13} | 755 |

[a] in ethanol at $T = 293.1 \text{ K}$.

The diameters from the DLS measurements of **M1a** - **M1e** (Table 4) correlate well with the values obtained from the SEM images (Table 3). Moreover, this demonstrates that the particles exist as single units. If the particles were aggregated, the d_{DLS} values would correspond to the spherical equivalent diameter of the aggregates [94].

The ACF also provides a polydispersity index and a standard deviation for the particle diameter. For example, the standard deviation obtained from the analysis of the DLS data for **M1b** is 4 nm. In comparison, the measurement of a large number of particles on the SEM pictures followed by the statistical analysis yielded a standard deviation of 25 nm for **M1b** (Table 3).

In the case of DLS, the particles are not physically separated nor counted at any point in the measurement. The light scattered from all the particles is detected simultaneously and then correlated. The *PDI* is obtained from the ACF, and the standard deviation is then calculated from the *PDI*. This is the inverse process as compared to that used for the statistical analysis of the measurements obtained from SEM. The standard deviation obtained from the DLS data analysis provides a good qualitative indication of the sample's polydispersity [93], which is useful to determine whether particle agglomerates or dust particles are present during the measurement. So, σ can be used to check that the diameter obtained for the particles is valid. However, σ from DLS is not a quantitative measure for the particle size distribution. Therefore, only σ from SEM is used to evaluate the polydispersity.

1.3.3 specific surface area and pore size distribution

1.3.3.1 Geometrical specific surface area from SEM

The SEM images of materials **M1** display monodisperse spherical particles (see 1.3.1.2). If the silica particles are considered as being perfect spheres, the geometrical specific surface area A can be expressed as a function of the diameter d (see 8.2):

$$A = \frac{6}{d \times \rho_{\text{SiO}_2}} \quad \begin{array}{l} \rho_{\text{SiO}_2} = \text{silica density} \\ d = \text{particle diameter} \end{array} \quad (5)$$

By using this relationship, the geometrical specific surface area (A_{SEM}) is determined from the particle diameter obtained from SEM measurements (d_{SEM}) (Table 6, page 31).

The value of ρ_{SiO_2} depends on the microporosity of the silica material. The reported literature values for Stöber particles are between 1.6 and 2.25 g cm⁻³ (most often 2.0 g cm⁻³) [82] depending on the specific reaction conditions. The highest density, which corresponds to the literature value of amorphous silica (2.2 g cm⁻³ [79]), are obtained after thermal treatment. The synthesis of the **M1** materials was performed with high water concentrations followed by a high temperature treatment in order to obtain a more condensed matrix. Therefore a high density is expected and the value of amorphous silica will be used in the calculations concerning the **M1** materials ($\rho_{\text{SiO}_2} = 2.2 \text{ g cm}^{-3}$).

Independently of its exact value, ρ_{SiO_2} is assumed to be constant for all **M1**. Therefore, A of perfectly spherical silica spheres is proportional to $1/d$ (Equation 5).

1.3.3.2 Physisorption isotherms

Gas physisorption measurements at very low temperature and under reduced pressure are widely used for determining the surface area and pore size distribution of solid materials [95].

Known doses of an inert gas are injected into the container with the outgassed sample. The uptake of the gas by the solid sample is determined from the change in the partial pressure. The shape of the physisorption isotherms depends on the intermolecular forces between the adsorbent and the adsorbate, the adsorbate-adsorbate interactions as well as the surface area,

pore size and pore size distribution of the solid sample. Adsorption-desorption isotherms can be classified in six types [95, 96] (Figure 7).

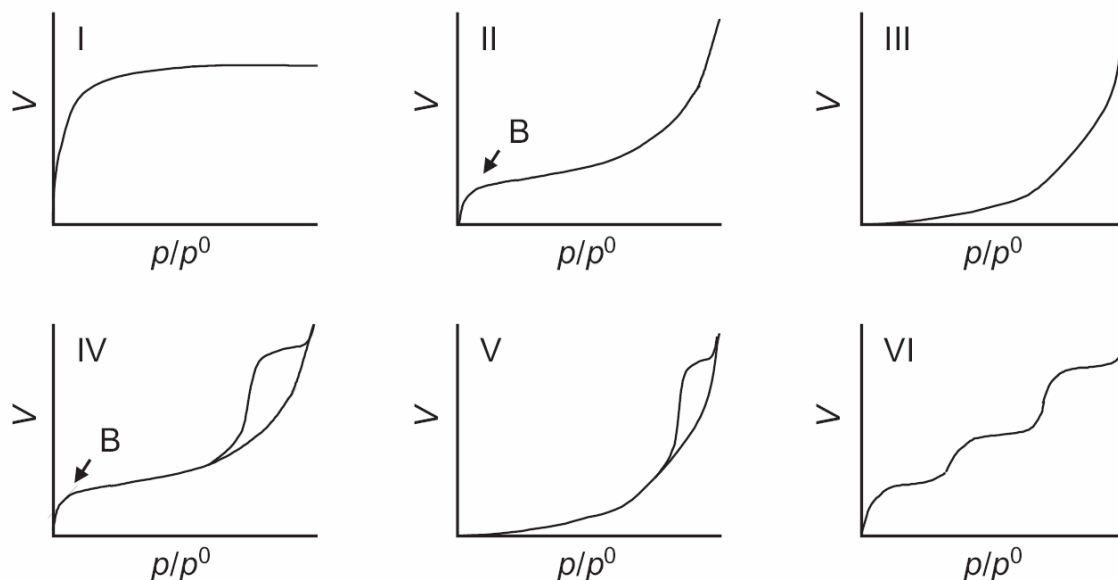


Figure 7: Types of physisorption isotherms [95].

Type I is typical for microporous solids with small external surface. Type II is shown by finely divided non-porous solids. Type III and type V are typical of weak adsorbent-adsorbate interactions. Type IV and type V feature a hysteresis loop generated by the capillary condensation in mesopores. The rare type VI, a step-like isotherm, is shown for example with argon on special carbon adsorbents [95].

Monolayer and multilayer adsorption may be differentiated from the physisorption isotherms. Surface area is measured by counting the number of molecules adsorbed in a monolayer. Pore size is determined from the gas condensation pressure into the pores. Micropores, mesopores and macropores (Table 1) [95] may be distinguished.

An experimental determination of the specific surface area of the **M1** materials was obtained from their low temperature nitrogen adsorption-desorption isotherms. The isotherm for **M1c** is presented in Figure 8. The shape of the isotherm of the other **M1** materials is similar to that of **M1c**.

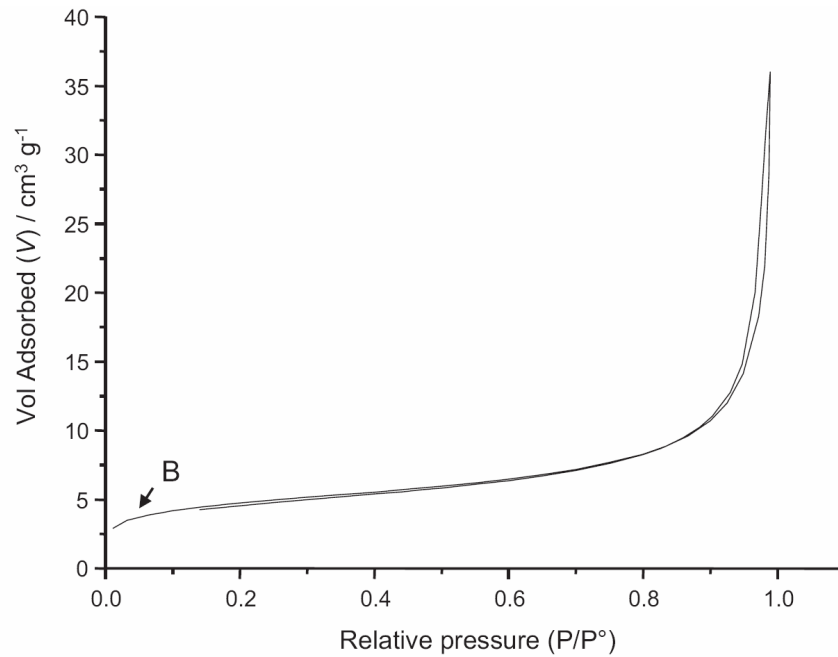


Figure 8: N_2 adsorption/desorption isotherm for **M1c** at 77 °K.

The adsorption-desorption isotherms of the **M1** materials correspond to type II, which is the characteristic isotherm for finely divided non-porous materials. The isotherm is divided into 3 main parts: From a relative pressure of 0 to point B, a monolayer of adsorbed gas molecules forms on the adsorbent surface. Point B indicates the stage at which monolayer coverage is complete and multilayer adsorption about to begin. Multilayer adsorption corresponds to the linear middle section of the isotherm. The sharp increase in amount of adsorbate at higher P/P° corresponds to the condensation of the nitrogen gas in pores of increasing diameter. The latter stage is not useful for the surface area determination.

1.3.3.2.1 Surface area from the BET method

The specific surface area may be obtained from the adsorbent's isotherms by using the Brunauer-Emmet-Teller (BET) model. The BET equation may be applied for type I, II and IV isotherms and is valid at low pressures [97] (Equation 6).

$$\frac{P}{V(P^\circ - P)} = \frac{1}{V_m C} + \frac{C - 1}{V_m C} \frac{P}{P^\circ} \quad (6)$$

where V is the volume of gas adsorbed at the relative pressure P/P° , V_m is the volume of gas needed to form a monolayer on the adsorbent surface and P° the saturation pressure of the

adsorbate. The dimensionless value C is related exponentially to the enthalpy of adsorption in the first adsorbed layer and is not needed for the determination of the surface area. Moreover, C does not provide a quantitative measure of enthalpy of adsorption but gives an indication of the magnitude of the adsorbent-adsorbate interaction energy [96]. High C values are associated with the presence of micropores [95].

The adsorbent's specific surface area (A_{BET} in $\text{m}^2 \text{g}^{-1}$) is calculated from the monolayer capacity (n_m in moles), provided that the area (a_m) effectively occupied by an adsorbed molecule in the complete monolayer is known (Equation 7).

$$A_{\text{BET}} = \frac{n_m N_A a_m}{m_{\text{SiO}_2}} \quad (7)$$

N_A is the Avogadro constant ($6.022 \times 10^{23} \text{ mol}^{-1}$) and m_{SiO_2} the mass of silica. For nitrogen, the a_m value is 0.162 nm^2 at 77 K [95]. The n_m value is directly obtained from the V_m value according to the ideal gas law at standard temperature and pressure (STP).

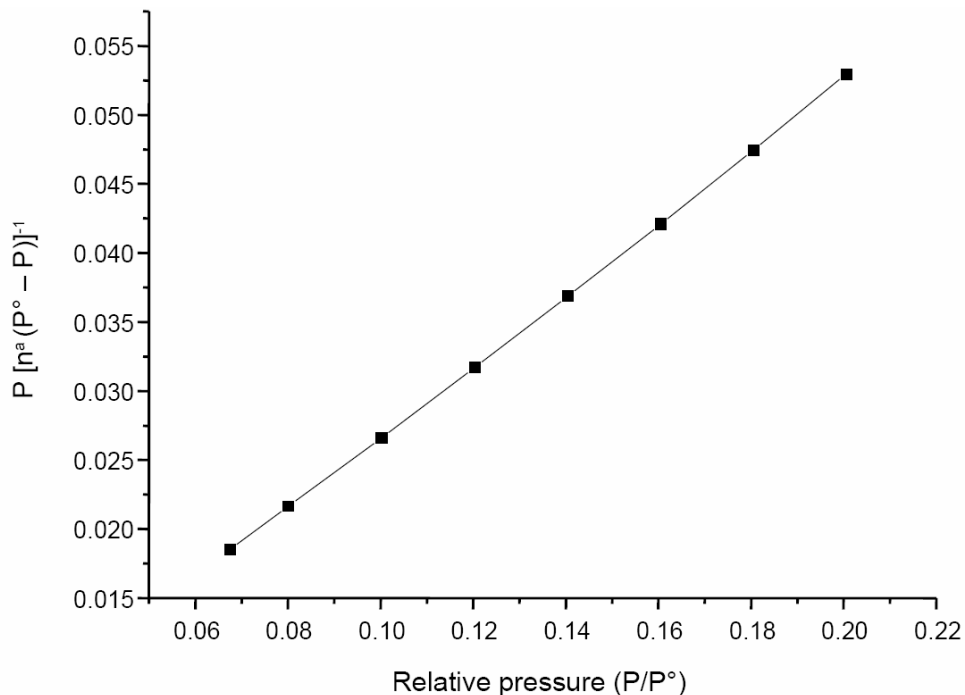


Figure 9: BET plot for **M1c** in the P/P° range 0.06 – 0.2.

The BET equation can be solved using a single or a multipoint method [95]. With the single point method, V_m is directly calculated from point B on the adsorption isotherm. In the case of the materials **M1**, there is no sharp knee in the N_2 isotherm. This is due to a low V_m value

corresponding to a low specific surface area of these materials. Therefore, a precise determination of point B and the V_m value is not possible for the **M1** materials from the single point method. Consequently, the BET multipoint method is better suited for the determination of the surface area in this case. For the multipoint method, the BET equation requires a linear relationship between $P/[V(P^\circ - P)]$ and P/P° (Figure 9). Since the linearity range is restricted to the low-pressure part of the isotherm, $P/[V(P^\circ - P)]$ is plotted versus P/P° for P/P° between 0.06 and 0.2.

As a result, V_m , as well as C values are obtained from the slope and the Y-intercept (Equation 6). The slope, Y intercept, C , V_m and A_{BET} values for **M1c** obtained from equation 7 are given in Table 5.

Table 5: BET data for **M1c**.

| quantity | value |
|------------------|---|
| m | 0.357 g |
| slope | 2.6×10^{-1} |
| Y-Intercept | 8.6×10^{-4} |
| C | 3.0×10^2 |
| V_m | $3.86 \text{ cm}^3 \text{ g}^{-1}$ (STP) |
| A_{BET} | $16.8 \pm 0.1 \text{ m}^2 \text{ g}^{-1}$ |

The same calculations were performed for all **M1** materials and the resulting A_{BET} are summarized in Table 6 together with d_{SEM} and A_{SEM} .

Table 6: Specific surface areas of the **M1** materials from physisorption isotherms as well as SEM measurements.

| material | d_{SEM} nm | $A_{\text{SEM}}^{\text{[a]}}$ $\text{m}^2 \text{ g}^{-1}$ | A_{BET} $\text{m}^2 \text{ g}^{-1}$ | A_t $\text{m}^2 \text{ g}^{-1}$ | A_{BJH} $\text{m}^2 \text{ g}^{-1}$ |
|------------|------------------------|--|---|--------------------------------------|---|
| M1a | 140 | 19.48 | 33.1 | 7.3 | 26.25 |
| M1b | 252 | 10.82 | 16.0 | 2.8 | 11.77 |
| M1c | 262 | 10.41 | 16.8 | 4.7 | 10.8 |
| M1d | 592 | 4.61 | 6.4 | 2.0 | 2.9 |
| M1e | 769 | 3.71 | 4.2 | 1.5 | 2.0 |

[a] geometrical specific surface area calculated from d_{SEM} according to Equation 5.

The low specific BET surface areas obtained for materials **M1a** – **M1e**, between 4 and 35 m² g⁻¹, correlate well with those expected for non-porous materials. In comparison, mesoporous silicas display specific surface areas up to 1000 m² g⁻¹ [98 - 100]. However, the specific surface area A_{BET} is larger than that expected for a perfect sphere (A_{SEM}) of the respective particle diameter. The surface area of the Stöber particles deviates from that of a perfect sphere probably because of surface heterogeneities or a minor presence of micro- and/or mesopores.

Moreover, as expected, a decrease in d_{SEM} results in an increase in A_{BET} . In order to demonstrate the relationship between d and A , A_{BET} is plotted versus d_{SEM} and versus d_{SEM}^{-1} (Figure 10).

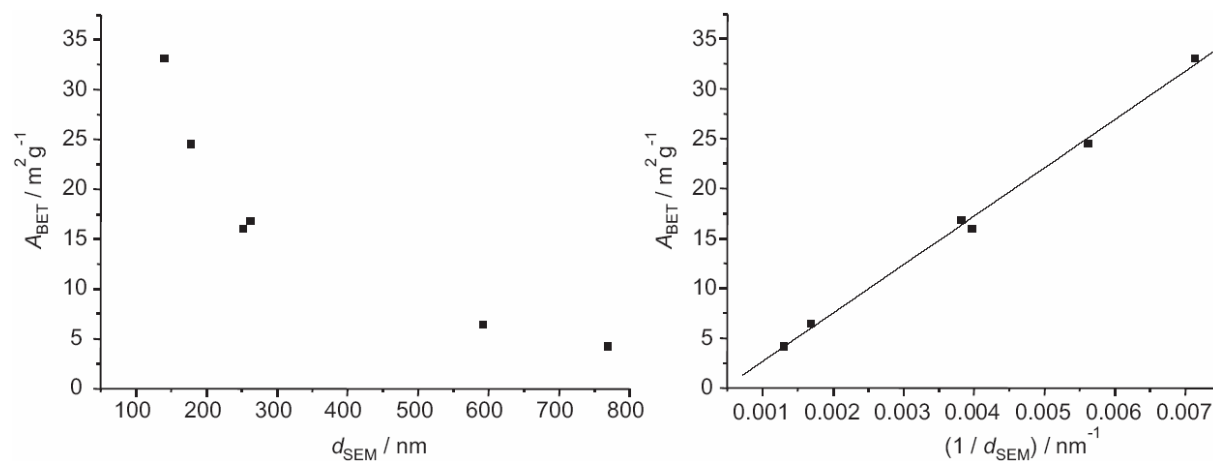


Figure 10: Plot of A_{BET} versus d_{SEM} (left) and versus d_{SEM}^{-1} (right).

The plot of A_{BET} versus d_{SEM} shows that the specific surface area as determined by BET increases hyperbolically with decreasing particle diameter. Furthermore, the linear relationship obtained for the plot of A_{BET} versus $1/d_{\text{SEM}}$ demonstrates that A_{BET} is proportional to $1/d_{\text{SEM}}$. As shown previously (see 1.3.3.1), this is the expected relationship for perfectly geometrical spheres and shows that, with the tuning of the experimental conditions of the Stöber process, it is possible to produce spheres of a precise diameter, and therefore of a precise surface area, as A is directly controlled by the diameter of the spheres.

1.3.3.2.2 Porosity

The specific surface area A_{BET} includes the surface area of micropores, mesopores and the external surface area [28]. The difference between A_{BET} and A_{SEM} (Table 6) indicate the presence of some pores (see 1.3.3.2.1). The shape of the physisorption model makes it possible to differentiate micropores and mesopores. Their specific surface area may be obtained from the t-method [95] and from the Barrett-Joyner-Halenda (BJH) model, respectively [101].

1.3.3.2.2.1 Micropores from the t-method

In order to obtain an estimation of the specific *micropores* surface area (A_t) of the silica materials, the so-called t-method is applied [95]. The t-method provides a simple means of comparing the shape of a given isotherm with that of a standard non-porous solid. The amount adsorbed is plotted against the corresponding multilayer thickness calculated from the standard isotherm obtained with a non-porous reference solid. Any deviation in shape of the given isotherm from that of the standard is detected as a departure of the 't-plot' from linearity and is used to estimate the surface area of the micropores A_t [95] (Table 6).

The t-method confirms the presence of micropores in the **M1** materials and their estimated specific surface areas roughly correspond to the difference between A_{BET} and A_{SEM} ($A_{\text{SEM}} \approx A_{\text{BET}} - A_t$, Table 6). This indicates that no other types of pores are present on the silica surface. The estimation of the diameter of the micropores present on Stöber particles is possible with the information obtained from the N_2 isotherms: First, the adsorption branch of the nitrogen isotherm is characteristic of an isotherm obtained for a non-porous material. However, the desorption branch of the nitrogen isotherm deviates slightly (for relative pressures between 0.2 and 0.4, Figure 8) from the adsorption branch. This is characteristic of an activated desorption process due to the presence of micropores of openings smaller than 0.5 nm [27]. Moreover, this is confirmed by the large C values (~ 300), the approximation for the enthalpy of adsorption, obtained for **M1c** (Table 5). Adsorbent-adsorbate interactions alone can not explain C values larger than 100 [95]. Therefore, the adsorption of the adsorbate in very narrow pores is assumed.

1.3.3.2.2.2 Mesopores from the BJH method

The specific surface area of the *mesopores* is obtained from the BJH model [101]. The BJH method is based on the Kelvin equation [102] (Equation 8) and calculates the volume (V_{BJH}) and average diameter (d_{BJH}) of mesopores.

$$\ln \frac{P}{P^\circ} = \frac{2 \gamma M}{r \rho RT} \quad (8)$$

where γ , M and ρ are the surface tension, molar mass and density of the liquid (liquid nitrogen in our case), respectively, and r is the radius of the pore.

The Kelvin equation assumes a hemispherical liquid-vapor meniscus and a well-defined surface tension. Also in the BJH model, a cylindrical pore shape is assumed [101]. Based on the values of V_{BJH} and d_{BJH} , the BJH cumulative surface area of these pores (A_{BJH}) is accessible.

The N_2 isotherms of the **M1** materials display characteristic features for the presence of mesopores: The hysteresis observed at high relative pressures (> 0.9 , Figure 8) in the isotherms of the **M1** is associated with capillary condensation in mesopore structures. This is confirmed by the BJH analysis, which results in significant mesopore surface area (from 2 to 26 m g^{-1} , Table 6). However, it was previously demonstrated that after subtraction of the estimated micropores surface area, A_{BET} of the **M1** materials are comparable to their geometrical value A_{SEM} (see 1.3.3.2.2.1). Therefore, these mesopores are not part of the Stöber particle structure itself. The hysteresis and the significant mesopore surface area are due to the interstices between particles in larger agglomerates which allow the condensation of nitrogen.

In summary, the only pores identified on Stöber particles are micropores of about 0.5 nm in diameter. These micropores are accessible for nitrogen molecules but not for the larger redox-active molecules used in this study. Therefore, Stöber particles will, in this context, be considered as non-porous.

As Stöber particles can be regarded as non-porous spheres, this implies that the geometrical surface area is more representative than A_{BET} of the surface accessible to the redox-active molecules. Therefore, the values of A_{SEM} will be used for the determination of the surface coverage of active centers on the silica surface later in this work.

1.4 The optimal particle size

Stöber particles with various diameters in the submicrometric range were synthesized. The choice of a specific diameter depends on the intended application of the particles.

For catalytic applications, the ideal particle size is related to the maximum amount of active molecules that can be immobilized in a monolayer on the particle surface. The possible loading of redox-active material is proportional to the specific surface area of the support. So, the hyperbolic increase of A with decreasing d is of critical importance: This makes the smaller particles advantageous for the immobilization of the redox catalysts. The limit in downscaling the particle size is set by the difficulty in separating extremely small particles from suspension after synthesis. As multiple separation cycles are needed for the recycling of the catalyst, the most convenient method to induce particle precipitation is centrifugation. However, smaller particles are very difficult to separate by centrifugation. For example, particles of 100 nm in diameter require centrifugation at 10000 rpm for 10 min, which is the limit of the available equipment for this thesis. Therefore, due to its high surface area and its relatively simple separation compared to smaller particles, material **M1a** is ideal for the immobilization of catalytically active complexes.

The higher surface area of the smaller particles is also an advantage for their chemical characterization. For example, it is only for the smallest particles (**M1a** - **M1c**) that the specific amount of modifying molecules is high enough to successfully perform ^{13}C solid state NMR spectroscopy (see 3.1.1.1).

The optimal characteristics of the Stöber particles for electrochemical investigations are different: Cyclic voltammetry of redox-actively modified Stöber particles makes it possible to study the kinetics of the electron transfer between redox-active molecules on the electrode surface [103]. The values of the kinetic coefficients are valid and can be determined precisely only if the dimensions in which the electron transfer takes place are well defined. These dimensions are precisely known for perfect spheres of a given diameter. So, only spherical and monodisperse silica materials can be used for the electrochemical investigations. Therefore, the smallest particles (**M1a**), which show the highest polydispersity, should not be used for these applications. Also with large particles, the dimension over which the electron transfer takes place is larger and therefore, the time scale available to measure the kinetics of

this transfer is also expanded. Therefore, for large particles (**M1e**), standard electrochemical equipment can be used for these investigations[103], while the smallest particles need custom made equipment [7].

In conclusion, the characterization demonstrates that materials **M1a** to **M1e** can be considered as non-porous and monodisperse spheres. The properties of the materials (specific surface area, diameter, size distribution and porosity) were precisely defined. The physical dimensions, which are relevant for the subsequent steps, are d_{SEM} and A_{SEM} (Table 6).

The non-porosity is necessary to ensure a homogeneous environment and a good accessibility to the redox-active (or catalytic) molecules. The monodispersity and the well-defined properties are required to make a quantitative analysis of electrochemical investigations possible. The diameter of the particles can be precisely tuned in the sub-micrometric range according to the need of a specific interphase application. With respect to the aim of this thesis (the redox-active modification of the silica surface, its characterization and electrochemical investigations), particles with small diameters and low polydispersity are preferred. Therefore, for the next steps of this work, particles of the type **M1b/M1c** (this includes **M1f** and **M1g**, see 7.4 and Chapter 2) will be used as the silica matrix.

2 Silicon hydride modified silica surface

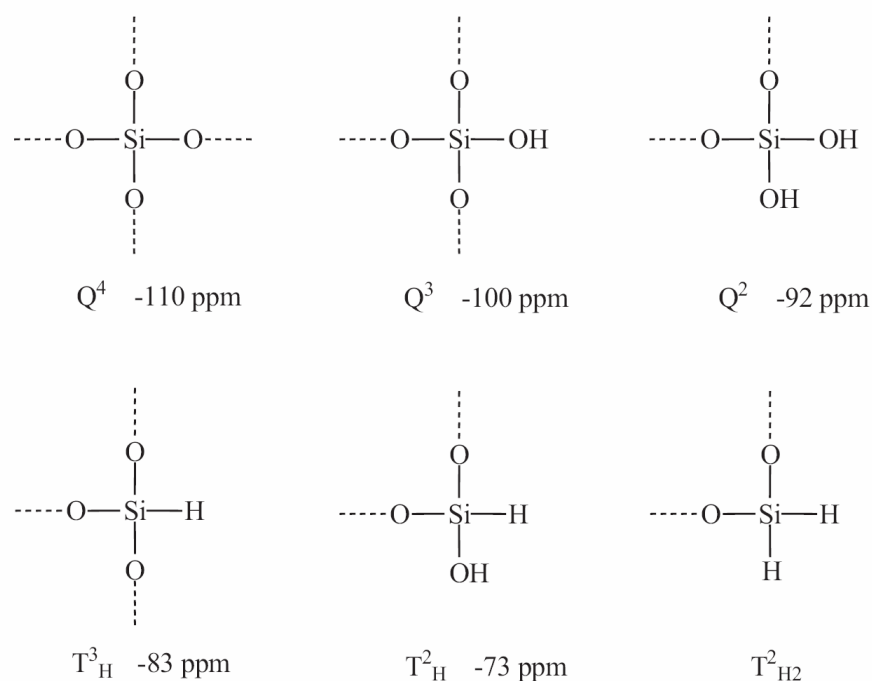
The first step toward the functionalization of a silica surface (e.g. based on the Stöber particles discussed in Chapter 1) via a hydrolytically stable Si-C bond involves the preparation of a silicon hydride (Si-H) modified surface (see Introduction).

To take advantage of the highly stable Si-C linkage, the silicon atom connected to the organic molecule needs to have three siloxane links to the silica matrix [104] (T^3 groups, Figure 1). Therefore, as a starting material, a silica surface bearing silicon hydride units connected in a similar manner (T^3_H groups, Scheme 10) is desired.

Silicon hydride groups chemically bound to a silica surface were obtained earlier [108] by condensation of triethoxysilane, $(EtO)_3SiH$ (TES), with surface silanol groups. The main reported advantage of this reaction is the high Si-H surface coverage, especially when the condensation is performed in the presence of water [108]. However, this also induces the polymerization [21, 109] of triethoxysilane [108] in the solution, yielding a heterogeneous Si-H modification. As a first attempt to produce the adequate Si-H modified starting material for the immobilization of redox-active molecules, we will perform the hydrosilylation

2. Silicon hydride modified silica surface

reaction under anhydrous conditions to avoid the polymerization of TES in solution. Under these conditions, TES can only react with the silica surface and a monolayer of silicon hydride is expected.



Scheme 10: Nomenclature of siloxane moieties and expected nuclear magnetic resonance chemical shifts for the ²⁹Si nuclei in CP/MAS NMR spectra of silica [1, 105, 106] and in modified silica [107, 108]. The dashed lines represent Si-O bonds to the silica bulk.

However, this modification is also a silylation reaction and therefore the resulting materials may still exhibit the same drawbacks as described previously: some Si-H groups may be linked to the silica matrix via only 2 Si-O-Si bonds (T²_H, Scheme 10). Thus the stability toward hydrolysis of materials synthesized by addition of the T²_H group to an alkene or alkyne is not expected to be higher than for materials prepared by the standard silylation method.

To prevent the problems of the silylation reaction, a more adequate method could be the reduction of the existing silanol groups on the silica surface. One possibility is the chlorination of the silanol groups in solution by thionyl chloride followed by reduction with LiAlH₄. The resulting silica shows a high silicon hydride surface concentration [108, 110].

2. Silicon hydride modified silica surface

However, the method proved to be time consuming and highly water sensitive [110]. In addition, reduction of the Q^2 groups (Scheme 10) present on the native silica surface, yields T^2_H groups [108]. Therefore, this hydride surface has a similar sensitivity towards hydrolysis than the one obtained from the triethoxysilane condensation route.

In order to provide a fully condensed matrix, and correspondingly a high proportion of T^3_H groups, the use of high temperatures is desired. This is the case for the direct reduction of silanol groups in fumed silica with hydrogen at 1000 °C [107, 111]. The reaction provides a clean hydride modified silica surface. However, according to our preliminary experiments with other silica materials, the resulting silicon hydride surface concentration is low and can not be used as a starting material for further surface modification.

An ideal procedure for silicon hydride modification of a silica surface should yield a high silicon hydride coverage and a fully condensed surface, free of silanol groups. None of the previously published procedures exhibits both of these properties. However, as discussed above, chlorination followed by reduction yields a high Si-H coverage and the use of high temperatures allows for the condensation of the silanol groups in the silica matrix.

The work presented in this chapter explores the silicon hydride modification of silica surfaces by a chlorination-reduction sequence at high temperatures. It is performed as a reaction between gaseous reactants and the surface to avoid any possible impurities and we expect to find a combination of the advantages in the resulting product. In parallel, an optimization of the TES condensation route will be performed and both Si-H modification methods will be compared.

2.1 Preparation of Si-H modified silica materials

The investigation on these new Si-H surface modification methods is performed on the Stöber particles surface. However, because of the shell structure of the modified silica, the maximum specific concentration of chemical groups introduced on the particle surface is so low that very sensitive methods for surface characterization are needed. Diffuse reflectance infrared Fourier transform (DRIFT) spectroscopy is one of the most sensitive methods for the characterization of organic or inorganic modifiers on the silica surface [112, 113]. On the other hand, the use of solid-state NMR experiments to successfully detect ^{13}C nuclei of the immobilized molecules or ^{29}Si nuclei of the modified surface will depend on the surface concentration of modifiers. Therefore, porous silica materials are more convenient as model systems to test the new surface modification method because of the high surface area.

2. Silicon hydride modified silica surface

Therefore, the surface modification will be performed on both Stöber particles and porous materials.

Four different kinds of silica were used for the Si-H surface modification (**M1** – **M4**; Table 7): The Stöber particles used here have a diameter of about 200 nm (**M1f** and **M1g**). In the context of the present surface modification, the well defined shape of such particles allows to investigate the effect of the reaction conditions on the particle structure. Kromasil (**M2**) is a commercial material consisting of spherical, porous, monodisperse silica particles with a diameter of 5 μm . Owing to its higher porosity and thus larger surface area, it was used for a precise characterization and quantification of the Si-H content of the modified surface. Laboratory grade column chromatography silica (**M3**) was also modified with Si-H to confirm the reproducibility of the method with other kinds of the base material. Fumed silica (**M4**) has a high surface area ($\sim 300 \text{ m}^2 \text{ g}^{-1}$) useful to obtain a sufficiently high specific Si-H amount for ^{29}Si CP/MAS NMR spectroscopy and was employed based on this property.

Table 7: Basic characteristics of the silica materials used for Si-H surface modification.

| material | description | diameter d | surface area $A / \text{m}^2 \text{ g}^{-1}$ |
|------------|--|-----------------------|---|
| M1f | spherical non-porous particles | 214 nm ^[a] | 12.6 ^[b] |
| M1g | spherical non-porous particles | 222 nm ^[a] | 12.3 ^[b] |
| M2 | spherical porous materials | 5 μm | 115.4 ^[a] |
| M3 | standard chromatography type 60 material | 63-200 μm | - |
| M4 | agglomerated silica nanoparticles | 7 nm ^[c] | 300 |

[a] d_{SEM} , determined in present work; [b] A_{SEM} ; [c] diameter of the single nanoparticle.

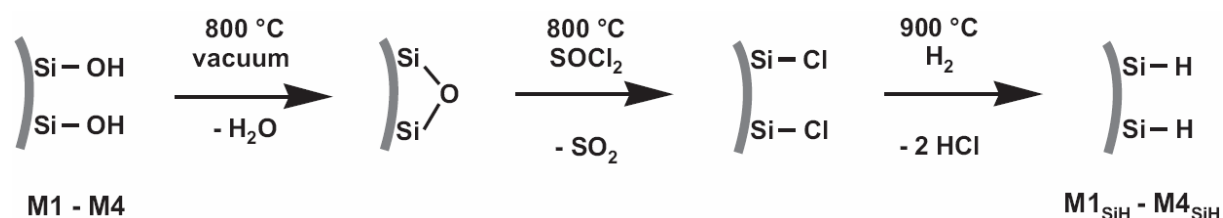
The Stöber particles **M1f** and **M1g** were obtained under the same conditions but from two different batches.

Note that the **M1** materials and **M2** have a clearly defined particle structure with low polydispersity, while **M3** and **M4** are materials that are structurally less defined. For example, **M4** is formed by a network of agglomerated particles [114].

For the introduction of the Si-H group, three modification steps were performed at high temperature as surface reactions *in vacuo* or with a gas as reactant: The silica is first

2. Silicon hydride modified silica surface

pretreated at 800 °C under vacuum for several hours, then chlorinated at the same temperature with SOCl_2 and finally reduced with H_2 to produce $\text{M1}_{\text{SiH}} - \text{M4}_{\text{SiH}}$. The temperature of the last step is critical for a high yield of the desired surface modification, and we will discuss its optimization below. We refer to these reactions as the chlorination-reduction sequence (Scheme 11).



Scheme 11: Surface chlorination-reduction sequence for Si-H formation on silica materials.

For comparison, **M1g** and **M2** were also modified with triethoxysilane (TES), by the silylation method, yielding materials **M1g_{TES}** and **M2_{TES}** (Scheme 12). The condensation of TES was performed under anhydrous conditions. Therefore, the maximum Si-H surface concentration from this procedure can not be higher than the one expected for a monolayer of Si-H groups on the silica surface.



Scheme 12: TES condensation for Si-H formation on silica materials. The dashed lines correspond to unspecified bonds accounting for the possible formation of T^2_{H} and T^3_{H} groups [108].

2.2 Physical properties of the Si-H modified silica materials

The size of particles as well as the surface area and pore structure are basic physical properties of the synthesized materials. The high temperatures employed for the preparation of the **M_{SiH}** materials might induce sintering of the silica matrix. To ensure that changes in

structure are negligible and no loss of surface area occurs during this procedure, the physical properties of the silica before and after Si–H modification are compared. This is done for materials synthesized according to the optimal conditions discussed later in paragraph 2.3.6.

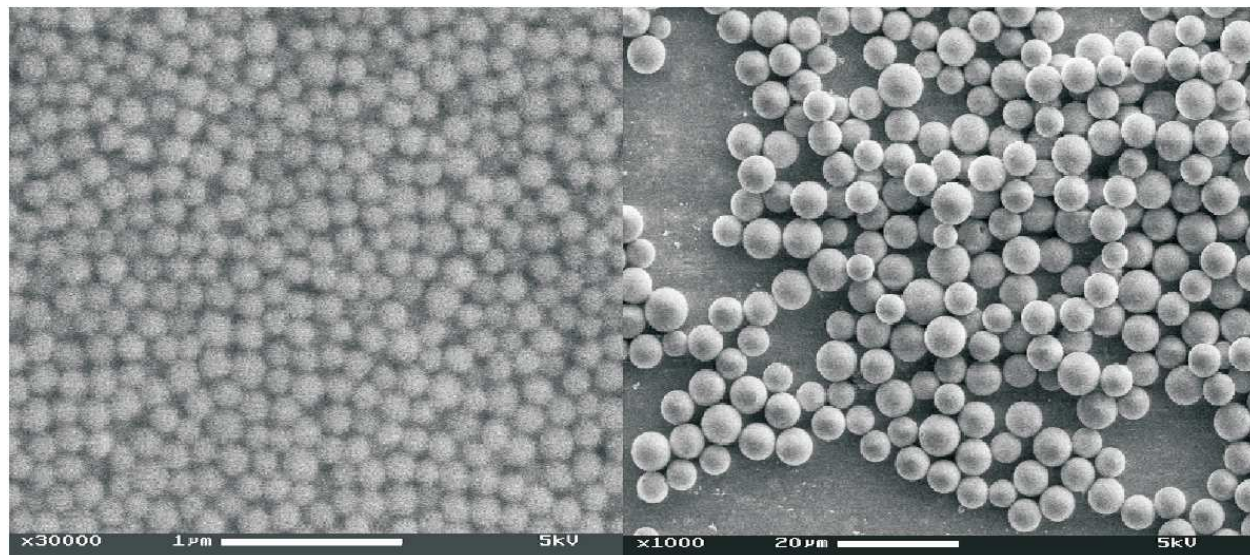


Figure 11: Scanning electron micrographs of $M1f_{SiH}$ (left) and $M2_{SiH}$ (right) after chlorination-reduction.

2.2.1 Size determination by SEM and DLS

Changes in particle sizes and inter-particle sintering as well as possible changes of particle shape might be detected by scanning electron microscopy (SEM) or dynamic light scattering (DLS). In the case of the Kromasil material $M2_{SiH}$ ($d \sim 5\mu\text{m}$), after the chlorination-reduction sequence the spherical shape of the particles clearly remains intact (Figure 11, right). For the monodisperse material $M1f$ with a smaller diameter of $d \sim 200\text{ nm}$ we expected to detect even small changes in structure which might not be seen in the case of the larger Kromasil particles. According to the DLS data, however, after the chlorination-reduction treatment, the particles are still monodisperse and both DLS and SEM prove that no significant changes in the diameter have occurred (Table 8). The slight decrease of d is smaller than the standard deviation of the average particle diameter. The chlorination-reduction sequence does not induce the condensation and agglomeration of individual silica particles (inter-particle sintering) as confirmed by SEM images (Figure 11, left). Furthermore, the particles are still spherical.

Table 8: Size characterization of **M1f** before and after Si–H modification.

| | diameter d / nm | |
|--------------------------|-------------------|--------------|
| | from DLS | from SEM |
| M1f | 220 | 214 ± 16 |
| M1f_{SiH} | 212 | 209 ± 14 |

2.2.2 Surface characterization by nitrogen adsorption-desorption isotherms

The extent of intra-particle sintering during the chlorination-reduction sequence was evaluated for the porous **M2** materials by nitrogen adsorption and desorption isotherms. Pore sizes and surface area were obtained using the Brunauer-Emmet-Teller (BET) and the Baret-Joyner-Halenda (BJH) models. The BET model determines the specific surface area (A_{BET}) including the surface area of micropores [28]. From the BJH method, the volume (V_{BJH}), the average diameter (d_{BJH}) and the specific surface area (A_{BJH}) of the mesopores is accessible. In contrast to A_{BET} , A_{BJH} does not include the surface area of the micropores (see 1.3.3.2.2).

Table 9: BET and BJH characterization of **M2** before and after Si–H modification; definition of symbols see text.

| | $A_{\text{BET}} / \text{m}^2 \text{g}^{-1}$ | $V_{\text{BJH}} / \text{cm}^3 \text{g}^{-1}$ | $d_{\text{BJH}} / \text{nm}$ | $A_{\text{BJH}} / \text{m}^2 \text{g}^{-1}$ |
|-------------------------|---|--|------------------------------|---|
| M2 | 115.4 | 0.94 | 34.1 | 130.3 |
| M2_{SiH} | 103.6 | 0.97 | 33.6 | 130.8 |

The difference between the absolute BET and BJH surface area values, both before and after the chlorination-reduction sequence (Table 9), is due to the different model assumptions of these methods. In general, the BET and BJH models agree fairly well for porous materials with a narrow pore size distribution. The overestimation of the surface area by the BJH model in our case is probably due to the broad pore size distribution [115] of **M2**.

The decrease in A_{BET} by $\sim 10\%$ during surface modification shows that indeed within the particles some sintering of the material occurs. However, A_{BJH} did not change. Thus, the decrease in A_{BET} must be due to a structural change of the micropores. This is supported by the values of V_{BJH} and d_{BJH} , showing that the average volume and diameter of the mesopores did not change significantly (Table 9). Therefore, the loss of surface area is due to the collapse of micropores yielding a more condensed matrix, while the mesopores are preserved.

According to the consistent results from adsorption-desorption isotherm analysis, the SEM experiments and DLS measurements, no significant changes in the physical macrostructure of the silica takes place even under the high-temperature conditions for the chlorination-reduction modification of the silica surface. The desired surface properties – high surface area as well as large pores for **M2** and monodispersity as well as spherical shape for **M1f** – are retained. The small decrease in A_{BET} of **M2_{SiH}** indicates the condensation of the micropores. The resulting more highly condensed matrix is advantageous, considering the need for a high hydrolytic stability.

2.3 Chemical properties of the Si–H modified silica materials

2.3.1 The silicon hydride groups (Si–H)

The hydride modified silicas **M1f_{SiH}** – **M4_{SiH}** show Si-H-characteristic signals in diffuse reflectance infrared Fourier transform (DRIFT) spectroscopy (Figure 12). The stretching vibration of Si–H (ν_{SiH}) on silica is expected around 2270 cm^{-1} [107, 108, 110]. Material **M1f_{SiH}** presents only a broad and weak signal in this region. In comparison, the large surface area materials **M2_{SiH}** – **M4_{SiH}** display strong and sharp signals for ν_{SiH} at 2283 cm^{-1} . The large intensity of this band provides evidence for a high silicon hydride surface coverage.

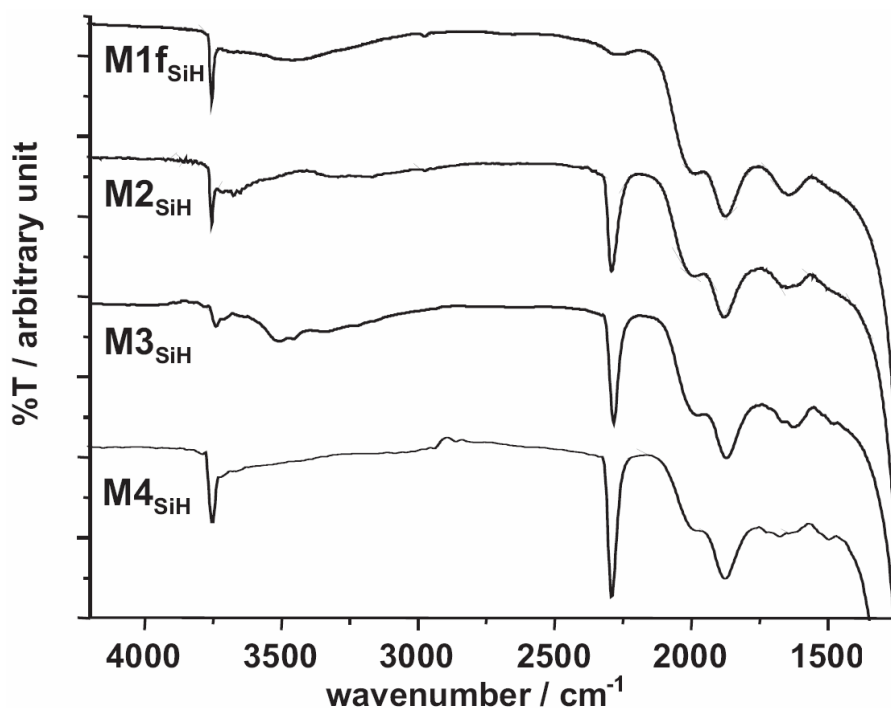


Figure 12: DRIFT spectra of materials **M1f_{SiH}** – **M4_{SiH}** after the chlorination-reduction sequence.

2. Silicon hydride modified silica surface

According to the Gaussian deconvolution (Figure 13), the ν_{SiH} band is composed of a main component at 2283 cm^{-1} and a second small component at 2250 cm^{-1} . In principle, beside the main product (silicon monohydride), silicon dihydride groups (SiH_2 or $\text{T}_{\text{H}_2}^2$, see Scheme 10) may also be produced. The signal for their stretching vibration (ν_{SiH_2}) is expected at 2200 cm^{-1} [116, 117]. However, any IR activity is absent at this wavelength in the DRIFT spectra. This demonstrates that SiH_2 groups are not present in materials $\text{M2}_{\text{SiH}} - \text{M4}_{\text{SiH}}$. Consequently, only silicon monohydride groups are produced by the chlorination-reduction sequence. The assignment for the signals at 2283 cm^{-1} and 2250 cm^{-1} to the T_{H}^3 and T_{H}^2 groups is not possible at this point since only the average wavenumber for ν_{SiH} (2270 cm^{-1}) is given in the literature.

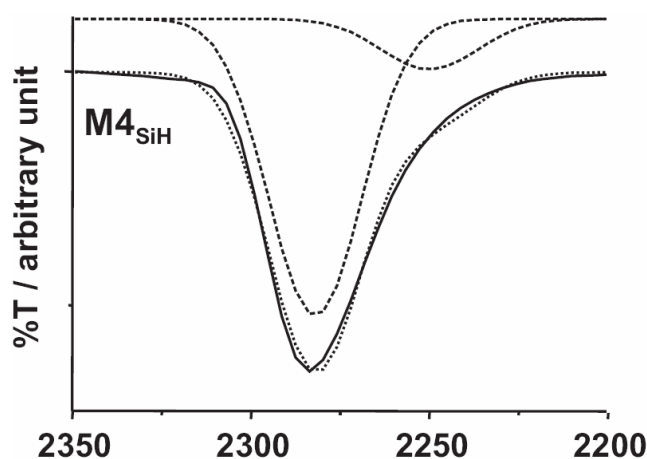


Figure 13: Gaussian deconvolution (top, dashed lines) with envelope (bottom, dotted line) of the ν_{SiH} signal (bottom) from the DRIFT spectrum of M4_{SiH} .

For a quantitative determination of the Si–H surface concentration (Γ_{SiH}), the silica materials were treated with KOH in the presence of ethanol as a proton source. Under these conditions, hydrogen gas evolves [118] which is then quantified by a thermal conductivity detector (TCD) after gas chromatographic separation (GC-TCD). Values of Γ_{SiH} were calculated from the specific Si–H amount n_{SiH} obtained from the GC-TCD method and the BET surface area of the silica materials (Table 10).

The Si–H content of non-porous M1f_{SiH} could not be determined by this method owing to the very low surface area of the material and the resulting low amount of H_2 produced. In the cases of $\text{M2}_{\text{SiH}} - \text{M4}_{\text{SiH}}$, however, the highest specific Si–H amount is obtained for M4_{SiH} , while the highest Γ_{SiH} is found for M2_{SiH} (Table 10).

Table 10: Specific surface area A_{BET} , specific Si–H amount n_{SiH} and Si–H surface concentration Γ_{SiH} after Si–H modification (reduction temperature 900 °C).

| | $A_{\text{BET}} / \text{m}^2 \text{g}^{-1}$ | $n_{\text{SiH}} / \mu\text{mol g}^{-1}$ | $\Gamma_{\text{SiH}} / \mu\text{mol m}^{-2}$ |
|--------------------------|---|---|--|
| M1 _{SiH} | 16.9 | - [a] | - [a] |
| M2 _{SiH} | 103.6 | 329 | 3.2 |
| M3 _{SiH} | 172.6 | 413 | 2.4 |
| M4 _{SiH} | 301.6 | 499 | 1.7 |
| M2 _{TES} | 115.0 | 309 | 2.7 |

[a] not detected.

The theoretical maximum Γ_{SiH} might be derived from the surface concentration of silanol groups (Γ_{SiOH}) in the starting material. However, both vicinal (Q^3) and geminal (Q^2) silanol groups are present on the native silica surface [88]. Since the DRIFT spectra show that only silicon monohydride groups but not SiH_2 groups are produced, the two hydroxyl groups from reaction of each Q^2 group results in one Si–H group only. This also applies to the Q^3 groups. Therefore, each silanol site (Q^3 and Q^2) initially present [119] might yield at most one Si–H group. Consequently, the difference in Γ_{SiH} between the materials might be related to the surface concentration of silanol sites in the starting silica and this concentration may be a more advantageous measure to use as a base for the calculation of the Si–H yield. The surface concentration of silanol sites is obtained as the sum of the surface concentrations of Q^3 and Q^2 groups and is on average lower by a factor of 1.15 [119] compared to the average Γ_{SiOH} of a fully hydroxylated silica surface ($7.6 \mu\text{mol m}^{-2}$ [88]). Therefore, the maximum possible Γ_{SiH} is about $6.6 \mu\text{mol m}^{-2}$ on average. Since the exact value of the surface concentration of silanol sites is not known for each of the silica materials, this average is used to estimate the yield of the chlorination-reduction sequence. On this basis, the Si–H yield is up to 50 %.

It should be noted that **M4**_{SiH} and **M2**_{SiH} differ strongly in their Γ_{SiH} values. According to infrared [120] and solid state NMR studies [121], the silica surface of **M4** displays a larger amount of Q^2 and Q^4 groups and a lower amount of Q^3 groups than the surface of precipitated silica such as **M2**. Therefore, fewer silanol sites are present overall [120], which explains the lower Γ_{SiH} obtained for **M4**_{SiH}.

The values of Γ_{SiH} from the chlorination-reduction sequence reported here are similar to those obtained from the chlorination-reduction sequence in solution with SOCl_2 and LiAlH_4 [108,

110]. Therefore, the chlorination-reduction sequence is as efficient as the previously published procedures for the production of a monolayer of Si-H groups on silica surfaces.

The DRIFT spectra of the hydride modified silicas **M1g_{TES}** and **M2_{TES}** also display ν_{SiH} signals (Figure 14) beside the intense ν_{SiOH} signal. However, the ν_{SiH} of the **M_{TES}** materials is shifted to lower wavenumbers ($\sim 2240 \text{ cm}^{-1}$) compared to the **M_{SiH}** materials.

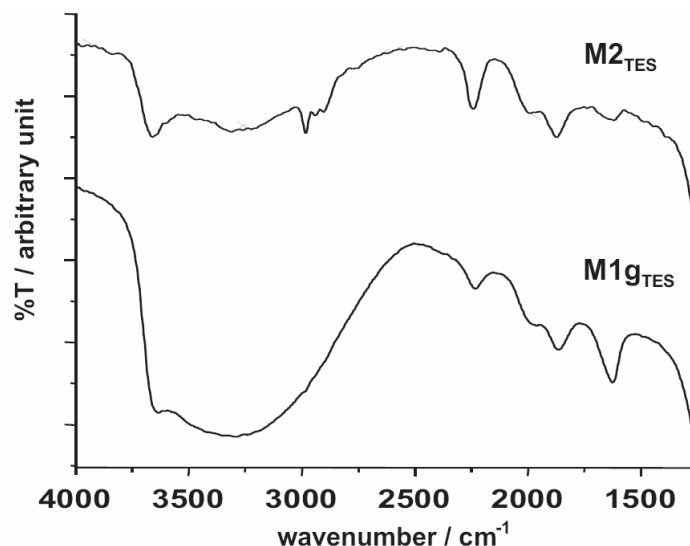


Figure 14: DRIFT spectra of materials **M1g_{TES}** and **M2_{TES}**.

After Gaussian deconvolution of the ν_{SiH} signals (Figure 15), **M2_{TES}** displays a main component at 2240 cm^{-1} and a very small one at 2283 cm^{-1} . Similarly to the **M_{SiH}**, we may expect T^3_{H} and T^2_{H} groups on the **M_{TES}** materials. Moreover, **M_{TES}** may also contain Si-H groups with unhydrolyzed ethoxy substituents. The presence of these ethoxy groups is consistent with the C-H stretching vibration (ν_{CH}) observed in the DRIFT spectrum of **M2_{TES}** between 2900 and 2990 cm^{-1} .

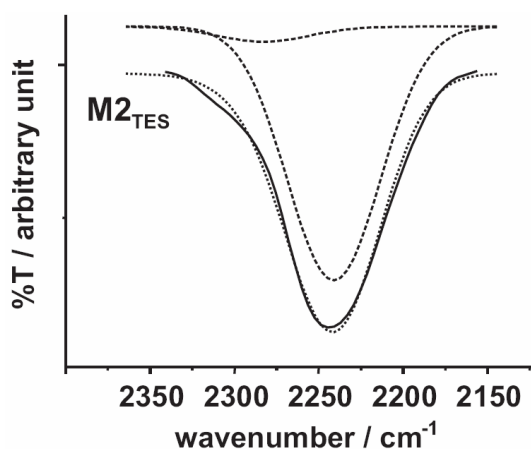


Figure 15: Gaussian deconvolution (top, dashed lines) with envelope (bottom, dotted line) of the ν_{SiH} signal (bottom) from the DRIFT spectrum of **M2_{TES}**.

In conclusion, the M_{SiH} and M_{TES} materials display different types of silicon monohydride groups. However, again, at this point it is not possible to clearly assign a specific Si-H group type to either of these materials. The Γ_{SiH} of M_{2TES} is similar to the one obtain for M_{2SiH} (Table 10). Therefore, both methods have the same absolute yield for the formation of Si-H groups.

2.3.2 The silanol groups (Si-OH)

The DRIFT spectrum of **M2** before Si-H modification (Figure 16, top) shows a strong signal between 3000 and 3800 cm^{-1} , corresponding to the Si-OH stretching vibration ν_{SiOH} of hydrogen bonded silanol groups. After chlorination and reduction, only a signal for isolated silanol groups remains at 3750 cm^{-1} (Figure 16, M_{2SiH}). From the ratio of the integrals of the signals between 3000 and 3750 cm^{-1} in the spectra of **M2** and M_{2SiH} we conclude that 95 % of the Si-OH groups have reacted. The silanol groups have been chlorinated and reduced and/or condensed to siloxane bonds [88] due to the high temperatures, producing water and siloxane bonds within the silica matrix (For the discussion of M_{2A} and M_{2B} , see 2.3.4).

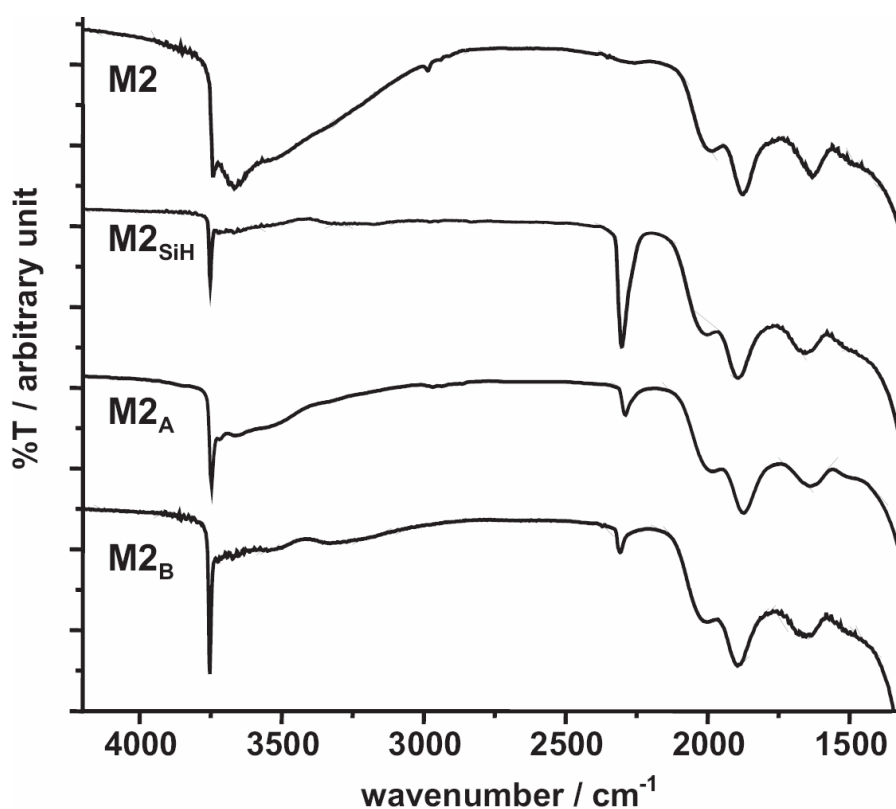


Figure 16: DRIFT spectra of **M2** before modification, after the chlorination-reduction sequence (M_{2SiH}) and after direct reduction with H_2 (M_{2A} and M_{2B}).

On the other hand, both **M1_{gTES}** and **M2_{TES}** materials still display strong ν_{SiOH} of hydrogen bonded silanol groups after Si-H modification (Figure 14). Similar ν_{SiOH} signal intensities were obtained from other Si-H modified silica surfaces prepared by various low temperature (<150 °C) procedures [108, 110].

This clearly demonstrates the advantage of the chlorination-reduction sequence for the elimination of the silanol groups.

2.3.3 The nature of the T_H groups

The Gaussian deconvolution of the Si-H signals in the DRIFT spectra (Figure 13) of the **M_{SiH}** materials suggests the presence of one main type of silicon monohydride groups. These Si-H groups may be either of type T²_H or T³_H. According to the IR spectra, most of the Si-OH groups have reacted and a high I_{SiH} is obtained. Since the T²_H groups would have still one OH substituent, this result indicates that the most likely product of the chlorination-reduction sequence are the desired T³_H groups. However, a direct characterization of the type of bonding between the silica surface and the Si-H group is not possible from the IR spectra.

To unambiguously differentiate between the T²_H and T³_H as well as Q³ and Q⁴ groups on silica surfaces, respectively, ²⁹Si CP/MAS NMR spectroscopy had advantageously been used [105, 107, 108]. The main requirement to record ²⁹Si CP/MAS NMR spectra of Si-H surface modified silica is a high n_{SiH} . Therefore, in this work ²⁹Si CP/MAS NMR spectroscopy was performed on the high surface area materials (**M2_{SiH}** – **M4_{SiH}**) modified by the chlorination-reduction sequence (Figures 17 and 18).

The ²⁹Si CP/MAS NMR spectrum of **M4_{SiH}** (Figure 17) confirms the presence of silicon nuclei in various environments (Scheme 10): In the Q region one maximum at -100 ppm, corresponding to Q³ groups, is observed. The main signal, however, appears in the T_H region (-60 to -90 ppm), with a maximum at -84 ppm, corresponding to T³_H groups. Overlapping of the signals does not allow a direct assignment of the respective other component and differentiation between the T³_H and T²_H groups. Optimized Gaussian deconvolution results in 4 peaks for T³_H (-84 ppm), T²_H (-73.5 ppm), Q³ (-100 ppm), and Q⁴ (-110 ppm). The envelope generated by summation of the individual peaks excellently fits the measured spectrum. If a peak for Q² (at -92 ppm) is added or one of the previously cited peaks is removed, a poorer fit is obtained. Thus, the main component of the T_H signals is due to the T³_H groups. The T²_H groups are only a minor component. The Q group identity is further discussed below. The spectrum of **M2_{SiH}** (Figure 18) displays similar features: After Gaussian deconvolution the

main T_H signal is clearly attributed to T^3_H while only a weak component can be assigned to T^2_H .

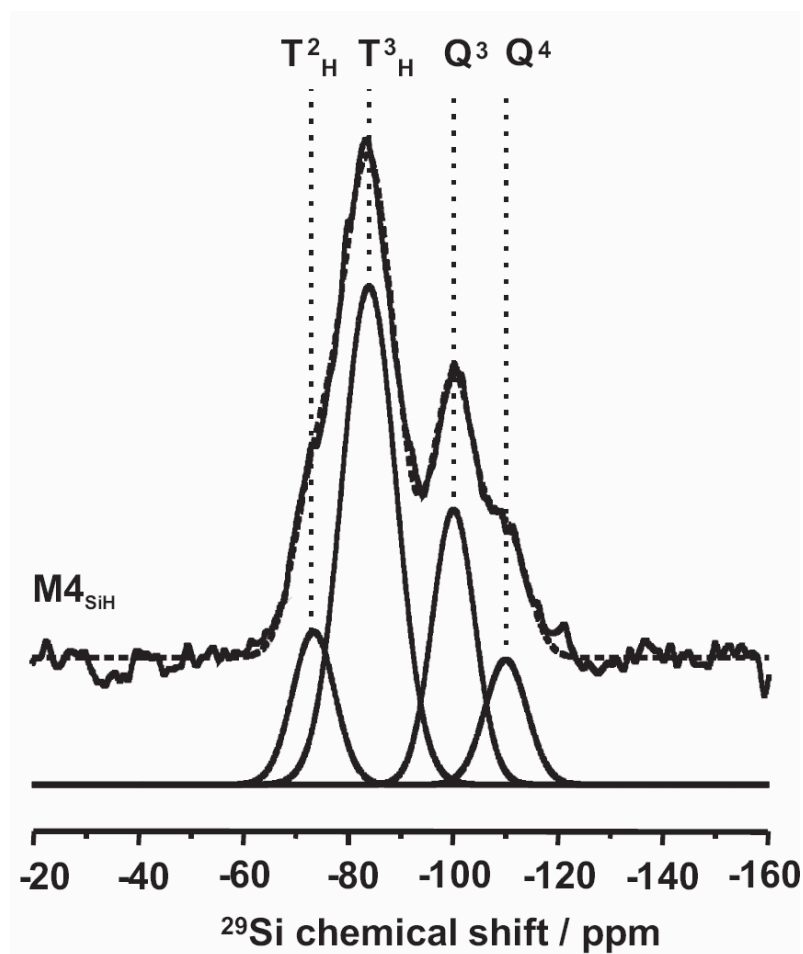


Figure 17: ^{29}Si CP/MAS NMR spectrum of $\mathbf{M4}_{\text{SiH}}$ (top) with Gaussian deconvolution results (bottom) and envelope of Gaussian components (top, broken line).

The ^{29}Si CP/MAS NMR spectrum of $\mathbf{M3}_{\text{SiH}}$ also displays the T^3_H signal. Thus, the ^{29}Si CP/MAS NMR spectra confirm that the chlorination-reduction sequence yields T^3_H groups whether $\mathbf{M2}$, $\mathbf{M3}$, or $\mathbf{M4}$ is used as silica matrix. In contrast, the low temperature conditions used for $\mathbf{M2}_{\text{TES}}$ generate considerably fewer T^3_H groups than the chlorination-reduction sequence. The incomplete condensation of TES on the surface leads mainly to undesired T^2_H functions in $\mathbf{M2}_{\text{TES}}$ (Figure 18). Finally, although a SiH signal was observed in their DRIFT spectra, materials $\mathbf{M1f}_{\text{SiH}}$ and $\mathbf{M1g}_{\text{TES}}$ do not show any detectable NMR-signals in the T_H domain due to their very low surface area (Table 7).

2.3.4 Nature of the Q groups

The ^{29}Si CP/MAS NMR spectra of **M2_{SiH}**, **M4_{SiH}**, and **M2_{TES}** (Figures 17 and 18) only reflect those sections of the materials which have silicon nuclei with protons in close proximity. Especially the amount of the Q^4 groups is not depicted correctly. In particular due to the small amount of surface T^3_{H} and Q^3 compared to bulk Q^4 groups a quantification by NMR techniques is difficult [122]. A single pulse excitation experiment with appropriate delay times will leave the T^3_{H} and Q^3 groups with poor signal to noise ratio, while contact time variation studies will be too time consuming and inaccurate owing to the large number of scans required for the investigated samples. Therefore the NMR study of the Q^3 groups will be limited to qualitative and semi-quantitative interpretations.

Gaussian deconvolution of the ^{29}Si CP/MAS NMR spectra gives direct evidence for the presence of Si–OH groups in all materials. The peaks at -100 and -110 ppm correspond to the Q^3 and Q^4 groups, respectively. On the other hand, no signals for Q^2 groups are detected. Therefore, the remaining Si-OH groups in the material are of Q^3 type.

For the comparison of the population of the Q^3 groups remaining in **M2_{SiH}** and **M2_{TES}**, the ^{29}Si CP/MAS NMR spectra of both materials were recorded with the same experimental parameters. Both **M2_{SiH}** and **M2_{TES}** materials have similar n_{SiH} (Table 10). Therefore, the relative intensities of the Q^3 and T_{H} resonances in the **M2_{SiH}** and **M2_{TES}** spectra (Figure 18) demonstrate that only few Q^3 groups remain in **M2_{SiH}**.

The Q^4 group resonances also provide information on the degree of condensation of the silica matrix. Based on the condensation of the Q^3 moieties to Q^4 groups at high temperature as explained above (see 2.3.2), the spectrum of **M4_{SiH}** (Figure 17) should display a large signal for the Q^4 groups. However, only a small component of the signal in the Q region can be assigned in this way. This seeming contradiction is explained as follows: In solid state ^{29}Si -NMR, cross-polarization (CP) of the ^{29}Si nuclei with the ^1H nuclei ($^1\text{H} \rightarrow ^{29}\text{Si}$) is needed as their natural abundance is only 4.7 %. As CP is based on heteronuclear dipolar interactions, it is sensitive to internuclear distances [122]. The signals of the Q^4 groups in the spectrum of **M4_{SiH}** have only a weak intensity due to the absence of protons in close proximity to these nuclei. In contrast, the spectrum of **M2_{TES}** (Figure 18) exhibits a strong signal for the Q^4 groups, because the protons of the internal silanol groups which are in close proximity to the Q^4 groups enable an efficient $^1\text{H} \rightarrow ^{29}\text{Si}$ cross-polarization of the Q^4 groups [105]. Therefore, the weak Q^4 signal obtained for **M4_{SiH}** provides further evidence that only few silanol groups (Q^3) remain in the silica matrix.

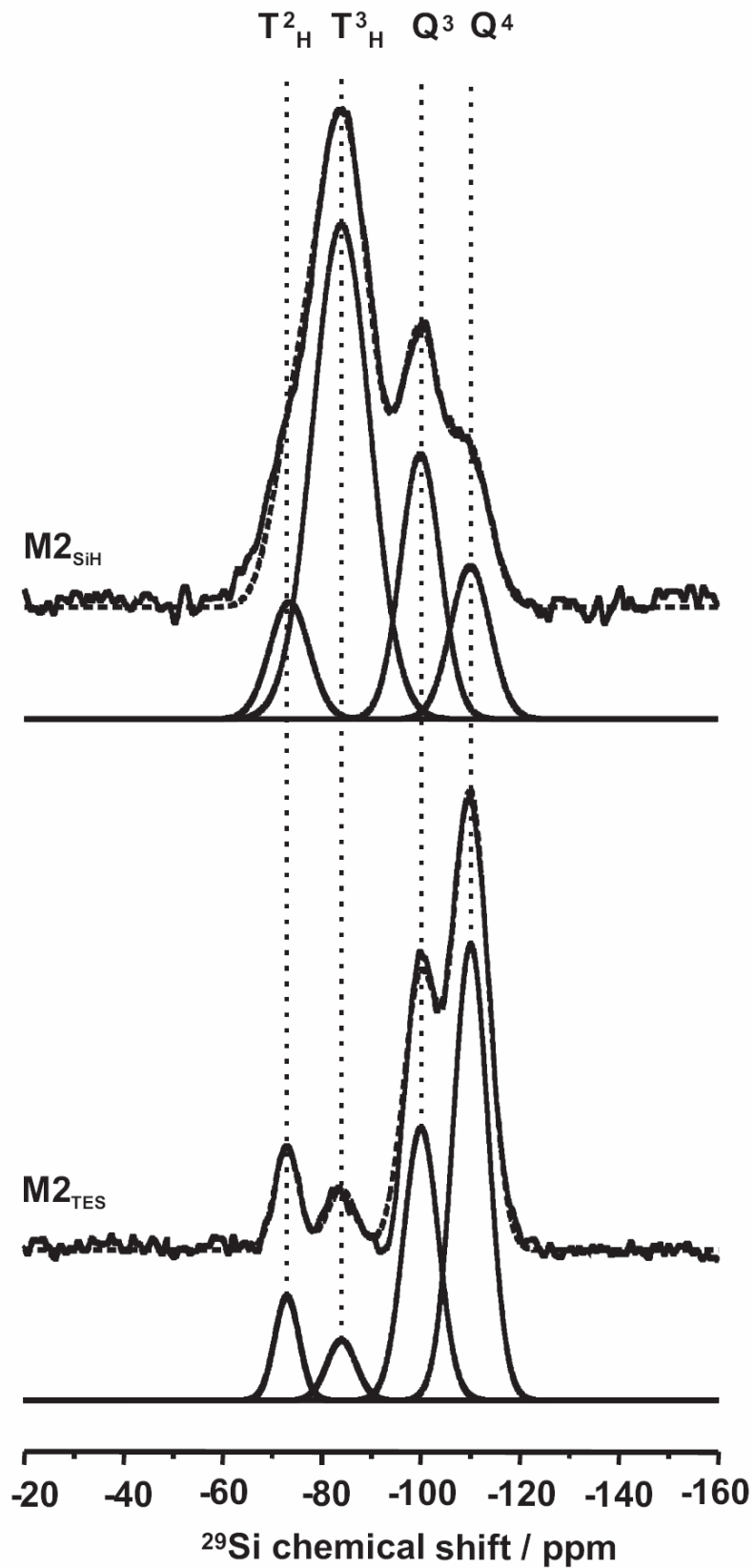
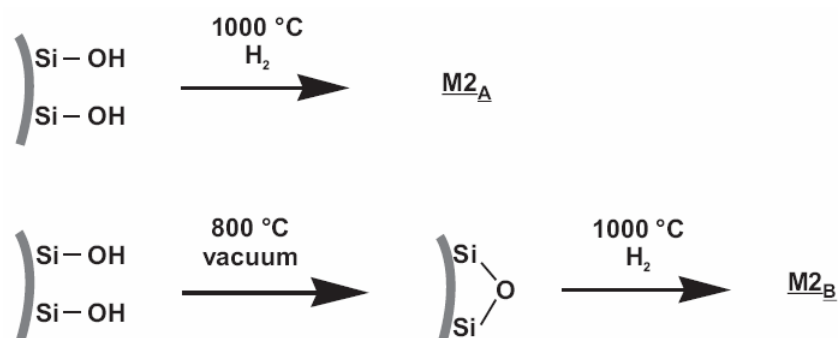


Figure 18: ^{29}Si CP/MAS NMR spectra of $M2_{\text{SiH}}$ (upper part) and $M2_{\text{TES}}$ (lower part) with Gaussian deconvolution results; details see Figure 17.

This confirms that the chlorination-reduction sequence ($\mathbf{M2}_{\text{SiH}}$) results in the condensation of the Si–OH groups compared to procedures where low temperature conditions are used ($\mathbf{M2}_{\text{TES}}$). Consequently, the ^{29}Si CP/MAS NMR results support the surface structure model based on the presence of Si–H groups and only few silanol groups in the \mathbf{M}_{SiH} materials. This is in agreement with the quantitative comparison of IR spectra. In addition, the Si–H groups are assigned as being mostly T^3_{H} groups, where the silicon hydride is linked to the silica matrix via 3 siloxane bonds. Therefore, the main component of the ν_{SiH} signal at 2283 cm^{-1} in the DRIFT spectrum of the \mathbf{M}_{SiH} materials can now be assigned to the T^3_{H} groups. This is the desired functional group for further surface modification as it provides a strong and stable bonding to the modifying molecules. The presence of T^3_{H} and the low amount of T^2_{H} groups is a direct consequence of the use of high temperatures as most silanol groups have condensed to siloxane bridges. A homogeneous surface where the main functional groups are of T^3_{H} type is obtained. The matrix is condensed and mostly consists of Q^4 groups.

2.3.5 The importance of the chlorination step

The importance of the silicon chloride intermediate for the production of a high Si–H surface coverage is demonstrated by processing $\mathbf{M2}$ in two alternative ways missing the chlorination step (Scheme 13). In procedure A, $\mathbf{M2}$ is treated directly with hydrogen at $1000\text{ }^\circ\text{C}$ as described in ref. [107]. In procedure B, $\mathbf{M2}$ is first pretreated at $800\text{ }^\circ\text{C}$ under vacuum and then subjected to hydrogen at $1000\text{ }^\circ\text{C}$. Each preparation was performed twice.



Scheme 13: Direct reduction of silica with H_2 at high temperatures (top: procedure A; bottom: procedure B).

The specific Si–H amounts in the resulting material obtained from the GC-TCD method and the integration of the ν_{SiH} from the DRIFT spectra for $\mathbf{M2}_A$ and $\mathbf{M2}_B$ are compared to the

values obtained for $\mathbf{M2}_{\text{SiH}}$ prepared by the chlorination-reduction sequence at 1000 °C (Table 11, Figure 19). The DRIFT spectra of $\mathbf{M2}_{\text{A}}$ and $\mathbf{M2}_{\text{B}}$ (Table 11, Figure 16) display a considerably weaker signal for the ν_{SiH} compared to the one obtained for $\mathbf{M2}_{\text{SiH}}$. The specific Si–H amount of $\mathbf{M2}_{\text{SiH}}$ is highest, while materials $\mathbf{M2}_{\text{A}}$ and $\mathbf{M2}_{\text{B}}$ display much lower values (Table 11, Figure 19), showing that the chlorination step is necessary to obtain a high Si–H coverage.

Table 11: Specific Si–H amount n_{SiH} and Si–H surface concentration Γ_{SiH} after Si–H modification (reduction temperature 1000 °C).

| | n_{SiH} / $\mu\text{mol g}^{-1}$ | Γ_{SiH} / $\mu\text{mol m}^{-2}$ | relative ν_{SiH} integral / % |
|----------------------------|--|---|---|
| $\mathbf{M2}_{\text{SiH}}$ | 341.3 | 3.3 | 100 |
| $\mathbf{M2}_{\text{A}}$ | 60.7 | 0.58 | 23.6 |
| $\mathbf{M2}_{\text{B}}$ | 26.5 | 0.25 | 14.3 |

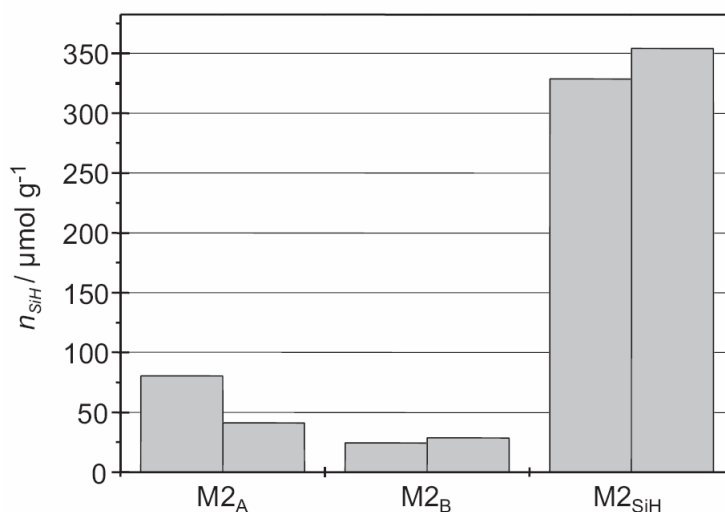


Figure 19: Specific Si–H amount n_{SiH} from GC-TCD measurements (two batches for each material).

The Si–H groups obtained for $\mathbf{M2}_{\text{A}}$ and $\mathbf{M2}_{\text{B}}$ result from the reaction of hydrogen with siloxane bonds: The thermal treatment of silica is known to induce the condensation of the surface silanol groups. Below 400 °C, strained siloxane bridges are produced. At higher temperature, these more reactive siloxane bonds are converted into more stable siloxane bonds [88]. The strained bonds may act as functional groups for further silica surface

modification [123, 124]. In the case of **M2_B**, the pretreatment at 800 °C has condensed the surface silanol groups to stable siloxane bonds [88]. The low Si–H yield obtained after reduction of the dehydroxylated surface shows that the stable siloxane bonds are mostly unreactive toward H₂, even at 1000 °C. The value of Γ_{SiH} obtained for **M2_B** is comparable to the estimated surface concentration of strained siloxane groups on a silica surface treated at 1000 °C ($\sim 0.25 \mu\text{mol m}^{-2}$) [117, 125]. This indicates that only the few highly reactive strained siloxane bridges remaining after the dehydroxylation treatment undergo cleavage by addition of hydrogen.

In the case of **M2_A**, the silica is directly exposed to H₂. As the temperature is raised, the silanol groups condense into the strained siloxane bridges. If the conversion of the strained siloxane bonds into the stable siloxane bonds is slow, the strained ones are still present when the highest temperatures are reached. The higher Si–H yield obtained for **M2_A** as compared to **M2_B** (about twice as much, Figure 19) correlates with the assumption that the strained siloxane bonds can indeed be reduced by H₂. However, compared to **M2_{SiH}**, **M2_A** still displays a much lower n_{SiH} (Figure 19). The reduction of the strained siloxane bonds seems to be far from quantitative due to the competing conversion into stable siloxane bonds, which can not be reduced by H₂. A low specific Si–H amount is obtained for **M2_A** because the surface is only partially activated toward reduction with H₂.

On the other hand, the chlorination of the silica surface activates all surface siloxane bonds for reduction, resulting in a higher Si–H surface concentration (**M2_{SiH}**). The following mechanism is proposed for the chlorination-reduction sequence: The pretreatment under vacuum at high temperatures induces the condensation of the silanol groups (dehydroxylation) accompanied by the elimination of water [88]. The resulting siloxane bonds [123, 124] and the remaining silanol groups are then chlorinated by thionyl chloride at 800 °C. This reaction is known to proceed in high yield [126]. The subsequent reduction of the activated Si–Cl surface with hydrogen is almost quantitative because the chlorine atoms are eliminated from the material in the form of HCl by the gas flow. Therefore, the equilibrium between Si–Cl and Si–H is constantly disturbed and the reaction is driven to completion.

The pretreatment at high temperatures under vacuum is necessary to ensure a reproducible outcome of the chlorination-reduction sequence. If omitted, the elimination of water from the matrix occurs during the chlorination and possibly still during the reduction step when the highest temperatures are reached. This water can react with the silicon chloride or silicon hydride on the surface, regenerating silanol groups. These can not be reduced by hydrogen quantitatively as previously explained.

2.3.6 Optimal reduction temperature

The optimal temperature for the chlorination of the silica surface is 800 °C [126]. To determine the optimal conditions for the reduction of the chlorinated surface, the reaction with H₂ was performed at various temperatures T between 600 and 1000 °C. The Si–H coverage obtained after exposure of the silica to hydrogen for 2 hours is determined by DRIFT and quantified with the GC-TCD method as a function of T . The integral of the Si–H stretching vibration signal (ν_{SiH}) in the DRIFT spectrum does indeed vary with the reaction temperature (Figure 20, left). The Si–H coverage determined by GC-TCD (Figure 20, right) correlates well with the IR results. Both methods show that no significant reaction takes place below 600 °C. Between 600 and 900 °C, the resulting Si–H surface concentration increases with temperature. At even higher temperatures, no further significant increase in the Si–H surface concentration is obtained. Thus, the optimal temperature for the reduction of the chlorinated silica surface with hydrogen is about 900 °C.

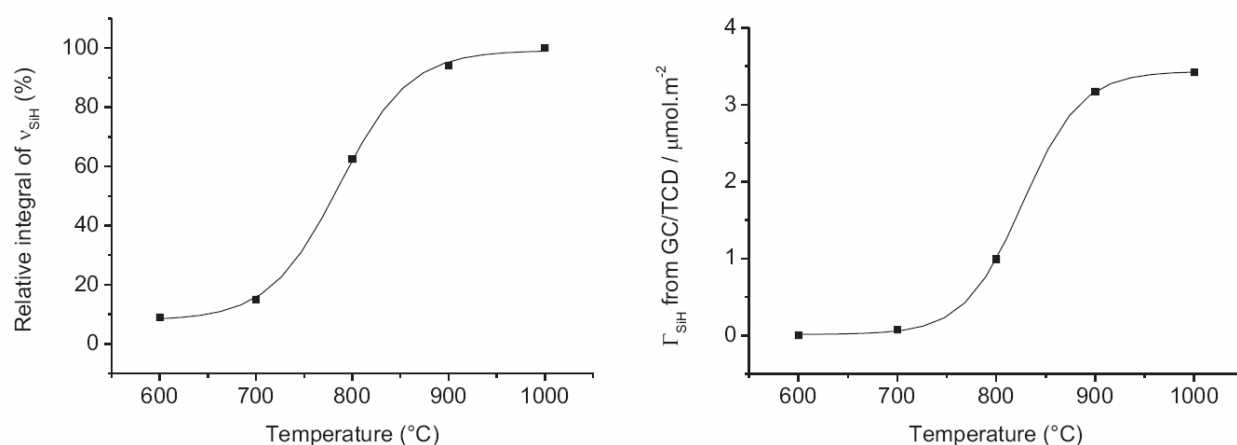


Figure 20: Effect of reduction temperature on the Si–H surface concentration of $\mathbf{M2}_{\text{SiH}}$: normalized integrals of the DRIFT ν_{SiH} bands (left) and Γ_{SiH} obtained from the GC-TCD quantification (right). Data are mean values of several batches (left) or experiments of several samples taken from the same batch (right).

2.2 Conclusion

The silica chlorination-reduction sequence at high temperatures yields a silicon hydride modified surfaces. The chlorination is the key step to achieve a high Si–H coverage, and the optimal temperature for the reduction step is about 900 °C. Under these reaction conditions, as

2. Silicon hydride modified silica surface

shown by the SEM and DLS measurements as well as by the BET and BJH analysis, the physical properties, such as shape, pore size and surface area, remain essentially unchanged. Only micropores are lost due to the high temperatures employed during the procedure. This results in a highly condensed surface, which is confirmed by DRIFT and ^{29}Si CP/MAS NMR spectroscopy: Only few Si–OH groups remain and the main functional groups present on the silica surface are of type T^3_{H} .

Furthermore, this surface is dramatically different from Si–H modifications obtained from TES condensation where Q^3 groups remain after the reaction and more T^2_{H} groups are present on the surface than T^3_{H} groups. The chlorination-reduction sequence yields a more homogeneous Si–H modified surface and a more condensed matrix. Simultaneously, the Si–H surface concentration is similar to the one obtained from the silylation with TES. Thus, the chlorination-reduction sequence represents an ideal strategy to provide the starting material for further silica surface modification by reaction of the Si–H groups.

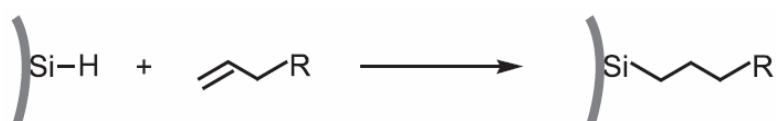
The extensive characterization of the Si–H modified materials was made possible by the use of porous, high surface area material. On the other hand, the Si–H modification on the Stöber materials could only be detected by the DRIFT method because of their low specific surface area. However, the Si–H modified Stöber materials are assumed to have a similar surface chemistry to the other amorphous silica materials used in this study.

3 Silicon-carbon bond formation

The hydrogen-terminated silica surface described in the previous chapter displays the required properties as starting material for further surface derivatization. The various possibilities to form a Si–C bond on such a surface will be explored now.

3.1 Free radical initiated hydrosilylation

The best documented method for the formation of a silicon–carbon bond on a silica surface is hydrosilylation [14, 15, 52, 110, 127, 130] (Scheme 14).

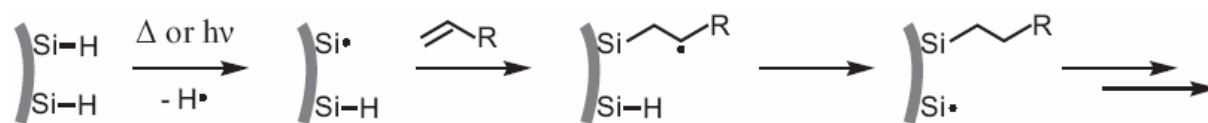


Scheme 14: Hydrosilylation reaction with surface Si–H groups.

Hexachloroplatinic acid has been used successfully for the catalytic hydrosilylation of HPLC separation selectors on porous silica [15]. However, the use of homogeneous catalysts leads to metal contaminations of the surface [56]. Therefore, it is not appropriate for the immobilization of redox-active molecules in our context. As an alternative, the hydrosilylation may also be induced by free radical starters [56]. In this case, the radical starter may also react directly with the surface [131]. In order to fully avoid impurities from catalytic or radical initiator residues, such methods were not used in the present work, and a reagentless radical addition [127] is preferred.

The addition of chlorosilanes to isolated or conjugated C=C bonds in homogeneous conditions, either under high pressure and temperature [53, 127] or under high energy irradiation [127, 132 - 134] has been reported.

Similar methods, with either photochemical [135, 136] or thermal initiation [131, 137], are also employed for the hydrosilylation on hydrogen-terminated *silicon* surfaces [16]. The reaction is believed to start with the homolytic cleavage of the Si-H bond (Scheme 15) [127, 138, 139], although a concerted mechanism has also been postulated [140].

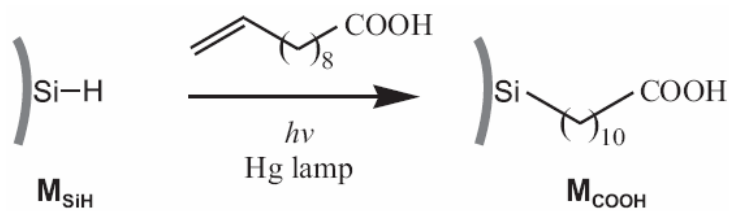


Scheme 15: Mechanism for radical-based hydrosilylation on silicon surfaces [16].

The free radical initiated hydrosilylation is supported on the *silicon* surface by the electron withdrawing effect of the Si bulk matrix [141]: the Si-H bond energy is decreased and the bond may be cleaved by UV light or thermal energy to form a silicon radical. The silicon hydride bond on a *silica* surface has also a low electron density due to the electron withdrawing effect of the silica matrix [69]. Therefore, the free radical induced hydrosilylation on this surface could also take place.

3.1.1 Photochemical hydrosilylation

Photochemical conditions provide a low temperature and reagentless way to induce the radical hydrosilylation reaction [142]. In order to test the photochemical variant on hydride modified silica surfaces, 10-undecylenic acid was used as a bifunctional spacer (Scheme 16).



Scheme 16: Reaction of 10-undecylenic acid with a silicon hydride terminated silica surface.

The carboxylic group does not react with the silicon hydride spontaneously nor under UV irradiation [143], in contrast to amino, hydroxyl or aldehyde groups [135]. On the other hand, the ethene double bond is expected to undergo the described hydrosilylation reaction.

The absence of a methyl group in 10-undecylenic acid will facilitate the characterization of the Si-C bond resulting from the photochemical reaction: methyl group resonances in a ^{13}C NMR spectrum appear in the same range as those of carbon bound directly to a silicon atom (see below). Also, the COOH group may permit a straightforward attachment of redox-active moieties by an amide bond in a subsequent step.

The Si-H modified silica materials used for the surface reaction are **M1g_{TES}**, **M1f_{SiH}**, and **M4_{SiH}** (non-porous materials) as well as **M2_{SiH}** (porous material). These different materials will be designated by the common abbreviation **M_{SiH}**. The non-porous and porous materials will be discussed separately.

3.1.1.1 Immobilization of 10-undecylenic acid via photochemical hydrosilylation on non-porous **M_{SiH}** materials

The following results and discussion refers to the non-porous materials only.

After a suspension of 10-undecylenic acid and **M_{SiH}** in dry hexane is irradiated with UV light from a medium pressure mercury lamp for several days, the DRIFT spectra (Figures 21 and 29, page 94) of the resulting **M_{COOH}** materials show signals for the stretching (2923 and 2857 cm^{-1}) and the bending vibrations (1455 cm^{-1}) of the alkyl C-H bonds as well as the stretching vibrations of the C=O group of the carboxylic acid (1708 cm^{-1}). The presence of the O-H stretching vibration signal may be attributed to the carboxylic group or to adsorbed water (which is likely to be retained via hydrogen bonds with the COOH groups, even after the drying step). The ^{13}C CP/MAS NMR spectra of the **M_{COOH}** resulting from **M1f_{SiH}**, **M1g_{TES}** and **M4_{SiH}** (see Figure 21 for the example of **M4_{SiH}**) show a weak signal at 180 ppm and signals between 10 and 50 ppm, corresponding to the carbon atoms of the carboxylic acid group and the methylene groups of the alkyl chain, respectively.

The presence of these signals in the ^{13}C CP/MAS NMR and DRIFT spectra of the M_{COOH} after several steps of washing and drying provides evidence for the strong attachment of the carboxylic acid spacer. If washing with acetic acid is omitted, the intensity of the signals of the carbonyl group and the alkyl chain in the DRIFT spectra of the M_{COOH} is higher. This demonstrates the importance of this particular washing step to remove non-reacted 10-undecylenic acid that could remain adsorbed through hydrogen bonding with the silica bound carboxylic acid units [142]. The absence of adsorbed 10-undecylenic acid on the particles is further supported by the fact that signals of the alkene carbons of the acid in the ^{13}C CP/MAS NMR spectra are missing.

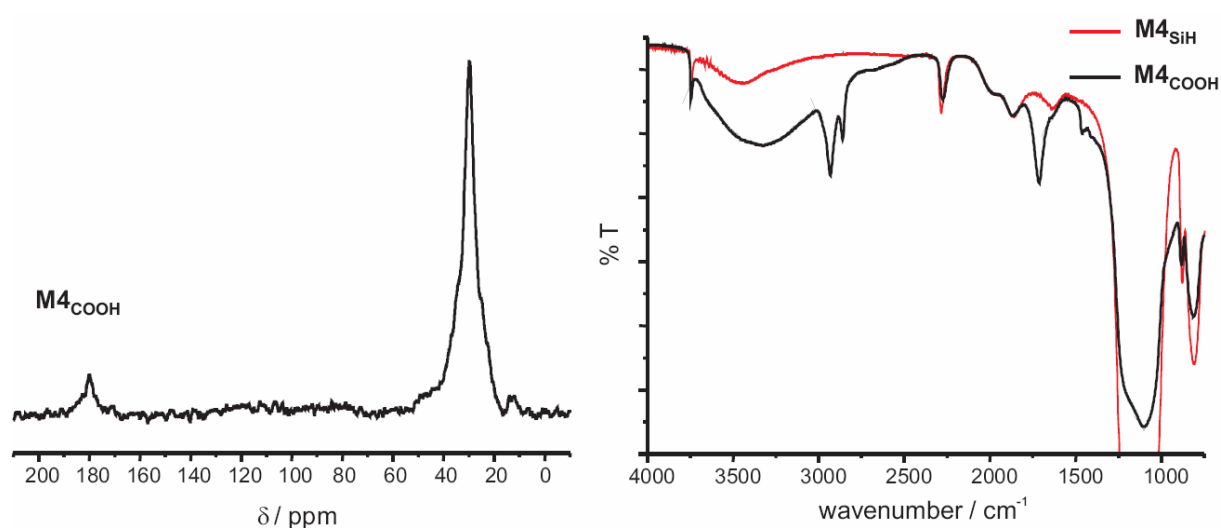


Figure 21: ^{13}C CP/MAS NMR (left) and DRIFT (right) spectra of $\text{M}_{4\text{COOH}}$.

The DRIFT and NMR spectra also indicate that the strong attachment of the carboxylic acid spacer occurs via a covalent silicon-carbon link between the silica surface and a carbon atom of the alkyl chain. First, the comparison of the DRIFT spectra of $\text{M}_{1\text{gTES}}$ and $\text{M}_{1\text{gCOOH}}$ (Figure 29, page 94) show that the Si-H signal at 2250 cm^{-1} has strongly decreased, suggesting that most of the silicon hydride sites have reacted. In the case of $\text{M}_{4\text{COOH}}$, the ν_{SiH} signal intensity has decreased as well (Figure 21), although to a lesser extent. The $\text{M}_{4\text{SiH}}$ nanoparticles are in an agglomerated state which may prevent the UV radiation to reach the nanoparticle surface within the aggregates.

As already mentioned, in the ^{13}C CP/MAS NMR spectrum, the signals at 114 and 139 ppm expected for the two sp^2 carbon atoms of the terminal carbon-carbon double bond of 10-undecylenic acid are not observed. This shows that the C=C bond has reacted. The signal at 180 ppm in the ^{13}C CP/MAS NMR spectrum is likely due to the unreacted carboxylic end of

the spacer. If this group had reacted directly with the silica surface, the carbonyl signal in the ^{13}C CP/MAS NMR spectrum would have been shifted upfield [144].

Two blank tests have been performed in parallel to check the assumption of the formation of a Si-C bond:

First, 10-undecylenic acid in anhydrous and degassed hexane was irradiated for 4 days in the absence of silica particles. According to the NMR spectra after irradiation, no reaction of 10-undecylenic acid is observed under these conditions. Similarly, the IR spectrum after irradiation of M1f_{SiH} under the same conditions, but in the absence of 10-undecylenic acid does not show any change in the surface chemistry of M1f_{SiH} . These results demonstrate that the Si-H groups on the silica and the C=C bond on the spacer only react when both are present under these conditions.

Second, the irradiation of *undecanoic* acid in presence of M1f_{SiH} does not yield any organic modification on the silica surface. Therefore, the attachment observed in the case of 10-undecylenic acid is due to the reaction of the C=C bond whereas the COOH group is not involved. This is in agreement with the observation of the ^{13}C NMR resonance for the carboxylic group in the spectrum of M1_{COOH} (see above).

These data are all consistent with the attachment of 10-undecylenic acid on the silica surface via a Si-C bond obtained from the reaction between the C=C and the Si-H groups. As a direct proof of our structural hypothesis, the resonance at 14 ppm in the ^{13}C CP/MAS NMR spectrum may be assigned to a carbon atom directly bound to a silicon atom on the silica surface [15] (Figure 21).

In order to prove the formation of a Si-C bond, a ^{29}Si CP/MAS NMR spectrum was recorded for M4_{COOH} . However, the T_H signals due to the remaining Si-H groups are broad and overlap with the region where T^3 groups are expected (- 65 ppm [145]).

The photochemical attachment is reproducible if the particles are suspended without large agglomerates and if the suspension is kept strictly oxygen free. Any side reaction of 10-undecylenic acid in the solution is prevented if the temperature of the suspension does not exceed 40 °C: The ^1H and ^{13}C NMR spectra of the solutions after separation from the particles show only the expected signals for 10-undecylenic acid. Therefore, under these conditions, only the desired hydrosilylation reaction occurs on the silica surface. If the temperature exceeds 60 °C, condensation of the carboxylic group with the silicon hydride and/or remaining silanol groups is observed and radical telomerization of the alkene moiety on the silica surface can be suspected from our results.

A high hydride concentration on the silica surface allows to suspend the particles **M_{SiH}** in hexane. In comparison, the more hydrophilic unmodified silica particles **M1** do not suspend in this solvent. In an attempt to generalize this procedure to the attachment of molecules with low solubility in hexane, other solvents have also been investigated for the hydrosilylation. However, only saturated aliphatic hydrocarbons (hexane, cyclohexane), which are highly transparent to UV light, gave satisfactory results. Signals for the alkyl carbons or for the carbonyl group can not be detected after photochemical treatment of 10-undecylenic acid in the presence of **M_{SiH}** in dioxane or toluene.

In conclusion, the reaction of non-porous **M_{SiH}** materials with 10-undecylenic acid takes place under photochemical conditions at the carbon-carbon double bond to provide a carboxylic acid terminated surface.

3.1.1.2 Photochemical reaction of 10-undecylenic acid with the porous **M2_{SiH}** materials

In the case of the porous **M2_{SiH}** material ($A_{\text{BET}} = 103.6 \text{ m}^2 \text{ g}^{-1}$), no organic modification is detected by DRIFT on the silica surface after irradiation in presence of 10-undecylenic acid. **M2_{SiH}** is the only porous material among the **M_{SiH}** used for this reaction. Since amorphous silica is not transparent to UV light, no photochemical reaction is expected to occur inside such a porous material. The reaction may take place at the external surface of porous particles. However, the specific external surface area of **M2_{SiH}** is very low ($A_{\text{SEM}} = \sim 0.5 \text{ m}^2 \text{ g}^{-1}$) due to the large diameter of these particles ($\sim 5 \mu\text{m}$). This explains why no signals for attached 10-undecylenic acid are detected in the DRIFT spectrum of **M2_{SiH}** after reaction. The difficulty to suspend the large **M2_{SiH}** particles in the solvent may also affect the surface reaction. Therefore, the photochemical hydrosilylation method described here is limited to the non-porous **M_{SiH}** materials (**M1f_{SiH}**, **M1g_{TES}**, **M4_{SiH}**).

3.1.2 Thermal hydrosilylation

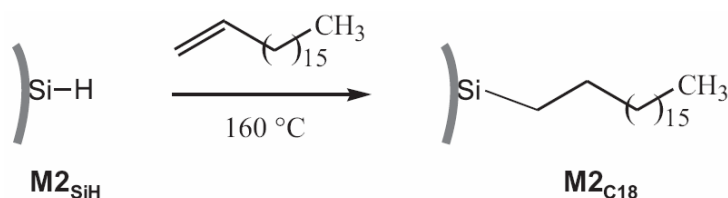
The heterogeneous hydrosilylation on Si-H terminated silica surfaces with small olefin molecules in the gaseous state under high pressure and temperature conditions was described [53]. On silicon surfaces, thermally induced hydrosilylation reactions also take place in the condensed phase and can therefore be used for larger olefin molecules [16]. If this

reaction were possible on the silica surface, it could also be applied for the immobilization of the redox-active molecules needed for our purposes.

3.1.2.1 Immobilization of 1-octadecene via thermal hydrosilylation

Since the high temperature conditions may induce the reaction of other functional groups beside the C=C bond, the reaction is first investigated with 1-octadecene. Moreover, the boiling point of this compound makes it possible to perform the reaction in neat olefin.

The porous $M2_{SiH}$ material, which did not react under the photochemical conditions, was used as the hydride modified silica matrix to test the hydrosilylation under high temperature conditions (Scheme 17). The higher surface area of porous materials enables a higher loading with modifiers, which facilitates their characterization.



Scheme 17: Reaction of 1-octadecene with a silicon hydride terminated silica surface.

We will denote the resulting alkyl modifier with 18 carbon atoms as C18 in the following.

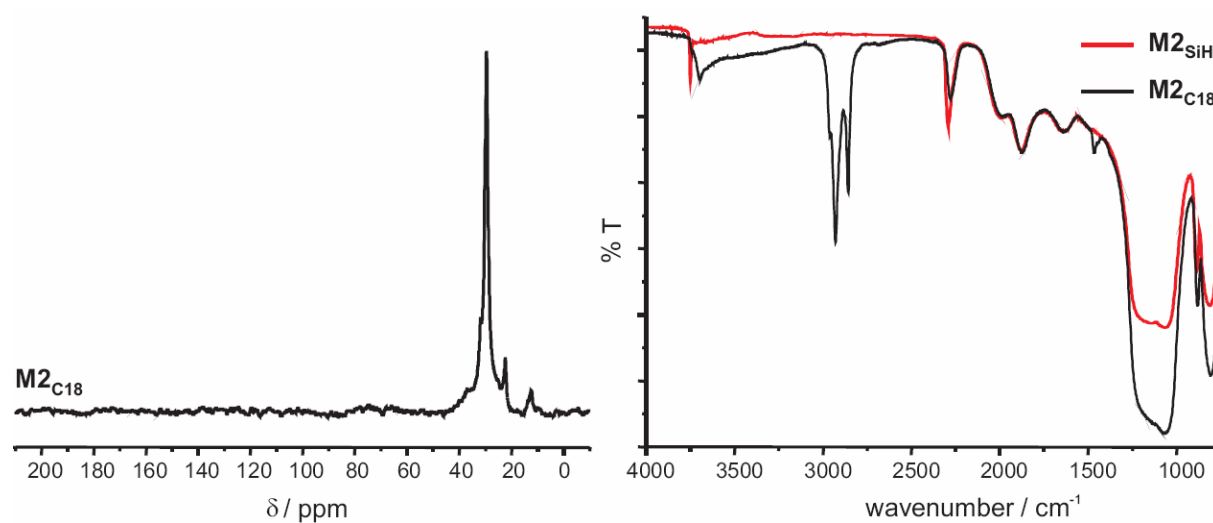


Figure 22: ^{13}C CP MAS NMR (left) and DRIFT (right) spectra of $M2_{C18}$.

3. Silicon-carbon bond formation

The immobilization of 1-octadecene on hydride modified silica **M2_{SiH}** was observed at temperatures above 160 °C. The material obtained from this reaction is referred to as **M2_{C18}**. The presence of the alkyl groups on the silica surface after thorough Soxhlet washing and drying steps is unambiguously shown by the signals between 20 and 40 ppm in the ¹³C-CP/MAS-NMR spectrum and between 2800 and 3000 cm⁻¹ in the DRIFT spectrum (Figure 22). Based on elemental analysis (carbon content: 3.4 %) and the value of the BET surface area (103.6 m² g⁻¹, Table 10), the surface concentration of alkyl groups is 1.5 μmol m⁻².

The absence of signals between 110 and 140 ppm in the ¹³C-CP/MAS-NMR spectrum and between 3000 and 3100 cm⁻¹ in the DRIFT spectrum shows that the carbon-carbon double bond has fully reacted. Moreover, the intensity decrease of the Si-H stretching vibration in the DRIFT spectrum after hydrosilylation also shows that some of the silicon hydride units have reacted:

The relative amount of the reacted Si-H groups may be semi-quantitatively determined from the DRIFT spectra. For this purpose, the materials are diluted in KBr, so that the absorbances of the signals between 1500 and 4000 cm⁻¹ are low enough to allow their quantitative analysis [113]. To enable an accurate comparison between different spectra, the integration value from the signal of the stretching vibration of Si–O–Si (ν_{SiOSi}) at 1870 cm⁻¹ was used as an internal standard [113]. The integration values for ν_{SiH} were normalized with respect to this integral. The absolute value of the specific Si-H amount n_{SiH} remaining in **M2_{C18}** is determined by the GC/TCD method.

The comparison of the integration of the Si-H signals in the IR spectrum as well as the n_{SiH} obtained from GC/TCD measurements of **M2_{SiH}** and **M2_{C18}** (Table 12), show that about 1/3 of the initial silicon hydride groups have reacted during the hydrosilylation reaction.

Table 12: Specific Si–H amount n_{SiH} and relative ν_{SiH} integral before and after C18 modification.

| | n_{SiH} ^[a] / μmol g ⁻¹ | relative ν_{SiH} integral ^[b] |
|-------------------------|---|--|
| M2_{SiH} | 337.3 | 1.41 |
| M2_{C18} | 230.0 | 0.91 |
| difference | -31.7 % | -35.7 % |

[a] from GC-TCD analysis. [b] from DRIFT measurements.

3. Silicon-carbon bond formation

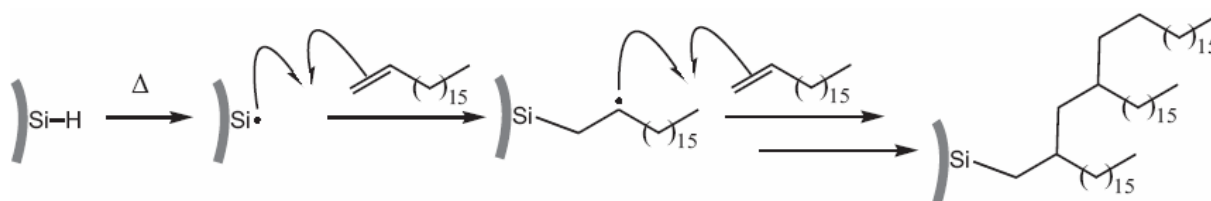
The absence of any C=C bond related signal and the decrease of the ν_{SiH} intensity in **M2**_{C18} are indirect evidence for the formation of a Si-C bond in a hydrosilylation reaction.

Direct evidence for this reaction is however not unambiguously provided from these techniques. Although the surface area of **M2**_{C18} is high enough to apply ²⁹Si CP MAS NMR spectroscopy, the same problem as for the characterization of **M4**_{COOH} arises: The T_H signals due to the remaining SiH groups are broad and overlap with the region where T³ groups are expected (- 65 ppm [145]).

In the ¹³C CP MAS NMR spectrum of **M2**_{C18}, the signal at 12.4 ppm may be assigned to the carbon atom of a Si-C bond but could as well be attributed to the CH₃ group of the C18 chain. However, the unsymmetrical shape of this signal is in agreement with the possible overlapping contribution from both the CH₃ and Si-C resonances.

The absence of any unexpected signal in the spectra of **M2**_{C18} is good evidence for the absence of side reactions occurring during this reaction. Also, the ¹H and ¹³C NMR spectra of 1-octadecene re-isolated from the reaction mixture after separation from the particles show only the known signals for 1-octadecene and for the impurities originally present in 1-octadecene (~10 % of octadecane and branched octadecene). Therefore, the reaction of 1-octadecene on the particle surface occurs without polymerization in the solution.

On the other hand, telomerization on a silica surface may occur [53, 127]. Indeed, the reaction between a silicon hydride and the C=C bond yields in a first step, a free radical center on the β -carbon in the addition product. This radical is expected to react with the hydrogen atom resulting from the homolytic cleavage of the Si-H bond. However, it may also react with a second C=C bond (Scheme 18). This yields a new C-C σ bond, which, after subsequent repetition of this step, would yield short polymers of the C18 groups covalently linked to the silica surface. The DRIFT and solid state NMR spectra do not make it possible to discriminate between the hydrosilylation product and this type of side reaction products (Scheme 19).

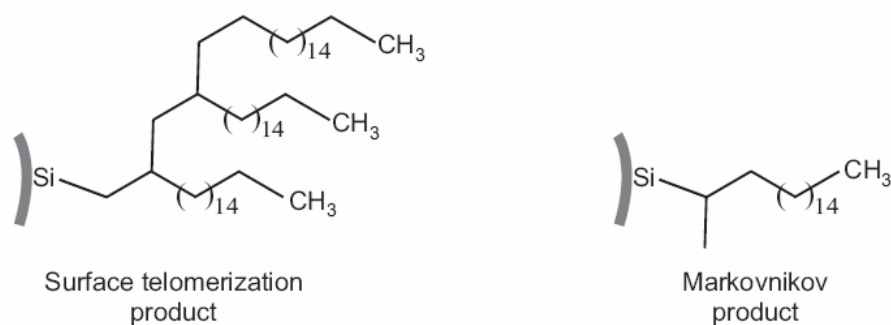


*Scheme 18: Possible mechanism for the telomerization of 1-octadiene on **M2**_{SiH} surface at high temperature.*

3. Silicon-carbon bond formation

The C18 surface concentration (Γ_{C18}) may give indirect information about this side reaction. From the GC-TCD analysis, we know that n_{SiH} of $\mathbf{M2}_{\text{C18}}$ is lower by $107 \mu\text{mol g}^{-1}$ compared to n_{SiH} of $\mathbf{M2}_{\text{SiH}}$. This corresponds to a decrease in Γ_{SiH} of $1.04 \mu\text{mol m}^{-2}$. In comparison, Γ_{C18} is $1.50 \mu\text{mol m}^{-2}$. Since the amount of C18 chains present on the surface of $\mathbf{M2}_{\text{SiH}}$ is about 50 % higher than the amount of Si-H groups that have reacted, some telomerization side reaction probably occurs.

Another possible side reaction may be Markovnikov addition. Neither the solid state NMR spectrum nor the DRIFT spectrum enables to discriminate the Markovnikov (Scheme 19) and the anti-Markovnikov products on the silica surface. However, since the reaction is induced by a free radical, the addition of the Si-H bond to the C=C bond is expected to yield the anti-Markovnikov product with high selectivity [146].



Scheme 19: Possible side-reaction of the free radical induced hydrosilylation reaction.

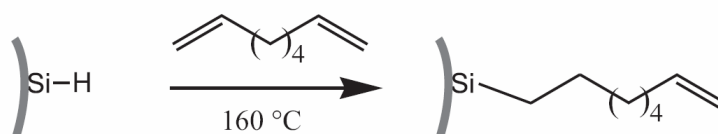
In summary, the covalent attachment of C18 on $\mathbf{M2}_{\text{SiH}}$ demonstrates the feasibility of a thermally induced hydrosilylation. Although this modified silica does not have any application in the attachment of redox-active molecules, it displays desired properties for reverse phase HPLC (See 6.1).

3.1.2.2 Immobilization of 1,7-octadiene via thermal hydrosilylation

In order to apply the thermal hydrosilylation for the attachment of active centers, a second functional group is needed on the spacer. However, as mentioned previously, many functional groups may react with the Si-H bond under the high temperature conditions used. In order to prevent such side reactions, one possibility is to use an α,ω -diene, for example 1,7-octadiene, instead of 1-octadecene (Scheme 20). Both C=C bonds might react with the silica surface;

however, in the case where only one bond reacts, the second one may be used for the immobilization of active centers.

The use of the diene would also facilitate the characterization of the type of bonding resulting from the thermal hydrosilylation reaction. Indeed, similarly to 10-undecylenic acid, used for the photochemical hydrosilylation reaction, the absence of a methyl group in the 1,7-octadiene, prevents the possible overlapping of a methyl group signal with the resonance from the carbon atom of the Si-C bond in the solid state ^{13}C NMR spectrum.



Scheme 20: Reaction of 1,7-octadiene with silicon hydride terminated surface.

The reaction of M2_{SiH} with 1,7-octadiene in hexadecane as a solvent at 160 °C yields material $\text{M2}_{\text{C=C}}$.

As for M2_{C18} , the presence of the organic modifier on $\text{M2}_{\text{C=C}}$ after the washing and drying steps is confirmed by IR and NMR spectroscopy as well as by elemental analysis.

The signal between 9.5 and 12.5 ppm in the ^{13}C CP/MAS NMR spectrum is consistent with a Si-C bond resulting from the radical hydrosilylation reaction.

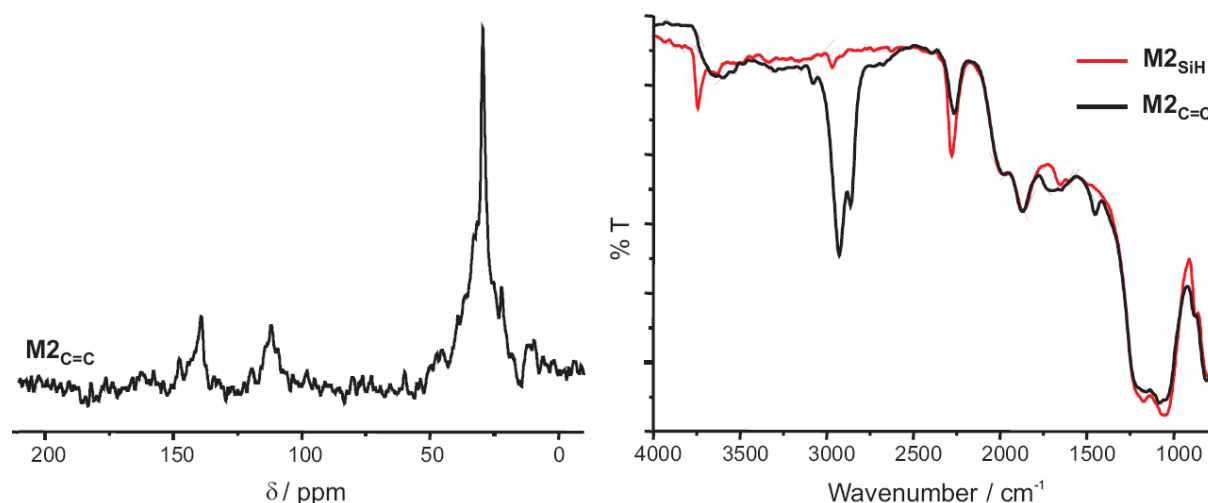


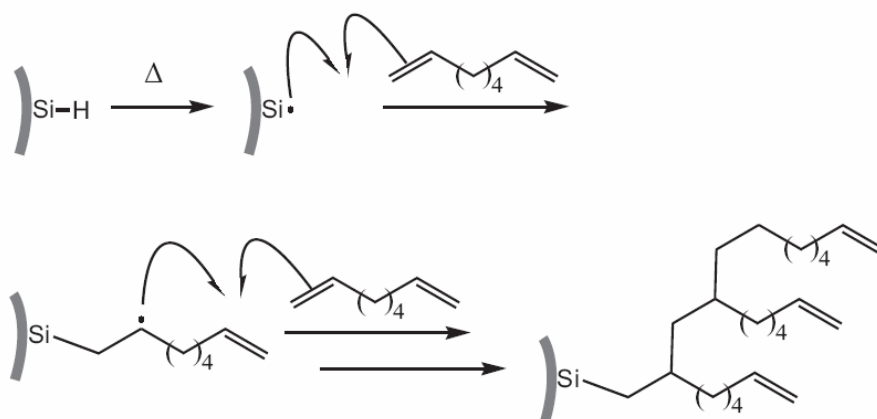
Figure 23: ^{13}C -CP/MAS-NMR (left) and DRIFT (right) spectra of $\text{M2}_{\text{C=C}}$ before (top) and after (bottom) radical hydrosilylation reaction.

3. Silicon-carbon bond formation

The presence of signals at 112 and 139 ppm in the ^{13}C CP MAS NMR spectrum as well as at 3077 and 1650 cm^{-1} ($\nu_{\text{C-H}}$ and $\nu_{\text{C=C}}$ respectively) in the DRIFT spectrum of $\mathbf{M2}_{\text{C=C}}$ (Figure 23) shows that not all carbon-carbon double bonds have reacted. These unreacted C=C bonds could be used as a functional group for further modification of the surface.

Based on the carbon elemental analysis results and the BET surface area, the surface concentration of alkenyl groups is 5.6 $\mu\text{mol m}^{-2}$ and the specific amount is 580 $\mu\text{mol g}^{-1}$ (n_{C18}) of silica $\mathbf{M2}_{\text{C=C}}$. The specific amount of Si-H that has reacted can not be quantitatively determined by DRIFT because in this case the internal standard band at 1870 cm^{-1} overlaps with the $\nu_{\text{C=C}}$ band. A qualitative comparison of the ν_{SiH} intensities in the DRIFT spectra of $\mathbf{M2}_{\text{C=C}}$ and $\mathbf{M2}_{\text{SiH}}$ (Figure 23), however, shows that the Si-H groups have partially reacted. Moreover, n_{SiH} of $\mathbf{M2}_{\text{SiH}}$ is only 330 $\mu\text{mol g}^{-1}$ (Table 10). Therefore, the n_{SiH} that has reacted is significantly lower than the n_{C18} that is present on the silica surface after reaction. This indicates that, in this case, telomerization of the diene, as a subsequent reaction to the hydrosilylation reaction, occurs to an appreciable extent.

On the other hand, according to NMR investigations of the supernatant of the hydrosilylation reaction mixture after separation of the silica, polymerization of 1,7-octadiene does not occur in solution. This confirms that the reaction only occurs on the silica surface, which is consistent with the hypothesis of a radical induced hydrosilylation followed by a telomerization reaction (Scheme 21).



Scheme 21: Possible mechanism for the reaction between $\mathbf{M2}_{\text{SiH}}$ and 1,7-octadiene at high temperature.

3. Silicon-carbon bond formation

The experiments discussed in this chapter demonstrate that the free radical initiated hydrosilylation reactions can be applied to modify Si-H terminated silica surfaces. Evidence for a strong attachment of the organic molecules on the silica surface is observed. However, only indirect evidence for the Si-C bond formation were established. Moreover, the possibility for a radical initiated surface telomerization as well as Markovnikov addition during the hydrosilylation can not be excluded.

Direct evidence for all of these issues could be obtained by using a 1-alkene with ^{13}C nuclei in position 1. This modifier type is investigated separately [147].

Both photochemical and thermal hydrosilylation may be employed for the functionalization of the silica surface for the subsequent immobilization of redox-active molecules. The photochemical induction is advantageous owing to its mild reaction conditions. However, it is limited to non-porous materials since amorphous silica is not transparent to UV light. Because of the higher loading and application possibilities of porous materials, their functionalization via a radical hydrosilylation is also desired. In order to achieve the hydrosilylation of the Si-H groups within porous materials, the thermal initiation is needed.

3.2 Base catalyzed dehydrogenative coupling of silicon hydride with terminal alkyne

As an alternative route to the addition reaction of Si-H groups to C=C bonds (hydrosilylation, see 3.1), the formation of a Si-C bond via substitution reactions of carbanions at the Si-H group was investigated. The purpose is to obtain a Si-C bond without any telomerization side reaction in order to achieve a homogeneous surface modification.

Silicon compounds in general display a higher reactivity toward substitution compared to the corresponding carbon compound. From a kinetic point of view, the larger covalent radius of the silicon atom results in a lower shielding against nucleophilic attack. Moreover, the empty d-orbitals of the silicon atom take part in substitution reactions, by increasing the coordination number of the transition state, leading to a lowering of the activation energy. Also, because of the presence of the d-orbitals, the nucleophile is not required to attack from the back with respect to the leaving group [148]. This is important, in order to make 2nd order substitution reactions possible on the silica surface as inversion of the configuration is prevented. Moreover, from a thermodynamic point of view, the lower electronegativity of Si compared to C as well as the generally lower bond strength of Si-X compared to C-X, makes the silicon compounds more reactive toward substitution than their carbon analogues [128].

3. Silicon-carbon bond formation

Si-Cl- or Si-O-Si-modified materials may be used as starting points for the formation of Si-C bonds. For example, strong nucleophiles, like methyl lithium (MeLi) or functionalized Grignard reagents were used to produce Si-C bonds from chlorinated [50] or dehydroxylated [30] silica surfaces. However, due to the strength of these nucleophiles, the extent of reaction on a single surface silicon atom is difficult to control and one or more surface siloxane bonds may be cleaved. For example, the reaction of a chlorinated silica surface with MeLi yields the T³, D² and M products (Figure 1) [50]. The latter two display a poorer stability due to their lower cross-linking to the silica matrix (2 and 1 Si-O-Si bond respectively). To prevent the cleavage of the siloxane bonds during the alkyl group attachment on Si-Cl groups, weaker nucleophiles may be used.

A second drawback with these starting materials is the production of silanol groups resulting from the cleavage of the siloxane bonds and the hydrolysis of the unreacted silicon chloride groups. To prevent the undesired formation of silanol groups, a less reactive silicon group should be used as electrophile for the reaction with carbanions. The Si-H group may be adequate for this purpose. Indeed, the Si-H bond is inversely polarized as compared to the C-H bond, and is therefore suitable for nucleophilic substitution [128] and is, at the same time, less reactive than the Si-Cl or siloxane bonds.

In summary, Si-C formation on a silica surface via nucleophilic substitution ideally would involve the reaction of weak carbanions with Si-H groups.

However, in this reaction, the hydride ion which is the leaving group, is a strong base itself. Therefore, the use of bases that are weaker than the hydride ion will yield a low amount of product as the equilibrium of the reaction will be shifted toward the starting material. One strategy for lowering the Gibbs free energy of the products would be to make the hydride a better leaving group. This is the case in the dehydrogenative coupling reaction (also called dehydrocondensation) where the hydride reacts with a proton, while the Si-C bond is formed. The resulting H₂ is eliminated from the reaction mixture and the equilibrium of the reaction is shifted toward the product. To form a Si-C bond by dehydrocondensation, protic C-H groups (terminal alkynes or sp³ carbon atoms, carrying a H atom, in α position to electron withdrawing groups) may be used as nucleophiles. However, in this reaction, a high activation energy is needed. For example, the reaction between a terminal alkyne and Si-H only occurs above 300 °C [128]. Moreover, under these conditions, the addition of Si-H to the C \equiv C bond also occurs as a side-reaction. Therefore, to make this reaction applicable, a catalyst is needed. For example, dehydrogenative cross-coupling reactions of hydrosilanes with monosubstituted alkynes to produce alkynylsilanes are catalyzed by transition metal complexes (H₂PtCl₆ [149],

3. Silicon-carbon bond formation

$\text{RhCl}(\text{PPh}_3)_3$ [150], $\text{Ir}_4(\text{CO})_{12}\text{-PPh}_3$ [151]). However, with these catalysts, the dehydrocondensation reaction competes with the hydrosilylation reaction. Higher selectivity toward the dehydrocondensation product was achieved when CuCl was used as catalyst [152]. However, as stated previously in the introduction, for our purpose transition metals should be avoided as catalysts, because of possible metal impurities remaining on the silica surface after modification.

The dehydrogenative coupling reaction may also be catalyzed by a base. For example, an alcohol in the presence of a Si-H group and a catalytic amount of a base will produce a Si-O bond and H_2 [128]. Similarly, primary amines react with Si-H, producing a Si-N bond and H_2 [52]. In this case, the amine is the nucleophile, and, at the same time, acts as the base to catalyze the reaction.

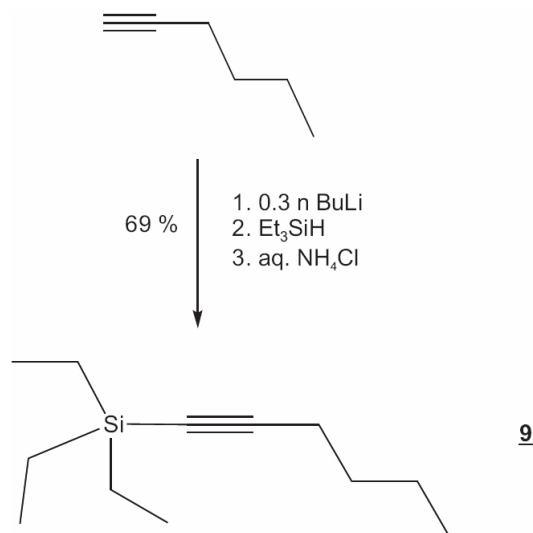
For the formation of Si-C bonds, the reaction between reactive silane species (Ph-SiH_3) and monosubstituted alkynes catalyzed by solid [153 - 156] as well as soluble bases [51] have been described. When the less reactive Et_3SiH is used, contradictory results have been reported about the success of the reaction [51, 156].

Since Si-H groups on the silica surface are also expected to be less reactive than Ph-SiH_3 , the base catalyzed dehydrogenative cross-coupling is first investigated in a model reaction with Et_3SiH . Moreover, in order to make this reaction compatible with the goal of surface modification, a soluble base will be used.

3.2.1 Base catalyzed dehydrogenative coupling between triethylsilane and 1-hexyne

Si-C bond formation via dehydrogenative coupling reaction was tested in solution with 1-hexyne and Et_3SiH . Lithium hexynide is used as the catalyst and was prepared in situ by reaction between butyllithium and 1-hexyne (Scheme 22). The base catalyzed reaction was performed in hexane as well as THF as solvents.

The use of hexane as solvent does not yield any reaction between the terminal alkyne and the silane probably because of the poor solubility of lithium hexynid in hexane. On the other hand, the spectrometric data of the product formed in THF correspond to those expected for triethylhex-1-ynylsilane (**9**).



Scheme 22: Base catalyzed dehydrogenative coupling of triethylsilane with 1-hexyne.

The ¹³C NMR spectrum unambiguously demonstrates the formation of the Si-C bond: The two sp hybridized carbons in triethylhexyn-1-ylsilane have chemical shifts of 81.2 (Figure 24) and 108.6 ppm. This is in agreement with literature values for other alkyn-1-ylsilane compounds [157, 158]. The signal at 81.2 ppm may be assigned to the sp carbon in the α position (C_α) to the Si atom, while the signal at 108.6 is assigned to the β sp carbon atom (C_β).

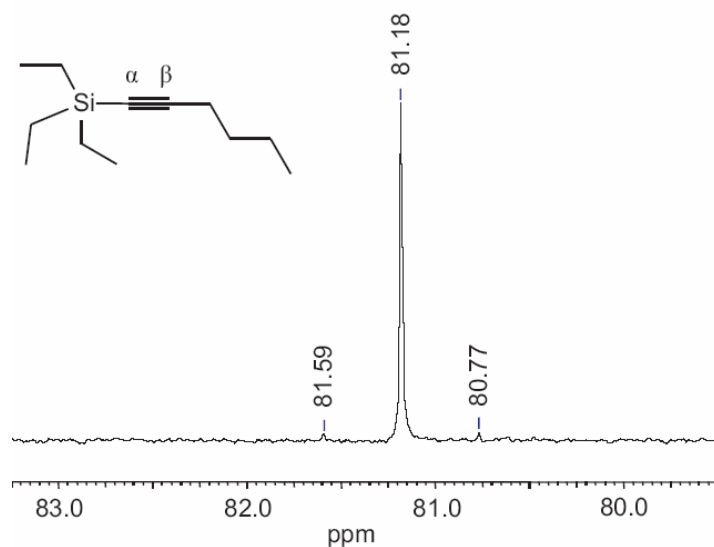


Figure 24: ¹³C NMR spectrum of **9** (excerpt showing resonance signal of C_α).

Compared to the expected chemical shift for ¹³C nuclei of C≡C bonds (60 - 90 ppm), the signal of C_β in the ¹³C spectrum of **9** is shifted strongly downfield. In contrast, from the

electronegativity difference between carbon and silicon, a shielding effect and therefore a high field shift are expected in alkynylsilane compounds. The opposite effect that is observed may be explained by interactions between the π -orbitals of the $C\equiv C$ bond and low-lying unoccupied orbitals on silicon. Indeed, this type of orbital overlapping has been previously demonstrated for $Si-C\equiv C$ compounds by IR spectroscopy [159] as well as electron transmission spectroscopy [160]. It results in a decrease of the electron density and a change of geometry of the π orbitals of the $C\equiv C$ bond. Consequently, the shielding of both C nuclei of the $C\equiv C$ bond, and particularly C_β , is decreased, resulting in the observed chemical shift to lower field.

Moreover, the presence of the ^{29}Si satellites for the signal at 81.2 ppm (C_α) provides evidence of the formation of a bond between the silicon atom and the sp hybridized carbon atom (Figure 24).

3.2.1.1 Kinetics

The kinetics of the coupling reaction were investigated with 1H NMR spectroscopy. The reaction was performed in the presence of a known amount of an internal standard (hexadecane) in order to make quantification of the product possible. Aliquots were taken from the reaction mixture at certain times up to 7 days and immediately quenched. The volatile components (educts and solvents) of the reaction mixture were evaporated under reduced pressure. The residual liquid (product, potential side-products and internal standard) was investigated with 1H NMR spectroscopy. The amount of product present in each aliquot was obtained from the integration of the 1H NMR resonances relative to the one of hexadecane.

Hexadecane was chosen as internal standard because of its high boiling point, preventing the loss of the standard during evaporation of the solvent. Moreover, aliphatic saturated alkanes were already present in the reaction mixture (heptane from the BuLi solution, which is evaporated after the reaction), therefore, hexadecane is not expected to interfere with the reaction. Finally, the strong CH_2 signal of hexadecane in the 1H NMR spectrum (at ~ 1.26 ppm) does not overlap with the signals of the product (Figure 25).

The signals observed in the 1H NMR spectra of the product mixture at different reaction times correspond to the expected product and to the internal standard (Figure 25). Although

distillation of the aliquots was not performed, significant signals for side products are not observed.

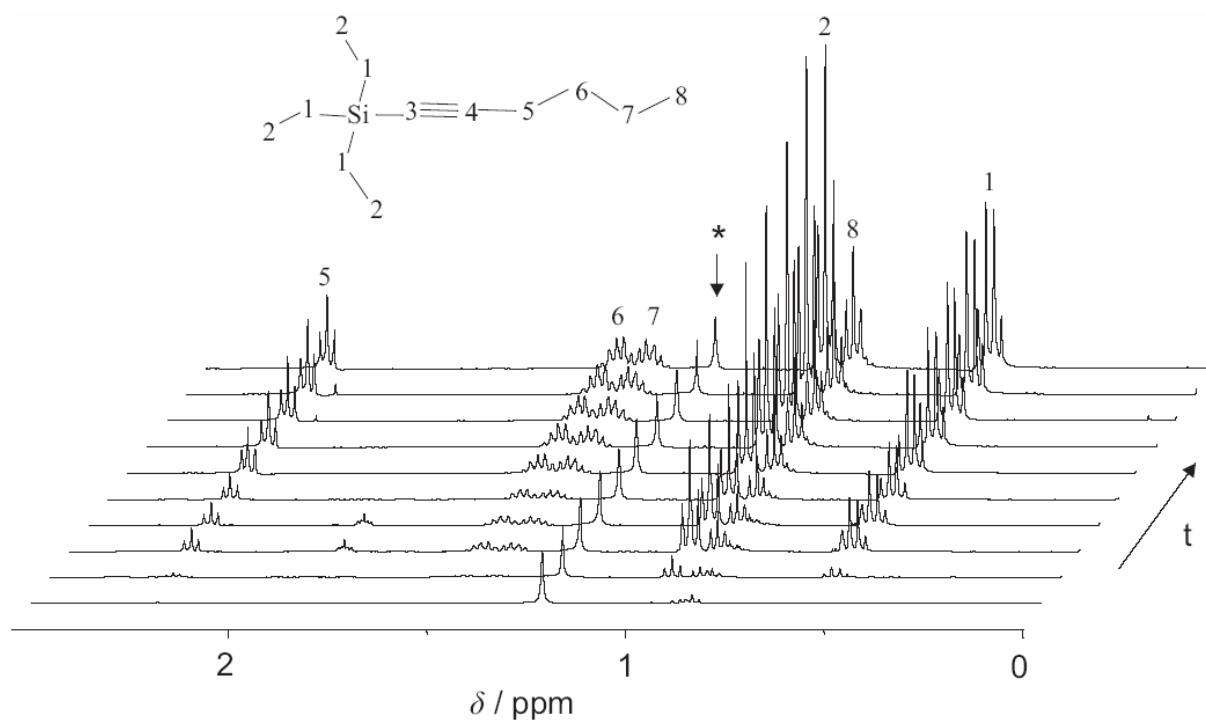


Figure 25: Time resolved ^1H NMR spectroscopic investigation of the production of **9** in THF; $[\ast]\text{CH}_2$ resonances of hexadecane (internal standard).

The determination of the amount of product in each aliquot from the NMR signal integration makes it possible to calculate the yields for the corresponding reaction times (Figure 26). Any signal of the product may be used for integration except the one due to the resonance of the methyl group 8. Indeed, it overlaps with the resonance of the methyl groups of hexadecane.

Since in ^1H NMR spectroscopy the integration of a signal is proportional to the amount of protons responsible for the resonance and since the amount of hexadecane initially present is known, the absolute yield of product **9** can be calculated. It is assumed that neither hexadecane, nor **9**, are lost by evaporation during the reaction. After 7 days, the reaction seems to come to completion and the yield is about 80 %.

Two additional experiments were also performed in order to determine the yield by isolating and weighing the product. After 1 and 6 days of reaction the yields were 21 and 69 % respectively. This is in good agreement with the yields obtained from the ^1H NMR investigations. The fact that a yield of 100 % is not achieved even after 7 days may be explained by the slow loss of the volatile 1-hexyne educt through the condensing system.

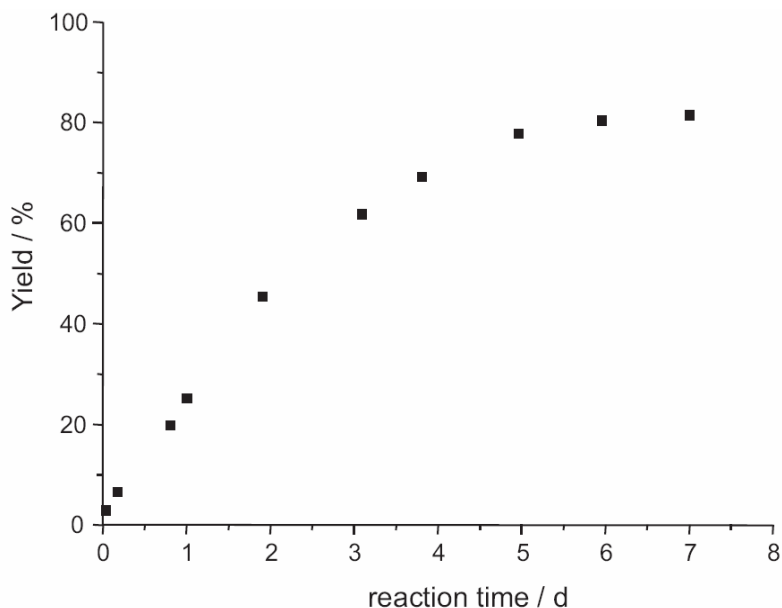
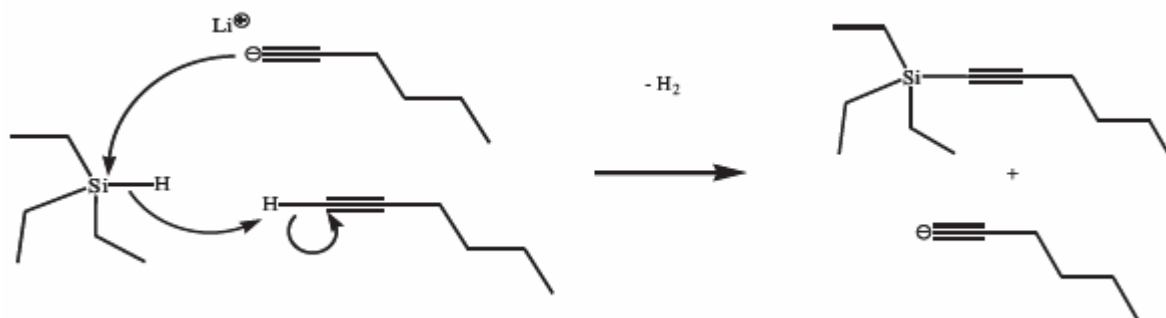


Figure 26: ^1H NMR spectroscopic investigation of the production of **9** in THF.

This experiment shows that long reaction times are required for the formation of a Si-C bond between triethylsilane and 1-hexyne. A more detailed determination of the reaction order and of the rate constant was not attempted.

3.2.1.2 Mechanism

We expect the reaction between triethylsilane and 1-hexyne in presence of a catalytic amount of lithium hexynide to occur via a dehydrogenative coupling pathway (Scheme 23). In order to verify this assumption, two additional experiments were performed, namely the detection of the evolved hydrogen gas and the reaction of hexynide with Et_3SiH in the absence of a proton source.



Scheme 23: Mechanism of the base catalyzed dehydrogenative coupling of triethylsilane with 1-hexyne.

3. Silicon-carbon bond formation

Because of the slow reaction kinetics, the expected hydrogen formation was not observed as a gas evolution from the reaction mixture. Therefore, to detect the produced hydrogen, the same reaction was performed in a sealed vessel and the gas present after the reaction was analyzed by gas chromatography with a thermal conductivity detector. Qualitatively, this analysis shows that H₂ is present in the closed vessel after reaction. It demonstrates that the leaving group of this reaction is H₂ and not LiH.

The quantification of the amount of evolved H₂ was attempted by using the same method. However, the H₂ leaks out of the sealed vessel at a significant rate after several hours. Owing to the long reaction time, this prevented a quantitative comparison between the amount of product and the amount of H₂ produced during the reaction.

The reaction of lithium hexynide with Et₃SiH in the absence of 1-hexyne was designed to demonstrate the importance of the proton source. In practice, 1-hexyne was first reacted with a 10 % excess of BuLi to ensure that lithium hexynide is exclusively present. The addition of the base to Et₃SiH results in the formation of triethylbutylsilane due to the excess of BuLi. However, triethylhex-1-ynylsilane **9** could not be detected. This demonstrates that only carbanions that are stronger nucleophiles than the hydride leaving group react with Si-H in the absence of a proton source. In this case the hydride from Si-H is expected to yield LiH instead of H₂. This confirms that the reaction occurring between Et₃SiH, hexyne and lithium hexynide is a dehydrogenative coupling reaction. In this case, the proton source acts as a Lewis acid to make the hydride a better leaving group in the form of H₂.

In summary, a Si-C link can be produced from a silane and a terminal C≡C bond in solution, and the experimental observations are consistent with the proposed mechanism (Scheme 23). The requirements for the base catalyzed dehydrogenative coupling reaction are the presence of a proton source and a nucleophile.

3.2.2 Dehydrogenative coupling on the Si-H modified silica surface

Since the dehydrogenative coupling of a terminal alkyne with a Si-H group is successful in solution, this reaction was also applied to a Si-H modified silica surface (**M4_{SiH}**). The product, **M4_{C≡C}**, was investigated with ²⁹Si CP/MAS NMR, in order to find a direct evidence for T³ groups resulting from the coupling of the surface Si-H groups with the terminal C≡C bond.

^{29}Si CP/MAS NMR spectra of the product resulting from the sol-gel process of $(\text{MeO})_3\text{Si-C}\equiv\text{C-R}$ display resonances at -79 (T^1), -87 (T^2) and -97 ppm (T^3) [161]. The same chemical shifts are expected for the T^3 group in $\text{M4}_{\text{C}\equiv\text{C}}$ since the Si nucleus of the Si-C bond is in a similar environment.

The ^{29}Si CP/MAS NMR spectrum of $\text{M4}_{\text{C}\equiv\text{C}}$ (Figure 27) shows a complex signal with overlapping peaks in the region where the T groups are expected. Therefore, Gaussian deconvolution was performed. The envelope of 4 individual peaks correlates with the measured spectrum for a deconvolution with resonances at -73.5 (T^2_{H}), -84 (T^3_{H}), -96 (T^3) and -109 ppm (Q^4). The signal at -96 ppm is too far downfield to be assigned to Q^3 groups and the assignment as T^3 is most likely, in accordance with ref. [161]. Despite the desired Si-C \equiv C unit formation, however, unreacted Si-H groups remain on the silica surface.

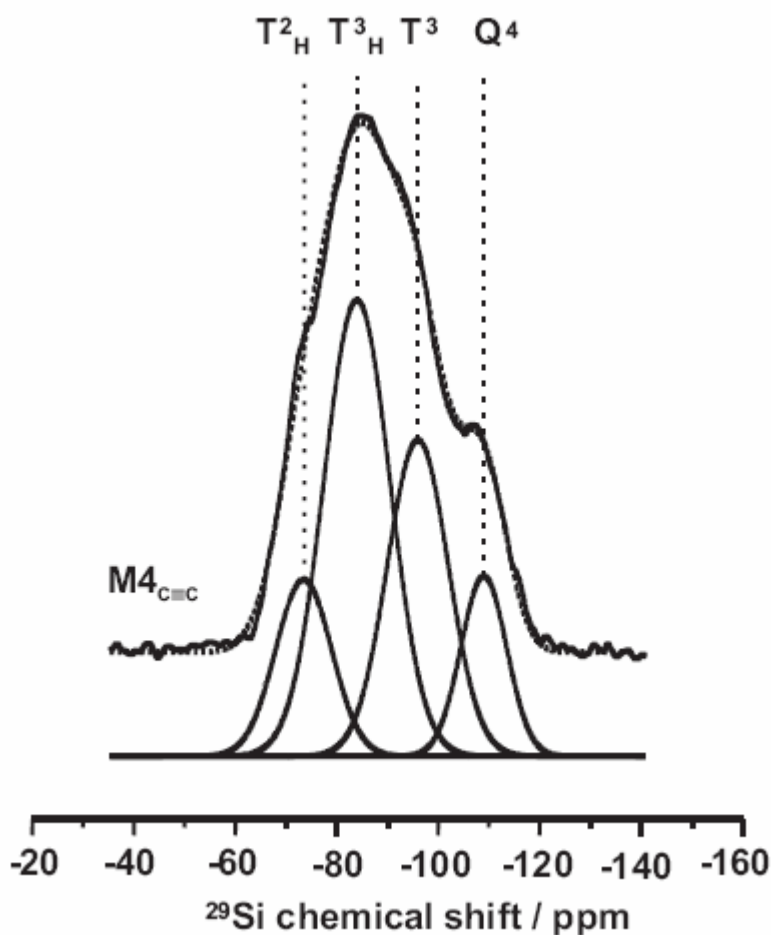


Figure 27: ^{29}Si CP/MAS NMR spectrum of $\text{M4}_{\text{C}\equiv\text{C}}$ (top) with Gaussian deconvolution results (bottom) and envelope of Gaussian components (top, broken line).

3. Silicon-carbon bond formation

An optimization of the reaction to obtain fewer remaining Si-H groups is desired to clearly characterize the Si-C bond and make the resulting silica the basis of modified materials.

In conclusion, 3 different methods were developed for Si-C bond formation from Si-H groups. The photochemically induced radical hydrosilylation reaction is adapted for the modification of non-porous particles. For amorphous porous silicas, the thermal variant is necessary to enable the reaction within the pores. Both methods make the functionalization of the silica possible. However, side reactions, especially radical induced surface telomerization, are suspected. The base catalyzed dehydrogenative coupling reaction of a terminal alkyne with the Si-H groups in solution is a promising alternative to the radical hydrosilylation methods. This reaction performed on soluble model compounds shows two valuable advantages: Side reactions are not detected, and direct evidence for the formation of the Si-C bond is obtained. Optimization of this reaction on the silica surface and the introduction of a second functional group are still required at this point.

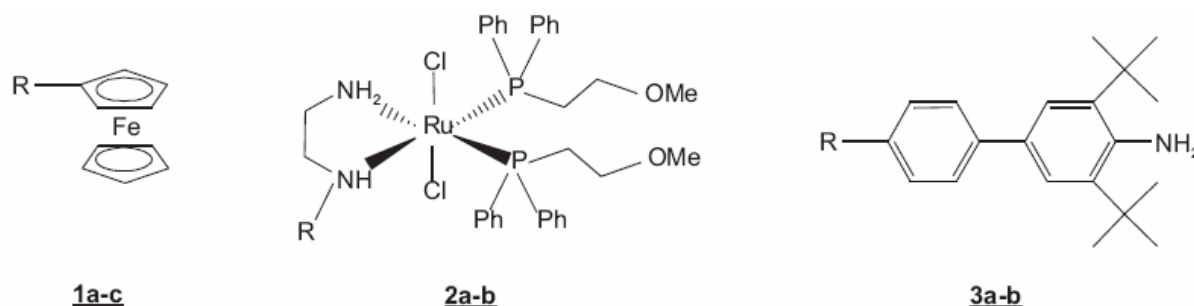
4 The redox-active molecules

4.1 Introduction

In the scope of interphase systems, the motivation to immobilize redox-active molecules on the Stöber particle surface is twofold :

The redox-active modification may enable the investigation of the redox-active molecules' interactions in interphases [103] as well as redox catalyses [9] in these systems by electrochemical means. In order to be suitable for both types of applications, the redox-active molecules must fulfill the following conditions: Both reduced and oxidized forms must be chemically stable, and electron exchange with the electrode must be fast and reversible [9].

Various derivatives of three different redox-active probes were chosen for the modification of the Stöber particles (the identity of R will be discussed later): Ferrocene derivatives (**1a-c**), diamine(ether-phosphine)dichlororuthenium (II) complexes (**2a-b**), and sterically hindered biphenyl amines (**3a-b**) were functionalized to enable their covalent attachment on the silica surface.



The discovery of ferrocene [162, 163], triggered intensive studies in the chemistry and electrochemistry [164] of organometallic compounds. The ferrocene/ferrocenium couple (Fc/Fc^+) has ever since been a widely used model and reference [12] in electrochemical studies. Moreover, the mostly reversible Fc/Fc^+ system was also used in electron transfer catalysis and redox catalysis [165]. Ferrocene is therefore the first choice for the redox-active modification of silica particles with a model compound [103] and will also be the main redox-active group applied in this thesis.

The diamine(ether-phosphine)dichlororuthenium(II) complexes **2** are similar to the Noyori type catalysts. The complexes developed by Noyori were successfully employed as precatalyst in the homogeneous hydrogenation of unsaturated ketones with high stereoselectivity and chemoselectivity [166, 167]. In an attempt to increase the stability of the catalytic intermediates of these complexes, an ether moiety was incorporated into the phosphine ligands. The hemilabile character of the ether-phosphines protects empty coordination sites at the metal center and the ether moieties act as intramolecular solvating ligands [168, 169]. These complexes display high activity, conversion and chemoselectivity as homogeneous catalysts for the hydrogenation of α,β -unsaturated ketones [168, 170]. Moreover, the complexes **2** were previously functionalized with trialkoxysilane groups and exhibited catalytic activity after incorporation into interphase systems [103, 171, 172].

The diamine(ether-phosphine)dichlororuthenium(II) complexes display reversible redox behavior and their redox potential can easily be influenced by variations in their ligands [13, 171]. Moreover, after chemical oxidation [169], the monocationic complexes are still catalytically active for the selective hydrogenation of conjugated ketones [173]. Due to these properties the complexes **2** are good candidates for the electrochemical monitoring and possibly control of catalysis in interphases.

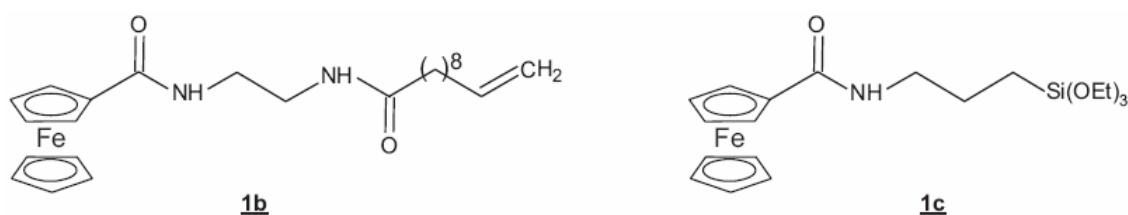
Organic redox-active mediators are less common than inorganic ones due to the often low stability of their radical ion form [9].

An example of organic electron transfer agents displaying stable radical cation states in the time frame of electroanalytical techniques are sterically hindered biphenyl amines **3** [174 - 176]. The stability of the radical cation state is attributed to the electron donating group in a position para to the amino group [174], the delocalization of charge and the odd electron in the aromatic ring as well as the steric effect of the *tert*-butyl groups. Because of this stability, the oxidation of **3** is electrochemically reversible, and this makes compounds of type **3** a suitable candidate for electron mediation in redox reactions.

In summary, molecules **1**, **2** and **3** are chosen as model compounds for this thesis because of their redox reversibility and their potential interphase applications. The redox-active molecules **1** and **2** were previously functionalized with alkoxy silane groups for the immobilization on a silica surface [83, 87]. For the purpose of the hydrosilylation alternative route to silylation, **1**, **2** and **3** will be derivatized with a terminal carbon-carbon double bond.

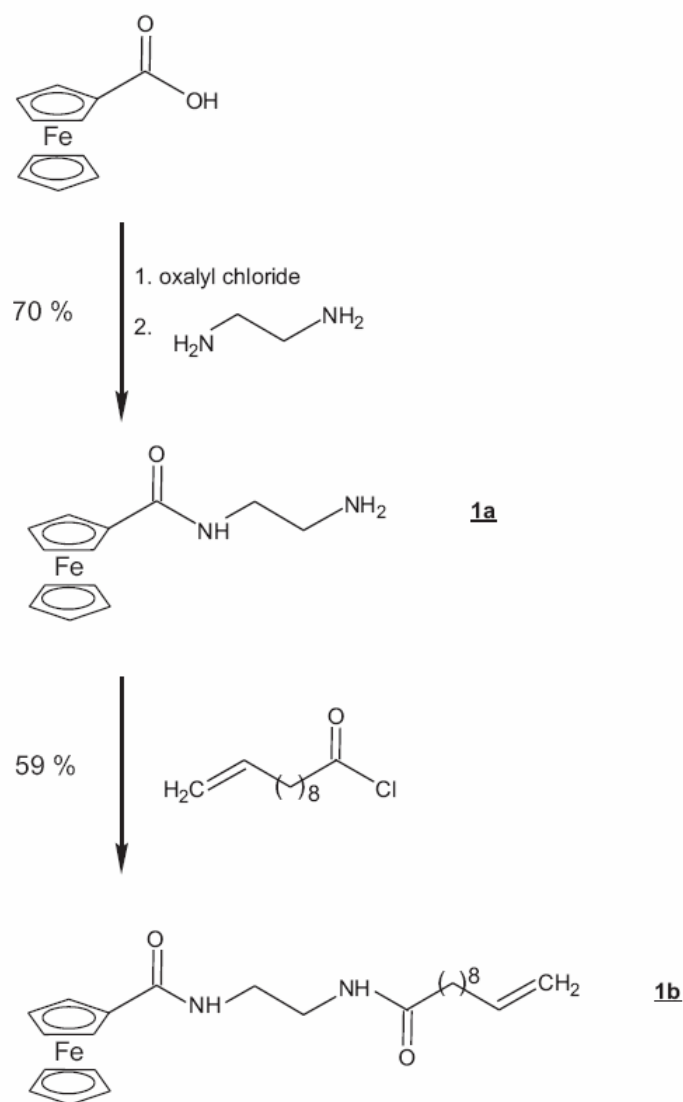
4.2 Synthesis of ferrocene derivatives

The formation of a ferrocene derivative with an alkoxy silane group bound via an amide bond (**1c**) was previously described [103]. A carbodiimide reagent was used for the coupling between ferrocenecarboxylic acid and the primary amine [177].



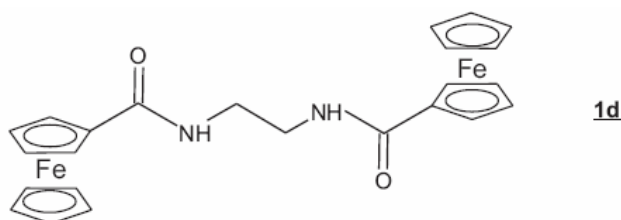
The straightforward amide formation strategy will also be used for the synthesis of the ferrocene moiety with a terminal C=C bond **1b**. However, due to the side-reactions associated with the use of carbodiimide, an acyl chloride intermediate [178] will be preferred for the synthesis of **1b**.

The reaction was performed in two steps, both involving amide bond formation from acyl chloride groups (Scheme 24). Oxalyl chloride was used for the activation of ferrocene-carboxylic acid.



Scheme 24: Synthetic route for the preparation of **1a** and **1b**.

The chlorination of ferrocenecarboxylic acid with oxalyl chloride yields red crystals of the known ferrocenylcarbonyl chloride [178]. The reaction of this intermediate, which was not isolated, with an excess of ethylene diamine favors the formation of [(2-aminoethyl)carbamoyl]ferrocene (**1a**). However, the disubstituted ethylene diamine side product (**1d**) was also obtained as a minor side-product. The derivative **1a** was separated from the mixture in high purity by taking advantage of its water solubility.



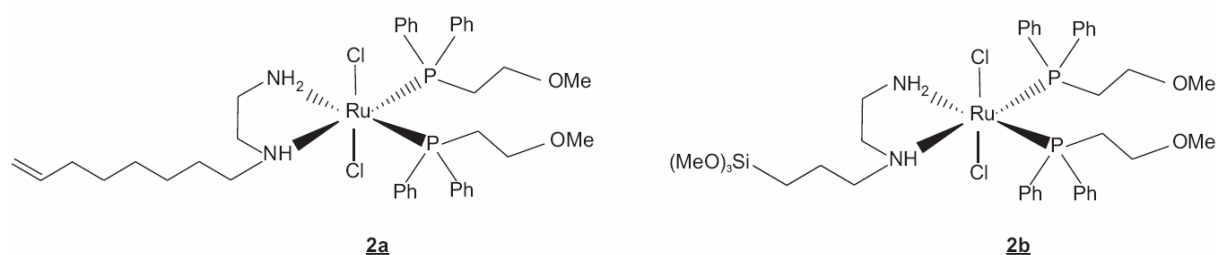
The subsequent reaction of **1a** with 10-undecenoyl chloride yields **1b** bearing the desired terminal C=C bond. Recrystallization from acetone yields the product in good purity in the form of yellow crystals.

The spectroscopic data, and in particular the signals at 171 and 175 ppm in the ^{13}C NMR spectra, demonstrate the formation of the amide bonds for both **1a** and **1b**. Other spectroscopic features (^1H and ^{13}C NMR, MS, IR) for **1a** and **1b** are in agreement with the expected structures and are detailed in the Experimental Part. The carbon content from elemental analysis for both **1a** and **1b** is lower than expected. In the case of **1a**, which was already described in the literature from a different synthetic route, the same observation was made and interpreted as the presence of water as an impurity [179].

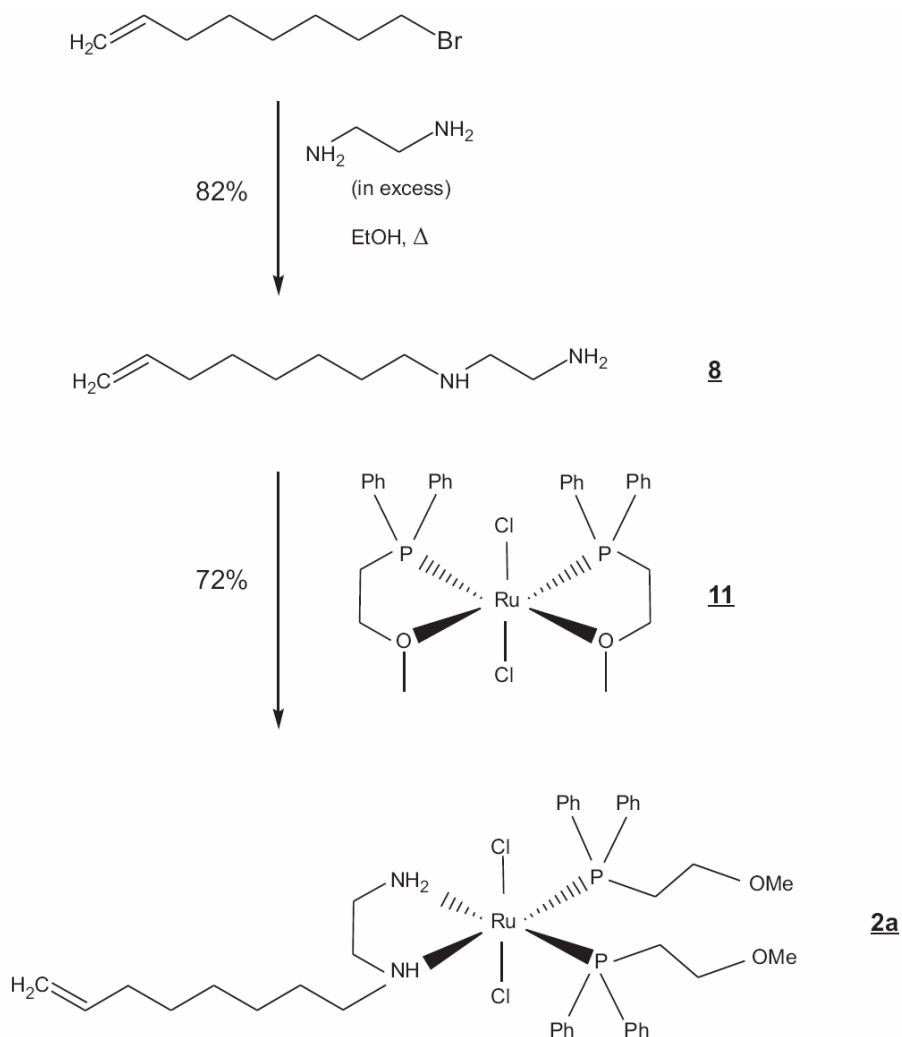
4.3 Synthesis of diamine(ether–phosphine)dichlororuthenium(II) complexes

The $\text{RuCl}_2(\eta^1\text{-Ph}_2\text{PCH}_2\text{CH}_2\text{OCH}_3)_2(\text{diamine})$ complexes **2a** and **2b** were prepared from the reaction of equimolar amounts of $\text{RuCl}_2(\eta^2\text{-Ph}_2\text{PCH}_2\text{CH}_2\text{OCH}_3)_2$ (**11**) with the diamine ligand to form five-membered chelates with ruthenium (see Scheme 25 for the preparation of **2a**) [169, 170]. The hemilabile character of the ether–phosphine ligand facilitates the formation of the diamine(ether–phosphine)ruthenium(II) complexes [169].

Complex **2b** was prepared according to previously described procedures [83, 172].



The diamine ligand for the ultimate formation of **2a**, N-oct-7-enylethylene-1,2-diamine (**8**), was prepared by monoalkylation of ethylenediamine with 8-bromo-1-octene (Scheme 25). The substitution may be effected by refluxing the mixture of both components in ethanol. A large excess of ethylenediamine was used in order to avoid the formation of other derivatives than the monoalkyl product and to bind the hydrobromic acid which is formed in the reaction.



Scheme 25: Synthetic route for the preparation of **2a**.

The spectroscopic data of the product from the reaction of ethylene diamine with 8-bromo-1-octene are consistent with those expected for **8** (see 7.4). Side-products with multiple alkylation of the nitrogen atom were not detected by NMR, nor by MS spectroscopy. The immiscibility of the product with ethylenediamine facilitates the work-up of this reaction. In comparison, when shorter alkenyl substituents are used, fractional distillation is needed for the separation of the product from the excess of ethylenediamine [180].

The reaction of **8** with **11** yields a yellow product. The octenyl ligand made the work-up of **2a** more difficult due to the good solubility of this ruthenium complex in hexane (similar complexes, e.g. **2b**, precipitate in this solvent and are separated based on this property [168, 169]). **2a** was obtained in good purity only after precipitation and washing with cold petroleum ether (40/60) instead of n-hexane.

The signals observed in the ^1H NMR spectrum of **2a** can be assigned to the phosphine as well as to the diamine ligand. The integration value of the signal of the aromatic resonances due to the phosphine ligands and those of the protons from the carbon-carbon double bond of the diamine ligand is in agreement with the expected diamine to phosphine ratio. In addition, the chemical shift of the methoxy groups indicates that the oxygen atom is not coordinated to the ruthenium atom. This is consistent with $\eta^1\text{-(P)}$ -coordinated ether-phosphine ligands.

The AB pattern observed for the ^{31}P resonances is consistent with the chemical non-equivalence of the two phosphine groups, resulting from the coordination of the non-symmetric diamine ligand to the metal center. The $^2J_{\text{PP}}$ value of about 36 Hz suggests that the phosphine ligands are coordinated cis to one another [181, 182]. This observation is in agreement with the characterization of related complexes of type **2** [168].

Table 13: ^{13}C NMR data^[a] of the resonances in the aromatic region of **2a** and **2b**.

| | ipso-C ₆ H ₅ | | o-C ₆ H ₅ | | m-C ₆ H ₅ | | p-C ₆ H ₅ |
|-----------|------------------------------------|------------------------|---------------------------------|------------------------|---------------------------------|------------------------|---------------------------------|
| | $\delta^{13}\text{C}$ / ppm | $^1J_{\text{PC}}$ / Hz | $\delta^{13}\text{C}$ / ppm | $^2J_{\text{PC}}$ / Hz | $\delta^{13}\text{C}$ / ppm | $^3J_{\text{PC}}$ / Hz | $\delta^{13}\text{C}$ / ppm |
| 2a | 136.57 (d) | 28.54 | 133.44 (d) | 8.05 | 128.41 (d) | 8.05 | 129.01 (s) |
| | 134.15 (d) | 32.93 | 133.26 (d) | 8.05 | 128.01 (d) | 8.05 | 128.76 (s) |
| | overlapping signals | | 132.03 (d) | 8.05 | 127.75 (d) | 8.05 | 128.66 (s) |
| | 132.07 (d) | 35.86 | 131.49 (d) | 8.05 | overlapping signals | | |
| 2b | 136.51 (d) | 28.97 | overlapping signals | | 128.31 (d) | 8.76 | 129.01 (s) |
| | 134.15 (d) | 32.34 | 133.31 (d) | 8.08 | 127.98 (d) | 8.76 | 128.99 (s) |
| | 133.36 (d) | 36.38 | 132.01 (d) | 8.08 | 127.72 (d) | 8.76 | 128.73 (s) |
| | 132.00 (d) | 36.38 | 131.51 (d) | 8.08 | 127.64 (d) | 8.76 | |

[a] The spectra were recorded in CDCl_3 , the coupling patterns are given in brackets.

The ^{13}C NMR spectrum of **2a** (recorded at 100.62 MHz) displays complicated signal patterns with signal overlap for the phosphine ligands in the aromatic region (Figure 28). The resolved signals may be assigned to the ipso, ortho, meta and para carbon nuclei according to their chemical shifts, coupling constants and coupling patterns (Table 13). In order to make the assignment of the overlapping signals possible, the spectrum of **2a** is compared to that of **2b**

which was recorded at a lower frequency. Since both spectra were recorded under different applied magnetic fields, the overlapping of the coupling pattern may not occur for the same signals in both spectra. Indeed, in the ^{13}C NMR spectrum of **2b** (measured at 62.90 MHz), two more doublets, at 133.36 and 127.64 ppm are identified (Table 13 and Figure 28).

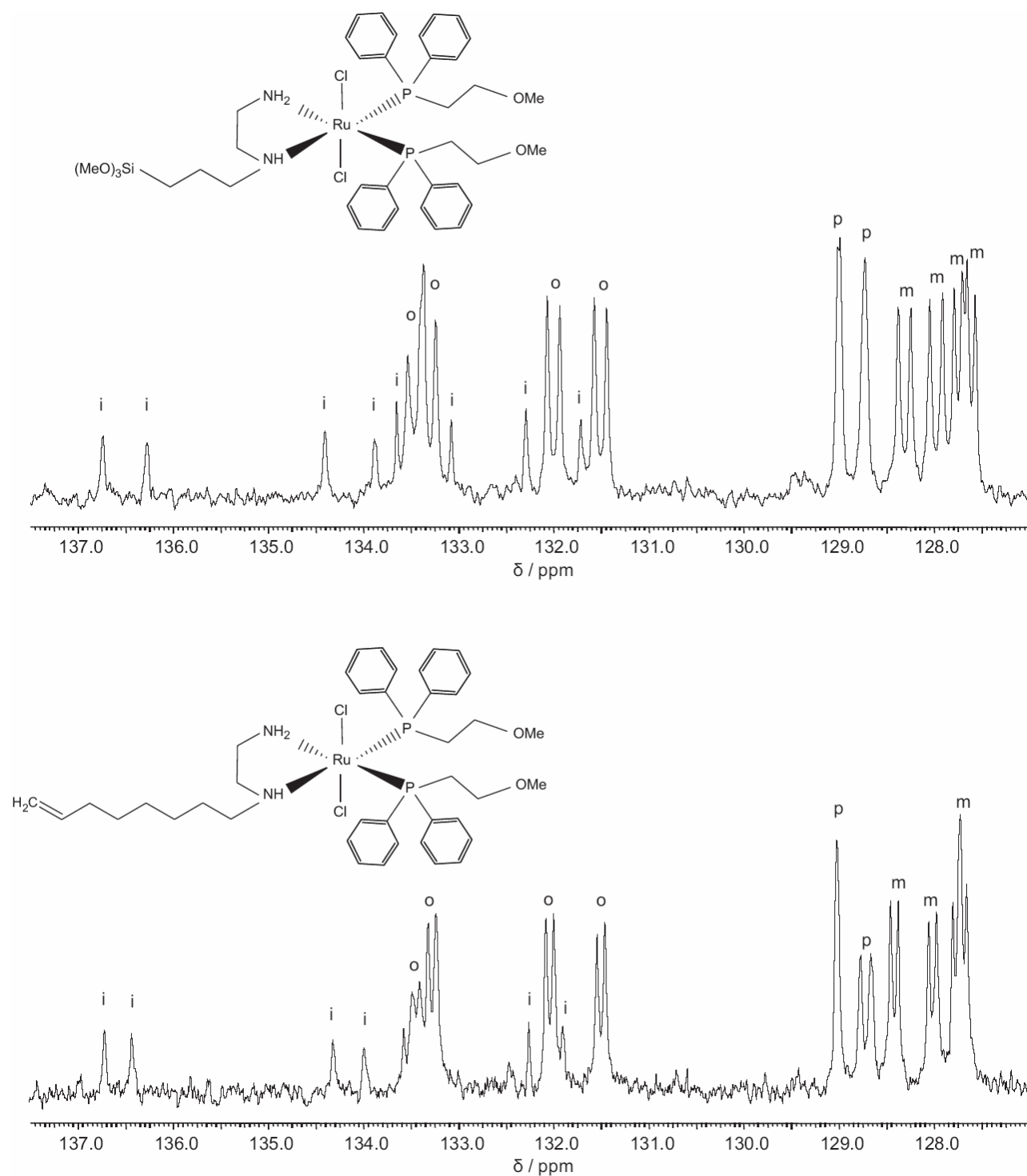
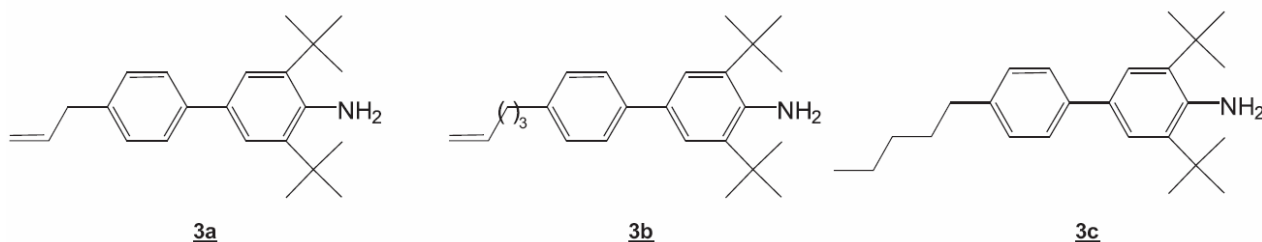


Figure 28: Aromatic regions of the ^{13}C NMR spectra of **2b** and **2a** measured at frequencies of 62.90 and 100.62 MHz, respectively.

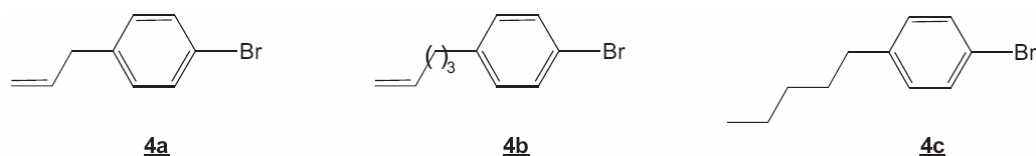
This makes it possible to assign 4 doublets to the ipso, ortho and meta C in each spectrum (Table 13). The para C displays overlapping signals that are identified as four singlets after processing of the spectra. This demonstrates that the 4 phenyl groups are chemically non-equivalent, which is consistent with the structure of the complexes **2a** and **2b**: Indeed, because of the non-symmetric diamine ligand, the two phosphine ligands are not equivalent. In addition, since the ruthenium atom is an asymmetric center, the two phenyl groups of each P ligand are not chemically equivalent either.

4.4 Synthesis of biphenylamine derivatives **3a-c**

The synthesis of three different derivatives of sterically hindered biphenyl amines (**3a-c**) was carried out (for **3b** see also ref. [183]). The biphenyl amine **3c** was synthesized in order to investigate the interaction of **3** with silica surfaces in the absence of a terminal C=C bond.



The two main steps in the preparation of **3a-c** both involve carbon-carbon σ -bond formation (Scheme 27). The first precursors are 1-bromo-4-(alkenyl)-benzene (**4a-b**), prepared from 1,4-dibromobenzene and an α,ω -bromoalkene. For the synthesis of **4c**, the corresponding 1-bromoalkane is used. The synthon with the shortest chain length, 4-allylbromobenzene (**4a**, $n = 1$), is obtained from the reaction between 1,4-dibromobenzene and allylmagnesiumbromide [184] (Scheme 27). For longer chain lengths ($n > 1$), the coupling of 1,4-dibromobenzene and the α,ω -bromoalkene requires a catalyst.



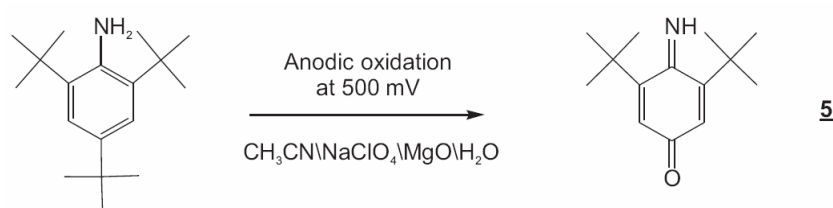
One possibility for the preparation of **4** with $n > 1$ is the Kumada cross-coupling reaction [185] between the corresponding α,ω -alkenyl Grignard reagent and 1,4-dibromo-benzene

(Scheme 27). The coupling reaction is catalyzed by Pd(dppf)Cl₂, where dppf stands for 1,1'-bis(diphenyl-phosphino)ferrocene [186, 187].

The second synthetic route to **4** involves a Cu(I)-mediated coupling [188, 189] of the α,ω -bromoalkene with the Grignard reagent obtained from 1,4-dibromobenzene (Scheme 27).

The Kumada cross-coupling reaction and the Cu(I)-mediated coupling reaction were tested during the synthesis of **4b** and **4c**, respectively. The advantages and disadvantages of both synthetic routes are discussed in 4.4.1.

The second precursor, the iminoquinone **5** is synthesized by the electrochemical oxidation of 2,4,6-tri-*tert*-butylanilin (Scheme 26), as described in the literature [190 - 192].

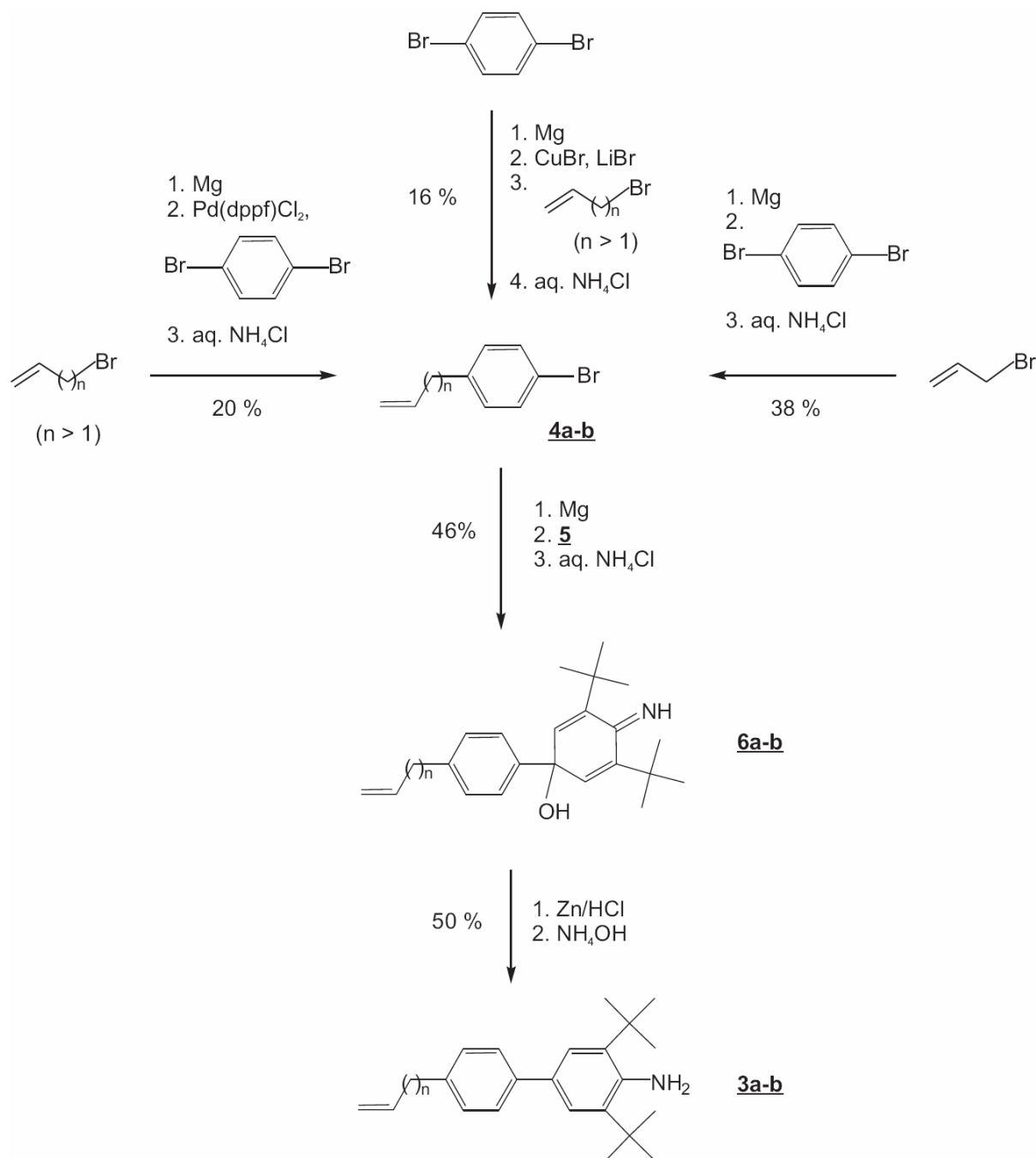


Scheme 26: Electrosynthesis of **5**.

The carbon-carbon σ -bond formation of the biphenyl backbone of **3a-c** results from the reaction between the Grignard reagent obtained from **4a-c** and the iminoquinone **5** (Scheme 27). The subsequent reduction of the iminoquinone **6a-c** induces the rearomatization of the aniline ring (Scheme 27). The product is obtained after deprotonation of the ammonium salt with aqueous ammonia.

4.4.1 1-bromo-4-(R)-benzenes (**4a-c**)

For the production of **4b** and **4c**, both the Kumada cross-coupling reaction and the Cu(I) catalyzed coupling reaction yield the desired product. Indeed, the signal at about 2.5 ppm in the ¹H NMR spectra of both **4b** and **4c** is characteristic of the benzylic CH₂ group resulting from the carbon-carbon σ -bond formation. Also, the coupling pattern of the aromatic protons (two doublets with equal coupling constants) is consistent with an 1,4-unsymmetrically disubstituted benzene ring. The other spectroscopic data (¹H and ¹³C NMR as well as MS) correspond to the values expected for **4b** and **4c** (see 7.4).



Scheme 27: General synthetic route for the preparation of **3a-b**.

Both synthetic routes give relatively low yields (~20%). The Cu(I) catalyzed reaction yields several side-products. In particular, the product from the reaction of both halogenated carbons of the educt is detected. Moreover, it was not possible to separate this particular side-product by column chromatography at this stage. On the other hand, the Kumada cross-coupling catalyzed by Pd(dppf)Cl₂, did not result in any detectable side-products. The only impurity present is the unreacted 1,4-dibromobenzene, which can be eliminated by crystallization followed by column chromatography.

The synthesis of **4a** also yields the expected product according to the spectroscopic data. It should be noted that 1,4-diallylbenzene is also obtained. However, in this case the product can be purified by distillation.

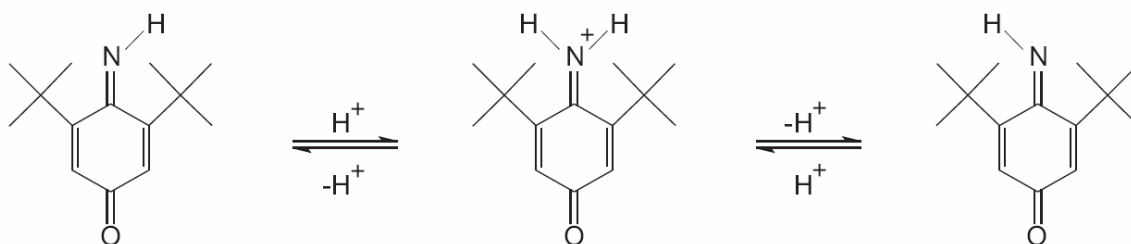
In summary, precursors **4a-c** were prepared in good purity. For $n = 1$, the reaction between allylbromide and bromophenylmagnesium bromide is used. For longer chain length ($n > 1$), the Kumada cross-coupling reaction is preferred over the Cu(I) catalyzed reaction.

The relatively low yield of **4a-c** is satisfactory because the yield limiting step of the synthetic route to **3a-c** is the production of **5**.

4.4.2 3,5-di-*tert*-butyl-4-iminocyclohexa-2,5-dien-1-one (**5**)

The absolute yield of the iminoquinon **5**, obtained from the electrooxidation of 2,4,6-tri-*tert*-butylanilin, is limited by the size of the electrochemical cell. Compared to the original references [190 - 192], a recrystallization step of the product from petroleum ether was introduced, yielding bright yellow crystals.

Due to the sp^2 hybridization of the N atom and the presence of the proton of the imine, the protons of the two *tert*-butyl groups as well as the two methine protons of the cyclohexadiene ring are not equivalent and should display separate signals in the 1H spectrum. However, this is not the case before recrystallization of the iminoquinon: The *tert*-butyl and the methine protons display one singlet, each. This may be explained by the presence of protic impurities, inducing a proton exchange at the imine group (Scheme 28).



Scheme 28: Proton exchange at the imine group catalyzed by protic impurities.

If this proton transfer is fast compared to the NMR timescale, the two *tert*-butyl groups as well as the two methine groups will be seen as equivalent [191].

4. The redox-active molecules

After recrystallization in petroleum ether, a singlet is observed in the ^1H NMR spectrum for the protons of each *tert*-butyl group and for each methine group. The splitting of the NMR signals, which is also observed in the ^{13}C NMR spectrum, demonstrates that the recrystallization step eliminates protic impurities from the product.

The absence of these impurities is important since **5** is reacted with a Grignard reagent in the next step.

4.4.3 3,5-di-*tert*-butyl-4-imino-1-(4-R-phenyl)cyclohexa-2,5-dien-1-ol (**6a-c**)

In order to facilitate the work-up of these products, **4a-c** are used in excess to ensure that a maximum amount of **5** reacts. Indeed, the unreacted iminochinon **5** is difficult to separate from the product, while **4a-c** are easily separated by filtering the product over silica and washing it with hexane. In this step, the excess of **4a-c** is recovered in good purity after evaporation of the solvent. The product is then eluted from the silica with ethyl acetate and further purified with column chromatography.

The main evidence for the production of **6a-c** is the signal at 71.8 ppm in the ^{13}C NMR spectrum corresponding to the carbon atom linked to the hydroxyl group resulting from the Grignard reaction. The other spectroscopic data correspond to those expected for the product.

4.4.4 3,5-di-*tert*-butyl-4'-R-1,1'-biphenyl-4-amine (**3a-c**)

The successful reduction with Zn and HCl is demonstrated by the disappearance of the C-OH signal in the ^{13}C NMR spectra. Moreover, the signal from the C-H groups of the cyclohexadiene ring is shifted from 6.23 to 7.34 in the ^1H spectrum. This shows that the reduction of the hydroxyl and imine groups also induces the rearomatization of the cyclohexadiene ring, yielding the biphenyl backbone of **3a-c**.

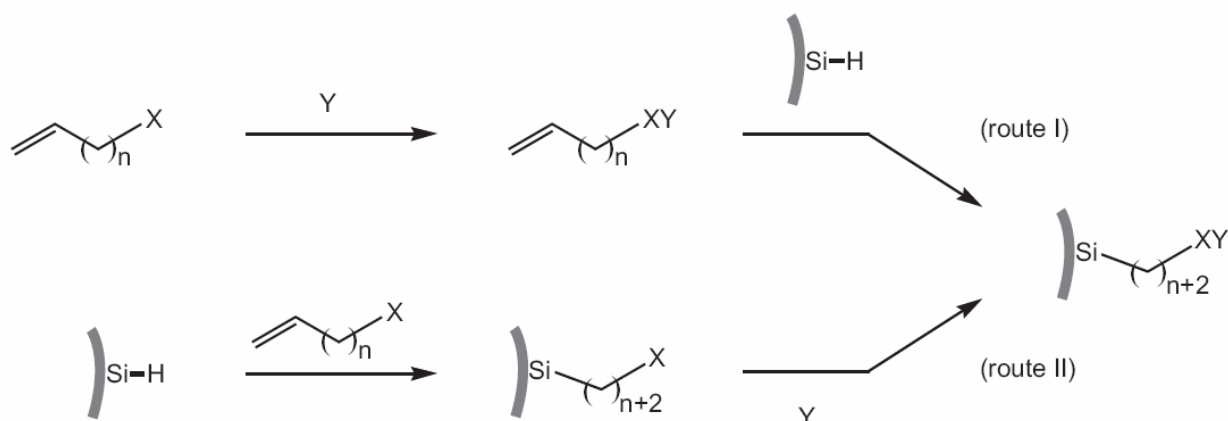
4.5 Conclusion

In summary, the redox-active molecules **1**, **2** and **3** were derivatized with a terminal C=C bond. This opens the possibility for their covalent attachment on Si-H modified surfaces via hydrosilylation reactions.

5 Covalent attachment of redox-active molecules on the silica surface via the radical addition of Si-H to C=C bonds.

In Chapter 3.1, the possibility to modify hydride terminated silica surfaces via free radical induced hydrosilylation reactions was demonstrated. The covalent attachment of a molecule (Y) by use of this reaction, can in general be achieved by two pathways (Scheme 29). In route I, Y is first coupled to an ω -substituted terminal olefin bearing a reactive group X. The covalent attachment of Y to the silica surface is then obtained from the hydrosilylation reaction between the surface Si-H and the terminal C=C bond. Therefore the silica material is only involved in the second step of the reaction.

On the other hand, in route II, all reactions are performed on the surface of the solid phase: The hydride modified silica surface is first reacted with the ω -substituted terminal olefin. In a second step, immobilized X reacts with Y, which results in the immobilization of the active center (Scheme 29).



Scheme 29: Modification pathway of hydride modified silica surface via hydrosilylation.

Route II has the potential disadvantage of leaving unreacted linkers after the attachment of Y. Therefore, we will first focus on route I.

5.1 Covalent attachment of active molecules on the silica surface via route I

Radical hydrosilylation reactions are applied to the covalent attachment of the previously synthesized redox-active molecules functionalized with a terminal alkene (Chapter 4).

As shown before (see 3.1.1.1), the photochemical hydrosilylation reaction only occurs if saturated hydrocarbons are used as solvent. This is not a drawback for the attachment of the

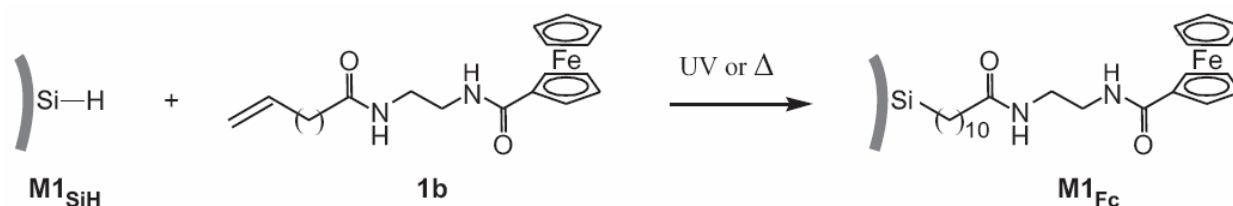
5. Covalent attachment of active molecules on the silica surface

redox-active molecules used here, since all of them are soluble in hexane. A possible problem arises from the need for a relatively high amount of olefin in order to achieve a high surface coverage with the modifiers: For the model reaction, the concentration of 10-undecylenic acid was 0.1 M. However, for the modification with **1b**, **2a** and **3b**, a lower concentration must be used due to the availability of these molecules.

The thermal hydrosilylation model reaction was performed in the neat olefin (see 3.1.2.1). However, the redox-active molecules **1b**, **2a** and **3b** need to be dissolved in a solvent due to their high melting points and their restricted availability. Mesitylene or hexadecane are used as high boiling point solvents for these reactions.

5.1.1 Ferrocene attachment

The *photochemical* hydrosilylation reaction of **1b** with M1_{SiH} (Scheme 30) was performed in hexane at a concentration of about 5 mM. In contrast to the photochemical hydrosilylation of 10-undecylenic acid, the concentration of modifying molecules is about 20 times lower. Material M1_{SiH} was used as the silica matrix.



*Scheme 30: Thermal or photochemical induction of hydrosilylation reactions between M1_{SiH} and **1b**.*

The resulting material displays only very weak C-H stretching vibrations in the DRIFT spectrum. Therefore, the reaction occurs only in low yields under these conditions. The ferrocene derivative **1b** was also exposed to the photochemical conditions in absence of silica. The characterization of the product after irradiation corresponds to **1b**. Therefore, no side-reaction occurs under UV irradiation.

The reaction was also performed with **1b** at the same concentration and M2_{SiH} as a Si-H modified silica matrix in mesitylene under the *thermal* conditions. Unfortunately, after 1 h of reaction, the reaction mixture turned black. ^1H and ^{13}C NMR investigations of the reaction solution indicated that thermal decomposition of the ferrocene moiety had occurred.

5. Covalent attachment of active molecules on the silica surface

5.1.2 Ruthenium complex attachment

The stability of the complex **2a** was tested under the radical hydrosilylation conditions, but in the absence of Si-H modified silica. A solution of **2a** in hexane was irradiated by UV light for several days and another solution of **2a** in hexadecane was heated to 160 °C for several hours. Under photochemical conditions, a light brown insoluble solid is obtained and under thermal conditions a dark brown precipitate is produced. This demonstrates the poor stability of **2a** under both types of conditions. Therefore, the attachment of **2a** to the silica surface was not attempted neither by thermal, nor by photochemical hydrosilylation reactions.

5.1.3 Biphenylamine attachment

The organic redox-active molecule **3b** was first exposed to the photochemical conditions in absence of silica. After irradiation, the spectroscopic data of the solid recovered from the solution correspond to the one expected for **3b**. This demonstrates the stability of **3b** under photochemical conditions.

Similarly to the reaction with **1b**, the photochemical hydrosilylation reaction of **3b** was performed in hexane at a concentration of about 5 mM in presence of **M1f_{SiH}**. The slightly yellow material resulting from the photochemical hydrosilylation of **M1f_{SiH}** and **3b**, displays a very weak C-H stretching vibration in the DRIFT spectrum. This confirms the results obtained for the experiment with the ferrocene derivative **1b**: the use of the redox-active molecules at this lower concentration does not yield a satisfactory surface concentration of modifiers.

The photochemical hydrosilylation of **3c** was performed under the same conditions as for **3b** in order to demonstrate that no attachment at all occurs in the absence of the C=C bond. As expected, no C-H signals are observed in the DRIFT spectrum. However, since **3b** itself displays only low yields, a clear conclusion can not be drawn from this result.

Due to the small amount of **3b** that was available, thermal hydrosilylation was not attempted.

In summary, two main factors prevent the application of route I for the immobilization of the redox-active molecules **1b**, **2a** and **3b**. First, the concentrations required for the photochemical hydrosilylation reaction are not compatible with the amount of redox-active molecules available. In order to improve the surface coverage in redox-active modifiers, longer reaction times may be applied. However this is difficult in practice, since 4-5 days are already necessary when the optimal olefin concentration is used (see 3.1.1.1). Secondly, in

5. Covalent attachment of active molecules on the silica surface

some cases, the stability of the redox-active molecules under thermal or photochemical conditions prevents the use of route I as a general synthetic pathway for the silica surface modification.

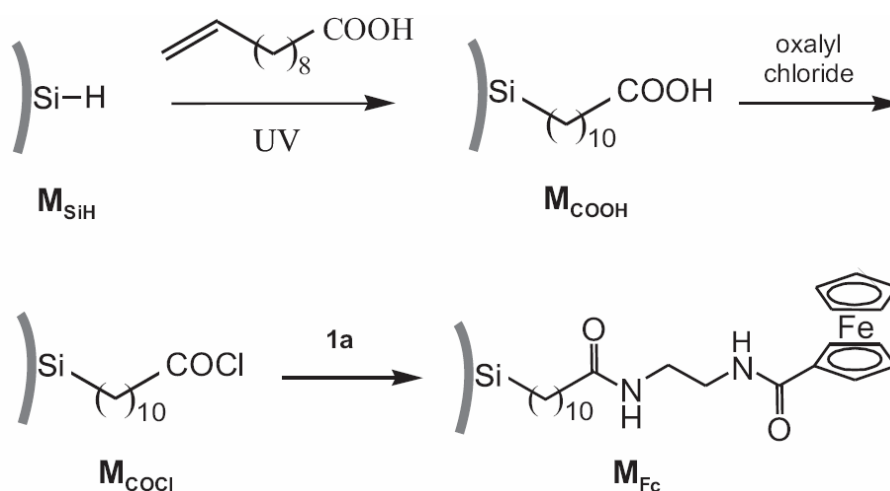
5.2 Covalent attachment of active molecules on the silica surface via route II

In contrast to route I, the alternative pathway of route II makes it possible to modify the Si-H surface with a reactive functional groups X that may be used in turn for the immobilization of the redox-active molecules. The group X may be chosen so that milder reaction conditions and lower concentrations of redox-active molecules can be applied.

Two starting materials for the immobilization of the redox-active molecules via route II have already been described in the previous chapter with the preparation of -COOH (M_{COOH}) and -C=C ($M_{\text{C=C}}$) terminated silica surfaces.

5.2.1 Immobilization of ferrocene by means of an activated carboxylic acid modified silica surface

A straightforward activation of the carboxylic acid modified surface is performed by chlorination with oxalyl chloride. The resulting acyl chloride is then reacted with the amine functionalized ferrocene derivative **1a** for the covalent attachment on the silica surface via an amide bond (Scheme 31). The reaction occurs at RT in short times and at low redox-active molecule concentration (~ 5 mM). The procedure was applied to materials M_{fSiH} , M_{gTES} , M_{4SiH} and yields the corresponding M_{Fc} materials.



Scheme 31: Synthesis of ferrocene-modified silica particles via route II based on photochemical hydrosilylation.

5. Covalent attachment of active molecules on the silica surface

The DRIFT spectra of the intermediates of the synthetic route to \mathbf{M}_{Fc} involving $\mathbf{M1g}_{TES}$, $\mathbf{M1f}_{SiH}$ and $\mathbf{M4}_{SiH}$, are represented in Figures 29, 30 and 31 respectively. The preparation and characterization of the materials \mathbf{M}_{COOH} were discussed previously (see 3.1.1.1). The DRIFT spectra of \mathbf{M}_{COOH} display the $\nu_{C=O}$ band of the carboxylic group at $\sim 1710\text{ cm}^{-1}$, the ν_{Si-H} band of the unreacted Si-H groups at $\sim 2280\text{ cm}^{-1}$ as well as the ν_{C-H} band expected for the CH_2 groups of the alkyl spacer (Figures 29, 30 and 31). A higher band intensity is observed for the $\mathbf{M4}$ materials compared to the $\mathbf{M1}$ materials. This is due to the higher specific surface area, and therefore the higher specific modifiers amount of the $\mathbf{M4}$ materials.

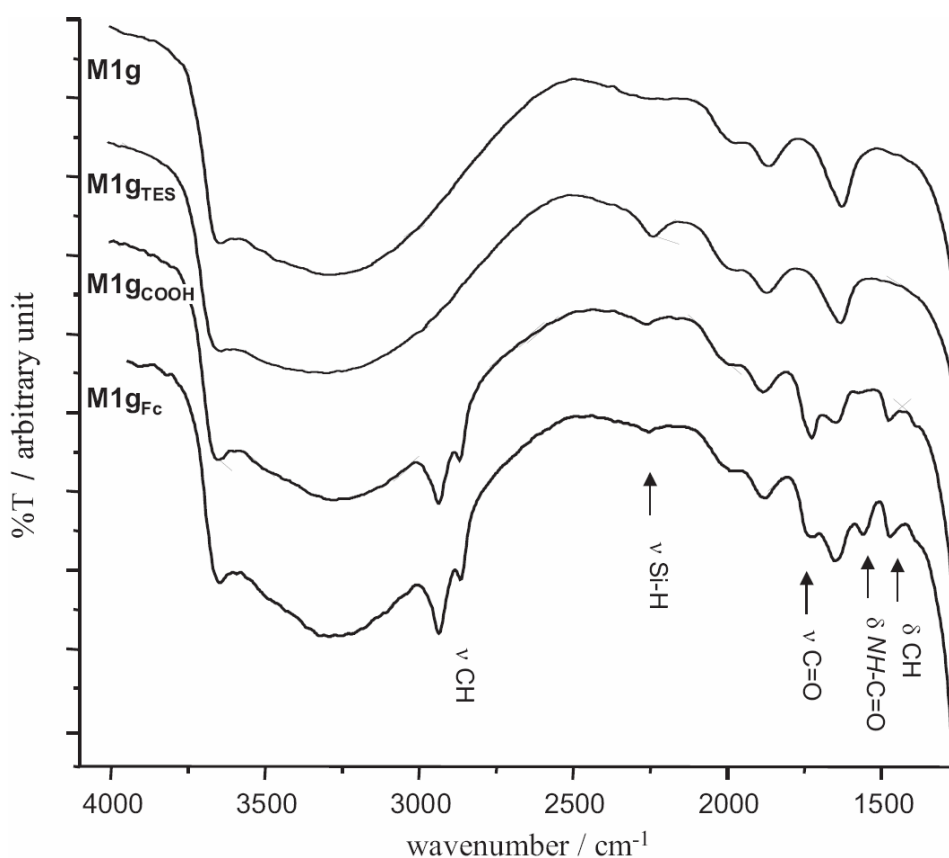


Figure 29: DRIFT spectra of bare silica $\mathbf{M1g}$, hydride modified silica $\mathbf{M1g}_{TES}$, 10-undecylenic acid modified silica $\mathbf{M1g}_{COOH}$ and Fc modified silica $\mathbf{M1g}_{Fc}$.

In the DRIFT spectra of $\mathbf{M4}_{Fc}$, and $\mathbf{M1f}_{Fc}$ an additional band at 3095 cm^{-1} corresponding to the ν_{C-H} of the C-H groups of ferrocene is detected. In the case of $\mathbf{M1g}_{Fc}$, the detection of this band is less obvious due to the overlapping of the Si-OH stretching vibrations. The signal at 1542 cm^{-1} due to δ_{NH} in the DRIFT spectra of the \mathbf{M}_{Fc} materials (Figures 29, 30 and 31), indicates the presence of amide groups. Moreover, the decrease of the intensity of the $\nu_{C=O}$ signal at 1708 cm^{-1} in the spectra of the \mathbf{M}_{Fc} materials compared to the corresponding band in

5. Covalent attachment of active molecules on the silica surface

the spectra of \mathbf{M}_{COOH} shows that the amide has been produced by reaction with the carboxylic acid group linked to the silica surface. This indicates that the ferrocene unit is covalently bound to the silica surface via the alkyl spacer.

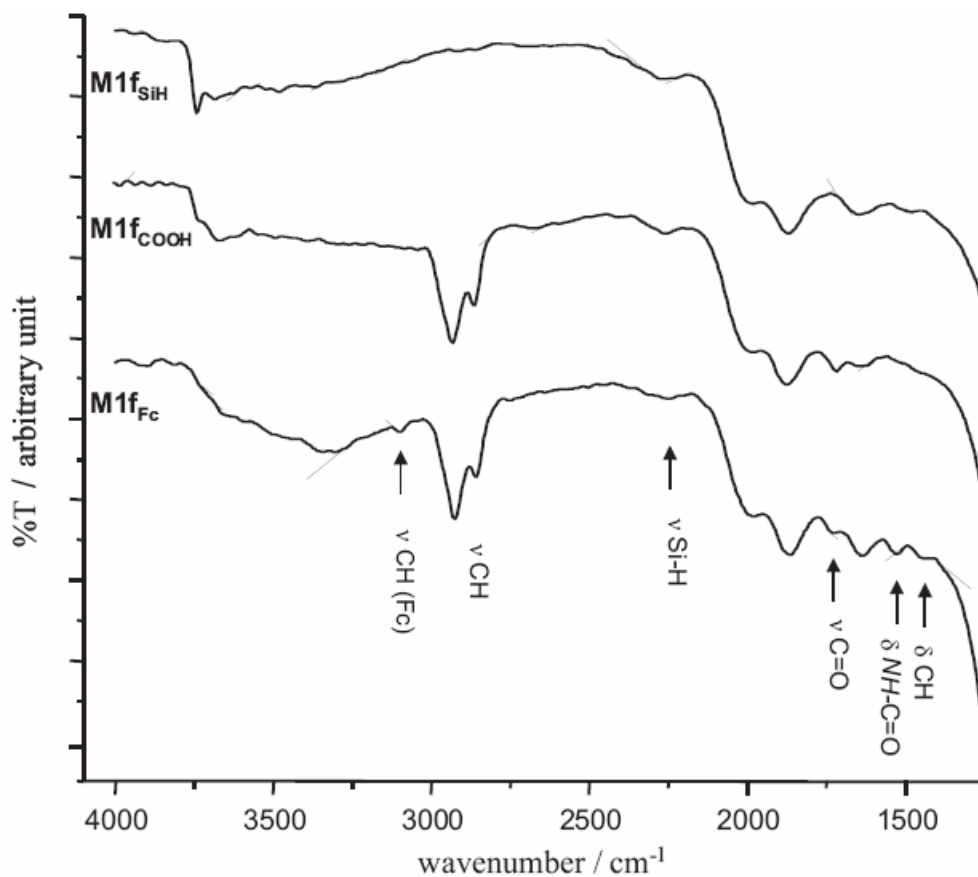


Figure 30: DRIFT spectra of modified Stöber particles: hydride modified silica $\mathbf{M1f}_{\text{SiH}}$, 10-undecylenic acid modified silica $\mathbf{M1f}_{\text{COOH}}$ and Fc modified silica $\mathbf{M1f}_{\text{Fc}}$.

The decrease of the $\nu_{\text{Si-H}}$ in the DRIFT spectrum of \mathbf{M}_{Fc} compared to the one of \mathbf{M}_{COOH} (Figures 29, 30 and 31) might be due to the chlorination of the remaining hydride during the activation of the carboxylic acid with oxalyl chloride. A similar decrease has been observed for the signal of the Si-H vibration in the IR spectrum of $\mathbf{M1g}_{\text{TES}}$ after treatment with oxalyl chloride as a blank test.

The same procedure for the immobilization of ferrocene was performed with $\mathbf{M1f}_{\text{SiH}}$ instead of $\mathbf{M1f}_{\text{COOH}}$. The absence of ν_{CH} , $\nu_{\text{C=O}}$ and δ_{NH} in the DRIFT spectrum of the resulting material indicates that **1a** does not directly react with the Si-H modified silica surface under these conditions.

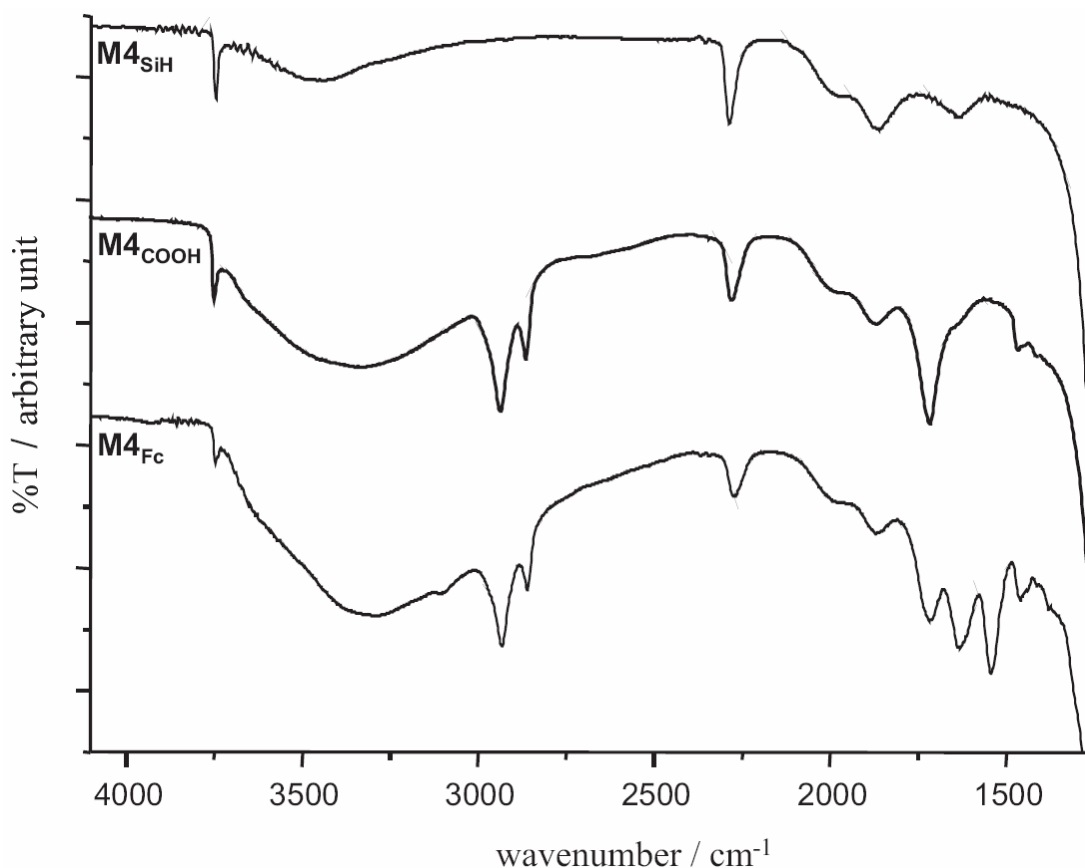


Figure 31: DRIFT spectra of hydride modified silica $M4_{SiH}$, 10-undecylenic acid modified silica $M4_{COOH}$ and ferrocene modified silica $M4_{Fc}$.

The ferrocene surface concentration on the silica was determined using atomic absorption spectroscopy (AAS) and UV-vis spectroscopy. For AAS, the particles are directly injected in to an acetylene-air flame, while for the UV-vis measurements the particles are first hydrolyzed with a strong base before analysis [94].

The quantitative determination of the ferrocene contents by AAS yields surface concentrations (Γ_{AAS}) of $1.26 \times 10^{-6} \text{ mol m}^{-2}$ for the materials prepared from $M1f_{SiH}$, and $1.96 \times 10^{-6} \text{ mol m}^{-2}$ for the materials prepared from $M1g_{TES}$. This corresponds respectively to 16 % and 25 % of the theoretical initial surface concentration of silanol groups [88] on $M1$ materials, and is comparable to the surface concentration of a monolayer of ferrocene prepared on other non-porous surfaces as for example platinum electrodes covalently modified with ferrocene [193].

UV-vis spectroscopy yields a surface concentration of $\Gamma_{UV} = 6.97 \times 10^{-7} \text{ mol m}^{-2}$, which is only 35% of Γ_{AAS} . The determination of Γ_{UV} , however, relies on the hydrolysis of the amide bond between the alkyl spacer and the ferrocene unit as well as a total destruction of the silica

5. Covalent attachment of active molecules on the silica surface

matrix. Indeed, centrifugation of the suspension of **M1g_{Fc}** in aqueous KOH (1M) before the UV measurements yields a yellow solution absorbing light at 405 nm, indicating that ferrocenecarboxylate ions are present. However, an orange sediment is also obtained, showing that the silica particles are not fully hydrolyzed in the basic solution. In comparison, materials obtained from a silylation route are fully dissolved when treated under these conditions [94]. Thus, in the case of **M1g_{Fc}** ferrocene units may remain either adsorbed or covalently attached to the silica sediment. This explains why Γ_{UV} is lower than Γ_{AAS} , and is not a reliable measure of the ferrocene surface concentration. Consequently, UV-vis spectroscopy can not be used for the quantitative determination of the ferrocene units in **M1g_{Fc}**. However, on the other hand, this experiment shows that the organic modification via a silicon-carbon link prevents the full hydrolysis of the silica particles under basic conditions in this material. This is desirable with regard to its stability.

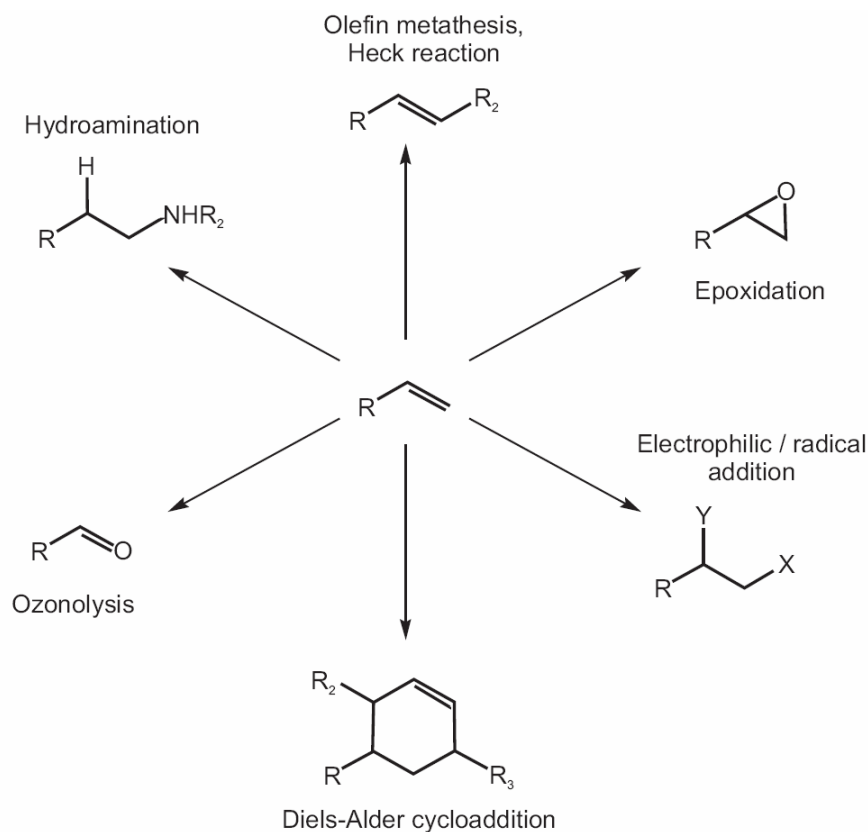
In summary, the carboxylic acid modified surface prepared by the free radical induced hydrosilylation can be converted easily into the corresponding acyl chloride, and then be used in a subsequent reaction to immobilize active centers bearing an amine functional group (here a modified ferrocene).

5.2.2 Free radical induced hydrobromination of a carbon-carbon double bond modified silica surface.

The terminal C=C bond of the **M2_{C=C}** material may also be employed for the attachment of redox-active molecules. C=C bonds can be modified by many reactions including electrophilic and radical additions, ozonolysis, metal catalyzed hydroamination [194], cross-coupling [195] or metathesis [196] reactions, as well as Diels-Alder cycloadditions (Scheme 32).

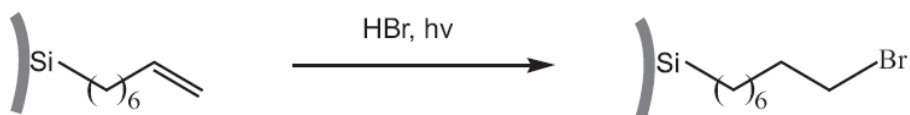
In order to limit the contamination of the silica surface as well as side reactions during subsequent modification steps, methods that involve gaseous reactants and reagents and that do not require metal catalysts, radical initiator or strong bases are preferred here. Thus, ozonolysis, epoxidation, cycloaddition and (initiator-less) radical addition reactions may be appropriate.

5. Covalent attachment of active molecules on the silica surface



Scheme 32: Possible reactions of terminal C=C bonds.

The conditions of the photochemically induced hydrobromination [197] (dry and acidic conditions, absence of catalysts, gaseous reactant) may be particularly compatible with the requirements for silica surface modification. Moreover, the homolytic cleavage of HBr by UV light should result in a selective anti-Markovnikov addition to the C=C bond. The resulting product with the bromo substituent in the 1-position would be useful for the further functionalization of the silica surface.



Scheme 33: Photochemically induced hydrobromination of a C=C terminated surface.

The hydrobromination was performed with material **M2_{C=C}** in dry hexane under UV irradiation according to Scheme 33.

The absence of carbon-carbon double bond signals in the NMR and DRIFT spectra of the hydrobrominated product (**M2_{Br}**) demonstrates that the functional group had reacted (Figure 32).

5. Covalent attachment of active molecules on the silica surface

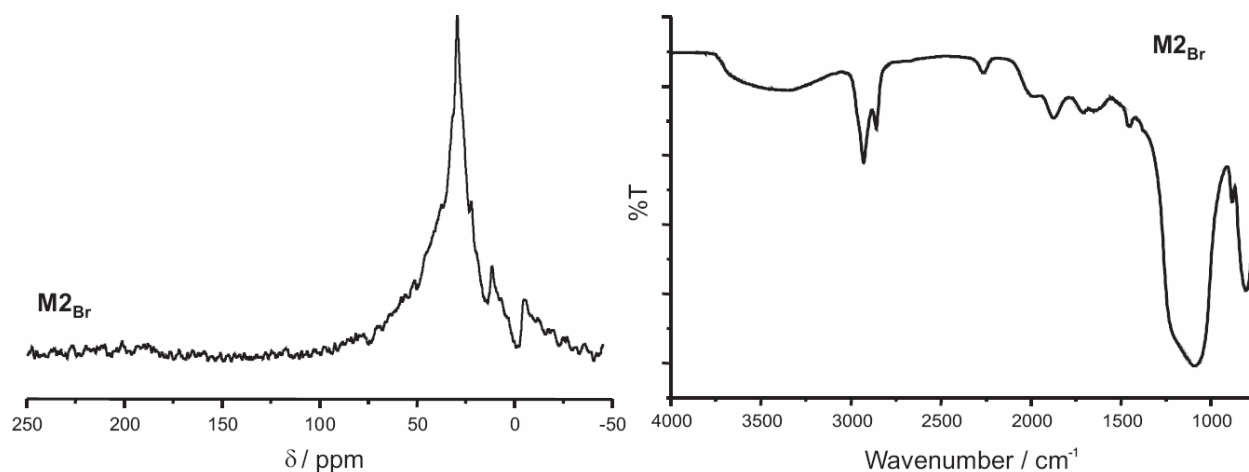


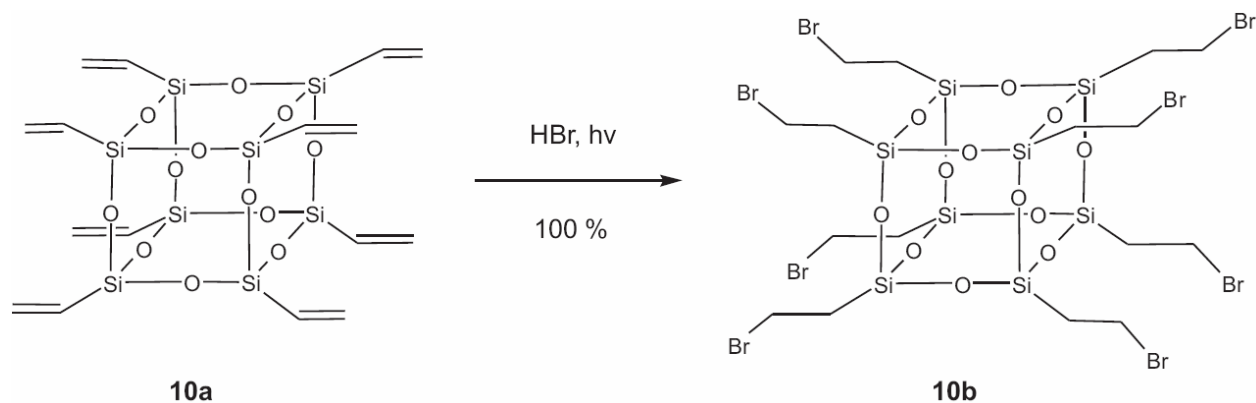
Figure 32: ^{13}C -CP/MAS-NMR (left) and DRIFT (right) spectra of M2_{Br} after radical hydrobromination reaction.

However, direct evidence for the presence of a bromo substituent in position 1 can not be obtained from these spectra: The C-Br vibrations are not detected in the IR spectrum due to their low absorptivities and the NMR spectrum displays only a broad signal at 60 ppm, where the signal for the C nucleus of $-\text{CH}_2\text{Br}$ is expected.

To obtain more information on the outcome of the radical hydrobromination reaction, 1-octene was added to the reaction mixture for the hydrobromination of the alkene modified silica in a competitive experiment. After reaction and sedimentation of the silica, the products present in the solution were analyzed with NMR spectroscopy. Resonances for ^{13}C or ^1H nuclei of C=C bonds are not detected in the corresponding NMR spectra, confirming that the hydrobromination reaction is quantitative. Moreover, according to the NMR spectra, the main product is 1-bromooctane. This is the expected product of an anti-Markovnikov addition of HBr to the carbon-carbon double bond of 1-octene. From the integration of the ^1H NMR signals, the ratio of anti-Markovnikov to Markovnikov products is about 9 : 1.

The reaction was also performed on octavinylsilsesquioxane **10a** that may be considered as the soluble low molecular weight equivalent of a C=C bond modified silica surface (Scheme 34). The expected product from this model reaction is 1,3,5,7,9,11,13,15-oktakis-(2-bromoethyl)octasilsesquioxane (**10b**).

5. Covalent attachment of active molecules on the silica surface



Scheme 34: Photochemically induced hydrobromination of 10a.

In the high-resolution ESI mass spectrum of **10b**, the most intense signals are obtained for $[M+K^+]$ and $[M+Na^+]$. The splitting pattern, owing to the presence of 8 bromine atoms, is expected to display 9 signals. Furthermore, owing to the isotopic composition of carbon and silicon, each signal is expected to split in two, at least. However not all signals are seen because of their low intensity. In the case of $[M+K^+]$, 8 signals are clearly detected when only the most abundant isotopes of carbon and silicon are present in **10b** and only 5 when one ^{13}C or one ^{29}Si nucleus is present (Figure 33).

The signal pattern owing to the isotopic composition of bromine, carbon and silicon as well as the corresponding molecular weights are in agreement with those obtained by simulation.

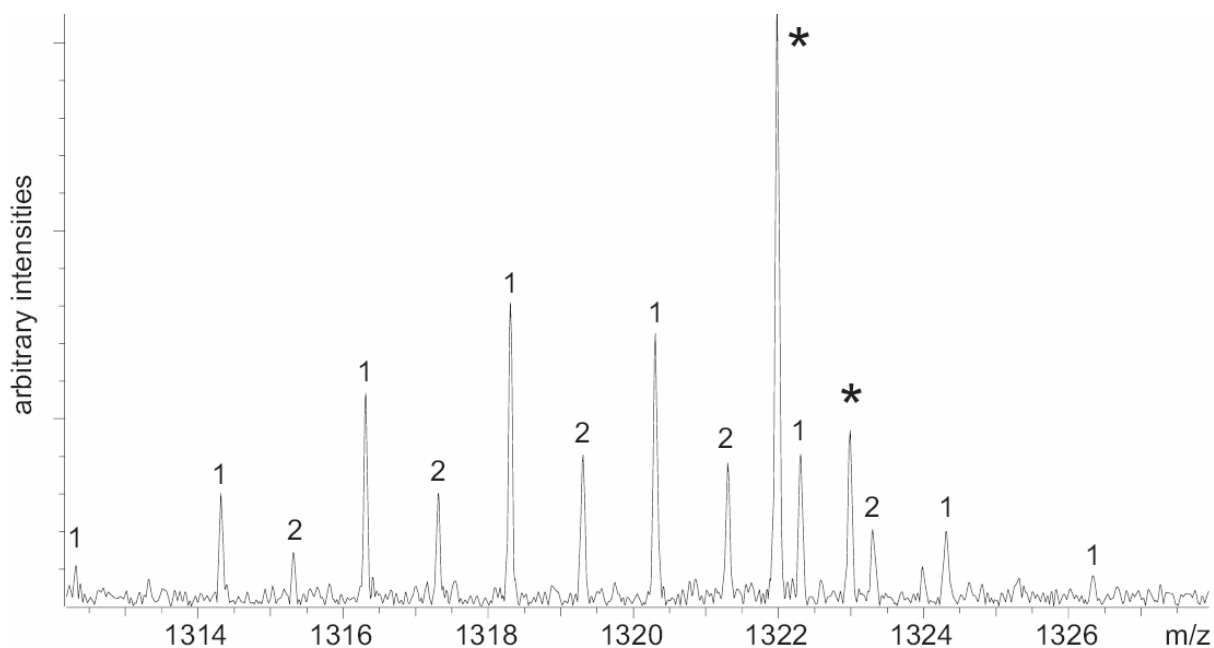


Figure 33: HR-ESI-MS of 10b (excerpt showing the signals for $[M+K^+]$ without ^{13}C or ^{29}Si nucleus [1], with one ^{13}C or ^{29}Si nucleus [2] and the internal standard []).*

5. Covalent attachment of active molecules on the silica surface

Resonances for carbon nuclei of C=C groups were not detected in the ^1H and ^{13}C NMR spectra. Therefore, all the vinyl groups were hydrobrominated. In addition, the ^1H NMR spectra display only two triplets, which demonstrate that the anti-Markovnikov product is obtained exclusively. The selectivity of the reaction is confirmed by the single signal observed in the ^{29}Si NMR spectrum assigned to the symmetrical silsesquioxane **10b** where all eight vinyl groups were converted into the anti-Markovnikov product.

It should be noted that the photochemically induced hydrobromination of octavinylsilsesquioxane produces **10b** in better yield and purity than the previously published procedures based on ref. [198].

In summary, the fact that the C=C bonds of 1-octene and of octavinylsilsesquioxane are fully hydrobrominated and that the anti-Markovnikov products are obtained in the homogeneous conditions, indicates that C=C bonds on the silica surface may react in the same manner.

However, the application of the brominated spacer for the immobilization of active molecules has several limitations. In particular, the amination of the brominated surface requires reflux and long reaction times [100]. Under these conditions an aliphatic amine will also react with the remaining Si-H groups on the silica surface. Only a primary aromatic amine may react with the brominated spacer without unwanted reactions with the silica surface.

It should be mentioned that other potential derivatives obtained from the C=C modified surface are promising for this purpose. In particular an aldehyde obtained by ozonolysis might enable a straightforward route for the attachment of active molecules.

However, for this thesis, the reactive acyl chloride modified silica surface is preferred for the immobilization of the ferrocene derivatives.

5.3 Conclusion

The direct attachment of terminal C=C bond functionalized redox-active molecules **1b**, **2a** and **3b** via route I was not achieved by photochemical or thermal hydrosilylation reactions because of two main factors. The need for a high concentration of the olefin is not compatible with the amount of redox-active molecules available. Moreover, in some cases, the redox-active molecules show poor stability under thermal or photochemical conditions.

Therefore, route 2 is necessary for the attachment of the redox-active molecules. The carboxylic acid modified surface prepared by the free radical induced hydrosilylation can be converted easily into the corresponding acyl chloride, and then be used in a subsequent

5. Covalent attachment of active molecules on the silica surface

reaction to immobilize **1a**. On the other hand, no straightforward reaction with either the activated M_{COOH} or $M_{C=C}$ surfaces makes the attachment of the ruthenium complex of type **2** and the biphenylamines **3** possible. Therefore for the subsequent steps of this thesis, we will only focus on ferrocene as the model for redox-active molecules.

6 Applications

The Si-H modification and the free radical hydrosilylation reactions described in Chapters E and F were carried out in order to meet the requirements for the immobilization of redox-active molecules and catalysts. The properties of the resulting surfaces are sought-after for HPLC applications as well. Indeed, the synthetic strategy for the surface modifications are driven by the need for a surface free of Si-OH groups and metal traces as well as a stable attachment. Those issues are important in HPLC in order to achieve high separation power and make a wide range of applications possible for a given stationary phase. Therefore, beside the electrochemical investigation of the ferrocene modified materials, the performance as HPLC phase of the Si-H and C18 modified materials will be evaluated.

6.1 HPLC separation with M_{SiH} and M_{C18}

Silica is the predominant solid support for HPLC stationary phases. Its desirable properties include high mechanical strength [32], thermal stability [18] and the ability to accurately tailor particles of a specific diameter, pore size, and surface area [39]. The limitations of silica for HPLC applications are the presence of strong adsorption sites (silanol groups and metal impurities) and the sensitivity of the siloxane bonds toward hydrolysis. These will be discussed in more detail below:

1. The polar acidic silanol groups on the silica surface induce peak tailing and loss of chromatographic resolution of basic analytes [32, 40, 41, 199]. Isolated silanols (non-hydrogen bonded) are the most acidic and believed to be responsible for the undesired interactions with organic bases [40]. One approach to minimize the effect of the isolated silanols consists in the rehydroxylation of the silica surface [200]. The aim of this strategy is to obtain a high Si-OH surface concentration to ensure that most groups can interact via hydrogen bridges.

An opposite and more common method to improve the separation efficiency consist in the end-capping of the remaining silanol groups after organosilanization [40, 201] with for example trichlorosilane or hexamethyldisilazane. Although these methods are not quantitative [39], the tailing is reduced and the chromatographic resolution enhanced because the end-capping groups block the access to the silanols groups [40]. Bulky substituents on the organic modifiers [202] or electrostatic shielding [203] may also be used to lower the accessibility to the silanols [40].

2. Metal impurities are another source of peak tailing in HPLC [204]. They are strong adsorption sites for complexing, and especially for chelating analytes. These interactions cause peak asymmetry and poor resolution of such analytes. The metal ions also affect the separation of organic bases by increasing the acidity of the adjacent silanols [205, 206]. The so-called “type A” silica materials, the first to be developed, have a high content of metal impurities [32]. Modern synthesis processes yield the so-called “type B” silica material with low metal content [32, 207], however contamination may still occur during surface modification if metals are involved in the reaction or during the HPLC separations.

3. The sensitivity of the bonded phase toward hydrolysis in an aqueous environment [208] at low [202, 209, 210] as well as at high pH values [15, 32, 33, 35] depends on the cross-linking degree [209] and the presence of silanol groups. An increase in the number of siloxane bonds between an individual alkyl ligand and the silica surface enhances the stability [36, 209]. The silanol groups that participate in the hydrolysis are again of the non hydrogen-bonded type. Therefore, the actions taken to minimize the activity of the isolated silanol groups, additionally enhances the hydrolytic stability.

The so-called “type C” silica, involving Si-H modified surfaces and hydrolytically stable Si-C bond formation by hydrosilylation reactions, were successfully developed to enhance the acid stability of silica-based bonded phases [15, 39]. The potential drawback of these materials may arise from the use of a metal catalyst for the hydrosilylation reaction. Metal residues which are strong adsorption sites for chelating compounds, may contaminate the silica surface. Also, the various Si-H modification procedures previously described leave unreacted Si-OH groups (Chapter 2).

In contrast, the Si-H modification procedure and the free radical hydrosilylation reactions described in Chapters 2 and 3 were designed in order to meet the requirements for a surface free of Si-OH groups and metal traces as well as enhanced bonding stability. The application of this methods for the synthesis of “type C” silica materials may also enhance their HPLC separation quality. Therefore, the properties of the Si-H and C18 modified silica materials prepared previously ($M2_{SiH}$ and $M2_{C18}$, respectively) were investigated as separation phase in HPLC.

The standard reference material 870 (SRM 870) from the National Institute of Standards and Technology (NIST) [211, 212] was used as a test mixture to examine the general characteristics of the synthesized materials ($M2_{SiH}$ and $M2_{C18}$) as chromatographic sorbents.

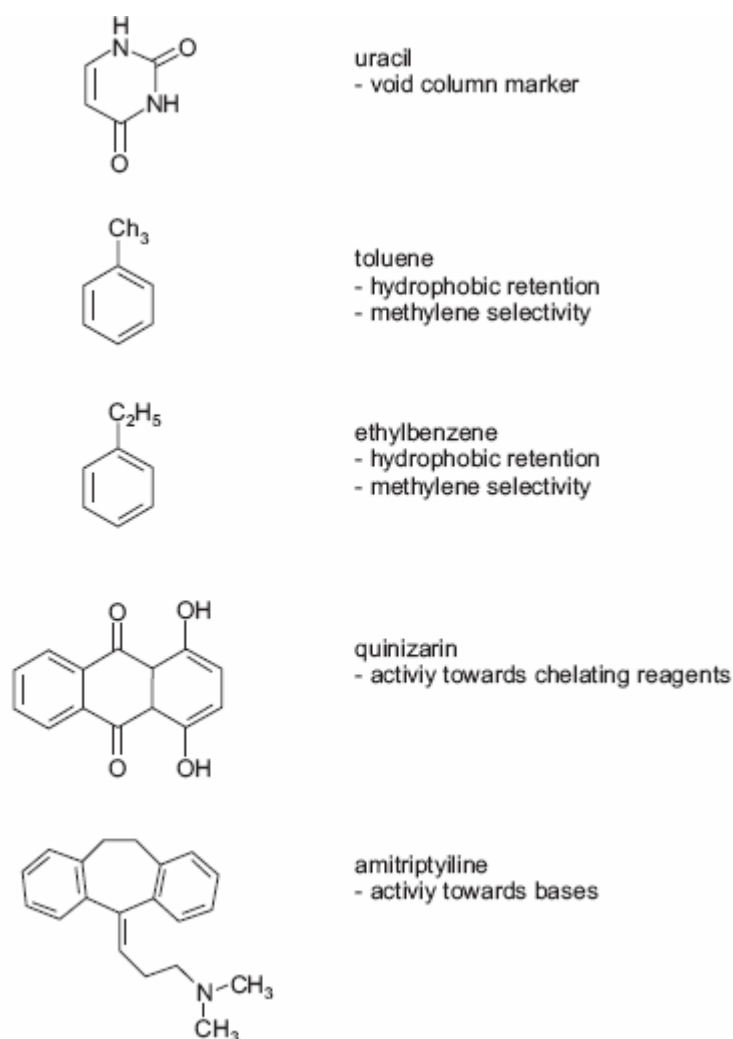


Figure 34: Structures and properties for components in SRM 870.

SRM 870 is a methanolic solution of uracil, toluene, ethylbenzene, quinizarin and amitriptyline and is used to characterize general aspects of liquid chromatographic (LC) column performance, including efficiency, void volume, methylene selectivity, retentiveness, and activity towards chelators and organic bases (Figure 34). Uracil is used as an indicator of the void time of the LC column. The retention of non-polar components such as ethylbenzene and toluene provides a measure of column retentiveness (column strength). Quinizarin (1,4-dihydroxyanthraquinone) is a strong metal chelating reagent. The retention behavior of this component is expected to be indicative of the presence of metals in the chromatographic system. Increasing amounts of metal ions on the surface are indicated by increasing tailing, i. e. asymmetry, of the quinizarin peak. Amytriptylin is an organic base commonly used for column characterization. The asymmetry of the amytriptyline peak is an appropriate measure of the silanol activity of the separation phase [212].

The retention times of quinizarin and amitriptyline are strongly dependent on the pH, and changes in column temperature strongly influence the absolute retention of all components in SRM 870. Therefore, the described separations were carried out at the recommended temperature under neutral, buffered conditions [211, 212]. Quinizarin typically elutes after ethylbenzene and before amitriptyline.

The peak identification was made on the basis of the relative absorption of the compounds at the various detection wavelengths (210, 254 and 480 nm). Quinizarin is the only compound of SRM 870 that shows a significant absorbance at 480 nm. On the other hand, uracil and quinizarin exhibit reduced absorbance at 210 nm. At 254 nm all 5 compounds may be detected.

As characteristics of the materials, the retention factor (k'), the peak asymmetry (A_s) and the efficiency (N) for the various compounds under the SRM 870 test conditions were calculated [212].

6.1.1 HPLC separation of SRM 870 with $M2_{SiH}$

The SRM 870 separation with $M2_{SiH}$ was performed under isocratic elution conditions as required by the SRM 870 test specifications. However, only two distinct signals are observed in the chromatogram (Figure 35). Based on the signal intensity in the spectrum at 254 nm as well as the absence of absorbance at 480 nm, the signal at $t = 1.30$ min is attributed to amytriptyline. The other components coelute without significant retention at $t = t_0 = 0.93$ min.

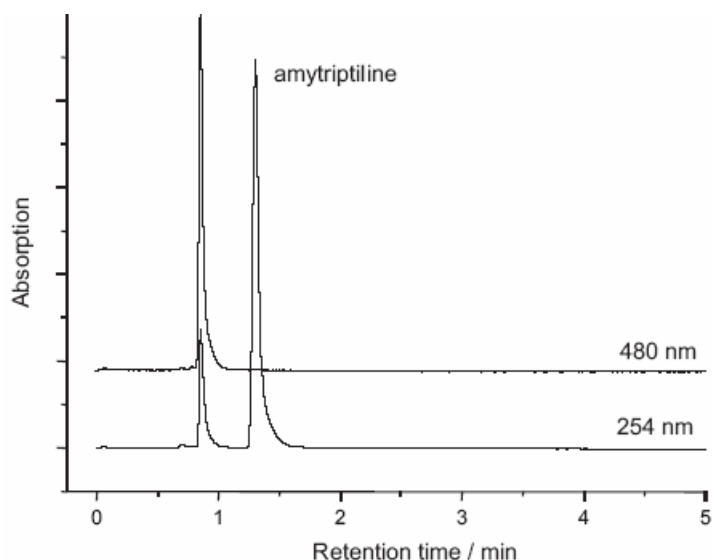


Figure 35: Separation of SRM 870 with the chromatographic sorbent $M2_{SiH}$ under isocratic elution conditions (MeOH/buffer 80/20) with UV detection at 254 nm and 480 nm.

The separation of amytriptiline from the other components of SRM 870 makes it possible to determine its chromatographic characteristics (Table 14).

The peak asymmetry for amytriptiline is low. This indicates a weak activity toward the retention of the organic base. Since no end-capping was performed and no bulky groups block the access to the surface, this result suggests that isolated surface silanol groups are very scarce in the $M2_{SiH}$ material.

Table 14: Chromatographic characteristics of $M2_{SiH}$ under isocratic elution conditions^[a].

| | k' | N / m^{-1} | A_s |
|---------------|------|--------------|-------|
| amitriptyline | 0.52 | 28000 | 2.02 |

a) UV detection at 254 nm, $t_{uracil} = t_0 = 0.93$.

Attempts to fully eliminate the silanol groups in order to diminish the silanol activity, by dehydroxylation for example, are generally counter productive [213]. Indeed, if only few silanol groups remain, those would be of the isolated type which are the most able to undergo ion-exchange interactions with organic bases [40]. According to the IR investigations of the M_{SiH} materials (see 2.3.2), isolated silanol groups are also present in the materials resulting from the chlorination-reduction sequence.

Still, the HPLC separation of amytriptiline with $M2_{SiH}$ does not display significant peak tailing. This indicates that the isolated silanol groups detected by DRIFT spectroscopy are not located on the surface. Therefore, the surface silanol groups, which are accessible to the chlorination and reduction have reacted to a large extend. On the other hand, the bulk silanol groups only undergo condensation which is known to leave unreacted isolated silanol groups whose amount depends on the applied temperature [88].

In summary, the HPLC separation demonstrates that the chlorination-reduction sequence produces materials with low silanol activity because of the condensation and reduction of the surface silanol groups including the isolated groups.

6.1.2 HPLC separation of SRM 870 with $M2_{C18}$

The $M2_{C18}$ phase obtained from the thermal hydrosilylation reaction of the C18 chains on $M2_{SiH}$ (Chapter 3) display improved separation power as compared to $M2_{SiH}$. The optimal separation of all 5 compounds of SRM 870 is achieved when a gradient elution is performed (Figure 36).

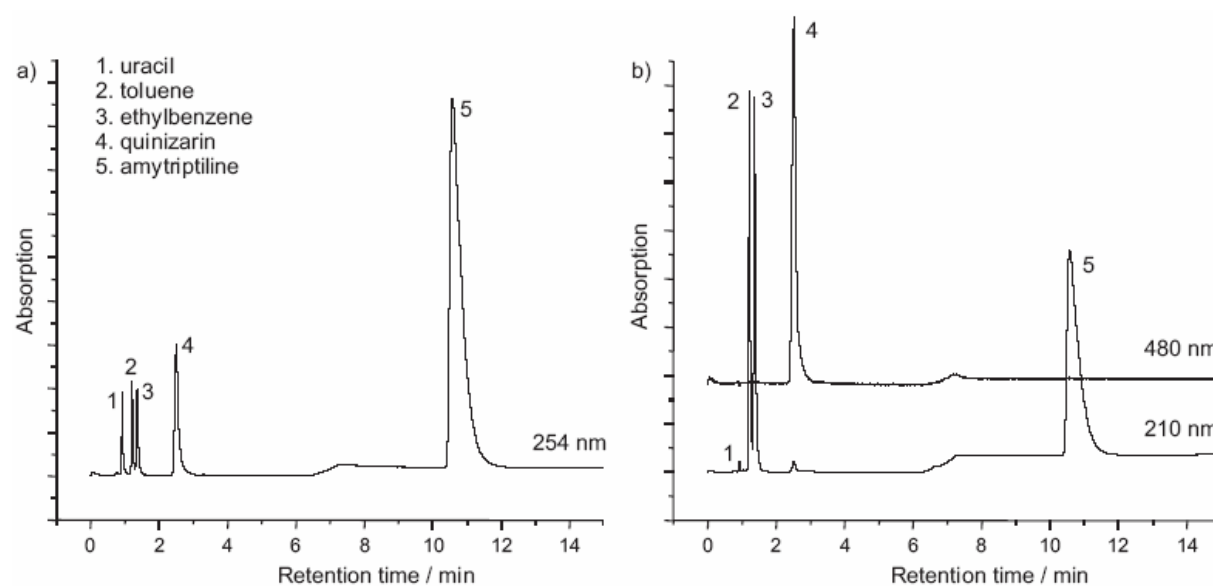


Figure 36: Separation of SRM 870 with the chromatographic sorbent $M2_{C18}$ a) UV detection at 254 nm, b) UV detection at 210 and 480 nm: Gradient elution: 60 % methanol/ 40 % buffer (v/v) hold 5 min to 80 % methanol/ 20 % buffer (v/v) between 5 min to 6 min.

The elution order is as follows: uracil, toluene, ethylbenzene, quinizarin and amitriptyline. This is in agreement with the elution order obtain with other C18 phases [212]. The separation factor is about 1.57 under the gradient elution conditions. The chromatographic value for the individual components of SRM 870 are given in Table 15. The resolution of toluene and ethylbenzene is not sufficient in order to determine A_s of these two components.

Table 15: Chromatographic characteristics of **M2**_{C18} with gradient elution^[a].

| | k' | N / m^{-1} | A_s |
|---------------|-------|---------------------|-------|
| toluene | 0.30 | 32100 | - |
| ethylbenzene | 0.47 | 31800 | - |
| quinizarin | 1.70 | 22100 | 1.72 |
| amitriptyline | 10.38 | 39800 | 2.96 |

a) UV detection at 254 nm, $t_{\text{uracil}} = t_0 = 0.93$, $\alpha_{\text{ethylbenzene/toluene}} = 1.57$.

In order to compare the chromatographic characteristics of the **M2**_{C18} material with other separation phases, the HPLC test must be performed under isocratic conditions [212]. In this case, ethylbenzene and toluene almost coelute with a retention factor of 0.18. Therefore, **M2**_{C18} as a HPLC separation phase shows a poor methylene selectivity. On the other hand, quinizarin and amitriptyline are well separated under the standard test conditions. This makes it possible to determine the chromatographic characteristics for these two components (Table 16).

Table 16: Chromatographic characteristics of **M2**_{C18} under isocratic elution conditions^[a].

| | k' | N / m^{-1} | A_s |
|---------------|------|---------------------|-------|
| quinizarin | 0.58 | 11000 | 3.34 |
| amitriptyline | 5.94 | 4700 | 3.59 |

a) UV detection at 254 nm, $t_{\text{uracil}} = t_0 = 0.87$.

The peak for amitriptyline shows an increased asymmetry compared to the separation with **M2**_{SiH}. This indicates that the surface concentration of isolated silanol groups has increased during the hydrosilylation reaction. The presence of water traces in the hydrosilylation

reaction mixture may explain the production of silanol groups by rehydroxylation of the surface siloxane bonds under the high temperature conditions. On the other hand, production of silanol groups by homolytic cleavage of siloxane bonds is unlikely under the radical conditions. However according to the DRIFT spectra, the production of isolated silanol groups is a minor side reaction. This is in accordance with the HPLC results. Indeed, the peak tailing ($A_s = 3.59$) remains moderate compared to commercial columns [212].

The asymmetry factor A_s of quinizarin is typically between 1 and 4 for commercial columns [212]. In comparison the **M2_{C18}** phase displays a relatively high peak tailing for quinizarin ($A_s = 3.34$). This indicates the presence of some metal ions on the silica surface. However, the free radical induced hydrosilylation reaction was performed without transition metal catalysts and therefore, is not the source of metal impurities.

6.1.3 Conclusion

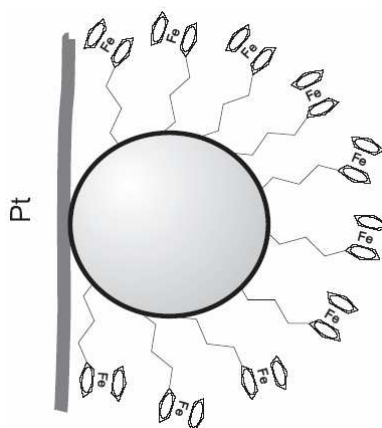
The HPLC investigations of **M2_{SiH}** and **M2_{C18}** deliver additional information on the surface chemistry of these materials. The peak asymmetry of amitriptyline after separation with **M2_{SiH}** demonstrates that the chlorination-reduction sequence produces a material almost free of surface isolated silanol groups.

On the other hand, according to the peak tailing of organic bases after separation with **M2_{C18}**, some silanol groups are produced during the hydrosilylation reaction. However, their effect on the HPLC separation is moderate, indicating that their surface concentration remains low.

The chlorination-reduction sequence followed by C18 surface modifications are a dramatically different strategy for the synthesis of C18 HPLC phases compared to the conventional silylation method. Still, at the early stage of their development, the **M2_{C18}** phases already match their silylated equivalent for the separation of organic bases. On the other hand the peak tailing of chelating analytes may still be improved. The source of metal impurities is not determined at this point. The solvent used during modification and HPLC tests as well as the original silica materials are two potential sources. Finally, the methylene selectivity of the **M2_{C18}** phase is low. Optimization of the thermal hydrosilylation reaction, in order to achieve higher surface concentration and lower the possible side reactions, may improve the separation quality.

6.2 Electrochemical properties of material **M1g_{Fc}**

It was shown in Chapter 5.2.1 that ferrocene derivatives may be covalently bound to a silicon hydride modified silica surface via a hydrosilylation reaction. In order to investigate the electron transfer on the particle surface with cyclic voltammetry, the redox-actively modified particles must be immobilized on an electrode surface (Scheme 35).



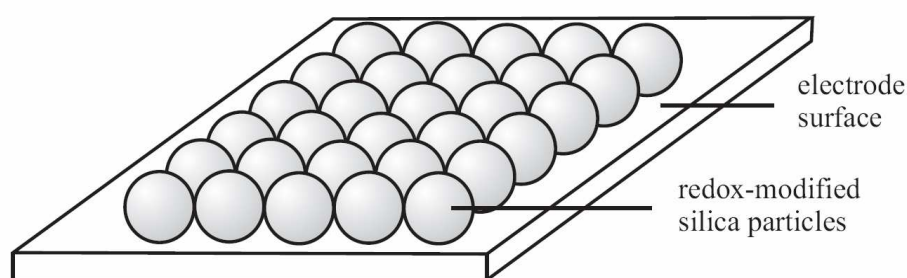
Scheme 35: Adsorption of ferrocene modified particles on the Pt surface.

It has been previously described that the immersion of a platinum electrode in a suspension of redox-actively modified particles results in the attachment of the particles on the Pt surface [103]. This behavior is attributed to the spontaneous adsorption of the modified particles on the Pt electrode. The spherical particles form a more or less ordered layer and display the redox behavior of immobilized redox-active species. A semi-quantitative analysis of the electrochemical properties of this system demonstrates the occurrence of a charge transfer between redox-active molecules on the particle surface. A quantitative analysis, however, was limited by the lack of periodicity and homogeneity in the particle layers: The presence of multilayers of particles disables a quantification of the total amount of silica particles present on the electrode surface. Knowledge of the amount of particles would allow to determine the amount of redox-active molecules present on the electrode surface which could be compared to the amount of redox-active molecules being electrochemically active. This information is important to determine the accessibility of the redox-active molecules to the redox process. Also, due to the lack of order, the benefit of the well defined shape and dimension of the particle is lost: indeed the presence of multilayers and clusters of particles opens the possibility for electron hopping between two layer of particles and therefore it is not possible

to precisely determine the distance over which the electron hopping is taking place and thus no kinetic information for this process can be gained.

6.2.1 2D arrangement of silica particles on Pt surface.

A monolayer (ideally a 2D hexagonally packed crystal) of particles is desired to clearly define the dimensions in which the electron transfer is taking place and to be able to determine which proportion of the redox-active molecules present on the particle surface are accessible for the redox process (Scheme 36).

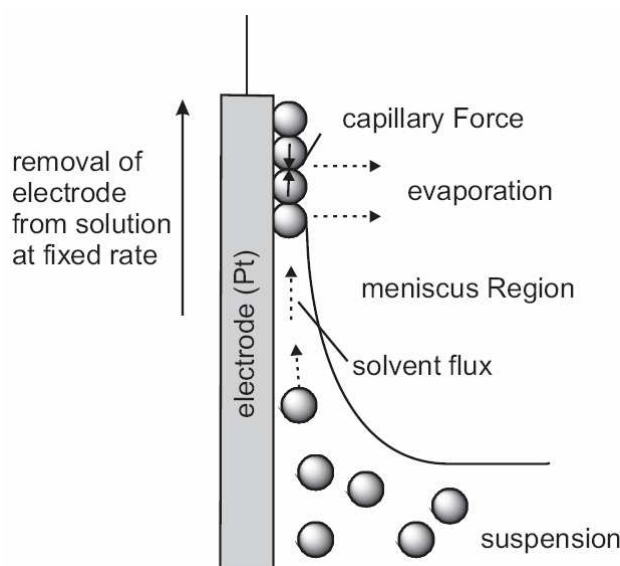


Scheme 36: Hexagonally packed 2D crystal of particles on a flat surface.

Several methods have been described for the preparation of periodic 2D (monolayer) and 3D crystals (multilayers) of colloid particles on flat substrates [61]. The most straightforward method is the gravitational sedimentation from a colloid suspension onto a horizontal substrate. However, this method is better suited for the preparation of 3D crystals. Also this method does not involve any adsorption interaction between the particles and the substrate and therefore a sintering step at 900 °C is needed to ensure a stable attachment of the particles [214, 215]. This requirement makes gravitational sedimentation unsuitable for the attachment of redox-actively modified particles. Another option is the use of capillary forces [216]. For example silica particles can be assembled in 2D crystals on glass substrates [217], or in 3D crystals on silicon wafers [218, 219] by dip-coating or by spin-coating methods [220]. 3D crystals of amino functionalized silica particles have also been prepared on hydrophilic glass substrates [221] and 2D crystals of carboxylic acid modified particles have been prepared on modified silicon substrates. The preparation of 2D crystals from redox-actively modified colloids or on platinum electrodes have – to our knowledge – not been described so far. As a first step toward the assembly of a monolayer of redox-actively modified silica particles, the immobilization of bare silica particles on Pt electrodes by capillary forces was tested.

The formation of the silica particle monolayer was performed by a vertical capillary method (dip-coating) [217]: Silica particles **M1c** were suspended under ultrasonication in ethanol/water mixtures at different pH. Hydrophilic Pt electrodes (after oxidation with HNO_3) were dipped into the suspension and drawn out in the vertical direction at a constant rate with a stepper-motor. At the meniscus, the evaporation of the solvent creates a convective flux which drives the particles toward the upper part of the platinum substrate (Scheme 37). At the particle surface - gas interface, the attractive capillary force allows the packing of the particles in a dense monolayer.

In order to allow the formation of the meniscus, the substrate should have a length of 1 cm in one of its dimensions at least. The dimensions of platinum spade electrodes (1×1 cm) as well as platinum wire electrodes (2 cm in length and 1 mm in diameter) are suitable for this purpose.



Scheme 37: Substrate-suspension-air interface during dip-coating [217].

The important variables associated with colloidal crystallization by dip-coating include the concentration of particles, the evaporation rate and surface tension of the solvent, the surface charges of the particle and substrate and the withdrawal speed [222].

The resulting electrode surface was investigated with scanning electron microscopy (Figure 37). The best results are obtained when the dip-coating of bare silica particles is performed in basic ($\text{pH} = 10$) and aqueous conditions on a hydrophilic Pt surface.

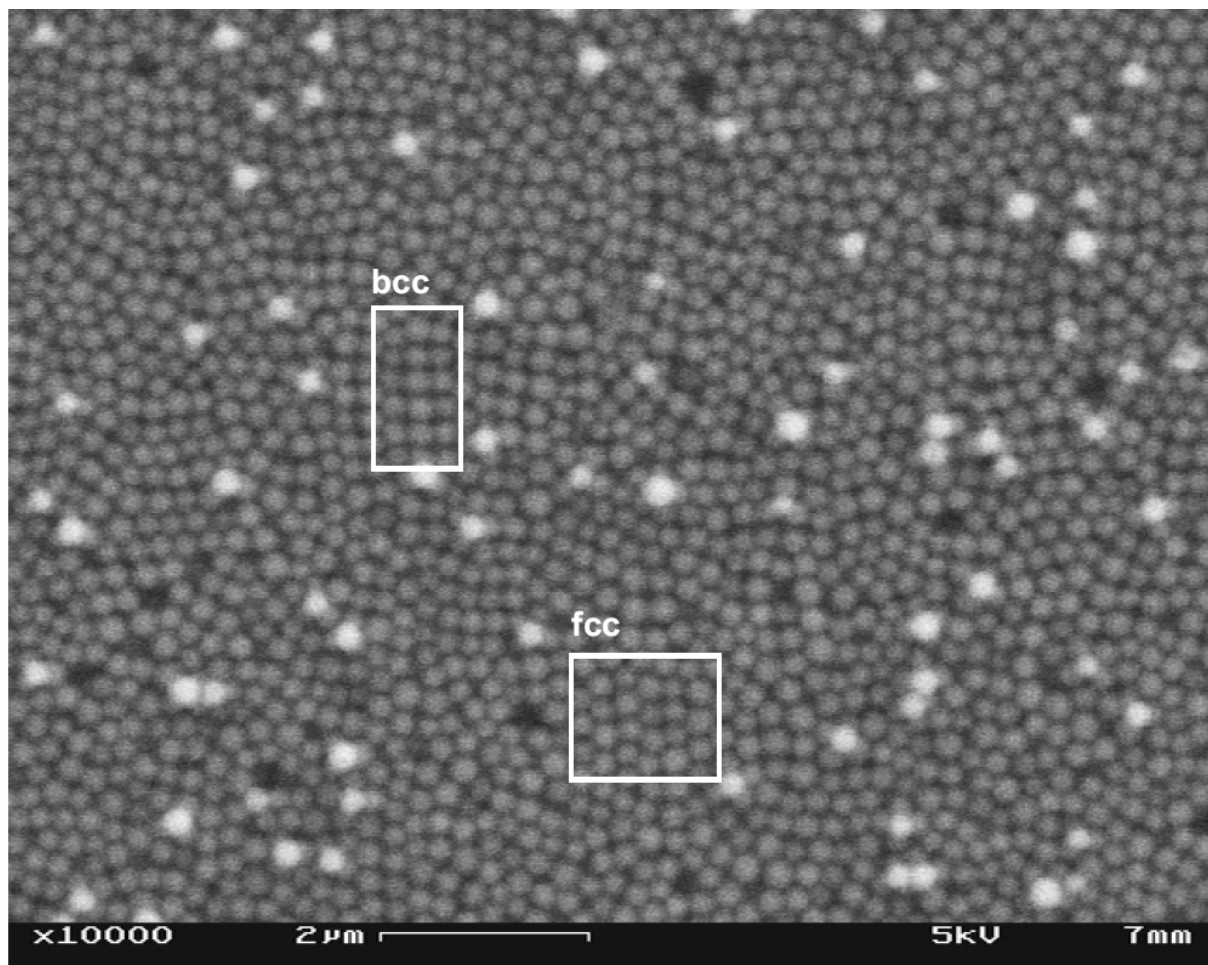


Figure 37: Scanning electron micrograph of **M1c** ($d \sim 250$ nm) after dip-coating on a Pt spade electrode.

The SEM pictures show a dense layer of silica particles over the whole electrode surface with some isolated particles (light spots) sitting on top of this layer as well as a few holes (dark spots). While the denser hexagonal arrangement (face centered cubic, fcc) of spheres is the predominant structure, occasional defects with body centered cubic (bcc) arrangement, such as those apparent in Figure 37, were observed. The deviation from a true 2D crystal is probably due to heterogeneity in the flatness of the Pt surface: The surface irregularities may act as a template resulting in the bcc packing observed in some regions [223, 224].

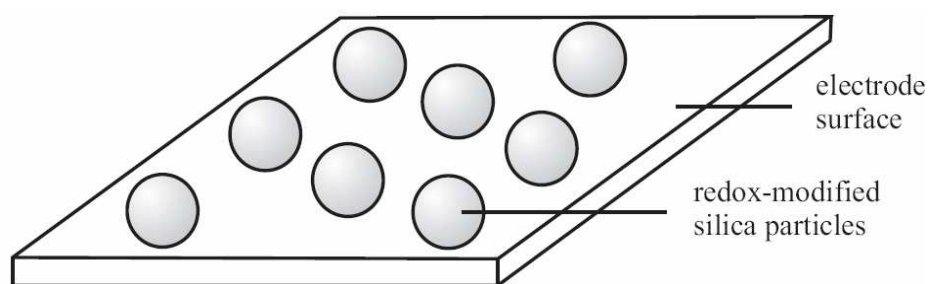
The absence of clusters and the high coverage of the electrode are desired properties for the adsorption of redox-active molecules for a quantitative analysis of the electrochemical data.

The 2D arrangement on the Pt surface was then attempted with the **M1f_{SiH}** and the **M1g_{Fc}** materials. However, after Si-H and Fc modification, the conditions described previously for

the dip-coating of bare silica particles can not be used because the Si-H modified particles can not be suspended in ethanol/water mixture. The hydrophobic character of these particles may be due to the absence of silanol groups on their surface. Therefore, the Si-H modified particles were suspended in ethanol, instead of an aqueous solution and the dip-coating procedure was performed from this suspension. The presence of the adsorbed particles is obvious as a colorless film on the electrode surface. However, after complete drying, the film was partially lost. After immersion of the electrode into a fresh solution or electrolyte without particles for electrochemical measurements, the film was completely lost.

6.2.2 Spontaneous adsorption of $\mathbf{M1g_{Fc}}$ on platinum electrode surfaces

Because of the poor film stability obtained after dip-coating of $\mathbf{M1f_{SiH}}$ and $\mathbf{M1g_{Fc}}$, an alternative adsorption procedure is needed. The spontaneous adsorption procedure may be adequate providing that the resulting particle film does not display multilayers or agglomerates of particles (Scheme 38). At this conditions, the potential electron transfer would occur in a well defined system (the surface of a single silica particle). Also the determination of the amount of redox-active molecules accessible to the electrochemical process may be achieved, since the total amount of silica particles on the electrode surface may be obtained (see 6.2.3).



Scheme 38: Isolated particles on a flat surface.

The adsorption of the ferrocene modified particles $\mathbf{M1g_{Fc}}$ was performed by immersing polished Pt disk electrodes in stirred suspensions of particles for several hours. Under these conditions, material $\mathbf{M1g_{Fc}}$ adsorbs spontaneously on platinum electrodes from a suspension in dichloromethane according to the SEM investigations (Figures 38 and 39). If the platinum electrode is exposed to the suspension of particles for a short time (1 h) only, isolated particles or small clusters are found on the surface (Figure 38). After longer exposure times (5 h),

however, large agglomerates of particles are obtained (Figure 39). In both cases, the electrodes may be dried and dipped in fresh solutions without significant loss of adsorbed particles. Therefore the particle film obtained after short times of spontaneous adsorption may enable the quantitative analysis of their electrochemical properties.

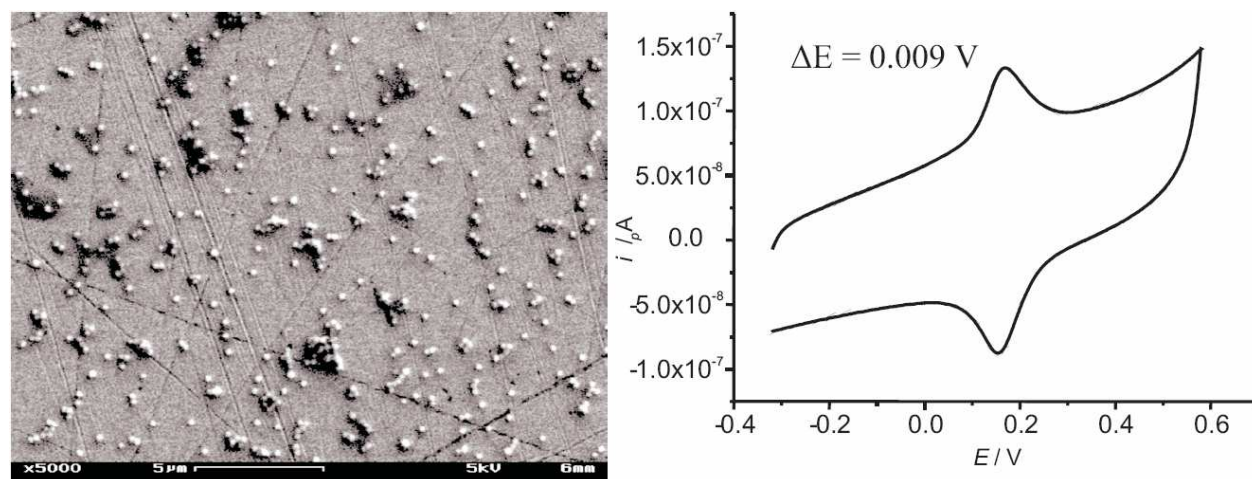


Figure 38: Isolated ferrocene-modified silica particles ($\mathbf{M1g_{Fc}}$) and small clusters on a platinum electrode after 1 h of exposure: SEM images at $5000 \times$ magnification (left) and cyclic voltammogram in $\text{CH}_2\text{Cl}_2/\text{NBu}_4\text{PF}_6$ (0.1 M) at 0.02 V s^{-1} (right).

On the other hand, the spontaneous adsorption of $\mathbf{M1f_{Fc}}$ results again in a weak adsorption with loss of the film after drying. It should also be mentioned that $\mathbf{M1g_{Fc}}$ is easily resuspended by means of ultrasonication under destruction of the adsorbate film.

This contrasts with previous observations when modified silica particles with remaining non-reacted silanol groups were adsorbed on a platinum surface [103]. In the latter case the adsorbed particles could only be removed by polishing the electrodes; ultrasonication did not significantly disturb the adsorbed layer. The strong adsorption is likely due to the interactions of the remaining Si-OH groups with the oxidized platinum surface. On the other hand, in $\mathbf{M1g_{Fc}}$, we expect that most of the Si-OH groups have reacted with triethoxysilane [108], and, after the photochemical step, unreacted hydride groups remain on the silica surface. In the case of $\mathbf{M1f_{Fc}}$, which results from the chlorination-reduction sequence, the absence of Si-OH groups on the surface was demonstrated in Chapters 2 and 6.1. Such surfaces are more hydrophobic than that of $\mathbf{M1}$ or the materials described in ref. [103], and therefore a different interaction with the platinum electrode occurs: The fact that the more hydrophobic particles preferentially agglomerate with those already adsorbed on the surface instead of forming a

dense layer, is also in contrast to earlier observations [103] and shows that in the present case the particle-particle interactions are stronger than the particle-Pt surface interactions.

6.2.3 Electrochemistry of adsorbed $\mathbf{M1g_{Fc}}$

The Pt-disk electrodes modified by spontaneous adsorption of $\mathbf{M1g_{Fc}}$ were used for the electrochemical investigations. Cyclic voltammograms of electrodes modified with $\mathbf{M1g_{Fc}}$ in an electrolyte without any redox-active compound show the characteristic signals for the reversible oxidation and reduction of the immobilized ferrocene for both the electrodes with isolated particles and small aggregates or with large clusters of particles (Figures 38 and 39).

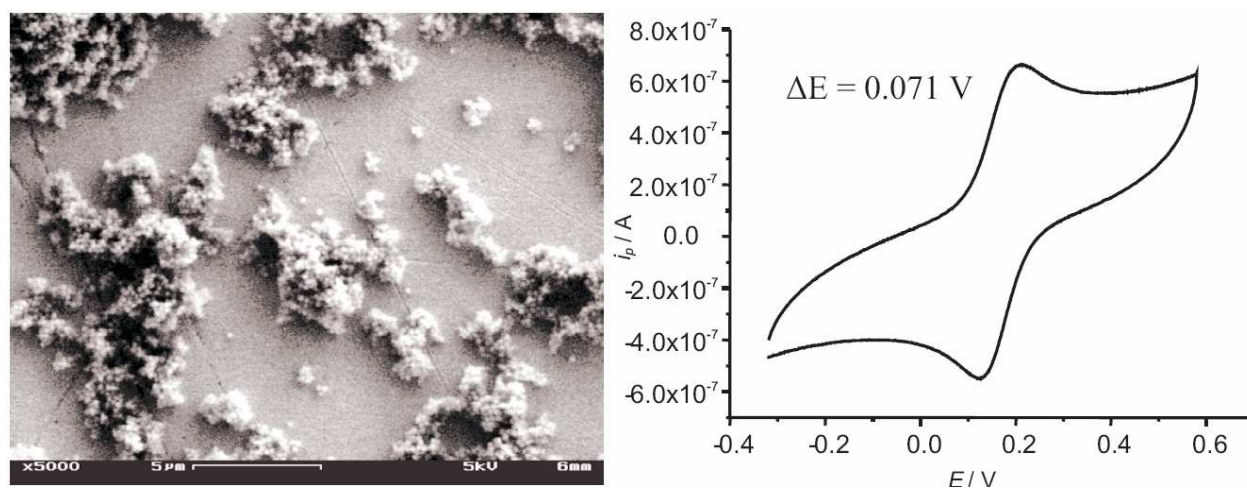


Figure 39: Clusters of ferrocene-modified silica particles ($\mathbf{M1g_{Fc}}$) on a platinum electrode after 5 h of exposure: SEM images at 5000 × magnification (left) and cyclic voltammogram in $\text{CH}_2\text{Cl}_2/\text{NBu}_4\text{PF}_6$ (0.1 M) at 0.02 Vs^{-1} (right).

The current/potential curves at electrodes with $\mathbf{M1g_{Fc}}$ show a slightly lower capacitive current than voltammograms at the bare electrode. Therefore, background correction leads to artifacts and the cyclic voltammograms are represented without background correction. However, for the determination of the electrochemical data of $\mathbf{M1g_{Fc}}$, the CV of the non-modified electrode were used for background correction, followed by a manual baseline correction in order to account for the difference in capacitive current. Values of the formal potential $E^0(\mathbf{M1g_{Fc}})$, measured as the mid-point potential ($E^0 = (E_p^{\text{ox}} + E_p^{\text{red}})/2$, with E_p^{ox} and E_p^{red} being the oxidation and reduction peak potentials), are presented versus the ferrocene/ferrocinium ion redox couple (Table 17). For isolated particles and for large agglomerates of $\mathbf{M1g_{Fc}}$ on

platinum electrodes, the same $E^0(\mathbf{M1g}_{\text{Fc}})$ are obtained. The difference to the redox potential of the ferrocene derivative **1b** is only 0.018 V. This is similar to the ferrocene modified material discussed in ref. [103].

Table 17: Electrochemical parameters of isolated and clustered ferrocene modified particles adsorbed on a Pt electrode^[a].

| parameter | isolated | clustered particles |
|--|-------------------|---------------------|
| $E^0(\mathbf{M1g}_{\text{Fc}})$ | 0.177 ± 0.003 | 0.177 ± 0.001 |
| $E^0(\mathbf{M1g}_{\text{Fc}}) - E^0(\mathbf{1b})$ | 0.018 | 0.018 |
| ΔE_p (0.02 V s ⁻¹) | 0.01 | 0.07 |
| ΔE_p (0.1 V s ⁻¹) | 0.06 | 0.09 |
| ΔE_p (0.25 V s ⁻¹) | 0.13 | 0.10 |
| $Q_{\text{red}}/Q_{\text{ox}}$ ^[b] | 0.99 | - |

[a] all potentials given in V vs Fc/Fc⁺, [b] at 0.02 V s⁻¹.

The redox process observed in the current/potential curves may be explained by the oxidation and reduction of the immobilized Fc units on the particles that are in direct contact with the electrode surface. In principle, a charge transport by electron hopping along the surface of adsorbed Fc-modified particles makes the Fc units over the whole particle surface accessible to the redox process [103]. Kinetic information for this charge transport may be obtained from variable scan rate experiments [7]. The shape of the voltammograms as well as the peak current – scan rate dependency makes it possible to determine the type of electron transfer (either adsorption or diffusion type).

However, slight decreases in peak current between subsequent measurements at constant scan rate indicate that the particles are slowly desorbing from the electrode surface. This variation in the amount of particles present on the electrode surface prevents the quantitative analysis of the CVs recorded at variable scan rates. Therefore, the study of the electron transfer from the variable scan rate experiment is restricted to a qualitative analysis of the shape of the CVs.

The voltammogram of the electrode with isolated particles at low scan rates ($\nu < 0.05$ Vs⁻¹) shows adsorption-type signals (Figure 38) with a small separation of the peak potentials ($\Delta E_p = 0.01$ V at $\nu = 0.02$ Vs⁻¹). The ratio of the transferred charges $Q_{\text{red}}/Q_{\text{ox}}$ indicates an almost fully reversible electron transfer ($Q_{\text{red}}/Q_{\text{ox}} = 0.98$). At faster scan rates ($\nu > 0.1$ Vs⁻¹), the

shape of the curves changes into an unsymmetrical one with larger ΔE_p (Table 1), which is characteristic of diffusion type signals.

The transition from adsorption-type to diffusion-type signals with increasing scan rates in the case of the isolated particles **M1g_{Fc}** has already been observed for other types of redox-actively modified particles [103] or dendrimers [7] immobilized on a platinum electrode. This transition depends on the ratio between the diffusion layer thickness δ at a given scan rate and the particle diameter.

At low scan rates, δ is much larger than the diameter of the adsorbed particles and, under these conditions, the electrochemical properties of the redox-active molecules bound to the particles resembles those of molecules directly attached to the electrode surface. As the scan rate increases, δ decreases. For scan rates fast enough, the diffusion layer thickness becomes comparable to or even smaller than the diameter of the adsorbed particles. At this point, the kinetics of the electron transfer between neighboring redox centers on the particle surface becomes significant in the voltammetric response. The diffusion-like shape of the current/potential curves at faster scan rates is not due to freely diffusing molecules but rather to the kinetics of electron-hopping along the redox-actively modified silica particle surface [103].

Further evidence for the occurrence of the charge transfer by electron hopping may be obtained from the amount of ferrocene units accessible to the redox process.

The surface concentration of ferrocene on **M1g_{Fc}** from cyclic voltammetry (Γ_{CV}) is calculated from the amount of electrochemically accessible ferrocene units on the particle surface ($N_{Fc(P)}$) and the geometrical surface area of one particle (A_p) according to Equation 10:

$$\Gamma_{CV} = \frac{N_{Fc(P)}}{A_p} \quad (10)$$

A_p is calculated from the diameter obtained from SEM measurements ($A_p = \pi d_{SEM}^2$) and $N_{Fc(P)}$ is obtained from the total amount of electrochemically accessible Fc units on the electrode surface ($N_{Fc(E)}$) and the amount of particles adsorbed on the electrode surface ($N_{p(E)}$).

$$\Gamma_{CV} = \frac{N_{Fc(E)}}{N_{p(E)} \pi d_{SEM}^2} \quad (11)$$

$N_{\text{Fc(E)}}$ is calculated from the charge (Q) associated with the oxidation of the adsorbed Fc which corresponds to the area under the oxidation wave ($N_{\text{Fc(E)}} = Q / n F$) [225]. This integration is performed for current-potential curves obtained at low scan rates (0.02 V s^{-1}) at which the charge transfer shows an adsorptive behavior and no kinetic characteristics to ensure that all accessible Fc units are oxidized. The SEM pictures of the electrodes with isolated particles makes it possible to determine $N_{\text{p(E)}}$ ($N_{\text{p(E)}} = \Gamma_{\text{p}} A_{\text{E}}$, where Γ_{p} is the surface concentration of particles on the electrode and A_{E} the geometrical surface area of the electrode). Therefore, the surface concentration of electrochemically accessible ferrocene units on the silica particle surface (Γ_{CV}) is calculated from Equation 12 (see 8.3):

$$\Gamma_{\text{CV}} = \frac{Q}{\Gamma_{\text{p}} A_{\text{E}} n F \pi d_{\text{SEM}}^2} \quad (12)$$

The value of $\Gamma_{\text{CV}} = 1.15 \times 10^{-6} \text{ mol m}^{-2}$ may be compared to the surface concentration of ferrocene obtained by AAS ($\Gamma_{\text{AAS}} = 1.96 \times 10^{-6} \text{ mol m}^{-2}$). As a result, 58 % of the Fc units present on the particle surface are accessible to the redox process. Obviously, not all Fc units are involved in the electrode reaction. However, the amount of Fc units immobilized on the particle surface that have a direct contact with the platinum electrode is expected to be much lower. The electron-hopping process between neighboring redox centers (*intermolecular* charge transfer) explains why a higher fraction of the metal centers than expected is involved in the electron-transfer process occurring between the electrode and the particles.

Current/potential curves of the electrode with large clusters of particles do not follow the same pattern. At all scan rates investigated, the shape of the cyclic voltammograms has diffusion-like characteristics (Figure 39 and Table 17). This is explained if the electron-hopping between neighboring redox centers also crosses over to the neighboring particles in different layers of the cluster. The SEM images of this electrode show that the clusters of particles have diameters in the range of several micrometers (Figure 39). These clusters are larger than the diffusion layer thickness even at low scan rates. Consequently, the shape of the cyclic voltammograms deviates from adsorption characteristics already at low scan rates, because the electron-hopping takes place over the whole cluster via an *interparticle* charge transfer. Nevertheless, the voltammetric results show that for large agglomerates as well as for isolated particles an important fraction of the redox centers are accessible to the redox process. This implies a charge transfer by electron-hopping.

6.2.4 Conclusion

Cyclic voltammetry of the **M1g_{Fc}** particles indicates that Fc units over the whole particle surface are electrochemically accessible by an electron hopping mechanism. In addition to the *intermolecular* charge transfer between ferrocene units on the surface, an *interparticle* charge transfer between adjacent particles within large agglomerates is also taking place. The latter mechanism was not observed in a previous study [103], probably because the contact between the particles was not tight enough owing to different surface properties. According to cyclic voltammetry and AAS measurements, more than half of the redox-active molecules is accessible to the electrochemical process.

However, the rate constant of the electron transfer could not be determined from variable scan rate experiments because of the poor stability of the adsorbate film. The strong adsorption on Pt surfaces necessary for quantitative electrochemical analysis was not achieved because of the absence of surface Si-OH groups. Still, turning back to materials with surface Si-OH groups is not pertinent in our opinion. Indeed, the inertness of the matrix, which implies the absence of Si-OH groups, is desired for interphase systems in general (see Introduction). Therefore, the search for an alternative electrode material for the adsorption of such hydrophobic particles should be one priority research direction. For example doped silicon with a chemically modified surface [226] may be a promising material for the adsorption and electrochemical investigation of the **M1g_{Fc}** materials.

7 Experimental part

7.1 General procedures

All reagents were used without further purification unless otherwise stated.

Anhydrous solvents were obtained as follows: THF, diethyl ether, dioxane, hexane and toluene by distillation from sodium and benzophenone followed by storage over molecular sieves (3 Å); dichloromethane from distillation followed by storage over basic alumina; CH₃CN by 3 successive distillations from P₂O₅, CaH₂ and again P₂O₅, followed by storage in presence of neutral alumina [236].

Argon 4.8 was used as the inert gas in all experiments. Argon was pre-dried with KOH, Mg(ClO₄)₂, and Sicapent columns before use. Oxygen impurities from argon were removed

with a heterogeneous Cu reagent (BASF, R 3-11). Hydrogen 5.0 was dried with a Sicapent column before use.

The reaction flasks were pre-dried with a heat gun under high vacuum. All chemicals, which were air or water sensitive, were stored under inert atmosphere. Compounds that are not described in the experimental part were synthesized according to the literature.

7.2 Materials

All chemicals were purchased from Aldrich, Fluka or Merck and were of reagent grade.

The Kromasil particles (**M2**, 5 μm , 300 \AA pore diameter) were received from EKA Chemicals. Chromatography grade (**M3**, type 60, 70–230 mesh, 60 \AA pore diameter) and fumed silica (**M4**, particle size 7 nm) were purchased from Aldrich.

7.3 Analytical techniques

High resolution NMR spectroscopy

The ^1H and ^{13}C solution NMR spectra were measured on a Bruker Advance 400, which operated at 400.16 MHz for ^1H and 100.62 MHz for ^{13}C nuclei. The ^{31}P and ^{29}Si solution NMR spectra were measured on a Bruker DRX 250 spectrometer, which operated at 250.13 MHz for ^1H , 62.90 MHz for ^{13}C , 101.25 MHz for ^{31}P and 49.69 MHz for ^{29}Si nuclei.

All NMR spectra were recorded at 295 K in CDCl_3 , chemical shifts were calibrated to the residual proton and carbon resonance of the deuterated solvent ($\delta_{\text{H}} = 7.25$ ppm, $\delta_{\text{C}} = 77.0$ ppm for CDCl_3), and/or to an external standard (TMS for ^1H , ^{13}C , ^{29}Si and 85 % H_3PO_4 for ^{31}P). Data are reported as follows: chemical shift (multiplicity: s = singlet, d = doublet, t = triplet, m = multiplet, br = broadened, integration, J = coupling constant (Hz), peak assignment).

Solid state NMR spectroscopy

^{29}Si CP/MAS NMR experiments were performed in 7 mm ZrO_2 rotors with a Bruker ASX 300 spectrometer equipped with a double-resonance MAS probe head and operating at a resonance frequency of 300.12 MHz for ^1H and 59.63 MHz for ^{29}Si . For **M4**_{SiH}, about 150000 scans were accumulated at a spinning speed of 3 kHz, with a CP mixing time of 500 μs and a cycle delay of 2 s. For **M2**_{SiH} and **M2**_{TES} about 78000 scans were accumulated at 300 K and 295 K respectively and a spinning speed of 4.5 kHz, a relaxation delay of 1 s and a contact time of 5 ms were chosen. For all experiments, the proton 90° pulse length was set to 6.5 μs

and heteronuclear two-pulse phased modulation (TPPM) decoupling was applied during acquisition. The chemical shifts were referenced to Q_8M_8 [235]. The spectra were deconvoluted into individual peaks for the various components under the assumption that the four different peaks are strictly Gaussian.

Mass Spectrometry

Mass spectra were recorded on a Finnigan Triple-Stage-Quadrupol Spectrometer (TSQ-70) from Finnigan-Mat with electron-impact (EI) or fast-atom bombardment (FAB) as ionization methods. High-resolution ESI-MS (FT-ICR) was carried out on a Bruker Daltonic APEX 2 spectrometer and results are reported as follows: (ESI): calculated mass for the most intensive isotope combination of the corresponding compound followed by found mass.

Cyclic voltammetry

Cyclic voltammograms were recorded with a BAS 100 B/W electrochemical workstation. All electrochemical experiments were carried out at room temperature under argon with a gas-tight full-glass three-electrode cell. The working electrode was a Pt disk electrode (Metrohm, electroactive area $A = 0.064 \text{ cm}^2$). The disk was polished before each experiment with α - Al_2O_3 (0.05 μm). The counter electrode was a platinum wire (diameter 1 mm) spiral with an outer diameter of 7 mm. As potential reference a Haber-Luggin double reference electrode [234] was used. The resulting potentials refer to the Ag/Ag^+ redox system (0.01 M in CH_3CN with 0.1 M NBu_4PF_6). All potentials are reported to an external Fc/Fc^+ standard [12] and were rescaled to $E^\circ(\text{Fc}/\text{Fc}^+) = +0.218 \text{ V vs. Ag}/\text{Ag}^+$ (dichloromethane).

IR spectroscopy

DRIFT experiments were performed on a Bruker IFS 25 IR spectrometer^[a] with the Praying Mantis DRIFT unit from Harrick. The samples were dried at 100 °C under reduced pressure for several hours and mixed with dry KBr at a ratio of 1:20. The DRIFT spectra were recorded from 4000 to 500 cm^{-1} versus pure KBr as blank. The Si–H and Si–OH contents were semi-quantitatively obtained from the integration of the stretching vibration bands in the DRIFT spectra. To enable an accurate comparison between different spectra, the integration value from the signal of the stretching vibration of Si–O–Si (ν_{SiOSi}) at 1870 cm^{-1} was used as an internal standard [113]. The integration values for ν_{SiH} and ν_{SiOH} were normalized with

^[a] Equipment from AK Wesemann, Institut für Anorganische Chemie.

respect to this integral. For the semi-quantification of Si–H and Si–OH groups, the highest normalized integral value for ν_{SiH} and ν_{SiOH} was set as 100 %, and values for the other silica materials of the same type are given relative to this.

Dynamic light scattering (DLS)

A Coulter N4 Plus PCS spectrometer^[a] (Beckman Coulter) with a 10 mW He-Ne laser (632.8 nm) was used. The silica particles (300 mg L⁻¹) were suspended in filtered ethanol (100 nm Millipore filter) under ultrasonication for 30 min. The DLS experiments were performed in quartz or glass cuvettes (d = 1 cm) with 4 transparent sides at an angle of 90°. All experiments were performed at 20 °C using temperature equilibration for 5 min before each run. Weight analyses of the data were performed using a size distribution processor (SDP) based on the Contin algorithm [227, 228] providing an analysis of sizes (31 bins analysis).

Scanning electron microscopy (SEM)

Sample preparation on aluminum support: The silica materials were suspended in ethanol at a concentration of ~ 10 mg mL⁻¹ and left under ultrasonication for one hour. One drop of the suspension was then placed on an aluminum support. The ethanol was evaporated by slowly spinning the Al support by hand.

Sample preparation on platinum support: The silica particles were immobilized on Pt electrodes by spontaneous adsorption as described in ref. [103] or by dip-coating as described below.

Scanning electron microscope (SEM) images of the silica materials on the Al or Pt support were obtained without sputtering from a ZEISS DSM 962^[b] at 5 keV. The diameter of the particles was determined from the SEM images as an average of at least 200 particles for each sample.

Nitrogen isotherm measurements - BET

Adsorption and desorption isotherms were measured at 77 °K with nitrogen on a ASAP 2010 instrument^[c] (Micrometrics). The samples were degassed at 423 °K and 1 mPa for 14 h before adsorption measurements.

^[a] Equipment from AK Oelkrug, Institut für Physikalische Chemie.

^[b] Equipment from AK Chassé, Institut für Physikalische Chemie.

^[c] Equipment from the Center for Applied Geosciences.

The specific surface area was calculated according to the multipoint Brunauer, Emmet and Teller (BET) method. The mean pore diameter was calculated according to Barrett, Joyner and Halenda [101] from the desorption branch of the isotherm (BJH desorption method). A cylindrical pore shape was assumed in the calculations.

Atomic absorption spectroscopy

The AAS measurements were performed on a SpectrAA-20 from Varian^[a] with a four-lamp turret in an air-acetylene flame.

Approximately 15 mg of **M1f_{Fc}** / **M1g_{Fc}** weighed to the nearest 0.1 mg were suspended in 10 mL of distilled water under ultrasonication for 2 h. For calibration, aqueous solutions of Fe(NO₃)₃ in the concentration range 2×10^{-5} to 2×10^{-4} M were prepared from the atomic spectroscopy standard solution. The absorbances of the suspension of **M1f_{Fc}** / **M1g_{Fc}** and of the calibration solutions were measured at a wavelength of 248.3 nm after injection in the air-acetylene flame. The ferrocene surface concentration (Γ_{AAS}) is calculated by dividing the specific ferrocene amount obtained from the AAS measurements by the specific surface area of the Stöber particles obtained from SEM measurements (A_{SEM}).

UV-vis spectroscopy

The UV-vis absorptions spectra were recorded on a Perkin Elmer Lambda 2 UV-Vis spectrometer^[b].

For the quantification of Γ_{Fc} , approximately 60 mg of **M1g_{Fc}** were weighted to the closest 0.1 mg and suspended in 1 M KOH for 2 h under ultrasonication. Before the UV-vis measurements, the suspension was centrifuged to remove non-hydrolyzed silica particles. For calibration, ferrocenecarboxylic acid solutions in a concentration range from 2×10^{-5} to 2×10^{-4} M in 1 M KOH were treated in the same way as the suspension of **M1g_{Fc}**. The UV-vis spectra of **M1g_{Fc}** and the ferrocenecarboxylic acid solutions were recorded between 800 and 200 nm and the signal at 405 nm was integrated after baseline subtraction. The ferrocene surface concentration (Γ_{UV}) is calculated by dividing the specific ferrocene amount obtained from the UV-vis measurements by the specific surface area of the Stöber particles obtained from SEM measurements (A_{SEM}).

^[a] Equipment from AK Wesemann, Institut für Anorganische Chemie.

^[b] Equipment from AK Oelkrug, Institut für Physikalische Chemie.

Dip-coating

Silica particles **M1c** (200 mg) were suspended under ultrasonication for 1 h in 10 mL of ethanol/water (1:1). The pH of the suspension was raised to pH 10 with KOH. Pt spade electrodes were polished with alumina 0.05 μm and hydrophilized in nitric acid (30 %) for 1 h under ultrasonication. They were dipped in the suspension at 25 °C and drawn out of the suspension in the vertical axis at a speed of 60 $\mu\text{m s}^{-1}$ with a computer controlled stepper-motor (Limes 90 from Owis). The resulting electrode surface was investigated with scanning electron microscopy.

Gas chromatographic determination of Si–H content^[a] [108, 118]

All gas chromatographic measurements were performed on a Carlo Erba GC6000 Vega Series 2 (Model 6300) at an oven temperature of 90 °C. The gas chromatograph was equipped with two packed columns filled with molecular sieve, type 13X, mesh size 80/100. The signal was detected by a thermal conductivity detector HWD 430, operating at 100 °C and 250 °C at the body and the filament, respectively. Signals were recorded and subsequently integrated by an electronic integrator HP 3390A. Argon 5.0 was used as carrier gas.

Sample preparation: A 12 mL glass vial was filled with 10 mL of a 1 M solution of potassium hydroxide in ethanol. The silica sample material was weighed into a capless plastic reaction tube of about 0.5 mL, which was then placed in the glass vial avoiding contact between the silica sample and the reaction solution. The glass vial was closed with a rubber septum and an aluminum cap. It was then shaken in order to immerse the reaction tube with the silica sample into the reaction solution. After the vial was left in a water bath for one hour at 60 °C, it was allowed to cool to room temperature for 20 min. Afterwards, a 200 μl gas sample was taken by a gas-tight syringe using a Chaney adapter for improved reproducibility and injected immediately for GC-TCD analysis. The system was calibrated with liquid samples of Et_3SiH from 0.1 to 2.0 μl (about 0.6 to 12.5 μmol). The calibration samples were treated exactly as described above and the resulting integration values could be fitted linearly with a standard deviation of 11 %.

HPLC Column packing^[b]

The chromatographic sorbents **M2_{SiH}** and **M2_{C18}** were slurry-packed into 125 mm x 4.6 mm stainless steel columns from Bischoff at 35 MPa employing a Knauer pneumatic HPLC

^[a] performed by D. Joosten, AK Wesemann, Institut für Anorganische Chemie.

^[b] performed by B. Dietrich, AK Albert, Institut für Organische Chemie.

pump^[a]. Thus, 1.6 g of the modified silica were dispersed in 25 mL 2-propanol, by sonication in an ultrasonic bath for about 10 s. This suspension was poured into the reservoir of the packing system and the system was topped off. The column was downward packed with 2-propanol as solvent. The excess of stationary phase on the top of the column was carefully removed and finally the inlet frit and end-fitting were installed and the ends plugged. The columns were conditioned for 10 h with a methanol/water mobile phase at a flow rate of 0.1 mL min⁻¹.

HPLC tests^[b]

Chromatographic tests were performed at 23 °C using a series 1100 HPLC instrument^[a] (Agilent) with UV-detection at 210, 254 and 480 nm. All solvents were filtered and degassed before use. The test mixture (Standard Reference Material 870; SRM 870) [211, 212] was a methanolic solution of uracil, toluene, ethylbenzene, quinizarin and amitriptyline. The mobile phase was a gradient of 60 % methanol/ 40 % buffer (v/v) hold 5 min to 80 % methanol/ 20 % buffer (v/v) between 5 min to 6 min. The buffer, 20 mmol/l aqueous potassium phosphate, was adjusted to pH 7.0 ± 0.1 by mixing solutions of the dibasic and monobasic form of the buffer. The mobile phase had a flow rate of 2.0 mL min⁻¹.

Spontaneous adsorption and electrochemistry of **M1g_{Fc}**.

Material **M1g_{Fc}** (200 mg) was suspended under ultrasonication in dichloromethane (10 mL). Platinum disk electrodes (diameter $d = 3$ mm) were mirror polished with α -Al₂O₃ (0.05 μ m) and dipped into the suspension under light stirring for at least 1 h. The electrodes were not washed after removal from the suspension, in order to prevent the loss of adsorbed particles. The solvent remaining at the electrode tip was first allowed to dry in air and then under reduced pressure at RT. SEM pictures of the electrodes (magnification 5000 \times) were used to determine the surface concentration of particles on the platinum surface by measuring the surface area occupied by 500 silica particles. The total amount of particles immobilized on the electrode surface was obtained by multiplying the surface concentration of particles by the area of the electrode. Electrochemical experiments were performed as described above. Baseline correction of the voltammograms was done with Origin 6.0 before determination of formal potentials. The number of electrochemically accessible ferrocene units on the electrode surface is obtained from the area under the oxidation wave of the cyclic voltammogram [193]

^[a] Equipment from AK Albert, Institut für Organische Chemie.

^[b] performed by B. Dietrich, AK Albert, Institut für Organische Chemie.

at a scan rate of 0.02 V s^{-1} . The value of Γ_{CV} (on the silica particle surface) is obtained from the total number of electroactive ferrocene units and the number of silica particles on the electrode surface (see 6.2.3 and 8.3).

7.4 Synthetic procedures

Stöber particles (M1a - M1g). The concentrations and volumes of reactants and reagents used for the synthesis of the **M1** materials are summarized in Table 18. Isopropanol was used as solvent for the synthesis of the larger particles (**M1d** – **M1e**) while ethanol was used for the smaller ones (**M1a** - **M1c** and **M1f** - **M1g**). A mixture of the respective alcohol and water was heated to $45 \text{ }^\circ\text{C}$. After the temperature of the mixture was equilibrated for 1 h, aqueous ammonia (25%) and TEOS were quickly added under strong stirring. After 3 h at $45 \text{ }^\circ\text{C}$ under continued strong stirring, the resulting particles were separated by centrifugation and washed twice with water and once with ethanol using ultrasonication and centrifugation after each step. The particles were dried at $100 \text{ }^\circ\text{C}$ overnight and then at $600 \text{ }^\circ\text{C}$ in a tubular furnace under reduced pressure for 4 days. The silica surface was rehydroxylated by suspending the particles in 1 L of aqueous HCl (3%) under reflux for 1 h. After centrifugation, the silica was then washed twice with water and once with ethanol. Finally, it was dried overnight at $100 \text{ }^\circ\text{C}$.

Table 18: Experimental conditions for the preparation of silica particles.

| material | volume / mL | | | | concentration / M | | |
|---------------------------|-------------------|-------------------|--------------------------|----------------------|-------------------|--------------------|--------------------|
| | V_{TEOS} | V_{NH_3} | $V_{\text{H}_2\text{O}}$ | V_{Alcohol} | [TEOS] | [NH ₃] | [H ₂ O] |
| M1a | 22.3 | 15.4 | 129.6 | 330 ^[c] | 0.20 | 0.41 | 15.61 |
| M1b | 27.9 | 17.5 | 72 | 383 ^[c] | 0.25 | 0.47 | 9.30 |
| M1c | 27.9 | 17.5 | 72 | 383 ^[c] | 0.25 | 0.47 | 9.30 |
| M1d | 33.5 | 22 | 57.6 | 390 ^[d] | 0.30 | 0.58 | 8.00 |
| M1e ^[a] | 540 | 203.4 | 251.1 | 3600 ^[d] | 0.53 | 0.59 | 4.70 |
| M1f ^[b] | 84 | 52.5 | 216 | 1150 ^[c] | 0.25 | 0.47 | 9.30 |
| M1g | 27.9 | 17.5 | 72 | 383 ^[c] | 0.25 | 0.47 | 9.30 |

[a] prepared by Straub [83], [b] 3 times scale-up from the procedure of **M1b/M1c/M1g**,

[c] ethanol, [d] isopropanol.

[(2-Aminoethyl)carbamoyl]ferrocene (1a). The following procedure is a combination of and a simplification from the original references [178, 179, 230]. Ferrocenecarboxylic acid (1 g,

4.4 mmol) was suspended in dichloromethane (50 mL). Oxalyl chloride (1 mL, 12 mmol) was added dropwise to the suspension. The cloudy orange suspension became dark red and clear. After 30 min, the dichloromethane and the excess oxalyl chloride were removed under reduced pressure. The resulting red solid was then dissolved under argon in 30 mL of dry dichloromethane and added dropwise to a stirred solution of ethylene diamine (5 mL, 75 mmol) in dry dichloromethane (30 mL). After 1 h, the orange and turbid suspension was mixed with aq. KOH (10 %, w/w). The dichloromethane phase was recovered after separation from the aqueous phase. After filtration and elimination of the solid, dichloromethane was recovered and evaporated under reduced pressure. The remaining solid product was washed with ethyl acetate/hexane 1:9 and then dissolved in water. After filtration the water was recovered and evaporated. The orange product was dissolved in dichloromethane and the solution was filtrated again. After evaporation of the solvent, the orange product is dried under high vacuum conditions; resulting raw yield: 0.83 g (3 mmol, 70 %). Mp: 118.4 °C. ¹H-NMR (CDCl₃, 400.16 MHz): δ (ppm) 1.36 (2H, s, NH₂), 2.81 (2H, m, CH₂NH₂), 3.35 (2H, m, CH₂NH), 4.1 (5H, C₅H₅), 4.25 and 4.65 (4H, C₅H₄), 6.5 (1H, s, NH). ¹³C{¹H}-NMR (CDCl₃, 100.62 MHz): δ (ppm) 42.0 (CH₂NH₂), 42.5 (CH₂NH), 68.5–70.7 (ferrocene), 171 (C=O). IR (DRIFT): $\tilde{\nu}$ (cm⁻¹), 3300 (br, ν_{NH}), 3083 (s, ν_{CH} , Fc), 2926, 2862 (s, ν_{CH} , CH₂), 1647 (w, $\nu_{\text{C=C}}$, Fc), 1626 (s, $\nu_{\text{C=O}}$, amide I), 1541 (s, δ_{NH} , amide II), 1455 (w, δ_{CH} , CH₂). Anal. Calcd for C₁₃H₁₆N₂OFe: C, 57.38; H, 5.93; N, 10.29. Found: C, 56.63; H, 5.92; N, 9.73. (Lit.: C, 55.40; H, 6.16; N, 9.90 [179]). EI-MS: 70 eV (m/z): 272.1 (M⁺). E°(**1a**) = 166 mV vs Fc/Fc⁺ in CH₃CN.

[2-(Undec-10-enamido)ethyl]carbamoyl]ferrocene (1b). The ferrocene derivative **1a** (100 mg, 0.37 mmol) was dissolved in 10 mL of dry CH₂Cl₂ and 10-undecenoyl chloride (80 μL, 0.37 mmol) was added dropwise under argon. The reaction mixture was left 1 h under stirring at RT and then quenched with aqueous KOH (20 mL, 10 % w/w). The organic phase was recovered and the solvent was evaporated. The resulting orange oil was recovered and purified by column chromatography (stationary phase: silica type 60, mobile phase: acetone/CH₂Cl₂ 1/1) to give a yellow solid. After recrystallization from acetone, yellow crystals were obtained. Yield: 95 mg (0.22 mmol, 60 %). ¹H-NMR (CDCl₃, 400.16 MHz): δ (ppm) 1.17-1.37 (12H, m, CH₂), 1.57-1.69 (2H, m, CH₂), 2.01 (2H, m, CH₂=CH-CH₂), 2.20 (2H, t, CH₂-C=O), 3.49 (4H, m, -CH₂NH-), 4.18 (5H, C₅H₅), 4.33 and 4.79 (4H, t, C₅H₄), 4.94 (2H, m, CH₂=CH-), 5.78 (1H, m, CH₂=CH-) 7.32 and 7.52 (2H, s, NH). ¹³C{¹H}-NMR (CDCl₃, 100.62 MHz): δ (ppm) 25.65, 28.65, 28.84 and 29.10 (-CH₂-), 33.54 (=CH-CH₂-),

36.39 (CH₂-C=O), 39.66 and 40.18 (-CH₂NH), 68.18 (CH, C₅H₄, Fc), 69.56 (C₅H₅, Fc), 70.40 (CH, C₅H₄, Fc), 75.30 (C, C₅H₄, Fc), 113.97 (H₂C=CH-), 138.85 (H₂C=CH-), 171.89 and 175.06 (C=O). Anal. Calcd for C₂₄H₃₄N₂O₂Fe: C, 65.75; H, 7.82; N, 6.39. Found: C, 64.63; H, 7.85; N, 6.35. EI-MS: 70 eV (m/z): 438 (M⁺), 229 (FcCONH₂)⁺, 213 (FcC=O)⁺, 185 (Fc)⁺. E^o(**1b**) = 161 mV vs Fc/Fc⁺ in CH₂Cl₂.

N-oct-7-enylethylene-1,2-diamine (8). To a mixture of ethylenediamine (10 g, 0.17 mole) and 8-bromo-1-octene (97%, 3 g, 0.016 mole) was added sufficient absolute ethanol (50 mL) to dissolve the two immiscible liquids. The solution was refluxed for 3 h and ethanol was evaporated, causing the residual liquid to separate into 2 layers. The upper layer was recovered, 30 mL of water were added and the precipitated colorless solid was extracted with ether (3 × 25 mL). The combined organic phases were washed with water (2 × 50 mL), dried over anhydrous sodium sulfate and the solvent evaporated. A slightly yellow liquid is obtained; yield 2.2 g (13 mmol, 82 %). ¹H-NMR (CDCl₃, 400.16 MHz): δ (ppm) 1.15-1.40 (m 8H -CH₂-), 1.69 (s -NH₂), 2.00 (quartet 2H H₂C=CH-CH₂-), 2.55 (t 2H -NH-CH₂-), 2.62 (t 2H NH₂-CH₂-), 2.76 (t 2H -NH-CH₂-), 4.83 (s 1H -NH-), 4.85-5.0 (m 2H H₂C=CH-), 5.76 (m 1H H₂C=CH-). ¹³C{¹H}-NMR (CDCl₃, 100.62 MHz): δ (ppm), 27.13, 28.76, 28.94 and 30.01 (-CH₂-), 33.64 (H₂C=CH-CH₂-), 41.64 (NH₂-CH₂-), 49.82 and 52.44 (-NH-CH₂-), 114.13 (H₂C=CH-), 139.02 (H₂C=CH-). EI-MS: 70 eV (m/z): 171.2 (M + H⁺), 154.2 (-NH₃), 140.2 (-CH₂-NH₂).

(N-oct-7-enylethylene-1,2-diamine)dichlorobis[(methoxyethyl)diphenyl]phosphine

ruthenium(II) complex (2a). The diamine ligand **8** (85 mg, 0.5 mmol, 10 % excess) was dissolved in dry dichloromethane (25 mL) and the solution added dropwise to a stirred solution of **11** [231 - 233] (300 mg, 0.45 mmol) in dry dichloromethane (25 mL) under argon. A color change from red-brown to green is observed. After the reaction mixture had been stirred for another 45 min at room temperature, the volume of the solution was concentrated to about 2 mL under reduced pressure. After addition of 15 mL of petroleum ether (40-60), the solvent was evaporated under reduced pressure until the precipitation of a yellow solid occurred. The solid was separated from the remaining solvent, washed three times with 15 mL portions of cold petroleum ether (40-60), and dried under vacuum. Yield : 270 mg (0.32 mmol, 72 %) of a yellow powder. ¹H-NMR (CDCl₃, 400.16 MHz): δ (ppm) 0.6-1.35 (m 8H -CH₂-); 1.8-2.0 (m 4H H₂C=CH-CH₂-, -NH₂), 2.19 (s 1H NH), 2.3-3.3 (m, 14H, PCH₂, CH₂O, NH₂CH₂-, -NHCH₂-), 2.85 and 2.91 (2s 6H OCH₃), 4.80-5.0 (m 2H H₂C=CH-), 5.71 (m 1H

H₂C=CH-), 7.0-7.8 (m, 20H, C₆H₅). ¹³C{¹H}-NMR (CDCl₃, 100.62 MHz): δ (ppm), 24.5, 26.5 (2d, ¹J_{PC} = 27.08 Hz, PCH₂), 26.7, 28.6, 28.7 (-CH₂-), 33.55 (H₂C=CH-CH₂-), 42.5 (NH₂CH₂), 49.1, 51.9 (2s NHCH₂), 57.5, 57.6 (2s OCH₃), 69.0 (m CH₂O), 114.2 (H₂C=CH-), 128.0, 128.4 (2d, ³J_{PC} = 8.05 Hz, *m*-C₆H₅), 131.5, 132.0 (2d, ²J_{PC} = 8.1 Hz, *o*-C₆H₅), 131.9, 132.3 (2s *p*-C₆H₅), 134.15, 136.55 (2d, *i*-C₆H₅), 138.9 (H₂C=CH-). ³¹P{¹H}NMR (CDCl₃, 161.98 MHz): δ (ppm) 37.5 (d, AB, ²J_{pp} = 36.27 Hz), δ 34.3 (d, AB, ²J_{pp} = 36.28 Hz). FAB-MS (m/z): 830.4 (M⁺), 795.4 (M - Cl), 660.1 (M - diamine ligand), 393.1 (M - 2 etherphosphine ligands), 245.2 (Etherphosphine ligand). Anal. Calcd for C₄₀H₅₆Cl₂N₂O₂P₂Ru: C, 57.83; H, 6.79; N, 3.37. Found: C, 57.25; H, 6.91; N, 3.67. E°(2a) = -18 mV vs Fc/Fc⁺ in CH₂Cl₂.

4-Allylbromobenzene (4a). 4-Allylbromobenzene **4a** was prepared according to ref. [184]. bp: 55 °C/ 5 × 10⁻² mbar (Lit. bp 93 °C/18 mbar); yield: 5.6 g (28 mmol, 38 %). ¹H-NMR (CDCl₃, 400.16 MHz): δ (ppm) 3.32–3.39 (m 2H CH₂), 5.01–5.11 (m 2H H₂C=CH), 5.83–6.03 (m 1H H₂C=CH-), 7.06 (d, *J* = 8.5 Hz, 2H arom), 7.41 (d, *J* = 8.5 Hz, 2H arom). ¹³C{¹H}-NMR (CDCl₃, 100.62 MHz): δ (ppm) 39.46 (=CH-CH₂-), 116.21 (H₂C=CH-), 119.80 (C-Br, Ar), 130.27 (meta C), 131.36 (ortho C), 136.67(H₂C=CH), 137.50 (para C).

4'-Allyl-3,5-di-*tert*-butyl-1,1'-biphenyl-4-amine (3a). Magnesium turnings (0.11 g, 4.5 mmol) were flame dried with a hot gun under vacuum and suspended in 4 mL of dry THF. A solution of 1,4-allylbromobenzene **4a** (1.2 mL, 4.5 mmol) in dry THF (40 mL) was added dropwise to the magnesium suspension under argon atmosphere at RT. The reaction was started by slightly heating and addition of one drop of CCl₄. Once the solution became turbid, the heating was stopped, and the rest of **4a** was added so that the reaction sustained a gentle reflux. After addition of all **4a** and disappearance of the Mg turnings, a solution of vacuum-dried **5** (0.7 g, 3.2 mmol) dissolved in 15 mL of dry THF (15 mL) was added dropwise under argon. The reaction mixture was left under stirring at RT for 1 h and was then quenched with aq. sat. NH₄Cl solution (50 mL). The aqueous phase was removed and extracted with Et₂O (4 × 25 mL). The combined organic phases were concentrated and dried overnight with K₂CO₃. After evaporation of the solvent, a yellow oil is obtained. The oil was dissolved in a mixture of EtOH (3 mL) and acetone (7 mL). Zinc powder (0.1 g, 1.5 mmol) was added under stirring. The reaction mixture was cooled with an ice bath and conc. HCl (1 mL) was added dropwise. After 2 h of stirring, aq. NH₃ solution (25 %, 10 mL) was added. The aqueous phase was removed and extracted with Et₂O (3 × 25 mL). The combined organic phases were dried overnight with Na₂SO₄. After filtration and evaporation of the solvent, the brown-red oil was

dissolved in hexane. The precipitate was discarded and after evaporation of the solvent, the oil was recovered and purified by column chromatography (stationary phase: silica type 60, mobile phase: hexane/ethyl acetate 4/1) to give **3a** as a red-brown oil (0.31 g, 0.97 mmol, 30.2 %). $^1\text{H-NMR}$ (CDCl_3 , 400.16 MHz): δ (ppm) 1.44 (s 18H CH_3), 3.34 (d, 2H, $J = 6.61$ Hz, $\text{H}_2\text{C}=\text{CH}-\text{CH}_2$), 4.15 (s 2H NH_2), 5.0-5.1 (m 2H $\text{H}_2\text{C}=\text{CH}$ -), 5.9 - 6.00 (m 1H $\text{H}_2\text{C}=\text{CH}$ -), 7.13 (d, $J = 8.14$ Hz, 2H arom), 7.34 (s 2H arom), 7.39 (d, $J = 8.14$ Hz, 2H arom). $^{13}\text{C}\{^1\text{H}\}$ -NMR (CDCl_3 , 100.62 MHz): δ (ppm) 30.22 ($-\text{CH}_3$), 34.56 ($=\text{CH}-\text{CH}_2-$), 39.85 ($-\text{C}(\text{CH}_3)_3$), 115.67 ($\text{H}_2\text{C}=\text{CH}$ -), 123.82 (CH, Ar- NH_2), 126.77, 128.74 (CH, Ar), 129.89 (para C, Ar- NH_2), 134.32 ($\text{C}-\text{C}(\text{CH}_3)_3$), 137.59 ($\text{H}_2\text{C}=\text{CH}$ -), 137.64, 140.52 (C, Ar), 143.04 (C- NH_2). EI-MS: 70 eV (m/z): 321.2 (M^+), 306.2 ($-\text{CH}_3$), 281.2 ($-\text{C}_3\text{H}_5$), 266.2 ($-t\text{-Bu}$).

1-Bromo-4-(pent-4-enyl)-benzene (4b). Magnesium turnings (1.03 g, 42 mmol) were flame dried under vacuum and suspended in 20 mL of dry Et_2O . A solution of 5-bromopent-1-ene (4.1 mL, 35 mmol) in dry Et_2O (10 mL) was added slowly to the magnesium suspension under argon atmosphere at RT. The reaction was slightly exotherm and the suspension became turbid. After complete addition, the suspension was stirred under reflux at 40 °C for 90 min. The solution was then separated from the remaining magnesium and added dropwise under argon at RT to a solution of 1,4-dibromobenzene (9.7 g, 41 mmol) and 1,1'-bis(diphenyl-phosphino)-ferrocene-palladium(II)chloride (0.41 g, 0.47 mmol) in dry THF (10 mL). After a few minutes a color change from red to yellow is observed. The reaction mixture is stirred under reflux at 70 °C overnight. A mixture of a white (MgBr_2) and a yellow precipitates (catalyst) and a colorless solution are obtained. The reaction is quenched with aqueous NH_4Cl (saturated, 20 mL) and extracted with pentane (3×20 mL). The combined organic phases were filtered over silica (type 60) and concentrated under vacuum. The resulting yellow liquid was cooled down to -18 °C to crystallize the unreacted 1,4-dibromobenzene. The liquid was recovered and purified by column chromatography (stationary phase: silica type 60, mobile phase: hexane) to give a colorless liquid, 1-bromo-4-(pent-4-enyl)-benzene (1.35 g, 6 mmol, 17.1 %). $^1\text{H-NMR}$ (CDCl_3 , 400.16 MHz): δ (ppm) 1.68 (m 2H $-\text{CH}_2-\text{CH}_2-\text{CH}_2-$), 2.07 (q 2H $=\text{CH}-\text{CH}_2-\text{CH}_2-$), 2.57 (t 2H $-\text{CH}_2-\text{CH}_2-\text{Ar}$), 4.99 (m 2H $\text{H}_2\text{C}=\text{CH}$ -), 5.81 (m 1H $\text{H}_2\text{C}=\text{CH}$ -), 7.04 (d 2H arom. *meta* H), 7.38 (d 2H arom. *ortho* H). $^{13}\text{C}\{^1\text{H}\}$ -NMR (CDCl_3 , 100.62 MHz): δ (ppm) 30.38 ($-\text{CH}_2-\text{CH}_2-\text{CH}_2-$), 33.08 ($=\text{CH}-\text{CH}_2-\text{CH}_2-$), 34.62 ($\text{CH}_2-\text{CH}_2-\text{Ar}$), 114.89 ($\text{H}_2\text{C}=\text{CH}$ -), 119.37 (Ar-Br), 130.18 (*meta* C), 131.28 (*ortho* C), 138.28 ($\text{H}_2\text{C}=\text{CH}$), 141.33 (*quart* C). EI-MS: 70 eV (m/z): 224.1/226.1 (M^+), 182.0/184.0 ($-\text{C}_3\text{H}_5$), 169.0/171.0 ($-\text{C}_4\text{H}_7$), 155.0/157.0 ($-\text{C}_5\text{H}_9$).

3,5-Di-tert-butyl-4-imino-1-(4-pent-4-enylphenyl)cyclohexa-2,5-dien-1-ol (6b).

Magnesium turnings (0.24 g, 9.9 mmol) were flame dried under vacuum and suspended in 10 mL of dry THF under argon. **4b** (1.35 g, 6 mmol) dissolved in 20 mL of dry THF was added dropwise to the magnesium turnings under argon. After 5 mL of **4b** was added, the suspension was heated to 50 °C in order to start the reaction. Once the solution became turbid, the heating was stopped, and the rest of **4b** was added so that the reaction sustained a gentle reflux. After addition of all the **4b**, the reaction mixture was heated to reflux for 3 h. The solution was then allowed to cool to RT, and if necessary, separated from the remaining Mg turnings with a pipette. The Grignard product was immediately used for the next step. Vacuum-dried **5** (0.57 g, 2.6 mmol), was dissolved in dry THF (15 mL) under argon and added dropwise to the Grignard mixture under argon. The reaction mixture was left under stirring at RT for 1 h and was then quenched with aq. sat. NH₄Cl solution (50 mL). The aqueous phase was removed and extracted with Et₂O (4 × 25 mL). The combined organic phases were concentrated and dried over night with K₂CO₃. After evaporation of the solvent, a brown-red oil is obtained. The oil is dissolved in 5 mL of hexane and filtered through a short silica column. The silica was washed with hexane (100 mL), resulting in the elution of the unreacted **4b**, which was recovered after evaporation of the solvent. The product, that remained adsorbed on the silica, was eluted with ethyl acetate (100 mL). After evaporation of the solvent, the product was purified by column chromatography (stationary phase: silica type 60, mobile phase: hexane/ethyl acetate 9/1) to give **6b** as a red oil, (0.44 g, 1.2 mmol, 46 %). ¹H-NMR (CDCl₃, 400.16 MHz): δ (ppm) 1.31 (s 18H CH₃), 1.70 (m 2H -CH₂-CH₂-CH₂), 2.08 (q 2H H₂C=CH-CH₂), 2.59 (t 2H -CH₂-Ar), 4.95 - 5.05 (m 2H H₂C=CH-), 5.77 - 5.87 (m 1H H₂C=CH-), 6.23 (s 2H CH of the cyclo-hexadiene ring), 7.12 (d *J* = 8.0 Hz, 2H arom), 7.30 (d *J* = 8.0 Hz, 2H arom), 10.02 (s 1H =NH). ¹³C{¹H}-NMR (CDCl₃, 100.62 MHz): δ (ppm) 30.44 (-CH₂-CH₂-Ar), 30.59 (CH₃), 33.25 (CH₂=CH-CH₂-), 34.84 (-C(CH₃)₃), 34.85 (-CH₂-Ar), 71.80 (C-OH), 114.71 (H₂C=CH-), 125.02, 128.58 (CH, Ar), 136.16 (CH of the cyclohexadiene ring), 138.5 (H₂C=CH), 140.33, (CH₂-C, Ar), 141.52 (COH-C, Ar), 143.71 (C-C(CH₃)₃), 167.10 (C=NH). EI-MS: 70 eV (m/z): 365 (M⁺), 348.2 (- OH), 308.2 (- OH - C₃H₅).

3,5-Di-tert-butyl-4'-pent-4-enyl-1,1'-biphenyl-4-amine (3b). The iminochinol **6b** (0.44 g, 1.2 mmol) was dissolved in Et₂O (30 mL) and zinc powder (0.08 g, 1.22 mmol) was added under stirring. The reaction mixture was cooled with an ice bath and conc. HCl (1.2 mL) was added dropwise. After 2 h of stirring, aq. NH₃ (25 %, 4 mL) was added. The aqueous phase was removed and extracted with Et₂O (3 × 25 mL). The combined organic phases were dried

over night with Na_2SO_4 . After filtration and evaporation of the solvent, the brown-red oil was dissolved in hexane. The precipitate was discarded and after evaporation of the solvent, the oil was recovered and purified by column chromatography (stationary phase: silica type 60, mobile phase: hexane/ethyl acetate 4/1) to give **3b** as a red-brown oil (0.2 g, 0.57 mmol, 48 %). $^1\text{H-NMR}$ (CDCl_3 , 400.16 MHz): δ (ppm) 1.44 (s 18H CH_3), 1.68 (m 2H $-\text{CH}_2-\text{CH}_2-\text{Ar}$), 2.06 (q 2H $\text{H}_2\text{C}=\text{CH}-\text{CH}_2$), 2.57 (t 2H $-\text{CH}_2-\text{Ar}$), 4.17 (s 2H NH_2), 4.8-5.0 (m 2H $\text{H}_2\text{C}=\text{CH}-$), 5.7 – 5.8 (m 1H $\text{H}_2\text{C}=\text{CH}-$), 7.13 (d, $J = 8.0$ Hz, 2H arom), 7.34 (s 2H arom), 7.37 (d, $J = 8.0$ Hz, 2H arom). $^{13}\text{C}\{^1\text{H}\}$ -NMR (CDCl_3 , 100.62 MHz): δ (ppm) 30.25 (CH_3), 30.63 ($-\text{CH}_2-\text{CH}_2-\text{Ar}$), 33.35 ($\text{CH}_2=\text{CH}-\text{CH}_2-$), 34.57 ($-\text{C}(\text{CH}_3)_3$), 34.92 ($-\text{CH}_2-\text{Ar}$), 114.65 ($\text{H}_2\text{C}=\text{CH}-$), 123.80 (CH, Ar- NH_2), 126.63, 128.63 (CH, Ar), 130.00 (para C, Ar- NH_2), 134.33 ($\text{C}-\text{C}(\text{CH}_3)_3$), 138.69 ($\text{H}_2\text{C}=\text{CH}$), , 140.08, 140.14 (C, Ar), 142.97 (C- NH_2). EI-MS: 70 eV (m/z): 349.2 (M^+), 334.0 ($-\text{CH}_3$), 308.0 ($-\text{C}_3\text{H}_5$).

1-Bromo-4-pentylbenzene (4c). Magnesium turnings (0.5 g, 20 mmol) were flame dried under vacuum and suspended in 4 mL of dry THF. A solution of 1,4-dibromobenzene (4.7 g, 20 mmol) in dry THF (20 mL) was added slowly to the magnesium suspension under argon atmosphere at RT. If the reaction did not start after the addition of a few drops, the suspension was slightly heated. Turbidity and coloration of the solution indicated the start of the reaction. After the addition of all the 1,4-bromobenzene, the suspension was stirred until it had cooled to RT. A catalytic amount of CuBr, codissolved with LiBr, in 1 mL of dry THF was added. Subsequently, 1-bromopentane (2.5 ml, 20 mmol) was added dropwise under argon. The reaction was started by slightly heating the suspension. The reaction mixture was stirred at RT overnight and quenched by the addition of aq. sat. NH_4Cl solution until pH 7 was reached. The reaction mixture became blue and was then extracted with Et_2O (3×6 mL). The combined organic phases were washed with a 0.5 N $\text{Na}_2\text{S}_2\text{O}_4$ solution and dried with MgSO_4 . After filtration and evaporation of the solvent, the oil was recovered and purified by column chromatography (stationary phase: silica type 60, mobile phase: hexane) to give a colorless liquid, **4c** (0.72 g, 3.2 mmol, 16 %). $^1\text{H-NMR}$ (CDCl_3 , 400.16 MHz): δ (ppm) 0.85 (m 3H CH_3), 1.24 (m 4H $-\text{CH}_2-$), 1.51 (m 2H $-\text{CH}_2-\text{CH}_2-\text{Ar}$), 2.48 (m 2H $-\text{CH}_2-\text{Ar}$), 7.00 (d, 2H arom. meta H), 7.30 (d 2H arom. ortho H). $^{13}\text{C}\{^1\text{H}\}$ -NMR (CDCl_3 , 100,62 MHz): δ (ppm), 13.98 (CH_3), 22.49 (CH_3-CH_2-) 30.98 and 31.35 ($-\text{CH}_2-$), 35.29 (CH_2-Ar), 119.24 (C-Br), 130.13 (*meta* C), 131.22 (*ortho* C) 137.81 (*quart* C). The signals for 1,4-bromobenzene are also present in both NMR spectra. EI-MS: 70 eV (m/z): 226.1/228.1 (M^+), 169.0/171.0 (M - C_4H_9), 155.0/157.0 (M - C_5H_{11}).

3,5-Di-*tert*-butyl-4'-pentyl-1,1'-biphenyl-4-amine (3c). Magnesium turnings (0.08 g, 3.2 mmol) were flame dried under vacuum and suspended in 2 mL of dry THF under argon. 1-Bromo-4-pentylbenzene **4c** (0.72 g, 3.2 mmol) dissolved in 10 mL of dry THF was added dropwise to the magnesium turnings under argon. Before all **4c** was added, the suspension was heated to 50 °C in order to start the reaction. Once the solutions became brown and turbid, the heating was stopped, and the rest of **4c** was added. The reaction mixture was then stirred at RT for 2 h. The Grignard product was immediately used for the next step. Vacuum-dried **5** (0.72 g, 3.2 mmol), was dissolved in dry THF (5 mL) under argon and added dropwise to the Grignard mixture under argon. The reaction mixture was stirred at RT for 2 h and was then quenched with aq. sat. NH₄Cl solution (50 mL). The aqueous phase was removed and extracted with Et₂O (4 × 25 mL). The combined organic phases were concentrated and dried over night with K₂CO₃. After evaporation of the solvent, a brown-red oil was obtained. The oil was then dissolved in Et₂O (30 mL) and zinc powder (0.2 g, 3.2 mmol) was added under stirring. The reaction mixture was cooled with an ice bath and conc. HCl (3.5 mL) was added dropwise. After 2 h of stirring, cold aq. NH₃ (25 %, 10 mL) was added. The aqueous phase was removed and extracted with Et₂O (3 × 25 mL). The combined organic phases were dried over night with Na₂SO₄. After filtration and evaporation of the solvent, the resulting brown-red oil was dissolved in hexane. The precipitate was eliminated and after evaporation of the solvent, the oil was recovered and purified by column chromatography (stationary phase: silica type 60, mobile phase: hexane/ethyl acetate 4/1) to give **3c** as a red-brown oil (0.22 g, 0.63 mmol, 19.8 %). ¹H-NMR (CDCl₃, 400,16 MHz): δ (ppm) 0.83 (s 3H CH₃-CH₂-), 1.28 (m 4H CH₂), 1.43 (s 18H C-CH₃), 1.55 (m 2H -CH₂-CH₂-Ar), 2.51 (m 2H -CH₂-Ar), 4.13 (s 2H NH₂), 7.14 (d, *J* = 8.0 Hz, 2H arom), 7.34 (s, 2H, arom), 7.38 (d, *J* = 8.0 Hz, 2H arom). ¹³C{¹H}-NMR (CDCl₃, 100,62 MHz): δ (ppm) 14.02 (CH₃-CH₂-), 22.55 (CH₃-CH₂-), 30.20 (-C(CH₃)₃), 31.24 and 31.56 (-CH₂-), 34.47 (-CH₂-Ar), 35.53 (-C(CH₃)₃), 123.70 (CH, Ar-NH₂), 126.51, 128.18 (CH, Ar), 130.01 (para C, Ar-NH₂), 134.19 (C-C(CH₃)₃), 139.93, 140.42 (C, Ar), 142.88 (C-NH₂). EI-MS: 70 eV (m/z): 351.2 (M⁺), 336.0 (- CH₃), 294.2 (- C₄H₉). E°(**3c**) = 427.9 mV vs Fc/Fc⁺ in CH₂Cl₂.

3,5-Di-*tert*-butyl-4-iminocyclohexa-2,5-dien-1-one (5). The iminoquinone **5** was prepared according to [190 - 192], followed by recrystallization from petrolether (60-90). The resulting bright yellow crystals (0.1 g, 0.46 mmol, 13 % yield) were dried under reduced pressure. mp 80.2 °C (Lit. 83 °C [191]). ¹H-NMR (CDCl₃, 400,16 MHz): δ (ppm) 1.34 (s 9H C-CH₃), 1.37 (s 9H C-CH₃), 6.29 (s 1H CH), 6.42 (s 1H CH), 11.36 (s 1H NH). ¹³C{¹H}-NMR (CDCl₃,

100.62 MHz): δ (ppm) 30.58 (-C(CH₃)₃), 31.06 (-C(CH₃)₃), 34.91 (-C(CH₃)₃), 36.81 (-C(CH₃)₃), 127.08 (CH), 128.04 (CH), 155.57 (C-C(CH₃)₃), 162.35 (C-C(CH₃)₃), 166.19 (C=NH), 188.60 (C=O). EI-MS: 70 eV (m/z): 219.2 (M⁺), 204.2 (-CH₃), 176.2. Anal. Calcd for C₁₄H₂₁NO: C, 76.67; H, 9.65; N, 6.39. Found: C, 76.40; H, 9.83; N, 5.82.

Si-H modified silica (M_{SiH}). The silica material (10 g) is placed in a quartz tube with a quartz frit located in its middle. The quartz tube is mounted vertically in a tubular oven (Figure 40). The bottom part of the quartz tube is connected to a 100 mL round bottom flask with gas connection, containing 15 mL of thionyl chloride. The connection between the round bottom flask and the quartz tube is closed and the top part of the quartz tube is connected to vacuum ($\sim 10^{-2}$ mbar). The silica is then heated to 200 °C under vacuum for at least 6 h. Under vacuum the temperature is raised from 200 to 800 °C in 4 h and then kept at 800 °C for another 6 hours. Subsequently, the connection to vacuum is closed and the quartz tube is flushed from the bottom with argon, bypassing the round bottom flask filled with SOCl₂. Once the argon pressure has equilibrated, the top of the quartz tube is connected to a water bubbler for evacuation of the exhaust gas. The argon flow fluidizes the silica, which approximately doubles in volume. The argon is then driven through the flask with thionyl chloride which is stirred and heated to 60 °C with a water bath. Within 3 h the argon flux has driven all the thionyl chloride through the silica still heated to 800 °C. 15 min after all the thionyl chloride has evaporated, the gas flow is changed to pass through the flask by-pass, argon is replaced by hydrogen and the temperature of the oven is raised to the desired value, typically 900 °C. After 2 h, the valve at the top of the quartz tube is closed, the hydrogen flow is stopped and the resulting M_{SiH} material is allowed to cool down under a hydrogen atmosphere.

M1_{SiH}.

Diameter = 212 nm (from DLS), 209 ± 14 nm (from SEM). $A_{\text{BET}} = 16.9 \text{ m}^2 \text{ g}^{-1}$. IR (DRIFT): $\tilde{\nu}$ (cm⁻¹), 3748 (isolated $\nu_{\text{SiO-H}}$, weak), 2265 ($\nu_{\text{Si-H}}$, broad), 1870 ($\nu_{\text{Si-O-Si}}$), 1300 – 1000 ($\nu_{\text{Si-O-Si}}$).

M2_{SiH}. Diameter = 5.8 ± 0.7 μm (from SEM). $A_{\text{BET}} = 103.6 \text{ m}^2 \text{ g}^{-1}$. ²⁹Si CP/MAS NMR: δ (ppm) -100.8 (Q³), -83.7 (T³_H). IR (DRIFT): $\tilde{\nu}$ (cm⁻¹), 3748 (isolated $\nu_{\text{SiO-H}}$, weak), 2286 ($\nu_{\text{Si-H}}$, strong), 1870 ($\nu_{\text{Si-O-Si}}$), 1300 – 1000 ($\nu_{\text{Si-O-Si}}$).

M3_{SiH}. $A_{\text{BET}} = 172.6 \text{ m}^2 \text{ g}^{-1}$. ²⁹Si CP/MAS NMR: δ (ppm) -100.7 (Q³), -83.8 (T³_H). IR (DRIFT): $\tilde{\nu}$ (cm⁻¹), 3743 (isolated $\nu_{\text{SiO-H}}$, weak), 2285 ($\nu_{\text{Si-H}}$, strong), 1870 ($\nu_{\text{Si-O-Si}}$), 1300 – 1000 ($\nu_{\text{Si-O-Si}}$).

M4_{SiH}. $A_{\text{BET}} = 301.6 \text{ m}^2 \text{ g}^{-1}$. ^{29}Si CP/MAS NMR: δ (ppm) -100.1 (Q^3), -83.5 (T^3_{H}). IR (DRIFT): $\tilde{\nu}$ (cm^{-1}), 3746 (isolated $\nu_{\text{SiO-H}}$, weak), 2283 ($\nu_{\text{Si-H}}$, strong), 1870 ($\nu_{\text{Si-O-Si}}$), 1300 – 1000 ($\nu_{\text{Si-O-Si}}$).

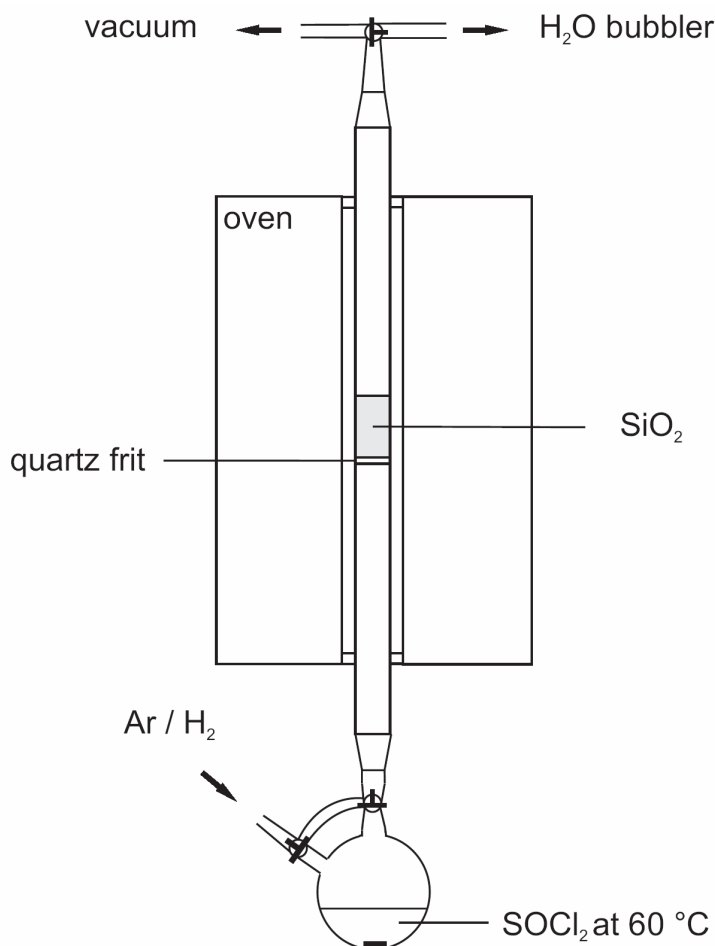


Figure 40: Experimental set-up for the chlorination and reduction of the silica materials.

Preparation of M2_A and M2_B. For the preparation of **M2_{SiHA}**, **M2** was heated from room temperature to $1000\text{ }^\circ\text{C}$ in 5 h with the set-up shown in Figure 40 under hydrogen gas flow. The temperature was kept at $1000\text{ }^\circ\text{C}$ for 2 h and the silica was then allowed to cool to room temperature under hydrogen atmosphere. For **M2_B** the same procedure as for **M_{SiH}** is performed, modified, however, by omitting the chlorination step.

M2_A. IR (DRIFT): $\tilde{\nu}$ (cm^{-1}), 3746 (isolated $\nu_{\text{SiO-H}}$, weak), 2288 ($\nu_{\text{Si-H}}$, medium), 1870 ($\nu_{\text{Si-O-Si}}$), 1300 – 1000 ($\nu_{\text{Si-O-Si}}$).

M2_B. IR (DRIFT): $\tilde{\nu}$ (cm^{-1}), 3748 (isolated $\nu_{\text{SiO-H}}$, strong), 2290 ($\nu_{\text{Si-H}}$, medium), 1870 ($\nu_{\text{Si-O-Si}}$), 1300 – 1000 ($\nu_{\text{Si-O-Si}}$).

Triethoxysilane modified silica (M_{TES}). Material **M1g** or **M2** (2 g) was dried overnight at 100 °C under reduced pressure and then suspended in dry toluene (30 mL). Triethoxysilane (500 μ L, 2.7 mmol) was added and the suspension was heated under reflux for 24 h. The resulting silica (M_{TES}) was washed with toluene and twice with ethanol and then dried under reduced pressure at 100 °C.

M1g_{TES}. IR (DRIFT): $\tilde{\nu}$ (cm^{-1}), 3800–2600 ($\nu_{\text{SiO-H}}$, strong), 2250 ($\nu_{\text{Si-H}}$, strong), 1870 ($\nu_{\text{Si-O-Si}}$), 1650 (hydrogen bonded H_2O on SiOH), 1200–1000 ($\nu_{\text{Si-O-Si}}$).

M2_{TES}. $A_{\text{BET}} = 115 \text{ m}^2 \text{ g}^{-1}$. ^{29}Si CP/MAS NMR: δ (ppm) -110.2 (Q^4), -100.2 (Q^3), -84.0 (T^3_{H}), -73.3 (T^2_{H}). IR (DRIFT): $\tilde{\nu}$ (cm^{-1}), 3800 – 2600 ($\nu_{\text{SiO-H}}$, strong), 2983, 2939, 2904 (ν_{CH}), 2243 ($\nu_{\text{Si-H}}$, strong), 1870 ($\nu_{\text{Si-O-Si}}$), 1650 (hydrogen bonded H_2O on SiOH), 1200 – 1000 ($\nu_{\text{Si-O-Si}}$).

10-Undecylenic acid modified silica (M_{COOH}). The hydride modified silicas **M1f_{SiH}**, **M1g_{TES}** or **M4_{SiH}** (500 mg) were dried under reduced pressure at 100 °C overnight and suspended under ultrasonication for 1 h in dry hexane (25 mL). The suspension was then mixed with 10-undecylenic acid (500 μ L, 2.5 mmol) in a 250 mL quartz flask and degassed by argon bubbling for 30 min. The suspension was irradiated with a 700 W medium pressure mercury lamp for 4 to 8 days. No filters were employed. The distance between the quartz flask and the UV lamp as well as the intensity of the UV light were adjusted so that the temperature of the suspension did not exceed 40 °C during the reaction. Silicas M_{COOH} were separated from the solution by centrifugation, washed with hexane, ethanol, acetic acid and again with ethanol, and dried overnight under reduced pressure at room temperature. ^{13}C CP/MAS NMR: δ 14.0 (Si- CH_2), 20–50 (CH_2 , broad), 180 ($-\text{COOH}$). IR (DRIFT): $\tilde{\nu}$ (cm^{-1}), 2923 and 2857 (m, ν_{CH} , CH_2), 2250 (w, ν_{SiH}), 1708 (m, $\nu_{\text{C=O}}$), 1455 (w, ν_{CH}).

10-undecylenic acid after the reaction: ^1H -NMR (CDCl_3 , 400.16 MHz): δ (ppm) 1.22 (m 10H $-\text{CH}_2-$), 1.55 (m 2H $\text{CH}_2-\text{CH}_2-\text{COOH}$), 1.96 (m 2H $\text{CH}_2=\text{CH}-\text{CH}_2-$), 2.26 (t 2H CH_2-COOH), 4.84–9.95 (m 2H $\text{CH}_2=\text{CH}-$), 5.66–5.78 (m 1H $\text{CH}_2=\text{CH}-$), 11.84 (br s 1H COOH). $^{13}\text{C}\{^1\text{H}\}$ -NMR (CDCl_3 , 100.62 MHz): δ (ppm), 24.55 ($\text{CH}_2-\text{CH}_2-\text{COOH}$), 28.81, 28.95, 28.97, 29.11, 29.19 ($-\text{CH}_2-$), 33.70 ($\text{CH}_2=\text{CH}-\text{CH}_2-$), 34.04 (CH_2-COOH), 114.07($\text{CH}_2=\text{CH}-$), 138.93 ($\text{CH}_2=\text{CH}-$), 180.64 (COOH).

1-Octadecene modified silica (M_{C18}). Hydride modified silica **M2_{SiH}** (2 g) was dried under vacuum at 100 °C and suspended in neat 1-octadecene (50 mL, 90 %). The suspension was heated to 180 °C under stirring for 3 days. After the reaction, the silica was separated from the

solvent by centrifugation and washed with hexane in a Soxhlet apparatus overnight. Finally, the silica was dried overnight under vacuum at 110 °C. ^{13}C CP/MAS NMR (50.32 MHz): δ (ppm) 12.42 (br, Si-CH₂, -CH₃), 22-35 (-CH₂-). IR (DRIFT): $\tilde{\nu}$ (cm⁻¹), 3760 – 3550 (w, ν_{OH} , SiOH), 2960 (m, ν_{CH} , CH₃), 2927, 2857 (s, ν_{CH} , CH₂), 2279 (s, ν_{SiH}), 1870 (m, $\nu_{\text{Si-O-Si}}$), 1466 (w, $\delta_{\text{C-H}}$) 1200 – 1000 ($\nu_{\text{Si-O-Si}}$). Elemental analysis: C = 3.36 %

Recovered 1-octadecene after the reaction: ^1H -NMR (CDCl₃, 400.16 MHz): δ (ppm) 0.91 (t 3H CH₃), 1.29 (m 26H -CH₂-), 1.41 (m 2H -CH₂-), 2.07 (m 2H CH₂=CH-CH₂-), 4.94-5.04 (m 2H CH₂=CH-), 5.79-5.89 (m 1H CH₂=CH-). $^{13}\text{C}\{^1\text{H}\}$ -NMR (CDCl₃, 100.62 MHz): δ (ppm), 14.13 (-CH₃), 22.73 (-CH₂-CH₃), 28.99, 29.21, 29.42, 29.57, 29.68, 29.75 (-CH₂-), 31.98 (-CH₂-CH₂-CH₃), 33.87 (CH₂=CH-CH₂-), 114.07 (CH₂=CH-), 139.23 (CH₂=CH-).

1,7-Octadiene modified silica (M2_{C=C}). Hydride modified silica M2_{SiH} (2 g) was dried under vacuum at 100 °C and suspended in 1,7-octadiene (20 mL) diluted in dry hexadecane (30 mL). The suspension was heated to 180 °C under stirring for 3 days. After the reaction, the silica was separated from the solvent by centrifugation and washed twice with each of the following solvents at about 50 °C: cyclohexane, hexane and ethanol. Finally the silica was dried overnight under vacuum at 110 °C. ^{13}C CP/MAS NMR (50.32 MHz): δ (ppm) 9.52 (Si-CH₂, -CH₃), 20-40 (-CH₂-), 111.93 (CH₂=CH-), 139.15 (CH₂=CH-). IR (DRIFT): $\tilde{\nu}$ (cm⁻¹), 3800 – 2600 (w, ν_{OH} , SiOH), 3077 (w, ν_{CH} , C=C-H), 2926, 2861 (s, ν_{CH} , CH₂), 2264 (s, ν_{SiH}), 1870 (m, $\nu_{\text{Si-O-Si}}$), 1647 (w, $\nu_{\text{C=C}}$), 1450 (w, δ_{CH}) 1200 – 1000 ($\nu_{\text{Si-O-Si}}$). Elemental analysis: C = 5.57 %.

Recovered 1,7-octadiene in hexadecane after the reaction: ^1H -NMR (CDCl₃, 400.16 MHz): δ (ppm) 0.95 (t, $^3J_{\text{HH}} = 6.87$ Hz, 6H CH₃, hexadecane), 1.33 (m 28H CH₂, hexadecane), 1.47 (m 4H -CH₂-), 2.11 (m 4H CH₂=CH-CH₂-), 4.94-5.14 (m 4H CH₂=CH-), 5.65-5.85 (m 2H CH₂=CH-). $^{13}\text{C}\{^1\text{H}\}$ -NMR (CDCl₃, 100.62 MHz): δ (ppm), 14.11 (CH₃, hexadecane), 22.80, 29.51, 29.81, 29.85, 32.06 (CH₂, hexadecane), 28.50 (CH₂), 33.74 (CH₂=CH-CH₂-), 114.31(CH₂=CH-), 138.83 (CH₂=CH-).

Triethylhexyn-1-ylsilane (9). A solution of 1-hexyne (3 mL, 26 mmol) in dry THF (60 mL) was cooled to 0 °C and n-butyllithium (2.7 M in heptane, 3 mL, 8.1 mmol) was slowly added under stirring. The solution was left to equilibrate to RT for 15 min. Triethylsilane (3 mL, 19 mmol) was then added and the solution was heated to reflux for 6 days. The reaction mixture was quenched with aq. sat. NH₄Cl solution (100 mL). The aqueous phase was separated and extracted with Et₂O (3 × 25 mL). The combined organic phases were concentrated and the

residual liquid was distilled under reduced pressure using a Vigreux column. A clear liquid (2.5 mL) was obtained as the main fraction at 125 °C/ 3 mbar. Yield: 2.43 g (12.4 mmol, 69 %). ^1H NMR (400 MHz, CDCl_3): δ (ppm) 0.57 (q, 6H, Si- CH_2 - CH_3), 0.91 (t, 3H, Si- CH_2 - CH_3), 0.98 (t, 9H, CH_2 - CH_2 - CH_3), 1.35-1.55 (m, 4H, CH_2), 2.24 (t, 2H). $^{13}\text{C}\{^1\text{H}\}$ NMR (100.62 MHz, CDCl_3): δ (ppm) 4.6 (Si- CH_2 - CH_3 , $^1\text{J}(^{13}\text{C}-^{29}\text{Si}) = 56.4$ Hz), 7.4 (Si- CH_2 - CH_3), 13.5 (CH_2 - CH_2 - CH_3), 19.5 (CH_2), 21.8 (CH_2), 30.9 (C- CH_2), 81.2 (Si- $\text{C}\equiv\text{C}$, $^1\text{J}(^{13}\text{C}-^{29}\text{Si}) = 82.7$ Hz), 108.6 (Si- $\text{C}\equiv\text{C}$, $^2\text{J}(^{13}\text{C}-^{29}\text{Si}) = 14.6$ Hz). ^{29}Si NMR (49.69 Hz, CDCl_3): δ (ppm) 8.65. MS (EI): m/z : 196.1 (M^+), 167.1 (- Et), 139.1 (- Bu), 111.1, 97.1. IR (KBr, cm^{-1}): 2954, 2934, 2912, 2874 (s, ν_{CH}), 2173 (s, $\nu_{\text{C}\equiv\text{C}}$), 1628 (br), 1457 (m), 1237 (m), 1013 (s), 973, 953 (m), 722 (s). Anal. Calcd for $\text{C}_{12}\text{H}_{24}\text{Si}$: C, 73.38; H, 12.32. Found: C, 73.30; H, 12.40.

Kinetic experiment - triethylhexyn-1-ylsilane (9). A solution of 1-hexyne (10 mL, 87 mmol) and hexadecane (0.5 mL, 1.7 mmol) in dry THF (60 mL) was cooled to 0 °C and *n*-butyllithium (2.7 M in heptane, 10 mL, 27 mmol) was slowly added under stirring. The solution was left to equilibrate to RT for 15 min. Triethylsilane (10 mL, 62 mmol) was then added and the solution was heated to reflux. Aliquots (~ 2 mL) were taken from the reaction mixture and immediately quenched with an aq. sat. NH_4Cl solution (5 mL). The time of quenching was recorded for each aliquot. The aqueous phase was removed and extracted with Et_2O (3×5 mL). The combined organic phases were concentrated under reduced pressure (3×10^{-2} bar at 40 °C) and the residual liquid was investigated with ^1H NMR spectroscopy. The integration of the resonance from hexadecane was set to 1 and the integration of the signals from 1.35 to 1.6 ppm from the product (Table 19) was plotted versus time.

Table 19: Reaction time and integration values of the signal from 1.35 to 1.6 ppm.

| reaction time / min | integration between 1.35 and 1.6 ppm | amount of 9 / mmol | yield / % |
|------------------------|---|------------------------------|--------------|
| 0 | 0.00 | 0 | 0 |
| 55 | 0.15 | 1.8 | 2.9 |
| 254 | 0.34 | 4.0 | 6.5 |
| 1170 | 1.03 | 12.3 | 19.8 |
| 1445 | 1.31 | 15.6 | 25.1 |
| 2750 | 2.36 | 28.1 | 45.3 |
| 4460 | 3.22 | 38.3 | 61.8 |
| 5495 | 3.60 | 42.8 | 69.1 |
| 7150 | 4.05 | 48.2 | 77.7 |
| 8580 | 4.19 | 49.9 | 80.4 |
| 10080 | 4.24 | 50.5 | 81.4 |

1-Hexyne modified silica (M4_{C≡C}). Material M4_{SiH} (1 g) was dried under vacuum at 100 °C overnight and suspended in dry dioxane (20 mL). A solution of 1-hexyne (3 mL, 26 mmol) in dry dioxane (20 mL) was cooled to 0 °C and n-butyllithium (2.7 M in heptane, 3 mL, 8.1 mmol) was slowly added under stirring. The solution was left to equilibrate to RT for 15 min, and then added to the suspension of M4_{SiH}. The suspension was heated to reflux under stirring for 7 days. After the reaction, the silica was separated from the solvent by filtration and washed with dioxane, diethylether and dichloromethane. Finally, the silica was dried overnight under vacuum at 110 °C. ²⁹Si CP/MAS NMR (59.63 MHz): δ (ppm) -73.5 (T²_H), -84 (T³_H), -96 (T³), -109 (Q⁴).

Acyl chloride modified silica (M_{COCl}). The carboxylic acid modified silicas M1f_{COOH}, M1g_{COOH} or M4_{COOH} (500 mg) were dried for 3 h at 100 °C under reduced pressure and then suspended under ultrasonication in dichloromethane (10 mL). Oxalyl chloride (100 μL, 1.2 mmol) was added and after 30 min of stirring, the solvent and the excess oxalyl chloride were removed under reduced pressure. Under an argon atmosphere, the resulting acyl chloride modified silica (M1f_{COCl}, M1g_{COCl} and M4_{COCl}) were used immediately, without further treatment, for the preparation of M_{FC}.

Ferrocene modified silica (M_{FC}). Substituted ferrocene **1a** (20 mg, 0.074 mmol) was dissolved in dry dichloromethane (15 mL) and added to M_{COCl} under argon. The mixture was left under ultrasonication at 40 °C for 2 h. The resulting M_{FC} was then washed with the following series of solvents: dichloromethane, ethanol, dichloromethane, ethanol, water and ethanol. The lightly yellow-colored material was dried overnight under reduced pressure. **M1_{FC}**, **M1g_{FC}**, and **M4_{FC}** displayed similar IR vibration bands. The intensities were larger in the case of **M4_{FC}** (high surface area material). IR (DRIFT): $\tilde{\nu}$ (cm⁻¹), 3350 (broad, ν_{N-H}), 3098, (w, ν_{C-H} , ferrocene), 2923 and 2857 (s, ν_{C-H} , CH₂), 2270 (ν_{Si-H}), 1712 (m, $\nu_{C=O}$, carboxylic acid), 1632 (m, $\nu_{C=O}$, amide I), 1542 (m, δ_{NH} , amide II), 1455 (m, δ_{C-H} , CH₂). The ferrocene surface concentration on **M1_{FC}** was determined from the total iron content obtained from AAS measurements: $\Gamma_{FC} = 1.26 \times 10^{-6}$ mol m⁻² for **M1f_{FC}**, and $\Gamma_{FC} = 1.96 \times 10^{-6}$ mol m⁻² for **M1g_{FC}**.

ω -Bromooctyl modified silica (M2_{Br}). Material **M2_{C=C}** (2g) was placed in a quartz round bottom flask and dried under vacuum at 100 °C overnight. The silica was suspended in 50 mL of dry n-hexane with 100 μ L of 1-octene. Dry HBr gas was prepared by dropwise addition of bromine to neat 1,2,3,4-tetrahydro-naphthalene in presence of iron powder as catalyst [197]. The HBr gas was passed through neat 1,2,3,4-tetrahydro-naphthalene and a cryo trap (dry ice / chloroform, -65 °C) for purification. The dry HBr gas was then passed through the suspension which was irradiated with a 700 W medium pressure mercury lamp for 2 h. No filters were employed. After reaction the particles were separated by filtration and washed with n-hexane (3 times). Finally, the silica was dried overnight under vacuum at 100 °C. The solution was evaporated under reduced pressure to recover the product from the hydrobromination of 1-octene. ¹³C CP/MAS NMR (50.32 MHz): δ (ppm) 11.49 (Si-CH₂), 20-50 (-CH₂-). IR (DRIFT): $\tilde{\nu}$ (cm⁻¹), 3760 – 3000 (br, ν_{OH} , SiOH), 2928, 2858 (s, ν_{CH} , CH₂), 2263 (m, ν_{SiH}), 1870 (m, $\nu_{Si-O-Si}$), 1455 (w, δ_{CH}) 1200 – 1000 ($\nu_{Si-O-Si}$).

Hydrobromination of 1-octene : 1-bromooctane. ¹H-NMR (CDCl₃, 400.16 MHz): δ (ppm) 0.92 (t 3H CH₃), 1.26 (m 8H -CH₂-), 1.42 (m 2H -CH₂-CH₃), 1.69 (d 3H CH₃-CHBr), 1.82 (m 2H -CH₂-CH₂Br), 3.39 (d 2H CH₂Br), 3.97 (m 1H -CHBr).

1,3,5,7,9,11,13,15-oktakis(2-bromoethyl)octasilsesquioxane^[a] (10b). Octavinylsilsesquioxane (0.250 g) was placed in a quartz round bottom flask and dried under vacuum at 50 °C

^[a] The synthesis and characterization of **10b** was performed in cooperation with D. Ruiz Abad, AK Mayer, Institut für Anorganische Chemie.

overnight and then suspended in 50 mL of dry n-hexane. Dry HBr gas, prepared in situ [197], was bubbled through the suspension which was irradiated with a 700 W medium pressure mercury lamp for 2 h. After reaction, the solvent was evaporated under reduced pressure, yielding **10b** as a white solid (0.506 g, quantitative yield). Mp: 235 °C. $^1\text{H-NMR}$ (CDCl_3 , 250.13 MHz): δ (ppm) 1.51 (t, 16H, $^3J_{\text{HH}} = 8.27$ Hz, Si- CH_2 -), 3.51 (t, 16H, $^3J_{\text{HH}} = 8.27$ Hz, - CH_2 -Br). $^{13}\text{C}\{^1\text{H}\}$ -NMR (CDCl_3 , 62.90 MHz): δ (ppm) 17.95 (Si- CH_2 -), 27.02 (- CH_2 -Br). ^{29}Si NMR (49.69 Hz. CDCl_3): δ 70.22 ppm. HR-MS (ESI): calcd for $\text{C}_{16}\text{H}_{32}\text{Br}_8\text{Si}_8\text{O}_{12}\text{K}$ [$\text{M}+\text{K}^+$]: 1318.30731, found 1318.30724. Anal. Calcd for $\text{C}_{16}\text{H}_{32}\text{Br}_8\text{Si}_8\text{O}_{12}$: C, 15.01; H, 2.50; Br, 49.94. Found: C, 14.74; H, 2.48; Br, 48.68.

8 Appendix

8.1 Polydispersity index (*PDI*)

In macromolecule chemistry, the standard deviation (σ) of the molecular weight distribution is given by Equation 13 [229]:

$$\sigma = \overline{M}_N \sqrt{\frac{\overline{M}_N}{\overline{M}_W} - 1} \quad (13)$$

where M_N is the number average molecular weight and M_W the weight average molecular weight.

The coefficient of variation (cv), also called g -index [91], is the standard deviation divided by the mean. Because M_N is also the statistical mean,

$$cv = \frac{\sigma}{\overline{M}_N} = \sqrt{\frac{\overline{M}_N}{\overline{M}_W} - 1} \quad (14)$$

The polydispersity index (*PDI*) [92], is defined as

$$PDI = \frac{\overline{M}_N}{\overline{M}_W} \quad (15)$$

therefore,

$$cv = \sqrt{PDI - 1} \quad \vee \quad PDI = cv^2 + 1 \quad (3)$$

8.2 Geometrical specific surface area (A)

$$A = \frac{A_p}{m_p} \quad A_p = 4 \pi r^2 \quad A_p = \text{surface area of one particle}$$

$$m_p = V_p \times \rho_{\text{SiO}_2} \quad m_p = \text{mass of one particle}$$

$$r = \text{radius of a particle}$$

$$A = \frac{4 \pi r^2}{V_p \times \rho_{\text{SiO}_2}} \quad V_p = \frac{4}{3} \pi r^3 \quad \rho_{\text{SiO}_2} = \text{silica density } (2.2 \times 10^6 \text{ g m}^{-3})$$

$$V_p = \text{volume of one particle}$$

$$d = \text{diameter of a particle (m)}$$

$$A = \frac{4 \pi r^2}{\frac{4}{3} \pi r^3 \times \rho_{\text{SiO}_2}}$$

$$A = \frac{3}{r \times \rho_{\text{SiO}_2}} \quad r = d / 2$$

$$A = \frac{6}{d \times \rho_{\text{SiO}_2}} \quad (5)$$

8.3 Surface concentration of ferrocene on M1_{Fc} from cyclic voltammetry (Γ_{CV}):

$$\Gamma_{\text{CV}} = \frac{N_{\text{Fc(P)}}}{A_p} \quad N_{\text{Fc(P)}} = \frac{N_{\text{Fc(E)}}}{N_{\text{p(E)}}} \quad N_{\text{Fc(P)}} = \text{amount of Fc on one particle}$$

$$A_p = \pi d^2 \quad A_p = \text{surface area of one particle}$$

$$d = \text{diameter of a particle}$$

$$N_{\text{Fc(E)}} = \text{amount of Fc on the electrode}$$

$$N_{\text{p(E)}} = \text{amount of particle on the electrode}$$

$$\Gamma_{\text{CV}} = \frac{N_{\text{Fc(E)}}}{N_{\text{p(E)}} \pi d^2} \quad N_{\text{Fc(E)}} = Q / n F \quad Q = \text{charge associated with the oxidation of Fc}$$

$$N_{\text{p(E)}} = \Gamma_p A_E \quad n = \text{number of electron}$$

$$F = \text{Faraday constant } (96485 \text{ C mole}^{-1})$$

$$\Gamma_p = \text{surface concentration of particles on the electrode}$$

$$A_E = \text{geometrical surface area of the electrode}$$

$$\Gamma_{\text{CV}} = \frac{Q}{\Gamma_p A_E n F \pi d^2} \quad (12)$$

9 Conclusion

The objective of the thesis is the immobilization of redox-active molecules on a simplified interphase system with a controlled geometry in order to investigate their interactions in such environments with, among other, electrochemical tools. Since the product resulting from the standard silylation modification procedure are not suitable for the preparation of the desired systems, the surface modification via a stable Si-C bond from a modified Si-H surface became the main synthetic challenge.

The spherical particles necessary as solid matrix for the simplified interphase system were synthesized by a modified Stöber process. The synthetic strategy involves high water concentration as well as post-synthesis high temperature treatment in order to reduce the microporosity. The characterization with scanning electron microscopy and dynamic light scattering, demonstrates that the silica particles are monodisperse and non-agglomerated spheres. Also the gas physisorption isotherms show that the materials can be considered as non-porous. The diameter of the particles can be tuned in the sub-micrometric range by a precise control of the reaction conditions. The non-porosity is necessary to ensure a homogeneous environment and a good accessibility to the redox-active molecules. The monodispersity and the well-defined properties makes them suitable for the quantitative analysis of electrochemical investigations.

For the silica surface modification via stable Si-C bonds, a Si-H terminated surface is desired as starting material. The chlorination-reduction sequence at high temperatures introduced in this thesis, opens a new route for the synthesis of Si-H modified silica surface. According to a quantitative analysis of the evolved hydrogen from the reaction of the modified surface with ethanol/KOH, a high Si-H surface concentration is achieved. Also the procedure is reproducible for many types of silica materials. IR as well as ^{29}Si CP MAS NMR spectroscopy demonstrate that the T^3_{H} groups are the main product while the reaction of Si-OH groups by reduction or dehydroxylation is almost quantitative. The high degree of cross-linking of the Si-H groups with the silica matrix as well as the absence of silanol groups are desired for the stability, homogeneity and inertness of the matrix. This contrasts with Si-H modifications obtained from low temperature methods where silanol groups remain after the reaction and a large proportion of T^2_{H} groups are produced.

The characterization of the Si-H modified materials also makes it possible to propose the assignment of the ν_{SiH} band at 2283 cm^{-1} in IR spectroscopy to the T^3_{H} groups.

The chlorination is the key step to achieve a high Si-H coverage, and the optimal temperature for the reduction step is about $900\text{ }^\circ\text{C}$. Under these reaction conditions, as shown by the SEM and DLS measurements as well as by the BET and BJH analysis, the physical properties, such as shape, pore size and surface area, remain essentially unchanged. Only micropores are lost due to the high temperatures employed during the procedure.

Thus, the chlorination-reduction sequence represents an ideal strategy to provide the starting material for further silica surface modification with redox-active molecules by reaction of the Si-H groups. Moreover, the simple and efficient access to Si-H terminated silica may also open new modification routes and further applications of such materials, e.g. in separation science and catalysis. To the best of our knowledge, this is the first procedure enabling a silicon hydride surface modification that may be applied to all types of silica surfaces, producing a high surface concentration, possibly allowing large scale ups and leaving the surface free of any other functionalities beside the Si-H groups.

Free radical initiated hydrosilylation reactions were developed to produce a Si-C bond from Si-H terminated silica surfaces. Both photochemical and thermal initiation may be employed. A strong attachment of the organic molecules on the silica surface is obtained. Indirect evidence, like decrease in the Si-H surface concentration, absence of C=C signals in the IR and NMR spectra of the modified materials are in agreement with the formation of a Si-C bond. Moreover the reaction occurs exclusively on the silica surface according to NMR investigations of the reaction solution. However, direct evidence for the Si-C bond formation could not be established with ^{13}C or ^{29}Si solid state NMR spectroscopy, because of weak signal intensity and signal overlapping, respectively. Moreover, the possibility for a radical initiated surface telomerization as well as Markovnikov addition during the hydrosilylation reaction can not be excluded. Still, the free radical hydrosilylation is advantageous over the transition metal catalysed- or radical initiator induced reactions because it leaves the silica surface free of impurities.

The photochemical induction is advantageous with regard to its mild reaction conditions for the modification of non-porous materials. A carboxylic acid functionalized surface was obtained via this method. Since amorphous silica is not transparent to UV light, hydrosilylation of the Si-H groups within porous materials requires a thermal initiation. A C18 as well as a terminal C=C bond modified surface were obtained from this route.

As an alternative to the radical hydrosilylation methods, a base catalyzed dehydrogenative coupling reaction of a terminal alkyne with Si-H groups is proposed. The reaction performed on soluble model compounds shows two valuable advantages: side reactions are not found, and direct evidence for the formation of the Si-C bond is obtained. The kinetics of the reaction were investigated with ^1H NMR spectroscopy. The reaction needs several days to complete, but a high yield is achieved. A dehydrogenative coupling mechanism was proposed and supported by experimental observations: No reaction occurs in absence of a proton source which is believed to act as a Lewis acid to make the hydride a better leaving group. This is confirmed by the experimental detection of H_2 when the reaction is performed in presence of a proton source. The optimization of this reaction on the silica surface and the attachment of redox-active molecules via this route are still needed at this point. However, this reaction is promising as a general modification method for silica surfaces.

The direct attachment of terminal C=C bond functionalized redox-active molecules was not achieved by photochemical or thermal hydrosilylation reactions because of the poor stability under the reaction conditions and / or the need for high concentration of the olefin. On the other hand, the carboxylic acid modified surface prepared by the free radical induced hydrosilylation can be converted easily into the corresponding acyl chloride, and then be used in a subsequent reaction to immobilize ferrocene units bearing an amine functional group. A surface concentration similar to the one expected for a ferrocene monolayer is obtained.

The terminal C=C bond modified silicas obtained by thermal hydrosilylation may also be further functionalized by radical hydrobromination. Characterization by DRIFT and NMR spectroscopy shows that the silica bound C=C groups have fully reacted. Indirect evidence on the outcome of the reaction is obtained from low molecular weight model compounds: the fact that the C=C bonds of 1-octene and of octavinylsilsequioxane are fully hydrobrominated and that the anti-Markovnikov products are obtained under homogeneous conditions, suggests that C=C bonds on the silica surface may react in the same manner. Furthermore, the use of a silsequioxane as model compound led to the production of the bromoethyl substituted octasilsequioxane by radical hydrobromination in better yield and purity than the previously published procedures.

However, the application of the brominated spacer for the immobilization of active molecules has several limitations. Therefore, the reactive acyl chloride modified silica surface was preferred for the immobilization of the ferrocene derivatives.

As a first application of the Si-H terminated silicas modified by radical hydrosilylation, their performances as HPLC separation phases were tested. The chlorination-reduction sequence followed by C18 surface modification opens a new synthetic strategy for the preparation of low silanol activity C18 HPLC phases compared to the conventional silylation method. At the early stage of their development, the C18 modified phases already match their silylated equivalent for the separation of organic bases. On the other hand the peak tailing of chelating analytes may still be improved. The source of metal impurities is not determined at this point. The solvent used during modification and HPLC tests as well as the original silica materials are two potential sources. Finally, the methylene selectivity of the C18 modified phase is low. Optimization of the thermal hydrosilylation reaction, in order to achieve higher surface concentration and lower the extent of possible side reactions, may improve the separation quality.

The HPLC investigation of the Si-H and C18 modified silicas delivers additional information on the surface chemistry of these materials. The peak asymmetry of organic bases after separation with Si-H modified materials demonstrates that the chlorination-reduction sequence produces a material almost free of surface isolated silanol groups. On the other hand, according to the peak tailing of organic bases after separation with C18 modified particles, some silanol groups are produced during the hydrosilylation reaction. However, their effect on the HPLC separation is moderate, indicating that their surface concentration remains low.

The second application of the silicon hydride terminated silicas modified with redox-active molecules by radical hydrosilylation is their electrochemical investigation, which is also the original objective of the thesis.

In order to support a precise quantitative analysis of the electrochemical results, a two dimensional particle assembly on electrode surface was carried out. Dip-coating experiments with bare silica particle yield the desired monolayer coverage on hydrophilic platinum surfaces. However, the hydrophobic character of the ferrocene modified particles resulted in weak particle-electrode interactions. The spontaneous adsorption of isolated particles on the electrode surface is preferred for the qualitative analysis of the charge transfer mechanism and quantitative analysis of the redox-active molecules' accessibility.

The electrochemical investigation makes it possible to elucidate the mechanism of the charge transfer within the simplified interphase system: Cyclic voltammetry of the ferrocene modified particles indicates that ferrocene units over a large part of the particle surface are electrochemically accessible by an electron hopping mechanism. In addition to the

intermolecular charge transfer between ferrocene units on the surface of a single particle, an interparticle charge transfer between adjacent particles within large agglomerates is also taking place. Moreover, the proportion of active molecules that are accessible to the redox reaction were determined from the comparison of the ferrocene surface concentration obtained from cyclic voltammetry with the one obtained from atomic absorption spectroscopy. The accessibility of more than half of the ferrocene units to the redox process is a further evidence for a charge transfer occurring along the particle surface.

These redox-active molecule interactions and the charge transfer by electron hopping observed for the ferrocene as a model system are important requirements for the scope of electrochemical investigation and control of immobilized catalyst in interphases, which should be the subject of future work.

References

- [1] E. Lindner, T. Schneller, F. Auer and H. A. Mayer, *Angew. Chem.* **1999**, *111*, 2288 - 2309. *Angew. Chem. Int. Ed.* **1999**, *38*, 2159 - 2174.
- [2] C. U. Pittman Jr. in *Comprehensive Organometallic Chemistry*, Vol. 8 (Eds.: G. Wilkinson, F. G. Stone, E.W. Abel), Pergamon, Oxford, **1982**, p. 553 - 611.
- [3] D.-Y. Wu, E. Lindner, H. A. Mayer, Z.-J. Jiang, V. Krishnan and H. Bertagnolli, *Chem. Mater.* **2005**, *17*, 3951 - 3959.
- [4] B. Lynch, J. D. Glennon, C. Tröltzsch, U. Menyes, M. Pursch and K. Albert, *Anal. Chem.* **1997**, *69*, 1756 - 1762.
- [5] H. Frank, G. J. Nicholson and E. Bayer, *Angew. Chem.* **1978**, *90* (5), 396 - 398. *Angew. Chem. Int. Ed.* **1978**, *17* (5), 363 - 365.
- [6] P. A. Levkin, A. Levkina and V. Schurig, *Anal. Chem.* **2006**, *78*, 5143 - 5148.
- [7] C. Amatore, Y. Bouret, E. Maisonhaute, J. I. Goldsmith and H. D. Abrunã, *Chem. Eur. J.* **2001**, *7*, 2206 - 2226.
- [8] F. Novak, B. Speiser, H. A. Y. Mohammad and H. A. Mayer, *Electrochim. Acta* **2004**, *49*, 3841 - 3853.
- [9] E. Steckhan, *Angew. Chem.* **1986**, *98*, 681 - 699. *Angew. Chem. Int. Ed.* **1986**, *28*, 683 - 701.
- [10] L. Forni, *Catal. Today* **1999**, *52*, 147 - 152.
- [11] W. Stöber, A. Fink and E. Bohn, *J. Colloid Interface Sci.* **1968**, *26*, 62 - 69.
- [12] G. Gritzner and J. Kuta, *Pure Appl. Chem.* **1984**, *56*, 461 - 466.
- [13] E. Lindner, Z.-L. Lu, H. A. Mayer, B. Speiser, C. Tittel and I. Warad, *Electrochemistry Communications* **2005**, *7* (10), 1013 - 1020.
- [14] J. J. Pesek, M. T. Matyska, M. Oliva and M. Evanchic, *J. Chromatogr. A* **1998**, *818*, 145 - 154.
- [15] J. E. Sandoval and J. J. Pesek, *Anal. Chem.* **1991**, *63*, 2634 - 2641.
- [16] J. M. Buriak, *Chem. Rev.* **2002**, *102*, 1272 - 1306.
- [17] p. 92 - 96 in [19].
- [18] p. 52 - 53 in [19].
- [19] K. K. Unger, *Porous Silica. Its Properties and Use as Support in Column Liquid Chromatography*, Vol. 16, J. Chromatogr. Library, Elsevier, Amsterdam, **1979**.
- [20] P. Van Der Voort and E. F. Vansant, *J. Liq. Chromatogr. Rel. Technol.* **1996**, *19*(17/18), 2723 - 2752.

- [21] J. G. Dorsey and K. A. Dill, *Chem. Rev.* **1989**, 89, 331 - 346.
- [22] L. C. Sander, S. A. Wise and C. H. Lochmüller, *Crit. Rev. Anal. Chem.* **1987**, 18, 299 - 415.
- [23] J. H. Clark and D. J. Macquarrie, *Chem. Commun.* **1998**, 853 - 860.
- [24] P. McMorn and G. J. Hutchings, *Chem. Soc. Rev.* **2004**, 33, 108 - 122.
- [25] C. E. Song and S.-G. Lee, *Chem. Rev.* **2002**, 102, 3495 - 3524.
- [26] A. Vidal and E. Papirer, Chapter 3C, p. 285 in [29].
- [27] p. 42 in [29].
- [28] Y. Grillet and P. L. Llewellyn, Chapter 2A, p. 23 – 27 in [29].
- [29] A. P. Legrand (Ed.), *The Surface Properties of Silicas*, Wiley, Chichester, **1998**.
- [30] J. E. Lim, C. B. Shim, J. M. Kim, B. Y. Lee and J. E. Yie, *Angew. Chem.* **2004**, 116, 3927 - 3930. *Angew. Chem. Int. Ed.* **2004**, 43, 3839 - 3842.
- [31] B. V. Zhmud and J. Sonnefeld, *J. Non-Cryst. Sol.* **1996**, 195, 16 - 27.
- [32] C. Stella, S. Rudaz, J.-L. Veuthey and A. Tchaplà, *Chromatograph. Suppl.* **2001**, 53, 113 - 131.
- [33] M. J. J. Hetem, J. W. de Haan, H. A. Claessens, L. J. M. van de Ven, C. A. Cramers and J. N. Kinkel, *Anal. Chem.* **1990**, 62, 2288 - 2296.
- [34] M. J. J. Hetem, J. W. de Haan, H. A. Claessens, L. J. M. van de Ven, C. A. Cramers, P. W. J. G. Wijnen and J. N. Kinkel, *Anal. Chem.* **1990**, 62, 2296 - 2300.
- [35] X. Liu, A. V. Bordunov and C. A. Pohl, *J. Chromatogr. A* **2008**, 1119, 128 - 134.
- [36] T. G. Waddell, D. E. Leyden and M. T. DeBello, *J. Am. Chem. Soc.* **1981**, 103, 5303 - 5307.
- [37] D. J. Cole-Hamilton, *Science* **2003**, 299, 1702 - 1706.
- [38] B. Lynch, G. H. Müller, L. O. Healy, J. D. Glennon, M. Pursch and K. Albert, *Anal. Bioanal. Chem.* **2003**, 377, 1014 - 1019.
- [39] J. J. Pesek and M. T. Matyska, *J. Sep. Sci.* **2005**, 28, 1845 - 1854.
- [40] J. Nawrocki, *J. Chromatogr. A* **1997**, 779, 29 - 71.
- [41] M. J. Wirth, R. W. P. Fairbank and H. O. Fatunmbi, *Science* **1997**, 275, 44 - 47.
- [42] N. C. Mehendale, C. Bezemer, C. A. van Waltree, R. J. M. K. Gebbink and G. van Koten, *J. Mol. Catal. A: Chem.* **2006**, 257, 167 - 175.
- [43] N. C. Mehendale, J. R. A. Sietsma, K. P. de Jong, C. A. vanWaltree, R. J. M. K. Gebbink and G. van Koten, *Adv. Synth. Catal.* **2007**, 349, 2619 - 2630.
- [44] D. Rechavi and M. Lemaire, *Org. Lett.* **2001**, 3, 2493 - 2496.
- [45] D. Rechavi and M. Lemaire, *Chem. Rev.* **2002**, 102, 3467 - 3494.

- [46] S. J. Bae, S.-W. Kim, T. Hyeon and B. M. Kim, *Chem. Commun.* **2000**, 31 - 32.
- [47] R. H. Crabtree, *The Organometallic Chemistry of the Transition Metals, Third Edition*, p. 252 - 254, John Wiley and sons, new York, **2001**.
- [48] T. M. Lancaster, S. S. Lee, and J. Y. Ying, *Chem. Commun.* **2005**, 3577 - 3579.
- [49] X. Huang and J. Y. Ying, *Chem. Commun.* **2007**, 1825 - 1827.
- [50] T. Tao and G. E. Maciel, *J. Am. Chem. Soc.* **2000**, *122*, 3118 - 3126.
- [51] J.-I. Ishikawa and M. Itoh, *Journal of Catalysis* **1999**, *185*, 454 - 461.
- [52] B. Marciniec, J. Gulinski, W. Urbaniak and Z.W. Kornetka (ed. by B. Marciniec), *Comprehensive Handbook on Hydrosilylation*, Pergamon, Oxford, **1993**.
- [53] V. A. Tertykh and L. A. Nelyakova, chap 1.6 *Solid-phase hydrosilylation reactions with participation of modified silica surface*, p. 147 - 189 in [54].
- [54] A. Dabrowsky and V. A. Tertykh, *Adsorption on New and Modified Inorganic Sorbents*, Vol. 99, Studies in Surface Science and Catalysis, Elsevier, Amsterdam, **1996**.
- [55] B. R. Bodsgard and J. N. Burstyn, *Chem. Commun.* **2001**, 647 - 648.
- [56] J. J. Pesek, M. T. Matyska, E. J. Williamsen, M. Evanchic, V. Hazari, K. Konjuh, S. Takhar and R. Tranchina, *J. Chromatogr. A* **1997**, *786*, 219 - 228.
- [57] I. Tissot, J. P. Reymond, F. Lefebvre, and E. Bourgeat-Lami, *Chem. Mater.* **2002**, *14*, 1325 - 1331.
- [58] E. Matijevic, *Acc. Chem. Res.* **1981**, *14*, 22 - 29.
- [59] E. Matijevic, *Chem. Mater.* **1993**, *5*, 412 - 426.
- [60] E. Matijevic, *Langmuir* **1994**, *10*, 8 - 16.
- [61] Y. Xia, B. Gates, Y. Yin, and Y. Lu, *Adv. Mater.* **2000**, *12*, 603 - 713.
- [62] C. T. Matsoukas and E. Gulari, *J. Colloid Interface Sci.* **1989**, *132*, 13 - 21.
- [63] C. T. Matsoukas and E. Gulari, *J. Colloid Interface Sci.* **1988**, *124*, 252 - 261.
- [64] V. K. LaMer and R. H. Dinegar, *J. Am. Chem. Soc.* **1950**, *72*, 4847 - 4854.
- [65] G. H. Bogush and C. F. Zukoski IV, *J. Colloid Interface Sci.* **1991**, *142*, 19 - 34.
- [66] H. Giesche, *Journal of the European Ceramic Society* **1994**, *14*, 189 - 204.
- [67] A. Van Blaaderen, J. Van Geest and A. Vrij, *J. Colloid Interface Sci.* **1992**, *154*, 481 - 501.
- [68] D. L. Green, J. S. Lin, Y.-F. Lam, M. Z.-C. Hu, D. W. Schaefer and M. T. Harris *J. Colloid Interface Sci.* **2003**, *266*, 346 - 358.
- [69] A. Van Blaaderen and A. P. M. Kentgens, *J. Non-Crystalline Solids* **1992**, *149*, 161 - 178.
- [70] L. W. Kelts, N. J. Effinger and S. M. Melpolder, *J. Non-Crystalline Solids* **1986**, *83*, 353 - 374.

- [71] G. H. Bogush and C. F. Zukoski, IV, *J. Colloid Interface Sci.* **1991**, *142*, 1 - 18.
- [72] K. Lee, J. Look, M. T. Harris and A.V. McCormick, *J. Colloid Interface Sci.* **1997**, *194*, 78 - 88.
- [73] J. K. Bailey and M. L. Mecartney, *Colloids Surfaces* **1992**, *63*, 151 - 161.
- [74] D. L. Green, S. Jayasundara, Y.-F. Lam and M. T. Harris, *J. Non-Crystalline Solids* **2003**, *315*, 166 - 179.
- [75] C. A. R. Costa, C. A. P. Leite and F. Galembeck, *J. Phys. Chem. B* **2003**, *107*, 4747 - 4755.
- [76] H. Boukari, J. S. Lin and M. T. Harris, *J. Colloid Interface Sci.* **1997**, *194*, 311 - 318.
- [77] J. Aleman, A. V. Chadwick, J. He, M. Hess, K. Horie, R. G. Jones, P. Kratochvil, I. Meisel, I. Mita, G. Moad, S. Penczeck and R. F. T. Stepto, *Pure Appl. Chem.* **2007**, *79*, 1801 - 1829.
- [78] J. L. Lippert, S. B. Melpolder and L. M. Kelts, *J. Non-Crystalline Solids* **1988**, *104*, 139 - 147.
- [79] R. K. Iler, *The Chemistry of Silica*, Wiley, New York, **1979**.
- [80] C. J. J. Den Ouden and R. W. Thompson, *J. Colloid Interface Sci.* **1991**, *143*, 77 - 84.
- [81] G. H. Bogush, M. A. Tracy and C. F. Zukosky IV, *J. Non-Crystalline Solids* **1988**, *104*, 95 - 106.
- [82] H. Giesche, *Silica*, chap. 2, p. 125 - 146 in T. Sugimoto, *Fine Particles: Synthesis, Characterization, and Mechanisms of Growth*, surfactant science series, Marcel Dekker, New York, **2000**, Vol 92.
- [83] D. Straub, Zulassungsarbeit, Universität Tübingen, **2004**.
- [84] C. G. Tan, B. D. Bowen and N. Epstein, *J. Colloid Interface Sci.* **1987**, *118*, 290 - 293.
- [85] A. Ruff, Diplomarbeit, Universität Tübingen, **2008**.
- [86] S. Bachmann, J. Wegmann and K. Albert, *GIT Spez. Sep.* **2000**, *20*, 24 - 26.
- [87] B. Schetter, Diplomarbeit, Universität Tübingen, **2003**.
- [88] L. T. Zhuravlev, *Colloids Surf. A* **2000**, *173*, 1 - 38.
- [89] B. Schetter and G. Fischer, *J. Sol-Gel Sci. Technol.* **2007**, *44*, 167 - 170.
- [90] L. Reimer, *Scanning Electron Microscopy: Physics of Image Formation and Microanalysis 2., completely rev. and updated ed.*, Springer, Berlin, **1998**.
- [91] J. W. Gooch, *Encyclopedic dictionary of polymers*, Springer, Atlanta, Volume 1, **2007** p. 458.
- [92] M. S. M. Alger, *Polymer science dictionary*, Elsevier Applied Science, London, **1989**, p. 339.

- [93] Coulter Corporation, *User Manual for "Coulter N4 Plus Submicron Particle Sizer"*, Miami, **1995**, p. 3 - 5.
- [94] F. Novak, N. Plumeré, B. Schetter, B. Speiser, D. Straub, H. A. Mayer, M. Reginek, K. Albert, G. Fischer, C. Meyer, H.-J. Egelhaaf and Borre Borresen, in preparation
- [95] K. S. W. Sing, D. H. Everett, R. A. W. Haul, L. Moscou, R. A. Pierotti, J. Rouquerol and T. Siemieniowska, *Pure Appl. Chem.* **1985**, *57*, 603 - 619.
- [96] S. Brunauer, L. S. Deming, W. S. Deming and E. Teller, *J. Am. Chem. Soc.* **1940**, *62*, 1723 - 1732.
- [97] S. Brunauer, P. H. Emmet and E. Teller, *J. Am. Chem. Soc.* **1938**, *60*, 309 - 319.
- [98] D. Zhao, J. P. Feng, Q. S. Huo, N. Melosh, G. H. Fredrickson, B. F. Chemelka and G. D. Stucky, *Science* **1998**, *279*, 548 - 552.
- [99] M. Vallet-Regi, L. Ruiz-Gonzalez, I. Izquierdo-Barbaa and J. M. Gonzalez-Calbet, *J. Mater. Chem.* **2006**, *16*, 26 - 31.
- [100] I. Olliges, Diplomarbeit, Universität Tübingen, **2007**.
- [101] E. P. Barrett, L. G. Joyner and P. P. Halenda, *J. Am. Chem. Soc.* **1951**, *73*, 373 - 380.
- [102] J. S. Rowlinson and B. Widom, *Molecular Theory of Capillarity*, Dover Publications New York, **2002**.
- [103] A. Budny, F. Novak, N. Plumeré, B. Schetter, B. Speiser, D. Straub, H. A. Mayer and M. Reginek, *Langmuir* **2006**, *22*, 10605 - 10611.
- [104] M. J. Wirth and H. O. Fatunmbi, *Anal. Chem.* **1993**, *65*, 822 - 826.
- [105] G. E. Maciel and D. W. Sindorf, *J. Am. Chem. Soc.* **1980**, *102*, 7607 - 7608.
- [106] E. Lippmaa, M. Mägi, A. Samoson, G. Engelhardt and A.-R. Grimmer, *J. Am. Chem. Soc.* **1980**, *102*, 4889 - 4893.
- [107] L. Heeribout, J. B. d'Espinose de la Caillerie, A. P. Legrand and G. Mignani, *J. Colloid Interface Sci.* **1999**, *215*, 296 - 299.
- [108] C.-H. Chu, E. Jonsson, M. Auvinen, J. J. Pesek and J. E. Sandoval, *Anal. Chem.* **1993**, *65*, 808 - 816.
- [109] L. C. Sander and S. A. Wise, *Anal. Chem.* **1984**, *56*, 504 - 510.
- [110] J. E. Sandoval and J. J. Pesek, *Anal. Chem.* **1989**, *61*, 2067 - 2075.
- [111] A. Reuter, K. Heger, M. Uhlig, L. Libera and G. Marx, *Fresenius J. Anal. Chem.* **1994**, *349*, 219 - 221.
- [112] R. S. S. Murthy, J. P. Blitz and D. E. Leyden, *Anal. Chem.* **1986**, *58*, 3167 - 3172.
- [113] R. S. S. Murthy and D. E. Leyden, *Anal. Chem.* **1986**, *58*, 1228 - 1233.

- [114] H. Barthel, L. Rösch and J. Weis, in N. Auner and J. Weis (Eds.), *Organosilicon Chemistry II. From Molecules to Materials*, VCH, Weinheim, **1996**, p. 761 - 778.
- [115] E. F. Vansant, P. Van Der Voort and K. C. Vrancken, *Characterization and Chemical Modification of the Silica Surface*, Vol. 93, Studies in Surface Science and Catalysis, Elsevier, Amsterdam, **1995** p. 31 – 58.
- [116] F. Rataboul, A. Baudouin, C. Thieuleux, L. Veyre, C. Copéret, J. Thivolle-Cazat, J.-M. Basset, A. Lesage and L. Emsley, *J. Am. Chem. Soc.* **2004**, *126*, 12541 - 12550.
- [117] P. Avenier, A. Lesage, M. Taoufik, A. Baudouin, A. De Mallmann, S. Fiddy, M. Vautier, L. Veyre, J.-M. Basset, L. Emsley and E. A. Quadrelli, *J. Am. Chem. Soc.* **2007**, *129*, 176 - 186.
- [118] R. West, *J. Am. Chem. Soc.* **1954**, *76*, 6015 - 6017.
- [119] D. W. Sindorf and G. E. Maciel, *J. Phys. Chem.* **1982**, *86*, 5208 - 5219.
- [120] J. P. Gallas, J. C. Lavalley, A. Burneau, O. Barres, *Langmuir* **1991**, *7*, 1235 - 1240.
- [121] C. C. Liu and G. E. Maciel, *J. Am. Chem. Soc.* **1996**, *118*, 5103 - 5119.
- [122] W. Kolodziejski and J. Klinowski, *Chem. Rev.* **2002**, *102*, 613 - 628.
- [123] S. L. Scott and J.-M. Basset, *J. Am. Chem. Soc.* **1994**, *116*, 12069 - 12070.
- [124] B. A. Morrow and I. A. Cody, *J. Phys. Chem.* **1976**, *20*, 1998 - 2004.
- [125] B. A. Morrow and I. A. Cody, *J. Phys. Chem.* **1976**, *80*, 1995 - 1998.
- [126] M. P. McDaniel, *J. Phys. Chem.* **1981**, *85*, 532 - 537.
- [127] p 532 - 562 in [129].
- [128] p 462 - 571 in [129].
- [129] E. Wiberg and E. Amberger, *Hydrides of the elements of main groups I-IV*, Elsevier, Amsterdam, London, New York, **1971**.
- [130] A. Traut, PhD thesis, Universität Köln, **2005**.
- [131] M. R. Lindford, P. Fenter, P. M. Eisenberger and C. E. D. Chidsey, *J. Am. Chem. Soc.* **1995**, *117*, 3145 - 3155.
- [132] K. J. Kulicke and B. Giese, *Synlett* **1990**, *1*, 91 - 92
- [133] E. W. Pietrusza, L. H. Sommer and F. C. Whitmore, *J. Am. Chem. Soc.* **1948**, *70*, 484 - 486.
- [134] R. Calas and N. Duffaut, *Bull. mens. inform. ITERG* **1953**, *7*, 438 - 440.
- [135] F. Effenberger, G. Götz, B. Bidlingmaier and M. Wezstein, *Angew. Chem., Int. Ed.* **1998**, *37*, 2462 - 2464.
- [136] R. L. Cicero, M. R. Linford and C. E. D. Chidsey, *Langmuir* **2000**, *16*, 5688 - 5695.

- [137] A. B. Sieval, A. L. Demirel, J. W. M. Nissink, M. R. Linford, J. H. van der Maas, W. H. de Jeu, H. Zuilhof and E. J. R. Sudhölter *Langmuir* **1998**, *14*, 1759 - 1768.
- [138] C. Chatgililoglu, *Acc. Chem. Res.* **1992**, *25*, 188 - 194.
- [139] R. L. Cicero, C. E. D. Chidsey, G. P. Lopinski, D. D. M. Wayner and R. A. Wolkow, *Langmuir* **2002**, *18*, 305 - 307.
- [140] C. Coletti, A. Marrone, G. Giorgi, A. Sgamellotti, G. Cerofolini and N. Re, *Langmuir* **2006**, *22*, 9949 - 9956.
- [141] J. M. Kanabus-Kaminska, J. A. Hawari, D. Griller and C. Chatgililoglu, *J. Am. Chem. Soc.* **1987**, *109*, 5267 - 5268.
- [142] A. Faucheux, A. C. Gouget-Laemmel, C. Henry de Villeneuve, R. Boukherroub, F. Ozanam, P. Allongue and J.-N. Chazalviel, *Langmuir* **2006**, *22*, 153 - 162.
- [143] R. Voicu, R. Boukherroub, V. Bartzoka, T. Ward, J. T. C. Wojtyk and D. D. M. Wayner, *Langmuir* **2004**, *20*, 11713 - 11720.
- [144] M. Wang, J. M. Weinberg and K. L. Wooley, *Macromolecules* **2000**, *33*, 734 - 742.
- [145] K. Albert, *J. Sep. Sci.* **2003**, *26*, 215 - 224.
- [146] K. Peter C. Vollhardt, *Organische Chemie*, VCH, Weinheim, **1988**, p. 495.
- [147] J. Schaefer, PhD thesis, Universität Tübingen.
- [148] S. H. Sommer, O. F. Bennet, P. G. Campbell and D. R. Weynberg, *J. Am. Chem. Soc.* **1957**, *79*, 3295 - 3296.
- [149] M. G. Voronkov, N. L. Ushakova, I. I. Tsykhanskaya, and V. B. Pukhnarevich, *J. Organomet. Chem.* **1984**, *264*, 39 - 48.
- [150] C.-H. Jun and R. H. Crabtree, *J. Organomet. Chem.* **1993**, *447*, 177 - 187.
- [151] R. Shimizu and T. Fuchikami, *Tetrahedron Letters* **2000**, *41*, 907 - 910.
- [152] H. Q. Liu and J. F. Harrod, *Can. J. Chem.* **1990**, *68*, 1100 - 1105.
- [153] M. Itoh, M. Mitsuzuka, T. Utsumi, K. Iwata and K. Inoue, *J. Organomet. Chem.* **1994**, *476*, C30 - C31.
- [154] M. Itoh, K. Inoue, K. Iwata and M. Mitsuzuka, *Macromolecules* **1997**, *30*, 694 - 701.
- [155] T. Baba, A. Kato, H. Yuasa, F. Toriyama, H. Handa, and Ono, *Catalysis Today* **1998**, *44*, 271 - 276.
- [156] R. Calas and P. Bourgeois, *C. R. Acad. Sci. Paris, Ser. C* **1969**, *268*, 72 - 74.
- [157] Stefan Bayer, PhD thesis, Universität Bayreuth, **2005**.
- [158] B. Wrackmeyer, W. Milius and O. L. Tok, *Chem. Eur. J.* **2003**, *9*, 4732 - 4738.
- [159] R. West and C. S. Kraihanzel, *Inorg. Chem.* **1962**, *1*, 967 - 969.
- [160] J. C. Giordan, *J. Am. Chem. Soc.* **1983**, *105*, 6544 - 6546.

- [161] B. Boury, P. Chevalier, R. J. P. Corriu, P. Delord, J. J. E. Moreau and M. Wong Chimam, *Chem. Mater.* **1999**, *11*, 281 - 291.
- [162] P. L. Pauson, *Journal of Organometallic Chemistry* **2001**, *637 - 639*, 3 - 6.
- [163] T. J. Kealy and P. L. Pauson, *Nature* **1951**, *168*, 1039 - 1940.
- [164] W. E. Geiger, *Organometallics* **2007**, *26*, 5738 - 5765.
- [165] M.-H. Delville, *Inorganica Chimica Acta* **1999**, *291*, 1 - 19.
- [166] R. Noyori and T. Ohkuma, *Angew. Chem.* **2001**, *113*, 40 - 75. *Angew. Chem., Int. Ed.* **2001**, *40*, 40 - 73.
- [167] R. Noyori, *Angew. Chem.* **2002**, *114*, 2108 - 2123. *Angew. Chem. Int. Ed.* **2002**, *41*, 2008 - 2022.
- [168] E. Lindner, I. Warad, K. Eichele and H. A. Mayer, *Inorganica Chimica Acta* **2003**, *350*, 49 - 56.
- [169] C. Nachtigal, S. Al-Gharabli, K. Eichele, E. Lindner and H. A. Mayer, *Organometallics* **2002**, *21*, 105 - 112.
- [170] E. Lindner, A. Ghanem, I. Warad, K. Eichele, H. A. Mayer and V. Schurig, *Tetrahedron: Asymmetry* **2003**, *14* (8), 1045 - 1053.
- [171] F. Novak, B. Speiser, E. Lindner, Z.-L. Lu and H. A. Mayer, *Angew. Chem.* **2004**, *116*, 2059 - 2062. *Angew. Chem. Int. Ed.* **2004**, *43*, 2025 - 2028.
- [172] M. Reginek, PhD thesis, Universität Tübingen, **2006**.
- [173] I. Warad, K. Eichele, H. A. Mayer and E. Lindner, *Inorganica Chimica Acta* **2004**, *357*, 1847 - 1853.
- [174] B. Speiser, A. Rieker and S. Pons, *J. Electroanal. Chem.* **1983**, *147*, 205 - 222.
- [175] B. Speiser, A. Rieker and S. Pons, *J. Electroanal. Chem.* **1983**, *159*, 63 - 88.
- [176] P. Hertl, A. Rieker and B. Speiser, *J. Electroanal. Chem.* **1986**, *200*, 147 - 158.
- [177] B. Schetter and B. Speiser, *Journal of Organometallic Chemistry* **2004**, *689*, 1472 - 1480.
- [178] A. Aguilar-Aguilar, A. D. Allen, E. P. Cabrera, A. Fedorov, N. Fu, H. Henry-Riyad, J. Leuninger, U. Schmid, T. T. Tidwell and R. Verma, *J. Org. Chem.* **2005**, *70*, 9556 - 9561.
- [179] P. D. Beer, A. R. Graydon, A. O. M. Johnson and D. K. Smith, *Inorg. Chem.* **1997**, *36*, 2112 - 2118.
- [180] F. Linkser and R. L. Evans, *J. Am. Chem. Soc.* **1945**, *67*, 1581 - 1582.
- [181] S. Berger, S. Braun and H.-O. Kalinowski, *NMR-Spektroskopie von Nichtmetallen, Band 3, ³¹P-NMR-Spektroskopie*, Thieme-Verlag, **1993**, p. 159 - 160.
- [182] J. G. Verdake, *Coord. Chem. Rev.*, **1972**, *9*, 1 - 106.

- [183] T. Wener, Zulassungsarbeit, Universität Tübingen, **2008**.
- [184] J. Müller, M. Brunnbauer, M. Schmidt, A. Zimmermann and A. Terfort, *Synthesis* **2005**, 6, 998 - 1004.
- [185] K. Tamao, K. Sumitani and M. Kumada, *J. Am. Chem. Soc.* **1972**, 94, 4374 - 4376.
- [186] T. Hayashi, M. Konishi and M. Kumada, *Tetrahedron Lett.* **1979**, 20, 1871 - 1874.
- [187] C. E. Janssen and N. Krause, *Eur. J. Org. Chem* **2005**, 2322 - 2329.
- [188] H. K. A. C. Coolen, J. A. M. Meeuwis P. W. N. M. van Leeuwen and R. J. M. Nolte, *J. Am. Chem. Soc.* **1995**, 117, 11906 - 11913.
- [189] B. H. Lipshutz, R. S. Wilhelm, and J. A. Kozlowski, *Tetrahedron* **1984**, 40, 5005 - 5038.
- [190] G. Cauquis, G. Fauvelot and J. Rigaudy, *Comptes Rendus des Seances de l'Academie des Sciences, Serie C: Sciences Chimiques* **1967**, 264 (22), 1758 - 1761.
- [191] J. Bracht and A. Rieker, *Synthesis* **1977**, 10, 708 - 711.
- [192] A. Budny, Zulassungsarbeit, Universität Tübingen, **2005**.
- [193] J. R. Lenhard and R. W. Murray, *J. Am. Chem. Soc.* **1978**, 100, 7870 - 7875.
- [194] T. E. Müller and M. Beller, *Chem. Rev.* **1998**, 98, 675 - 703.
- [195] I. P. Beletskaya and A. V. Cheprakov, *Chem. Rev.* **2000**, 100, 3009 - 3066.
- [196] T. M. Trnka and R. H. Grubbs, *Acc. Chem. Res.* **2001**, 34, 18 - 29.
- [197] Organikum 21, *Wiley-VCH*, **2001**.
- [198] E. A. Drylie, C. D. Andrews, M. A. Hearshaw, C. Jimenez-Rodriguez, A. Slawin, D. J. Cole-Hamilton and R. E. Morris, *Polyhedron* **2006**, 25, 853 - 858.
- [199] Y. Sudo and T. Wada, *Journal of Chromatography A* **1998**, 813, 239 - 246.
- [200] J. Köhler and J. J. Kirkland, *J. Chromatogr.* **1987**, 385, 125 - 150.
- [201] Y. Sudo, *Journal of Chromatography A*, **1997**, 757, 21 - 28.
- [202] J. J. Kirkland, J. L. Glajch and R. D. Farlee, *Anal. Chem.* **1989**, 61, 2 - 11.
- [203] B. Buszewski, J. Schmid, K. Albert and E. Bayer, *J. Chromatogr.* **1991**, 552, 415 - 427.
- [204] T. Lobert and H. Engelhardt, *Anal. Chem.* **1999**, 71, 1885 - 1892.
- [205] J. Nawrocki and D.L. Moir, W. Szczepaniak, *J. Chromatogr.* **1989**, 467, 31 - 40.
- [206] J. Nawrocki, *Chromatographia*, **1991**, 31, 177 - 192.
- [207] B. Buszewski, M. Jezierska, M. Welniak and D. Berek, *J. High Resol. Chrom.* **1998**, 21, 267 - 281.
- [208] H. A. Claessens, C. A. Cramers, J. W. de Haan, F. A. H. den Otter, L. J. M. van de Ven, P. J. Andree, G. J. de Jong, N. Lammers, J. Wijma and J. Zeeman, *Chromatographia* **1985**, 20, 582 - 586.
- [209] H. Luo and P. W. Carr, *Anal. Bioanal. Chem.* **2008**, 391, 919 - 923.

- [210] N. Sagliano Jr., T. R. Floyd, R. A. Hartwick, J. M. Dibussolo and N. T. Miller, *J. Chromatogr.* **1988**, *443*, 155 - 172.
- [211] US National Institute of Standards & Technology Certificate of Analysis, *Standard Reference Material SRM 870*, Department of Commerce United States of America, **2000**.
- [212] L. C. Sander and S. A. Wise, *J. Sep. Sci.* **2003**, *26*, 283 - 294.
- [213] J. Köhler, D. B. Chase, R. D. Farlee, A. J. Vega and J. J. Kirkland, *Journal of Chromatography* **1986**, *352*, 275 - 305.
- [214] M. R. Newton, K. A. Morey, Y. Zhang, R. J. Snow, M. Diwekar, J. Shi and H. S. White, *Nano Letters*, **2004**, *4*, 875 - 880.
- [215] S. Zheng, E. Ross, M. A. Legg, and M. J. Wirth, *J. Am. Chem. Soc.* **2006**, *128*, 9016 - 9017.
- [216] N. D. Denkov, O. D. Velev, P. A. Kralchevsky, I. B. Ivanov, H. Yoshimura and K. Nagayama, *Nature* **1993**, *361*, 26.
- [217] H.-Y. Ko, H.-W. Lee and J. Moon, *Thin Solid Films* **2004**, *447 - 448*, 638 - 644.
- [218] Y. A. Vlasov, X.-Z. Bo, J. C. Sturm and D. J. Norris, *Nature* **2001**, *414*, 289 - 293.
- [219] Y. A. Vlasov, *Adv. Mater.* **1999**, *11*, 165 - 169.
- [220] P. Jiang and M. J. McFarland, *J. Am. Chem. Soc.* **2004**, *126*, 13778 - 13786.
- [221] P. Massé and S. Ravaine, *Chem. Mater.* **2005**, *17*, 4244 - 4249.
- [222] N. D. Denkov, O. D. Velev, P. A. Kralchevsky, I. B. Ivanov, H. Yoshimura and K. Nagayama, *Langmuir* **1992**, *8*, 3183 - 3190.
- [223] A. van Blaaderen, R. Ruel and P. Wiltzius, *Nature* **1987**, *385*, 321 - 324.
- [224] N. V. Dziomkina and G. J. Vancso, *Soft Matter* **2005**, *1*, 265 - 279.
- [225] A. J. Bard and L. R. Faulkner, *Electrochemical Methods - Fundamentals and Applications*, John Wiley Sons, New York, **1980**, p. 522.
- [226] B. Fabre and F. Hauquier, *J. Phys. Chem. B* **2006**, *110*, 6848 - 6855.
- [227] S. W. Provencher, *Comp. Phys. Commun.* **1982**, *27*, 229 - 242.
- [228] S. W. Provencher, *Comp. Phys. Commun.* **1982**, *27*, 213 - 227.
- [229] M. D. Lechner, K. Gehrke and E. H. Nordmeier, *Makromolekulare Chemie: ein Lehrbuch für Chemiker, Physiker, Materialwissenschaftler und Verfahrenstechniker. 3., überarb. und erw. Aufl.*, Birkhäuser Verlag, Basel, **2003**, p. 14.
- [230] K. Chen, C. A. Mirkin, R.-K. Lo, J. Zhao and J. T. McDevitt, *J. Am. Chem. Soc.* **1995**, *117*, 6374 - 6375.
- [231] E. Lindner, U. Schober, R. Fawzi, W. Hiller, U. Englert and P. Wegner, *Chem. Ber.* **1987**, *120*, 1621 - 1628.

- [232] G. M. McCann, A. Carvill, E. Lindner, B. Karle and H. A. Mayer, *J. Chem. Soc., Dalton Trans.* **1990**, 3107 - 3115.
- [233] E. Lindner, A. Möckel, H. A. Mayer, H., Kühbauch, R. Fawzi and M. Steimann, *Inorg. Chem.* **1993**, 32, 1266 - 1271.
- [234] B. Gollas, B. Krauss, B. Speiser and H. Stahl, *Curr. Sep.* **1994**, 13, 42 - 44.
- [235] W. Kolodziejwski and J. Klinowski, *Solid State Nucl. Magn. Res.* **1992**, 1, 41 - 44.
- [236] S. Dümmling, Einführung in die Arbeitstechniken der Elektroanalytik im AK Speiser, **1996**.

My academical teachers were:

M. Rombourg, C. Bergmann, A. Bernhard, A. Vierling, D. Schontz, D. H. Vaughan, F. Smith, R. Durand, J. N. Chacon, G. L. Patrick, H. M. Rendall, S. Gorham, A. S. Hursthouse, A. McLean, K. Albert, H. Bertagnolli, E. Lindner, H. A. Mayer, U. Nagel, C. Ochsenfeld, V. Schurig, B. Speiser, L. Wesemann, K.-H. Wiesmüller.

Curriculum Vitae

Nicolas Plumeré

Date of birth: 06 february 1979

Place of birth: Schiltigheim, France

- 2004 (November)-
2008 (October) **PhD in chemistry, University of Tübingen, Germany.** Title: “Redox-active modification of silica surfaces via Si-C bond formation”.
Fellowship at the Graduate College “Chemistry in interphases”.
Supervisor: Prof. Dr. Bernd Speiser.
- 2002-2004 **B. Sc. Honours Degree in Chemistry at the University of Paisley, Glasgow, UK.**
Received grade: **A** (first class honours)
October 2003-May 2004, Honours research project
Title: “Development of prototype multi-analyte wells for high throughput screening applications” (biosensor project).
Supervisor: Prof. Dr. Huw D. Vaughan.
- 2000 (January-August)
1999 (May-August) **Research Technician at the Nitrate Elimination Co. Inc., Lake Linden, MI, USA.**
Nitrate biosensor project based on direct electron transfer between Nitrate reductase and pyrolytic graphite electrodes.
Supervisor: Prof. Dr. Bill H. Campbell.
- 1997-1999 **DUT Genie Biologique, Université Louis Pasteur, Strasbourg, France.**
A two year degree in biologic engeneering and chemistry.
- 1997 **Baccalaureat scientifique (Abitur), Lycee Kléber, Strasbourg, France.**